# Spontaneous Compressive Raman technology: developments and applications


Camille Scotté

under the supervision of

Hervé Rigneault

and

Didier Marguet


submitted this thesis in partial fulfillment
of the requirements for the degree of

Doctor
by

Aix-Marseille Université, France

January 2020

PhD Thesis as part of the doctoral school

PHYSICS AND SCIENCES OF MATTER: ED 352

with specialization in: OPTICS, PHOTONICS AND IMAGE PROCESSING

by

Camille Scotté

# Spontaneous compressive Raman technology: developments and applications

## Members of the thesis committee

| | | |
|---|---|---|
| President | Anne Sentenac | Institut Fresnel, France |
| Reviewer | Laurent Jacques | UC Louvain, Belgium |
| Reviewer | Cees Otto | University of Twente, The Netherlands |
| Examiner | Nick Stone | University of Exeter, UK |
| Examiner | Randy Bartels | Colorado State University, USA |
| Advisor | Hervé Rigneault | Institut Fresnel, France |
| Co-advisor | Didier Marguet | CIML, France |
| Invited | Mossadek Talby | Coordinator of the DOC2AMU program |

# Abstract

Spontaneous Raman scattering is a physical process that provides a unique knowledge of materials at the molecular level. Its high chemical specificity with no labels motivates its use in many different fields, ranging from biomedical research to industrial quality control. Nevertheless, the efficiency of this simple process is limited by its extremely weak cross-section.

Typically, the Raman scattered light is dispersed and collected onto an array detector, for several spatial positions of the sample, resulting in a hyperspectral image. Yet, this leads to the generation of overwhelmingly large data sets and to lengthy acquisitions. In situations where hyperspectral measurements simply aim to map the spatial distribution of molecules, the spectral data is unmixed in a postprocessing step, in order to detect molecular species and/or estimate their concentrations. In those cases, acquiring a complete vibrational spectrum per spatial pixel may be inefficient, and a massive speed-up can be achieved by encompassing compressive techniques in the acquisition process. Some strategies, including compressive Raman technology (CRT), use spectral *a priori* information to integrate chemometric analysis directly into the spectrometer hardware: the measurement is designed to directly probe quantities of interest to be estimated (e.g., molecular concentrations), rather than deducing them from complete hyperspectral measurements. In CRT, this is made possible by replacing the array detector by a single-pixel-detector, combined with a programmable optical filter. Based on the *a priori* known spectra of pure molecular species contained in the sample, these filters select accurately chosen spectral components and combine them into the detector.

This thesis develops some theoretical and technological aspects of CRT and applies it to several concrete applications. In a first part of the work, we investigate the estimation precision achieved by CRT, show that our method of estimation is efficient, and experimentally validate this analysis. In a second part of the work, we compare CRT, to some extent, to commercial state-of-the-art instrumentation. We find some clear advantages in terms of acquisition speed and limit of detection. We also show some preliminary results that suggest its usefulness for fields related to biomedical imaging, pharmaceutical industry and the environment. Last, we take further advantage of the single-pixel architecture of CRT to perform multiplexed line-scan imaging. We quantify the potential gain of this approach in terms of signal-to-noise ratio, when the measurements are shot-noise limited.

# Résumé en français

La diffusion Raman spontanée permet de caractériser la composition d'un système chimique avec une forte sélectivité moléculaire. Ne nécessitant pas de marqueur, elle est utilisée dans de nombreux domaines, aussi variés que la recherche biomédicale ou que le contrôle qualité industriel. Néanmoins, l'efficience de ce simple processus est limitée par sa très faible section efficace.

Généralement, le signal Raman est dispersé et détecté par une caméra, et ce pour plusieurs positions spatiales de l'échantillon, pour *in fine* former une image hyperspectrale. Cependant, cela génère de conséquents volumes de données, ainsi que des temps d'acquisition très longs. Dans les cas où l'acquisition d'une image hyperspectrale vise à cartographier la distribution spatiale des molécules, les données spectrales sont dé-mélangées dans une étape de post-traitement, afin de détecter les espèces moléculaires présentes ou estimer leurs concentrations. Dans ces situations, l'acquisition d'un spectre Raman complet par pixel spatial semble inefficace, et des vitesses plus rapides peuvent être obtenues grâce à des techniques d'acquisition comprimées. Certaines de ces stratégies, dont la technologie Raman comprimée (CRT), utilise de l'information *a priori* sur les spectres pour intégrer la chimiométrie directement dans le spectromètre: les mesures sont conçues pour sonder directement les quantités d'intérêt à estimer (ex. concentration des espèces), plutôt que de les déduire de l'image hyperspectrale. Dans CRT, la caméra est remplacée par un détecteur monocanal couplé à un filtre optique programmable. En utilisant les spectres Raman des espèces pures de l'échantillon – connus *a priori* – ces filtres sélectionnent des combinaisons de longueurs d'ondes bien choisies, qui sont ensuite sommées au niveau du détecteur.

Cette thèse développe certains aspects théoriques et technologiques du CRT, et l'applique à des applications concrètes. Dans une première partie, nous étudions la précision d'estimation atteignable par CRT, montrons que notre méthode d'estimation est efficiente, et validons expérimentalement cette analyse. Dans un deuxième temps, nous comparons CRT, dans une certaine mesure, à l'état de l'art des spectromètres Raman commerciaux. Nous trouvons des avantages clairs en termes de vitesse d'acquisition et de limite de détection. Nous montrons aussi des résultats préliminaires qui suggèrent l'utilité de CRT pour certaines applications dans les domaines de l'imagerie biomédicale, de l'industrie pharmaceutique et de l'environnement. Enfin, nous utilisons l'architecture de CRT pour scanner l'échantillon ligne-par-ligne par multiplexage spatial. Nous quantifions le gain potentiel de cette approche en termes de rapport signal sur bruit, quand la mesure est limitée par le bruit de photon.

# Contents

# Introduction

Macroscopic observations constitute our primary understanding of the surrounding world. Our ability to recognize spatial features informs us on the size and morphology of objects, while their color and appearance tell us about their chemical composition. It is the interaction of light with matter that makes metals appear shiny, water transparent, and fruits colorful to the human eye. Despite our capability to perceive many different colors [1], this perception is subjective; our eyesight is not only limited spatially – to features larger than about ten micrometers, but also spectrally - to a narrow range of wavelengths - called the 'visible' spectrum. Undeniably, extending our vision to smaller objects, with a more quantitative perception of colors, is essential to broaden our understanding of the world.

To discern parts of the microscopic realm, simple magnifying instruments have been used for millennia [2, 3], but the advent of optical microscopes in the XVII century revolutionized our knowledge of it. They enabled to observe in detail yet invisible sub-micrometric structures, leading to countless breakthroughs. Optical microscopes are now routinely employed in medical laboratories or for fundamental research, while their performance and practicality are continuously improved [4–6].

Optical microscopes, in their standard form, enhance our spatial vision, but do not ameliorate our color vision. Instead, they essentially reproduce it at the microscopic scale, by using the photoreceptors of our own eyes or a color camera. Nevertheless, when studying living organisms, most molecules appear transparent. Then, with no colors, the optical microscope lacks fundamental information about the chemical nature of the sample. To overcome this problem, colored labels - that target specific molecules – may be employed. For example, in histology, different stains attach to distinct parts of cells: this leads to colorful cell images with violet nuclei and pinkish cytoplasm and membranes [7]. Another technique relies on fluorescent labels: they are designed to attach to specific targets (e.g. proteins, antibodies), or to genetically label the organism under study [8, 9]. These fluorescent probes emit visible light under adequate illumination. This method generally results in chemically specific and highly contrasted images, which greatly improve our understanding of biological structures. Nevertheless, the need for labels may influence the behavior of the target and surrounding organism, and certainly requires time-consuming sample preparation.

To obtain chemically specific images in a label-free way, one solution is to leave the visible spectrum and exploit light-matter interaction in the infrared. Indeed, while most biological molecules

do not absorb visible light, they do absorb infrared light. More interestingly, the wavelengths at which absorption happens are characteristic of the molecular vibration: they provide signatures for molecules, in the form of spectra [10]. Measuring this spectrum directly gives access to the molecular composition of a sample, with high specificity. In order to do so, vibrational spectroscopy is employed. In infrared spectroscopy, infrared light is shined onto a sample and the absorbed frequencies are detected [11]. In spontaneous Raman spectroscopy, visible light is shined onto a sample and the energy absorbed by the molecules during a vibrational transition is indirectly measured by detecting a change of energy in the scattered radiation [12]. Both mechanisms provide a molecular fingerprint solely based on low-energetic light-matter interaction: they are thus label-free and non-destructive. In addition, unlike fluorescence, they are not subject to bleaching. Yet, due to the strong water absorption at infrared wavelengths, Raman spectroscopy is generally preferred for studying samples containing water, such as biological tissues [13]. Overall, combining optical microscopy with Raman spectroscopy results in highly informative content. The resulting hyperspectral images – associating a Raman spectrum in each image pixel - provide quantitative knowledge at the molecular level. Our vision of the microscopic world is not only retrieved, but greatly improved.

Although the advantages of Raman hyperspectral imaging are manifold, two main factors hinder its wider use. Firstly, the Raman signal is inherently weak [14]: this leads to lengthy acquisitions. With the current instruments, imaging an area of a few hundreds of micrometers can easily take minutes to hours. This limits the implementation of spontaneous Raman imaging to slow dynamics and ex-vivo studies. Coherent Raman Scattering could be used to increase the signal, but at the expense, for example, of spectral range or resolution, cost, and complexity [15]. Secondly, while the information contained in a hyperspectral image is considerably more informative than its white light counterpart, it also comprises an incommensurably larger volume of data. A Raman hyperspectral image of a few hundreds of micrometers is often several gigabytes. In general, as our quantity of knowledge increases, so does the required volume of recorded data. This subsequent acceleration in data production starts to challenge our ability to process and store them in a sustainable way. When the information and communication technology ecosystem as a whole is expected to represent between 10 and 20% of our total electricity demand by 2030 [16, 17], such questions cannot be ignored. Surely, various improvements and technological breakthroughs might help us to partly contain this exploding demand [18, 19] , but they are unlikely to diminish our appetite for information and its consequent energy consumption [20, 21].

In such a context, it is relevant, when possible, to search for more efficient ways not only to store, but also to acquire data. In the case of hyperspectral imaging, the acquired data is in general highly compressible [22, 23]. Recent theoretical and technological advances [22, 24–26] offer the tools not only to better compress the data after acquisition, but also to use this compressibility upstream to directly acquire less data, for faster and less memory intensive acquisitions. In some specific cases, this new paradigm can be pushed further: the acquisition process can be modified so that partial processing is performed directly into the hardware [27–29] thereby alleviating

post-processing needs.

In this thesis, we apply the latter concept to Raman hyperspectral imaging in order to mitigate the speed and storage drawbacks. Most of the time in Raman hyperspectral imaging, the actual data of interest is not the hyperspectral data cube itself, but a subset of information derived from it. Even worse, in a number of cases, the chemical species contained in the sample are known, and the user simply wants to map the distribution of molecular species or estimate their concentrations. In this framework at the core of the thesis, the measurements can be specifically designed to probe quantities of interest rather than deducing them from hyperspectral measurements. Instead of recording a complete Raman spectrum onto an array-detector, some of its spectral components are chosen and combined into a single-pixel-detector. The spectral components are selected (i) numerically with an optimization procedure that minimizes the estimation variance, and (ii) physically with a programmable optical filter (digital micromirror device [26]). In this way, this technique, named 'Compressive Raman' (CRT), aims to achieve substantial speed up together with a massive reduction in the generated volumes of data.

This thesis develops some theoretical and technological aspects of CRT and applies it to several concrete applications. Chapter 1 highlights the main underlying mechanisms of Raman scattering and presents the state-of-the-art instrumentation of Raman hyperspectral imaging. The necessity to collect large volumes of data is questioned, especially when the chemical species present in a sample are a priori known. Chapter 2 explains how to use this a priori information in an efficient way to estimate the proportions of chemical species. It presents the fundamental concepts of CRT, both in terms of estimation theory and experimental implementation. Chapter 3 assesses the performances of CRT as compared to state-of-the-art instrumentation, both with theoretical and experimental considerations. Some clear advantages are found, in terms of acquisition speed and limit of detection. Consequently, Chapter 4 shows some preliminary results that suggest the usefulness of CRT for biomedical imaging, pharmaceutical industry, and environmental science. Chapter 5 explores some improvements in the acquisition strategy of CRT. In particular, the single-pixel architecture of the system is further exploited to perform multiplexed line-scan imaging. In Chapter 6, the potential gain of this approach is quantified in terms of signal-to-noise ratio, when the measurements are shot-noise limited.

*This work, initiated by H.B de Aguiar and H. Rigneault, results from a collaboration with P. Réfrégier and F. Galland from the signal processing team (PhyTI) of Institut Fresnel. External collaborations include the groups of N. Stone (University of Exeter) and R. Bartels (Colorado State University). More details are given in the relevant sections. The project has received funding from the European Union's Horizon 2020 research and innovation programme under the Marie Sklodowska-Curie grant agreement 713750. It also received the financial support of the Regional Council of Provence-Alpes-Côte d'Azur and of AMIDEX (ANR-11-IDEX-0001-02).*

# Chapter 1

# Spontaneous Raman scattering: Theory and Instrumentation

**Contents**



Spontaneous Raman scattering is a physical process which involves inelastic scattering of light by matter. When interacting with the molecules present in matter, some portion of the scattered light may experience an energy shift which imprints natural molecular motion, in particular the vibrational motion of molecules about their bonds. These vibrations typically occur at infrared frequencies and are characteristic of each molecule. The scattered signal thus carries a molecular fingerprint solely based on light-matter interaction: This makes the Raman scattering process highly specific and label-free, and explains its use in many different fields, as diverse as biology [30], material science [31, 32], environment [33, 34] or archeology [35].

Although inelastic scattering of light was predicted by A. G. Smekal in 1923 [36], the Raman effect was experimentally demonstrated for the first time in 1928, by C. V. Raman and K. S. Krishnan [12] in India and by G. Landsberg and L. Mandelstam [37] in Soviet Union. Raman

was awarded the Nobel prize in 1930 for this discovery. While Raman scattering was demonstrated by focusing a beam of sunlight onto a sample, the initial commonly used light source was a mercury arc lamp. Nevertheless, the resulting signal was extremely weak. Later, the advent of lasers in the 1960s and the onset of cameras in the 1980s largely contributed to its wider implementation. Yet, the intrinsic low efficiency of the process [14], still restricts its use to slow dynamics and ex-vivo studies, and would benefit from more efficient acquisition strategies.

This chapter provides a general overview of spontaneous Raman scattering, both in terms of theory and instrumentation. We present the main underlying mechanisms of the physical process and describe the simple state-of-the art instrumentation required for Raman hyperspectral imaging. We highlight the drawbacks that motivate the search for alternative acquisition methods, and depict some of them. We conclude on the fact that speeding-up the acquisition certainly requires extensive use of potential *a priori* knowledge held about the data.

## 1.1 Spontaneous Raman scattering

In this section, we highlight the salient principles of spontaneous Raman scattering. Most explanations are based on a classical description of light-matter interaction through the Lorentz oscillator model. Light is thus treated as electromagnetic waves and atoms or molecules are modelled as classical dipole oscillators. Although this simple description is insufficient to understand the mechanisms in detail, it provides a qualitative general understanding and allows to briefly explain the principles of spontaneous Raman scattering. This chapter is mostly inspired from the books of D. Long [14] and M. Fox [38], a book chapter of E. Potma and S. Mukamel [39], a tutorial article of H. Rigneault and P. Berto [40], and from the PhD thesis of X. Audier [41].
Raman scattering can be understood to arise from the coupling of oscillations happening at two different scales : the atom and the molecule. We propose to first describe the behaviour of oscillating dipoles at the atomic level, second to extend the model to molecules, and third to study the coupling of electronic dipoles with the molecular motion.

### 1.1.1 The atomic oscillator model

In classical mechanics, a harmonic oscillator is a system that, when displaced from its equilibrium position, experiences a restoring force proportional to its displacement. This system approximates well many physical phenomena close to their equilibrium state, down to the description of matter at the atomic scale. The idea of considering atoms as oscillating dipoles was originally proposed by H. A. Lorentz in 1878, before J. J. Thomson discovered the electron and E. Rutherford proposed his model of the atom. The oscillator model of the atom assumes that electrons are held in stable orbits around the nucleus. A negatively-charged electron is bound to the positively-charged nucleus via the Coulomb force, and form together an electric dipole.

### Natural Harmonic Oscillator

We consider the oscillator model of an atom introduced above. For simplicity, we consider an hydrogen atom consisting of a positively charged $(+q)$ proton and a negatively charged $(-q)$ electron. This allows us to consider a one dimensional problem and scalar quantities. Since the proton mass can be considered as infinite as compared to the electron mass $(m)$, the proton is treated as stationary. At equilibrium, the electron is situated at a distance $x_{eq}$ from the proton.

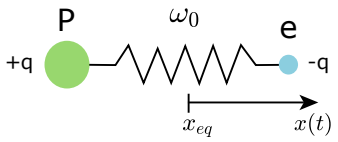


FIGURE 1.1: Simple model of the hydrogen atom

For small displacements about its equilibrium position, the restoring force experienced by the electron can be expressed via the spring constant $k$ and the displacement $x(t)$ :

$$F_k = -kx(t). \tag{1.1}$$

Applying the fundamental principle of dynamics to the electron leads to the harmonic oscillator equation which is:

$$\frac{d^2x}{dt^2} + \omega_0^2 x = 0 \tag{1.2}$$

The solution to this differential equation is a sinusoid of angular frequency $\omega_0 = \sqrt{k/m}$. These natural oscillations produce an oscillating dipole that radiates en electric field at its resonant angular frequency $\omega_0$.
Over time, the electron may lose energy, for instance via internal collisions in the material. This can be modelled by a damping term $\gamma$, characteristic of a friction force proportional to the velocity:

$$F_\gamma = -m\gamma\frac{dx}{dt}. \tag{1.3}$$

Adding this force to Eq. (1.2) results in a equation describing a damped harmonic oscillator:

$$\frac{d^2x}{dt^2} + \gamma\frac{dx}{dt} + \omega_0^2 x = 0 \tag{1.4}$$

The solution to (1.4) depends on the strength of the damping coefficient as compared to $\omega_0$. In the underdamped case $(\gamma < \omega_0)$, the electron displacement $x(t)$ is proportional to a sinusoid with an exponential envelop.

**Driven Harmonic Oscillator**

When a light wave interacts with the atom, it exerts a driving force on the electron of charge $-q$ through the Lorentz force. We restrict the description to the cases where the magnetic field contribution is negligible, and thus write the Lorentz force as:

$$\vec{F_L} = -q\vec{E} \tag{1.5}$$

Since we only handle linear optics in this thesis, we also assume this force to be negligible as compared to the binding force between the electron and nucleus. We consider a monochromatic light wave expressed as an electric field aligned with the oscillator and oscillating at the angular frequency $\omega$. We neglect its spatial dependence since the optical wavelengths are much larger than the atoms or molecules sizes. It is expressed as:

$$E(t) = 2E_0 cos(\omega t) = E_0 e^{-i\omega t} + E_0 e^{i\omega t} \tag{1.6}$$

where $E_0$ refers to the amplitude of the oscillations. The displacement of the electron from its equilibrium position is now governed by an equation of the form:

$$\frac{d^2x}{dt^2} + \gamma\frac{dx}{dt} + \omega_0^2 x = \frac{-q}{m}(E_0 e^{-i\omega t} + E_0 e^{i\omega t}) \tag{1.7}$$

The following generic solution for Eq. (1.7) is considered:

$$x(t) = 2x_0 cos(\omega' t + \Phi) = x_0 e^{-i\Phi} e^{-i\omega' t} + x_0 e^{i\Phi} e^{i\omega' t} \tag{1.8}$$

where $\Phi$ is the phase lag of the electron response to the exciting field. The solution is expressed via its Fourier transform $x(\omega') = x_0 e^{i\Phi}\delta(\omega - \omega') + x_0 e^{-i\Phi}\delta(\omega + \omega')$, which left-term reads:

$$x_0 e^{i\Phi} = \frac{-qE_0/m}{\omega_0^2 - \omega^2 - i\gamma\omega} \tag{1.9}$$

The electric field of the light wave induces forced oscillations of the atomic dipole at its own frequency $\omega$: the displacement $x(t)$ of the electron from its equilibrium position produces a time-varying electric dipole moment :

$$p(t) = -qx(t) \tag{1.10}$$

This oscillating dipole radiates an electric field at angular frequency $\omega$, with a certain phase lag $\Phi$. The field radiated by this dipole is called Rayleigh scattering. The response in amplitude is small unless the light frequency is close to resonance with the natural frequency of the oscillator. The system response to the incoming field can be split in three regimes depending on the value of the driving angular frequency $\omega$ :

- $\omega << \omega_0$: Oscillators are driven below resonance. The amplitude of the oscillations is weak. The oscillations are in phase ($\Phi = 0$) with the exciting field.

- $\omega = \omega_0$: Oscillators are driven at resonance. The amplitude of the oscillations is large. The electron oscillations lag behind the exciting field, in phase quadrature ($\Phi = \pi/2$).
- $\omega >> \omega_0$ : Oscillators are driven past resonance. The amplitude of the oscillations is weak. The electron oscillations lag behind the exciting field, in phase opposition ($\Phi = \pi$).

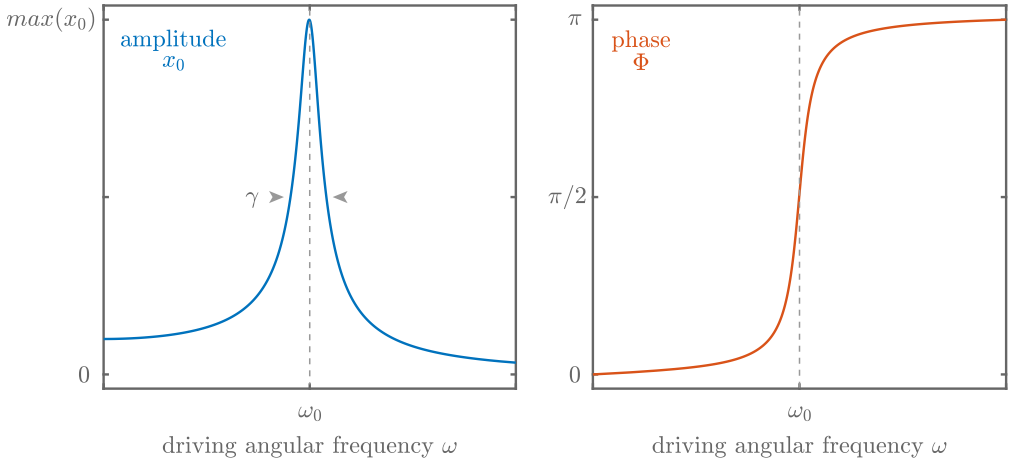


FIGURE 1.2: Representative amplitude and phase spectra of an oscillating dipole response to an electric field of angular frequency $\omega$. At resonance, the oscillations amplitude is large and their phase lags of $\pi/2$.

### Ensemble of Driven Harmonic Oscillators: Optical properties

The above description only involves a single dipole, but many dipoles may be involved. Assuming a medium made of $N$ atomic dipoles per unit volume and that all dipoles point in the same direction, the density of dipoles can be written :

$$P(t) = Np(t) = -Nqx(t) \tag{1.11}$$

$P$ corresponds to the induced polarization, which is a macroscopic measure of the material response to an applied electric field. In the time domain, it can be viewed as a linear convolution between the material time-response and the exciting electric field. In the frequency domain, it writes as a product between the material linear electric susceptibility $\chi^{(1)}$ and the electric field:

$$P(\omega) = \epsilon_0 \chi^{(1)}(\omega) E(\omega) \tag{1.12}$$

$\chi^{(1)}$ is linked to the medium relative permittivity $\epsilon_r$ through :

$$\epsilon_r(\omega) = 1 + \chi^{(1)}(\omega) \tag{1.13}$$

Eq. (1.22) and Eq. (1.9) lead to the following expression for the relative permittivity:

$$\epsilon_r(\omega) = 1 + \frac{\omega_p^2}{\omega_0^2 - \omega^2 - i\gamma\omega} \tag{1.14}$$

where $\omega_p$ is the plasma frequency (collective oscillation frequency): $\omega_p = \sqrt{\frac{Nq^2}{\epsilon_0 m}}$.
The relative permittivity is a complex quantity whose real part $\epsilon_1(\omega)$ and imaginary part $\epsilon_2(\omega)$ can be expressed as:

$$\epsilon_1(\omega) = 1 + \omega_p^2 \frac{\omega_0^2 - \omega^2}{(\omega_0^2 - \omega^2)^2 + (\gamma\omega)^2} \tag{1.15}$$

$$\epsilon_2(\omega) = \omega_p^2 \frac{\gamma\omega}{(\omega_0^2 - \omega^2)^2 + (\gamma\omega)^2} \tag{1.16}$$

It is related to the medium complex refractive index $\tilde{n} = n + i\kappa$, with $\kappa$ the extinction coefficient, through : $\tilde{n}^2 = \epsilon_r$, with : $\epsilon_1 = n^2 - \kappa^2$ and $\epsilon_2 = 2n\kappa$. For a medium with weak absorption ($\kappa << n$), the refractive index is determined by the real part of the relative permittivity though:

$$n(\omega) = \sqrt{\epsilon_1(\omega)} \tag{1.17}$$

While the absorption involves its imaginary part:

$$a(\omega) = \frac{4\pi\kappa(\omega)}{\lambda_0} = \frac{2\pi}{\lambda_0 n(\omega)} \epsilon_2(\omega) \tag{1.18}$$

Relating these optical properties (Fig. 1.3) to the dipole behaviour given in (1.9), one can predict the response of such a medium to an applied electric field. If the light frequency does not coincide with any of the resonant frequencies of the oscillators, there is no absorption and the medium is transparent. Conversely, at $\omega = \omega_0$, there is a resonant phenomenon: energy is absorbed. For these electronic oscillators, the resonant frequency $\omega_0$ typically lies in the UV, VIS or NIR regions. The applied electric field may also induce a phase lag that depends on its angular frequency. The accumulated phase lag in the medium causes a slowing of the wave front propagation thereby modifying the refractive index. We note that close to resonance in dense media, local field effects should be taken into account. Indeed, the individual atomic dipoles respond to the local field experienced, which may not necessarily be the same as the external field, since the dipoles themselves generate electric fields that are felt by the surrounding dipoles.

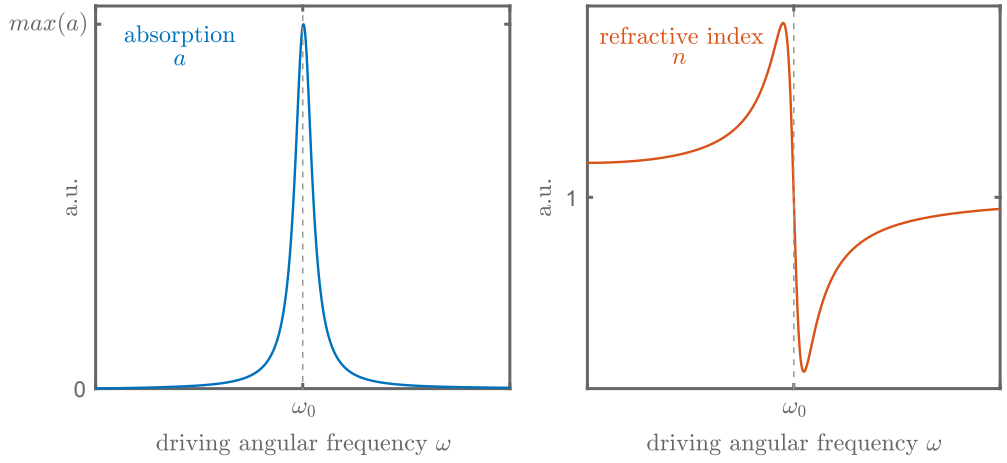


FIGURE 1.3: Representative absorption and refractive of a medium constituted of several dipoles, given by Eq. (1.17) and Eq. (1.18).

### 1.1.2 Vibrational dipoles

The above model provides explanations for electronic resonances, Rayleigh scattering and optical properties of media constituted of a collection of atomic dipoles. In addition to atomic oscillators, a medium may also contain other types of dipole oscillators. For instance, dipoles can be formed by oppositely charged ions in a ionic medium or by oppositely charged atoms in polar molecules. Dipoles can also be induced through molecular vibrations, as we will see in this section.

The dipoles from atoms constituting molecules may be supplemented by dipoles exhibited by the molecules themselves. These dipoles can be permanent (e.g. in polar molecules), or induced (e.g. by the oscillations of the molecular structure itself). If the molecular motion does not modify the electron distribution, the molecule can simply be seen as a juxtaposition of atomic dipoles. The nuclear displacement may lead to a displacement of charges that creates an oscillating molecular dipole. This molecular dipole absorbs electric fields with frequency matching its vibrational frequency. This process corresponds to infrared (IR) absorption. Last, when the nuclear displacement simply perturbs the electron cloud without necessarily creating a molecular dipole, the process of Raman scattering happens.

#### Molecules

The atoms constituting a molecule are bounded by covalent bonds, and may translate, vibrate and rotate. A molecule constituted of $N$ atoms has $3N$ degrees of freedom and $3N-6$ vibrational modes (or $3N-5$ for linear molecules). A vibrational normal mode is associated with a specific resonant frequency that depends on the molecule symmetry, geometry, constitutive atoms, bond types (e.g. $\sigma$ or $\pi$ bond), etc. The vibrational motion of the entire molecule can be described by a superposition of these normal modes, which are specific to each molecule. Normal modes of vibration can also be viewed as phonons. The energy of a vibrational oscillation of angular frequency $\Omega$ is quantized and is equal to $(n+1/2)\hbar\Omega$, where $n$ is the number of quanta excited : molecules therefore vibrate even in their vibrational ground state (Fig. 1.4). These vibrational energies lie in the mid-IR (400 - 4000 $\text{cm}^{-1}$ or 2.5 - 25 $\mu$m). They can occur in conjunction with rotational modes with energies in the far IR (10-400$\text{cm}^{-1}$ or 25-1000$\mu$m).

#### Infrared absorption

In infrared (IR) spectroscopy, one can observe the absorption of molecules at specific frequencies of a broadband infrared light source.
IR absorption can be explained by considering molecules as oscillating dipoles. For this assumption to hold, the molecule must exhibit an oscillating distribution of charges, thus its nuclear

motion must induce an antisymmetric displacement of the center of charges. Second, the applied electric field angular frequency $\omega$ is of the order of the vibrational modes resonant frequencies $\Omega$. Therefore, in this section, the considered electric field angular frequency does not carry enough energy to excite electronic transitions ($\omega \approx \Omega << \omega_0$). The electronic dipole response is negligible, and only molecular oscillating dipoles are considered.
When the internuclear distance is small, the molecule vibrational mode can be approximated by an harmonic oscillator of resonant frequency $\Omega$ (Fig. 1.4).

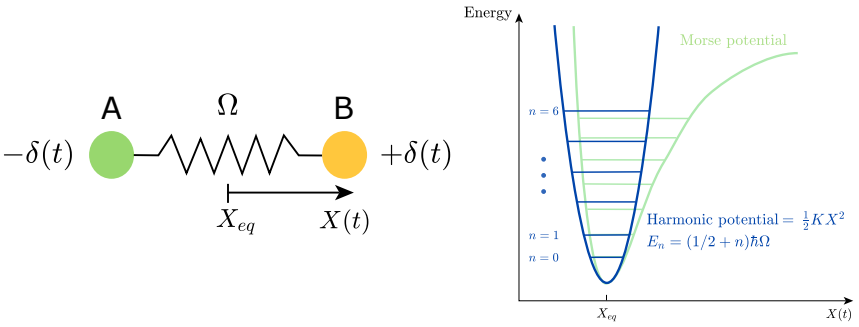


FIGURE 1.4: In infrared spectroscopy, the contribution of the electronic dipoles can be neglected. The molecule motion is assumed to induce an antisymmetric displacement of the center of charges, leading to time-dependant effective charges $\delta(t)$. Close to equilibrium ($X_{eq}$), the elongation vibrational mode can be interpreted by an harmonic oscillator. Vibrational modes are separated by energies of $\hbar\Omega$.

For simplicity we consider the above diatomic molecule and one of its nuclei bound to the center of mass at a distance $X + X_{eq}$ from it. Applying Eq. (1.7) to this molecular dipole leads to :

$$\frac{d^2X}{dt^2} + \Gamma\frac{dX}{dt} + \Omega^2 X = \frac{\delta(t)}{M}(E_0 e^{-i\omega t} + E_0 e^{i\omega t}) \tag{1.19}$$

Where $M = M_A M_B/(M_A + M_B)$ is the reduced mass, $\Gamma$ is the damping coefficient, $\Omega$ is the resonance angular frequency of the molecular dipole, and $\delta(t)$ is the time dependant charge associated with nucleus B. The nuclear displacement $X$ solution to this equation writes similarly to the solution of Eq. (1.9):

$$X_0 e^{i\Psi} = \frac{\delta(t)\ E_0/M}{\Omega^2 - \omega^2 - i\Gamma\omega} \tag{1.20}$$

where $\Psi$ is the response phase lag of the nucleus to the exciting field. Applying this solution to a medium constituted of N of these molecules leads to an induced polarization:

$$P(t) = N\delta(t)X(t) \tag{1.21}$$

which, in the frequency domain, is characterised by:

$$\epsilon_r(\omega) = 1 + \frac{\omega_p'^2}{\Omega^2 - \omega^2 - i\Gamma\omega} \tag{1.22}$$

With $\omega'_p = \sqrt{\frac{N\delta(t)^2}{\epsilon_0 M}}$.

As previously described, the material relative permittivity is related to the medium refractive index and absorption. By measuring the medium absorption and/or phase response, one can gain access to the molecular constitution and behaviour of the medium. When the applied angular frequency $\omega$ does not match molecular vibrational modes, the molecular response of the medium is small. However, if $\omega = \Omega$, the energy is absorbed. In infrared spectroscopy, a broadband IR source is sent onto a sample: the absorbed frequencies - matching the vibrational modes $\Omega_i$ of the $i$ different kinds of present molecules - inform on the molecular constitution of the medium. The interferometric measurement generally associated to the technique allows one to gain access to the phase response and therefore to the medium dispersion. However, not all molecules can be probed with IR spectroscopy, since not all molecules express an oscillating molecular dipole moment. For example, if the diatomic molecule considered is made of two identical atoms (A = B), their electronegativity is the same and therefore the center of charges does not move with molecular motion. For a molecule to be 'IR-active', its motion needs to induce an antisymmetric displacement of the center of charges.

### 1.1.3 Spontaneous Raman scattering

#### Simplified physical picture

Even when the molecular motion does not create an oscillating molecular dipole, it may nevertheless perturb the electron cloud response to an applied electric field. Raman scattering results from such a perturbation.
Unlike the direct absorption processes described above, in Raman scattering, the frequency of the applied electric field does not need to match the resonant frequencies of the system. Rather, the electric field simply needs to induce a perturbation. In general, the exciting field angular frequency is lower than the electronic resonance $\omega_0$ and much higher than the nuclear resonance $\Omega$ ($\Omega << \omega < \omega_0$). The applied frequencies drive the atomic dipoles at $\omega$ but are too high to directly drive nuclear motion.
Let us take the example of a dihydrogen molecule into this electric field of angular frequency $\omega$. This molecule can be modelled as in Fig. 1.5 with A = B = H. Its motion does not exhibit an asymmetric distribution of charges. If the two hydrogen atoms were considered separately, the two atomic dipoles would radiate independently at $\omega$ (Rayleigh scattering). In a $H_2$ molecule, the two atoms are linked by a covalent bound which behaves like a natural oscillator characterized by its resonant frequency $\Omega$ in the ground state. Neglecting damping, its motion can be approximated by:

$$X(t) = 2X_0 cos(\Omega t + \Psi) \tag{1.23}$$

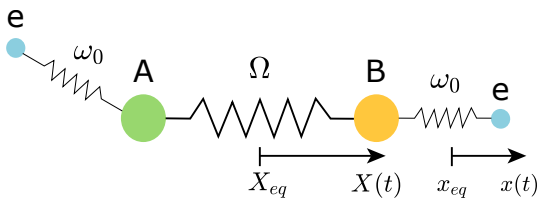


FIGURE 1.5: Simplified model of a diatomic molecule with only one electron represented per nucleus. The nuclear charges and electronic charges are treated as oscillators bound to their respective center of mass. In Raman scattering, the electronic oscillator is directly driven by the external electric field while the molecular oscillator is treated as an undriven natural oscillator.

Raman scattering can be viewed as the coupling between the driven electronic harmonic oscillator - rapidly oscillating at $\omega$ - and the natural molecular oscillator - slowly oscillating at $\Omega$. Since the oscillations happen at very different scales, the nuclei or electrons do not directly drive each other, but are coupled. The coupling could be described via coupled equations as in [41] or better described with a quantum approach. Instead, we choose to describe the coupling with the commonly used notion of polarizability. Although simplistic, this description allows one to envision the notion of coupling and the necessary conditions to induce Raman scattering. We define an equivalent molecular dipole moment:

$$p(t) = \epsilon_0 \alpha(t) E(t) \tag{1.24}$$

where $\alpha$ is the molecular polarizability. It evaluates the response of the electron cloud to the external electric field. Although a material in general cannot polarize instantaneously, in Raman scattering the polarization response can be considered as quasi-instantaneous due to the involved very short-lived virtual states (Fig. 1.7). The perturbation due to the presence of nuclear modes is accounted for by correcting the polarizability with a first order term:

$$\alpha(t) = \alpha_0 + \left.\frac{\partial \alpha}{\partial X}\right|_{X_{eq}} X(t) \tag{1.25}$$

where $\alpha_0$ is the polarizability unperturbed by the nuclear motion. Combining Eq. (1.6), (1.24) and (1.25) leads to a three-termed molecular dipole moment:

$$p(t) = 2\epsilon_0 \alpha_0 E_0 cos(\omega t) + \epsilon_0 \left.\frac{\partial \alpha}{\partial X}\right|_{X_{eq}} E_0 X_0 cos[(\omega - \Omega)t - \Psi] + \epsilon_0 \left.\frac{\partial \alpha}{\partial X}\right|_{X_{eq}} E_0 X_0 cos[(\omega + \Omega)t + \Psi] \tag{1.26}$$

The first term describes Rayleigh scattering, i.e. the unperturbed electronic dipole radiation at the same frequency of the applied electric field $\omega$. The two other terms account for the electronic-nuclear coupling. The latter creates electronic dipoles radiating at $\omega - \Omega$ (Stokes) and $\omega + \Omega$ (anti-Stokes). This scattering process is called Raman scattering (Fig. 1.6(b)).

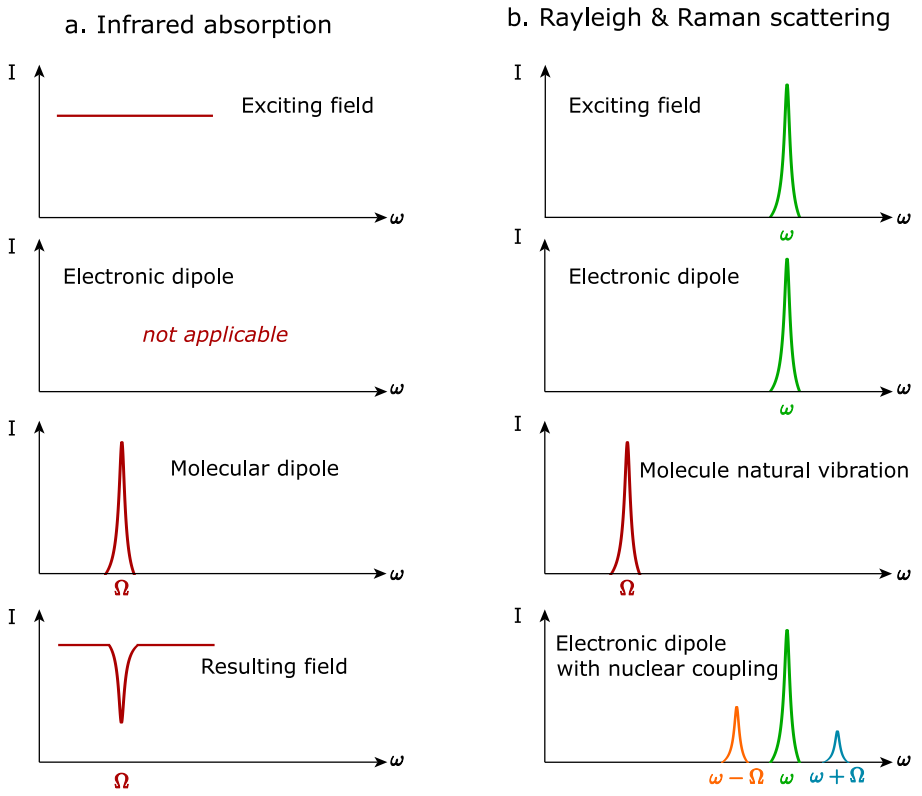


FIGURE 1.6: Electronic and molecular oscillators influence on infrared absorption, Rayleigh scattering and Raman scattering. Infrared absorption is characterised by driven molecular oscillations (a), Rayleigh scattering by driven electronic oscillations (b), and Raman scattering by the coupling of driven electronic oscillations and natural molecular oscillations (b).

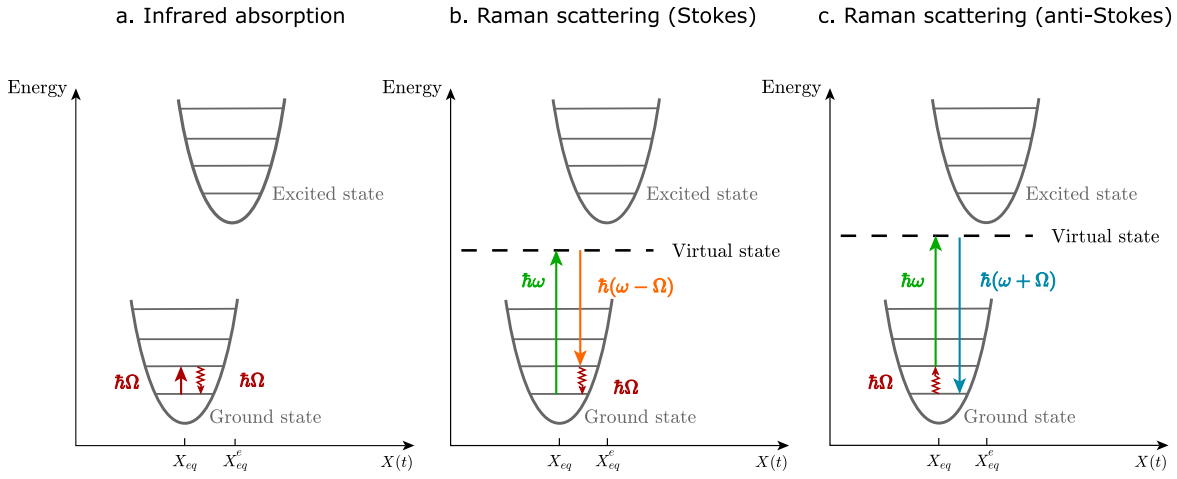


FIGURE 1.7: Energy diagrams for the infrared absorption mechanism (a), Stokes Raman scattering (b) and anti-Stokes scattering, with the molecule already in an excited state of vibration (c). In Raman, the energy $\hbar\omega$ does not correspond to any electronic transition energy and thus is not strictly absorbed. The role of the incident radiation is rather to perturb the molecule and open the possibility of spectroscopic transitions other than direct absorption.

The description of Raman scattering via the molecule polarizability allows to identify a selection

rule for a molecule to be 'Raman-active': its polarizability must be depend on the vibrational coordinates ($\frac{\partial \alpha}{\partial X}|_{X_{eq}} \neq 0$). In other words, the molecule vibrational motion must modify the molecular electron cloud distribution. In the example of the $H_2$ molecule, when the internuclear separation tends to zero the polarizability tends towards that of a helium atom, and as the internuclear separation tends to infinity the polarizability tends to that of two hydrogen atoms: in this case it is clear that the polarizability does change with the internuclear separation. The change in polarizability with nuclear motion can also be viewed in a slighlty different way. Let us suppose for a moment that $\omega \approx \omega_0$ (Resonant Raman). In this case, an electronic transition is excited: the electron experiences large oscillations thus the atomic orbital is largely modified. The equilibrium internuclear distance $X_{eq}$ is thus as well modified into $X^e_{eq}$ (Fig. 1.7). The molecule relaxing to this new equilibrium position generates a vibrational motion: Energy is lost due to the molecule reconformation. This is at the origin of the Stokes shift, which contrasts with perfect isolated atoms in which the absorption and emission lines occur at the same frequency. In non-resonant Raman scattering, there is no real electronic transition ($\omega < \omega_0$) but only very short-lived 'virtual states': The electronic dipole oscillates at $\omega$ with low amplitude. This induces a slight modification of the electron cloud and the molecule has to adapt its internuclear distance very fast such that it is again at equilibrium.

The provided description highlights that Raman scattering arises from the coupling of electronic and vibrational modes of molecules, modelled as a driven atomic harmonic oscillator and a natural molecular oscillator. With an applied electric field of angular frequency $\omega$ ($\Omega < \omega < \omega_0$), the atomic dipoles within molecules radiate a field at $\omega$. Their amplitude oscillations are weak and quasi in phase with the incoming field. They may nevertheless perturb the molecular conformation which itself perturbs the response of the electron cloud to the electric field. This simple picture explains the generation of two new frequencies which relate to the intrinsic molecular identity.

#### Some characteristics of Spontaneous Raman scattering

In the following we give some further characteristics of spontaneous Raman scattering which are relevant for the rest of the thesis.

#### Spectral characteristics

In a Raman spectrum, the wavelength measurement of spectral lines attest for molecular structure and gives a signature of the studied molecular system. The line intensity is proportional to the transition probability, and the natural linewidth is proportional to the inverse of the lifetime of the involved virtual state, which is very short [10, 14]. Raman scattering - associated with picoseconds lifetimes - can be considered as a quasi-instantaneous process, as compared for instance to fluorescence which implies nanoseconds transitions [10, 14]. Another characteristic

of Raman spectra is their asymmetry about the frequency $\omega$. Indeed, often, at laboratory temperatures most molecules occupy their vibrational ground state, as shown by the Boltzmann distribution of the phonon population [10]. Therefore, except at high temperatures, the Stokes signal at $\omega - \Omega$ is stronger than the anti-Stokes signal at $\omega + \Omega$ (Fig. 1.6 - 1.7).
Raman spectra are generally expressed in terms of energy shift rather than absolute energy. In this way, spectral line positions are independent of the excitation wavelength $\lambda$. Raman shifts are typically reported in wavenumbers units ($\mathrm{cm}^{-1}$).

$$\Delta\tilde{\nu} = \frac{1}{\lambda} \pm \frac{1}{\lambda_s} = \frac{1}{2\pi c}(\omega \pm \Omega) \tag{1.27}$$

**Incoherence property**

Spontaneous Raman scattering is an incoherent process: the phase of the molecular vibrations are imprinted on the scattered field, but each molecule in the probed ensemble has a different phase. The fields scattered by each molecule thus add incoherently onto the detector, and the molecules act as independent sources of radiation irrespective of the degree of correlation between their positions [14, 39]. This is in contrast to coherent Raman scattering which drives all molecules in phase, leading to coherent sum of scattered fields and thus to a much higher signal [14, 39]. In addition, the scattered field from N molecules is isotropic.

**Scattered signal properties**

The amplitude of the electric field at frequency $\omega_s = \omega \pm \Omega$ radiated by the associated oscillating dipoles from $N$ incoherent molecules leads to the Raman-shifted light intensity [39]:

$$I(\omega_s) \propto N\omega_s^4 X_{eq}^2 I_0 \left( \frac{\partial\alpha}{\partial X}\bigg|_{Xeq} \right)^2 \tag{1.28}$$

The intensity of the Raman scattered light exhibits:

- a linear dependence regarding the exciting intensity $I_0$
- a linear dependence regarding the number of molecules $N$
- a quadratic dependence on the molecular polarizability change with nuclear coordinates
- a dependence on $\omega_s^4$, and therefore a drastic dependence on the frequency of the exciting field $\omega$.

The latter dependence shows that the strength of the Raman scattered field can mostly be tuned by choosing the frequency of the applied electric field within the range $\omega_0 < \omega < \Omega$. Blue wavelengths are preferred for stronger Raman signal, but their relatively high energy may

excite unwanted electronic states, resulting in overwhelming fluorescence background. On the other hand, NIR wavelengths lead to lower levels of signal but are less likely to excite electronic transitions. They also benefit from low water absorption and are therefore necessary for any use in aqueous media such as tissue.
In all cases, the Raman scattering cross-section $\sigma(\omega_s)$ - related to the signal intensity through:

$$I(\omega_s) \propto N\sigma(\omega_s)I_0 \tag{1.29}$$

- remains extremely small. Only an extremely small fraction of incoming photons, experiences Raman scattering. The spontaneous Raman scattering cross-section is of the order of $10^{-30}$ cm$^2$. This is to compare with fluorescence cross-sections ($10^{-16}$ cm$^2$) or infrared absorption cross section ($10^{-22}$ cm$^2$). This leads in general to very low Raman signal and thus to long integration times.

Overall, vibrational spectroscopy techniques based on Raman scattering and IR absorption offer a label-free optical contrast which gives access to the molecular fingerprint of samples. Both contrast mechanisms are solely based on light-matter interaction and are thus label-free. In addition, Raman and IR spectroscopy offer complementary information. Since their respective selection rules are different, both may be necessary to characterise all vibration modes of molecules.
Yet, for most purposes, only one of the two spectroscopy techniques is sufficient to uniquely identify molecules. At the first look, the lower costs and higher signal levels of IR spectroscopy seem to make it the method of choice for probing samples at the molecular level. However, IR absorption spectroscopy has some severe drawbacks that make it inconvenient for several applications. While Raman spectroscopy involves excitation and detection wavelengths in the visible or NIR, IR absorption involves wavelengths ranging from 2.5 $\mu$m to 25 $\mu$m. This implies low spatial resolution and the use of detectors with poor noise characteristics. Furthermore, water exhibits strong absorption at such wavelengths. Consequently, IR spectroscopy is unsuitable for samples containing water, unless they are dehydrated.
Therefore, spontaneous Raman scattering possesses some key advantages as compared to IR absorption that make it the vibrational technique of choice is number of cases, especially for samples involving water. Nevertheless, its small scattering cross-section leads to low signal levels and long integration times that undermine its utility. In this low signal level regime, the instrumentation must be chosen with care and search to maximize the process efficiency, in terms of speed and signal-to-noise ratio.

## 1.2 Instrumentation for Spontaneous Raman scattering

Spontaneous Raman scattering instrumentation requires: (i) a light source, to illuminate the sample, (ii) a spectrometer, to separate and measure spectral components of the scattered light, and (iii) an imaging system such as a microscope, if an image of the sample is needed. The combination of Raman spectroscopy and microscopy - called 'Raman Hyperspectral Imaging' or 'Raman micro-spectroscopy' - associates a Raman spectrum to each spatial pixel of the sample image. The collected signals can thus be represented as a data cube (Fig. 1.8): each pixel contains two-dimensional spatial information ($x$ and $y$), and one dimensional spectral information ($\lambda$). The information value of such data is substantial, since the chemical composition of the sample can be characterized in each of its resolved spatial points.

In this section, we present different modalities to acquire a Raman hyperspectral image. The aim is to explore which solutions to exploit to acquire this data in the fastest and most efficient way. In the first part, we give a brief overview of some possible ways to acquire a Raman spectrum and image. In the second part, we describe the state-of-the-art instrumentation and its limitations. In the third part, we give examples of alternative instrumentation that could partly improve the conventional setups.

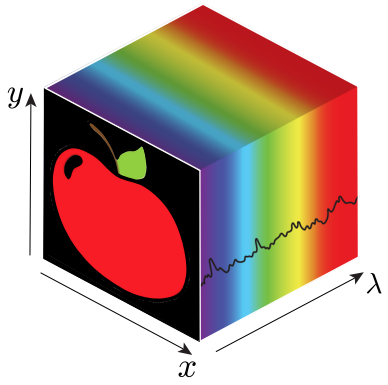


FIGURE 1.8: Schematic representation of an hyperspectral data cube. Each spatial pixel is associated with a spectrum.

### 1.2.1 How to acquire signal in the spatial and spectral domains ?

To acquire an hyperspectral image efficiently, we need to understand how to acquire a Raman spectrum, a Raman image and how to combine the measurements of the two domains.

#### Some acquisition strategies

The hyperspectral data is 3D, while conventional detectors are 0D, 1D or 2D. Thus, one needs to decide how to exploit in the best way the available dimensions of the detector to collect the

3D data (Fig. 1.15). To detect a spectrum or an image, one can for instance implement: (i) parallel acquisition, (ii) raster acquisition and (iii) multiplex acquisition. Parallel acquisition consists in detecting the signals from each channel in parallel onto an array detector. In raster and multiplex acquisition, the detector has only one pixel (single-pixel-detector - SPD) and the measurements are sequential. In the figure below, we define 'channel' as one energy bin of a spectrum or one pixel of an image.

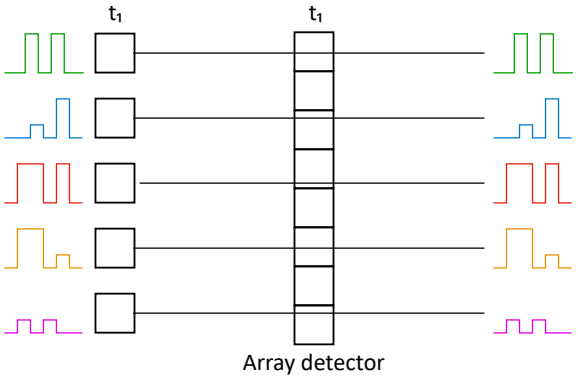


: In parallel acquisition, the signal from each channel is measured separately on different parts of an array detector. All the channels signals are probed and acquired at the same time. The complete information is acquired in one shot after $t_1$.

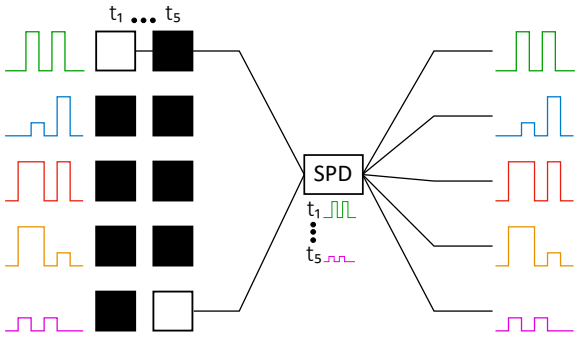


: In raster acquisition, the channels are probed sequentially. The detector detects the signal from each channel separately and one at a time. The entire information from all channels in then recovered after $\sum_i t_i$ .

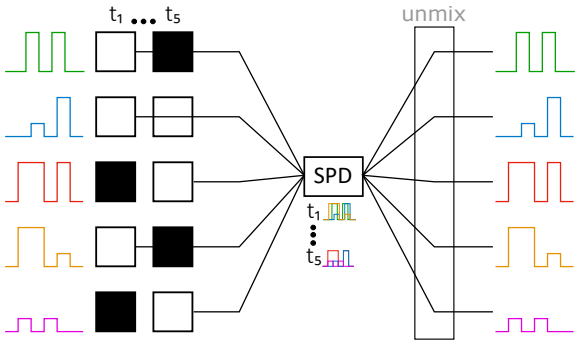


: In multiplexed acquisition, each measurement carries information from several channels. The information can be combined in different ways at the detector. The entire information is recovered after $\sum_i t_i$ or less, depending on the signal nature and multiplexing strategy. It requires a demultiplexing step.

### Implementation in spectroscopy and microscopy

These acquisition strategies are implemented independently in the spectral and spatial domain, in spectroscopy and microscopy (Table 1.1, Fig. 6.2). In spectroscopy, parallel acquisition is performed with a dispersive spectrometer. The latter sorts electromagnetic radiation into its distinct wavelengths components - using a diffractive element such as a grating - and each frequency is measured in parallel onto an array detector. Raster acquisition is performed similarly

with a monochromator : the dispersed wavelengths are probed sequentially with an exit slit and single-pixel-detector. Multiplexed acquisition can be achieved on dispersive spectrometers by replacing the slit by encoding patterns or with Fourier spectroscopy. The various wavelengths combinations measured on a single-pixel detector are then demultiplexed to retrieve the spectrum.

In microscopy, parallel acquisition can be performed with wide-field imaging, using plane wave illumination and an array detector. Raster acquisition is usually performed by scanning a focused laser beam or the object, and by sending the signal to a single-pixel detector. Multiplex acquisition is performed by encoding some pattern in the illumination. This can be achieved by focusing the light at different object locations at the same time, or by modulating an incoming plane wave with a Spatial Light Modulator (SLM). Table 1.1 and Fig. 6.2 give a simplified overview of the examples of implementation mentioned above.

| | Microscopy | Spectroscopy |
|---|---|---|
| Parallel acquisition | Wide-field imaging<br>Camera | Diffraction spectrometer<br>Grating + Camera |
| Raster acquisition | Raster-Scanning<br>Scanning system + SPD | Monochromator<br>Grating + SPD |
| Multiplex acquisition | Patterned illumination<br>Light modulator device + SPD | Fourier-transform / coded apertures<br>Interferometer / coded slits + SPD |

TABLE 1.1: Examples of acquisition strategies in optical microscopy and spectroscopy. (SPD: single-pixel-detector)

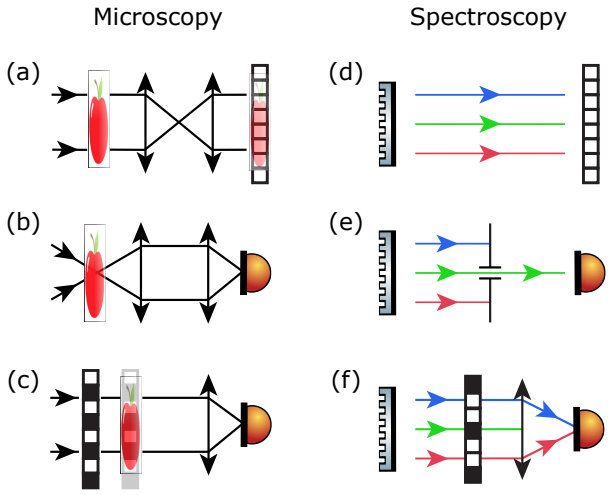


FIGURE 1.12: (a) Wide-field imaging, (b) Raster-Scanning, (c) Patterned illumination, (d) Diffraction spectrometer, (e) Monochromator, (f) Coded-aperture spectrometer.

### 1.2.2 Conventional instrumentation for Raman hyperspectral imaging

#### Typical implementation

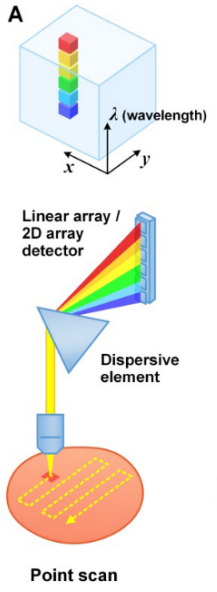


FIGURE 1.13: *Figure from [42]*

The detector used in most of the Raman instruments is a linear array or a 2D camera. Indeed, the wavelength ranges involved in Raman make it possible to exploit silicon-based cameras with relatively good performances, as compared to other spectral ranges (e.g. IR). The use of single-pixel-detector is restricted to specific applications demanding extreme resolutions or detection in spectral domains where cameras are poorly developed. Among the possible combinations, Raman hyperspectral instruments generally makes use of parallel acquisition in the spectral domain, and raster acquisition in the spatial domain. The data cube is generally built by raster-scanning the sample with a point-focus illumination, and recording a spectrum in each of these spatial positions. Less often, the second dimension of the camera is exploited to scan the sample line-by-line (Fig. 1.15 (B)), but this includes other problems discussed in (1.2.3).

In all, conventional Raman hyperspectral imaging systems - combining focused excitation and parallel spectral detection - constitute the state-of-the-art implementation of the technique.

#### General characteristic of the optical system

In a typical hyperspectral imaging system, a laser beam is focused onto a sample. The Raman scattered light is collected and spectrally dispersed onto an array detector - for each spatial position of the sample (Fig. 1.15 A). The essential components of a conventional Raman hyperspectral system involve, in the excitation path:

- An excitation source, typically a continuous-wave laser. It should at least (i) have an narrow line shape (e.g. on the order of 0.1 $cm^{-1}$) - adequate with the desired spectral resolution, (ii) be stable in frequency – to allow accurate measurements, (iii) be very stable in intensity (e.g. $\leq 1\%$ power fluctuations) – to allow quantitative measurements.

- A microscope and objective. Ideally, the optics should not exhibit fluorescence or Raman background. The objective should have a good transmission and a high numerical aperture (NA) to detect the scattered light within a sufficient solid angle.
- A scanning system, which scans the excitation beam (e.g. with galvanometer mirrors) or the sample itself (e.g. with a piezo-electric stage).

And in the detection path:

- Filters that separate the Raman scattered light from the excitation beam and Rayleigh scattered light. Typically, a dichroic mirror separates the excitation wavelength from the collected signal wavelengths, and notch-filters removes most of the remaining laser light and elastically scattered light.
- A confocal slit or pinhole that rejects part of the out-of-focus light.
- A diffractive component such as a prism or grating. The grating dispersion, together with the relay-optics and confocal system, determines the system spectral resolution. Commercial spectrometers achieve resolutions down to 1 $cm^{-1}$.
- Relay optics: Components should be chosen to optimize the spectrometer throughput and to introduce negligible chromatic aberration (e.g. through the use of mirrors instead of lenses).
- A detector array, such as a charged-couple device (CCD) or an electron multiplying charged-couple device (EMCCD), see Appendix B.

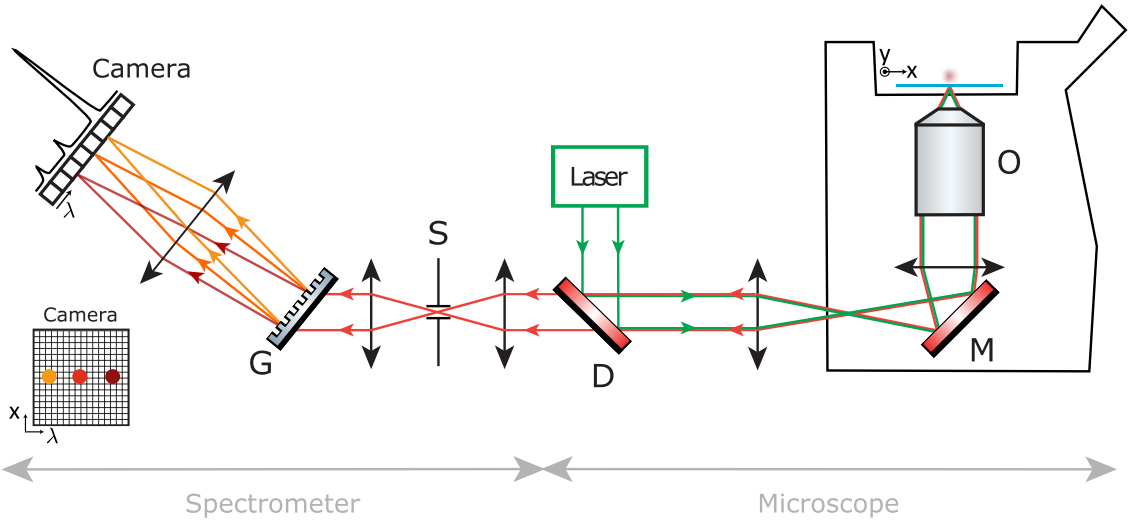


FIGURE 1.14: Schematic of a conventional setup for Raman hyperspectral imaging. Typically, a focused laser beam is imaged onto the sample. The Raman scattered light is collected and selected by filters and a confocal element (e.g. slit). Its frequency components are dispersed (e.g. with a grating) onto a camera. Scanning the laser beam or sample in x and y leads to an image. O: objective, M: mirror, D: dichroic mirror, S: slit, G: grating. Relay optics is represented as lenses but mirrors are often used in the spectrometer (e.g. in the Czerny-Turner design).

### Conventional implementation performances and limitations

The experimental implementation of Raman hyperspectral imaging is thus relatively simple: The label-free optical contrast entails limited sample preparation, and the instrumentation involves a small amount of elements and alignment constraints, as compared to coherent Raman for instance. Nevertheless, it carries some drawbacks.

### Long acquisition times and poor SNR

In most cases, the main limitation of Raman hyperspectral imaging is its associated long acquisition times. This is mainly due to the inherent weak spontaneous Raman cross-section, but also to the detection method itself. The grating combined with the detector array allows to capture a whole Raman spectrum onto the camera at once. This parallel detection scheme is an asset, but it divides the total Raman signal into its spectral components onto different camera pixels. This may lead to very limited flux impinging on each camera pixel. At such low flux, the SNR is typically limited by the camera readout noise (for CCDs - see Appendix B), in which the Raman signal may be buried.
Even at high SNR when noise is not an issue, (EM)CCD cameras are limited by their read-out speeds. This is due to the readout step and to the time necessary to transfer electrons from each pixel row to the readout register (Appendix B). This readout time depends on the number of pixels used (readout of the entire chip, of only a few pixels along x or of all x−axis pixels binned together). Commercially available CCD cameras can at best record one spectrum in 10 ms (with an associated significant readout noise of tens of electrons per pixel). EMCCD cameras can achieve speeds of 1 ms per spectrum with full x−axis binning [43, 44], down to 760$\mu$s when using less than 10 rows along x [45, 46].
Advertised as 'ultra-fast Raman systems' by commercializing companies [45, 46], such speeds still require a minimum of 10 seconds for acquiring an image of 100 $\times$ 100 pixels. Therefore, even the fastest commercial Raman systems are limited to applications requiring relatively slow dynamics.

### Data high dimensionality and heavy post-processing

Hyperspectral images are high dimensional: in many applications one routinely encounters images over 1 GB in size. For example, consider a spectroscopic 16 bits camera with 1600 $\times$ 200 pixels. With full binning along the x−axis, a single spectrum readout from such a camera consists of 2 $\times$ 1600 integer values (pixel number and intensity), which corresponds to a size of 2$\times$ 1600$\times$ 2 bytes/integer = 6400 bytes per spectrum. If a Raman image of 512 $\times$ 512 spectra is recorded, the acquired data accounts for 512 $\times$ 512 $\times$ 6400 = 1.56 GB.
This high dimensionality greatly limits the speed of the post-processing steps generally involved after the acquisition. Indeed, in many cases, the actual data of interest is not the hyperspectral

data cube itself but a subset of information derived from it. Post-processing permits to extract this information. Its purpose may be to detect one specific component (such as a pollutant or contaminant), to classify the image pixels according to spectral signatures, or to obtain a quantitative map of the amount of each chemical species present in each pixel. The strategies may differ if spatial pixels contain pure chemical species or a mixture of chemical species. They also differ whether spectral signatures of components are *a priori* known (supervised case) or not (unsupervised case). In the unsupervised case, the first step generally involves pure components identifications. Numerous techniques have been developed for these different purposes [47–49], including, to name a few, principal component analysis (PCA), Independent component analysis (ICA), Multivariate Curve Resolution (MCR), Non-Negative Matrix Factorization (NMF), or classifiers based on Support Vector Machine (SVM). Then, the final data (e.g. a few-colors image, with each color corresponding to one chemical species) is of very low dimension compared to the initial highly-dimensional hyperspectral image.

**Cost**

Although relatively simple, Raman systems are relatively expensive (between 100k€ and 150k€). This is partly due to the high cost of cameras, best performances EMCCD being worth about 50k€.

Overall, the weak Raman cross-section, coupled with some aspects of the detection scheme and technology, limits the effectiveness of spontaneous Raman hyperspectral imaging. To circumvent the drawbacks of the state-of-the-art implementation, different methods have been or are being explored. One option is to use Coherent Raman Scattering [15], but at the expense of a number of other drawbacks including cost and complexity. In this thesis, we rather keep the physical process identical and rather improve its instrumentation. Based on acquisition strategies presented in 1.2.1, we review in the following some ways to retrieve the spontaneous Raman hyperspectral datacube more efficiently. First, we focus on systems that, as the conventional system, make use of a 2D sensor: they aim at better using the potential for parallel acquisition. Second, we elaborate on alternatives based on single-pixel-detectors.

### 1.2.3 Sources of improvement based on 2D sensors

Hyperspectral imaging is used in a much broader way than just for microscopy, therefore number of strategies have been proposed to acquire hyperspectral datacube efficiently, especially in astronomy. The aim of this section is not to provide an exhaustive list of alternative implementations to conventional Raman hyperspectral systems. Rather, we present a few other techniques of acquisition that have been implemented in Raman (or fluorescence) hyperspectral imaging, based on the use of cameras.
First, we mention some techniques that can improve the collection efficiency of a conventional system. Secondly, we mention different ways of using the 2D sensor, by for instance exploiting

the sensor second dimension to line-scan the sample (Fig. 1.15 B). Another option is to use the 2D sensor to perform wide-field imaging, but then raster-scanning the spectral domain (Fig. 1.15 C). Last, it is possible to use strategies that encode the 3D spatio-spectral information onto the 2D sensor, thereby acquiring the datacube in a single shot (Fig. 1.15 D).

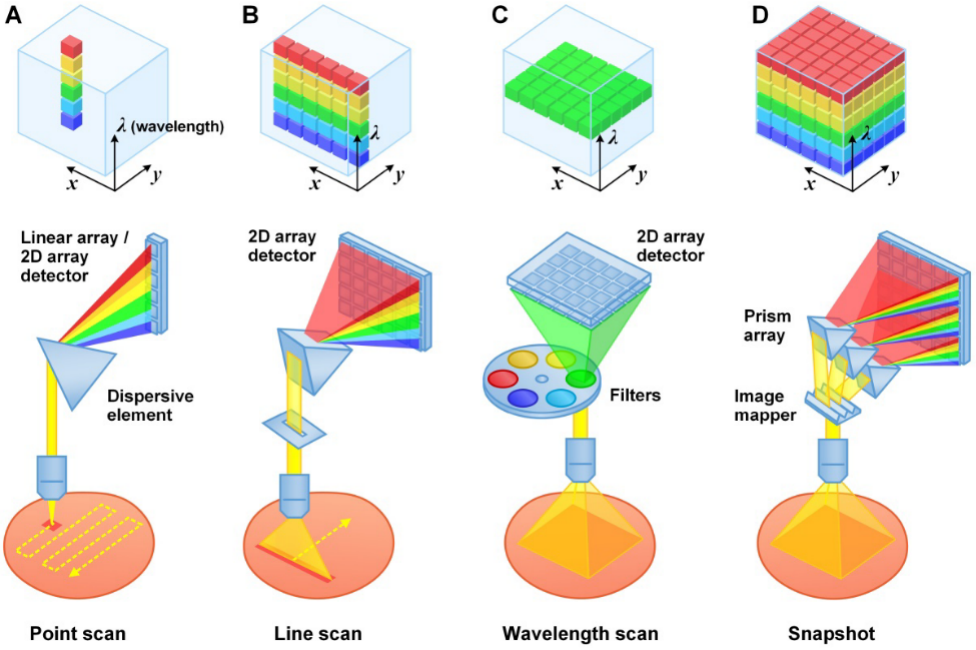


FIGURE 1.15: Typical hyperspectral imaging approaches based on 2D sensors. *Figure from [42]*

### Increase the collection efficiency of conventional spectrometers

Some techniques have been developed to improve conventional spectrometers collection efficiency. In the conventional spectrometer described above [Fig. 1.16], closing the entrance slit improves the spectral resolution at the expense of the amount of light collected by the spectrometer. This throughput-resolution tradeoff can be bypassed, to some extent, by adapting the light distribution to the spectrometer original slit or by modifying the slit itself. Some techniques include fiber-based spot-to-line converters, multi-slits [50], coded-apertures [51, 52] or virtual slits [53–57]. Usually, these techniques come at the price of increasing complexity and are sometimes not suitable for imaging spectrometers. Some Raman spectrometers using these techniques are being commercialized at small scales but are not widely implemented.

### Perform spatial-line scanning

The most straight-forward way to speed-up the acquisition is to make use of the two-dimensionalities of the sensor by perform line-scanning of the image (Fig. 1.15 B). A cylindrical lens creates a line-focus which is imaged onto the CCD pixels along the x-axis [58]. The image can thus be

build line-by-line instead of point-by-point.
However, trade-offs include [59]: (i) an increase of the readout-speed and/or noise of the cameras (since more pixels have to be readout), (ii) a diminished signal since the laser power is distributed over a larger area - or the need for more powerful laser sources, (iii) typically a non-uniform line profile that leads to variations in spectrum intensity along the line. Some strategies have been developed to partially mitigate these disadvantages [60], and a line-scanning modality is implemented in some commercial Raman micro-spectrometers.

#### Perform wide-field imaging and wavelength scanning

An alternative is to use well-resolved and fast-scanning techniques to scan the spectral axis (Fig. 1.15 C). Methods using fast rotating Bragg tunable filters have for instance been developed and applied to Raman hyperspecral imaging [61].

#### Collect the entire datacube simultaneously: Snapshot-spectrometers

If the 3D spatio-spectral information can be encoded onto the 2D sensor, the entire datacube can be acquired in a single shot (Fig. 1.15 D). Snapshot spectrometers simultaneously measure all elements of the datacube; thereby removing the need for any scanning part and increasing the collection efficiency. They typically incorporate specialized components to distribute the 3D spatio-spectral information in 2D. Postprocessing is then required to reconstruct the 3D hyperspectral datacube from the 2D data. Many different snapshot spectrometers have been introduced, especially in astronomy. Some implementations, reviewed in [62], include: (i) techniques based on spectral filters [63–65], which use for instance spectrally resolved cameras, (ii) computed tomography imaging [66], which uses 2D dispersion elements, (iii) integrated-field spectrometry, based on image reformatting, and (iv) compressive coded aperture spectral imaging, based on coded apertures and data compressibility. Although snapshot spectrometers are relatively well-established and common in astronomy, only a few have been implemented recently in fluoresence microscopy [67–69] and Raman microscopy [70]. They fall in the categories (iii) and (iv) that we chose to briefly describe in the following. More details and references can be found in the review from Hagen and Kudenov in [62].

#### Integrated Field Spectroscopy

The first snapshot spectrometers were introduced in the 1930s. They can be grouped under what is known as Integrated Field Spectroscopy [62, 71]. In these methods, each individual measurement results from integrating over a region of the object.
Some are based on image slicers made of mirror arrays: A series of tilted mirrors (for example a Bowen-Walraven image slicer [72, 73]) slices the image into strips. The object is thus divided into sub-objects which are then reorganized along the slit.

Others techniques are based on fiber reformatting [74, 75]. For example, the object is imaged onto the face of a coherent fiber bundle. At the opposite end of the bundle, the fibers are reformatted into a linear array compatible with the input of a standard slit spectrometer. In this way, one spectrum is obtained for each fiber.
Other options, also introduced in the early 1960s make use of lenslet arrays [76]. A lenslet array is placed in the entrance slit plane, essentially acting as spatial pixels. The fourier transform of each subpixel then undergoes dispersion, and the signal from each individual lenslet signal results into a spectrum.
Such techniques are mostly used in astronomy and have been implemented on some telescopes. These approaches present some limitations in terms of resolution and bandwidth and come at the price of higher complexity. They have been only recently implemented in microscopy [67, 68], with optical sectioning capabilities comparable to that of a confocal microscope [69].

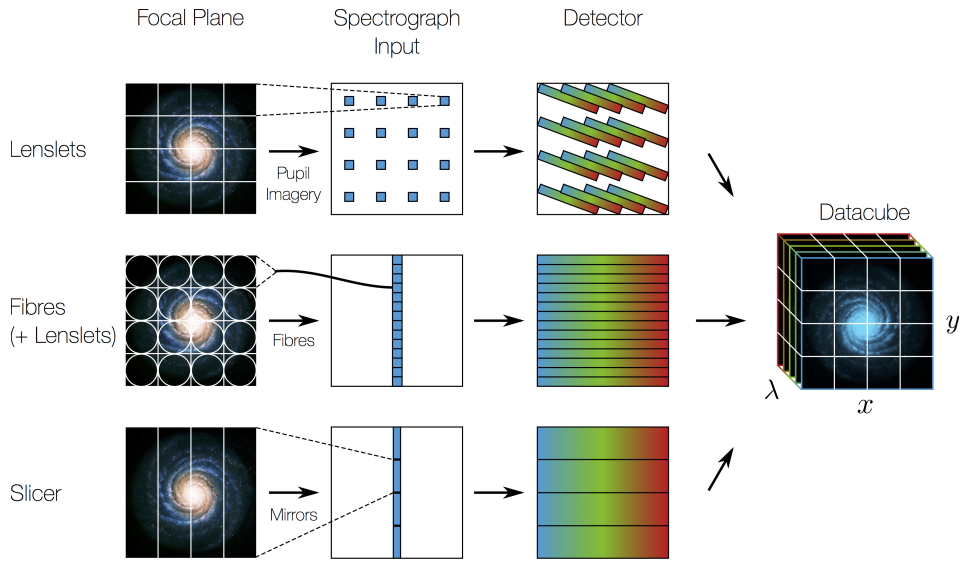


FIGURE 1.16: Common designs for integrated field spectrometry. *Figure available* here.

### Compressive Coded Aperture Spectral Imaging (CASSI)

CASSI is the first snapshot technique to make use of the compressibility of the data cube. It multiplexes space via an encoded aperture, and uses the camera to record the spatio-spectral information (Fig. 1.17) [77–84].
The concept for CASSI can be seen as a generalization of coded aperture spectroscopy [51, 52]. The entrance slit of a conventional dispersive spectrometer is replaced with a wide aperture, inside which is inserted a binary-coded mask. The signal from the object $f(x, y, \lambda)$ is encoded by this spatial mask $T(x, y)$, and then dispersed along one dimension with a dispersive element $S(\lambda)$. This results in smeared columns: On the camera, one axis carries only spatial information, while the other axis carries a mixture of spatial and spectral information. If the dimensions of the hyperspectral datacube to recover is $N \times N \times L$ (for x, y and $\lambda-$axis respectively), the

dimensions of the measured intensity map is $N \times (N + L - 1)$. The recovery of the hyperspectral signal thus entails solving an undetermined linear system of equations, and using of post-processing strategies based on compressive sensing [25, 85–88].
In all, CASSI allows light collection over a wide aperture and sensing of the entire data cube in a single shot. However, except for simple spatio-spectral objects, most often a single-shot measurement is not sufficient. Additional measurements are usually required, each with a distinct coded aperture that remains fixed during the integration time of the detector. Further limitations lie in the compressive sensing reconstruction methods which are currently sensitive to perturbations of the system matrix, which thus needs to be carefully calibrated. Although very promising, experimental implementations (e.g. in Raman microscopy [70]) are not yet convincing enough as compared to their scanning counterparts.

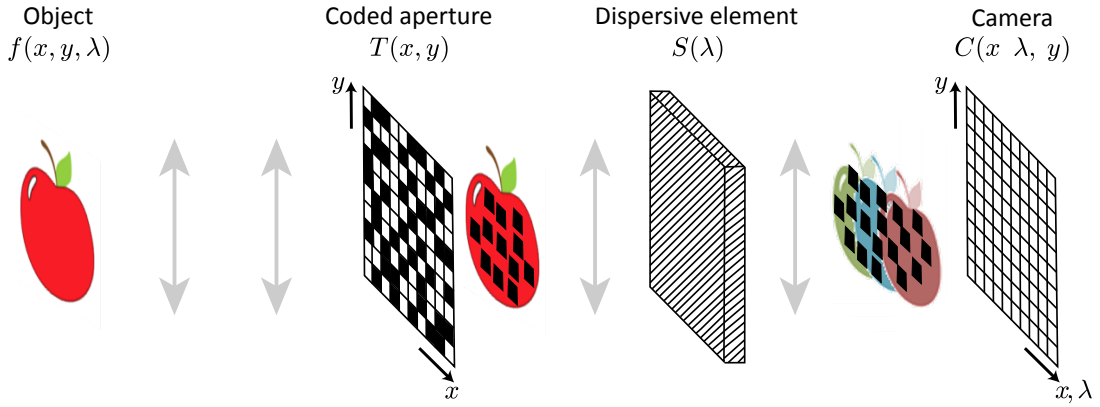


FIGURE 1.17: CASSI principle.

**Conclusion on the sources of improvement using 2D sensors**

We briefly presented some alternative instrumentation for Raman hyperspectral imaging. Implementations bringing some improvement in collection efficiency or better scanning-efficiency (line-scanning) are sometimes implemented for commercial use but at small scales. Groundbreaking change for Raman acquisition may lie in single-shot acquisition of a hyperspectral data cube. Still, while snapshot systems are featured prominently in the research literature and were first introduced more than 80 years ago, none of these instruments have seen wide adoption outside the professional astronomical community. In this context, the current state-of-the-art Raman micro-spectrometer is still the conventional setup described in 1.2.2.
Snapshot spectrometers certainly offer many advantages: there is no moving parts, the entrance slit of the spectrometer is removed or better exploited to bring a major improvement in light collection efficiency, and the whole hyperspectral data cube is acquired at once. Therefore, they are very promising techniques that may benefit from future improvement in detectors array technology and that may drastically reduce the acquisition times. However, these advantages can only be achieved by making use of large detectors arrays, which exhibit drawbacks such as readout speed and noise - the latter being worse with the number of pixels used. In the low flux regime which is typical in Raman, the measurements are thus likely to be limited by the

detector readout noise. Furthermore, while the potential of snapshot systems is great to improve the acquisition speeds, it does not bring improvements in terms of cost, since the setups require costly large detector arrays and more complexity than the conventional system. Most importantly, these measurements generate overwhelming volumes of data that must be dealt with in order to take full advantage of them. This high dimensionality is more problematic than in the conventional system. Indeed, the entire datacube must be stored, transmitted (e.g. with onboard compression [89]) and postprocessed in a more complex way than in the conventional system. Reconstruction of the entire datacube can be significantly long. Although the measurement itself may be fast, this high dimensionality seriously undermines the snapshot spectrometers capabilities, especially for real-time imaging. As an example, in CASSI recent Raman implementation [70], the acquisition of the whole hyperspectral data cube ($1024 \times 205 \times 1024$) on one core of a 2.4 GHz processor (Intel, Xeon) required approximately 10 GB of RAM and 22 h, though this time could be reduced with better processors.

### 1.2.4 Sources of improvement based on single-pixel-cameras

Overall, the acquisition of an hyperspectral datacube seems relatively inefficient. Significant time and/or storage is spent acquiring overwhelmingly large data sets, which then undergoes postprocessing to extract useful information of very low dimensionality. Yet, most of the time, substantial *a priori* information about the hyperspectral datacube is held and may be used efficiently.

The first valuable *a priori* information is that, in their vast majority, hyperspectral images are extremely redundant. Consider the case of a sample composed of two pure chemical species to be classified. The whole hyperspectral datacube typically represents several GB of data. Yet, first, the spectral information is highly redundant (only two possible types of spectra). Second, unless the species spatial distribution is random at the pixel level, the sample presents some spatial structure and thus compressibility. Beyond this simple example, hyperspectral datacubes present significant structure and therefore little information content as compared to their dimensionality[22, 49]. In other words, the spatio-spectral matrix derived from this datacube is highly compressible. This significant *a priori* information perfectly falls in the framework of compressive sensing [25, 85–88], matrix completion [22, 90], and single-pixel cameras [91]. The main idea is to use the data compressibility together with a single-pixel detector, to reduce the number of measurements and be faster. Although the use of single-pixel detectors requires sequential scanning, they largely surpass cameras in terms of readout speed and noise properties. The compressibility of images is exploited in the microscopy community (e.g. [92, 93]). Some experimental work has been reported in hyperspectral imaging but either use cameras or imaging at only a few wavelengths [94–96]. To our knowledge, single-pixel imaging applied to hyperspectral microscopy has only been shown experimentally in the past 3 years [97–102]. Among them, only [101] reports the use of a single-pixel-camera for Raman hyperspectral imaging.
The mentioned techniques are powerful since they rely on *a priori* information which holds

for most hyperspectral datacube. They can lead to substantially fewer measurements than the original data dimensionality, and thereby faster speeds. However, they still require two post-processing steps: (i) the reconstruction of the entire hyperspectral datacube (ii) the extraction of relevant information from it. In all, compressibility is used in the measurement, but highly dimensional data is still generated before applying a chemometric step to extract useful information of low dimensionality.

Another type of *a priori* information one might hold about an hyperspectral data cube is the chemical species it contains. Many practical cases fall in this class of problems, such as the detection of contaminants, quantification or classification of some chemicals – in industry, histology, environmental science, etc. When one *a priori* knows the chemical species contained in the sample, and simply wants to estimate their proportions or spatial distribution, reconstructing a whole hyperspectral datacube is highly inefficient. The latter considerations are at the origin of alternative approaches based on compressive Raman technology (CRT) that have recently been proposed for quantification or classification of know species. The idea is to incorporate chemometric analysis directly into the spectrometer hardware. Thus, the measurement is designed to directly probe quantities of interest (species proportions or class) instead of deducing them from complete hyperspectral measurements. This technique constitutes the core of this thesis.

## 1.3 Conclusion

In this chapter, we briefly described the optical contrast used in this thesis. A simple description of the underlying theory helped to understand some important properties of spontaneous Raman scattering. Although it is incoherent and exhibits an extremely small scattering-cross section, this effective process probes molecular fingerprint of samples. The necessary instrumentation to obtain a Raman hyperspectral image is relatively simple. However, the cameras characteristics limit the signal-to-noise ratio or speeds of state-of-the-art systems: the minimum achievable pixel-dwell times about 1 ms per spectrum limit the implementation of spontaneous Raman to slow dynamics. Alternative techniques have been proposed, but none have yet demonstrated enough efficiency to replace the conventional systems. More recently, some techniques have used the hyperspectral datacube compressibility together with single-pixel-detectors, but they still exhibit some limitations and generate highly dimensional data. Nevertheless, in many situations, the chemical species contained in the sample are already known, and Raman hyperspectral measurements actually simply aims to map the spatial distribution of molecules. Then, acquiring or estimating the whole hyperspectral datacube is inefficient, and a massive speed-up can be achieved by encompassing compressive techniques directly into the hardware. Designing the measurement according to the quantities of interest to be estimated is the core of what we call 'Compressive Raman technology' (CRT) and the subject of the four following chapters.

# Chapter 2

# Principles of Compressive Raman

**Contents**



In the previous chapter, we focused on different strategies to acquire hyperspectral datacubes in an efficient way. Yet, we questioned the necessity to collect such large volumes of data, especially when *a priori* information is held. In particular, when the chemical species present in a sample are known, the acquisition of a whole hyperspectral datacube is inefficient. Essentially, the spectra do not need to be recorded. In this thesis, the aim is no longer to acquire the full Raman hyperspectral datacube, but rather to use the *a priori* information in an efficient way for a specific task - such as determining chemicals proportions. This is at the essence of compressive Raman: the knowledge is used directly into the hardware to directly probe quantities of interest, instead of extracting them from the hyperspectral datacube.

This chapter presents the salient principles of compressive Raman. In the first part, we introduce the general concept of compressive spectrometers, together with a short historical review. In the second part, we highlight the key points of the underlying estimation theory. In the third part, we show two proof-of-concept experiments that support the theory and methodology.

## 2.1 Compressive Spectrometers

### 2.1.1 General concept

With a conventional spectrometer (Fig. 2.1 (a)), each pixel of an hyperspectral datacube contains a spectrum. Each spectrum may result from the mixture of several pure chemical components. To estimate the chemicals proportions in each pixel, two post-processing steps are involved: the first step generally requires the extraction of endmembers such as the pure species spectra (1.2.2); the second step can for example consist in projecting each recorded spectrum onto these endmembers (1.2.2).
When the chemical species present in a sample are *a priori* known, the spectrometer may be modified to perform certain operations optically. The camera can be replaced by a combination of spectral filters and a single-pixel-detector. These two elements allow to perform an optical dot-product in the spectral domain: the spectrally dispersed signal is filtered and summed onto a single-pixel-detector (Fig. 2.1 (b)). The resulting signal contains chemical information that is extracted without recording a spectrum. The spectral filters, also called 'multivariate optical elements', can for instance take the form of interference filters, spatial light modulator (SLM) or digital-micromirror device (DMD). Their design is application specific: it depends on the spectra of the pure chemical species and on the type of chemical analysis performed (classification, estimation of concentrations, etc.). Since it performs optical operations, the resulting instrument is referred to as a 'multivariate optical computer' [103]. And since it directly probes information of low dimensionality, it is also sometimes named 'compressive spectrometer'. When applied to Raman spectroscopy, we refer to it as Compressive Raman or Compressive Raman Technology (CRT).

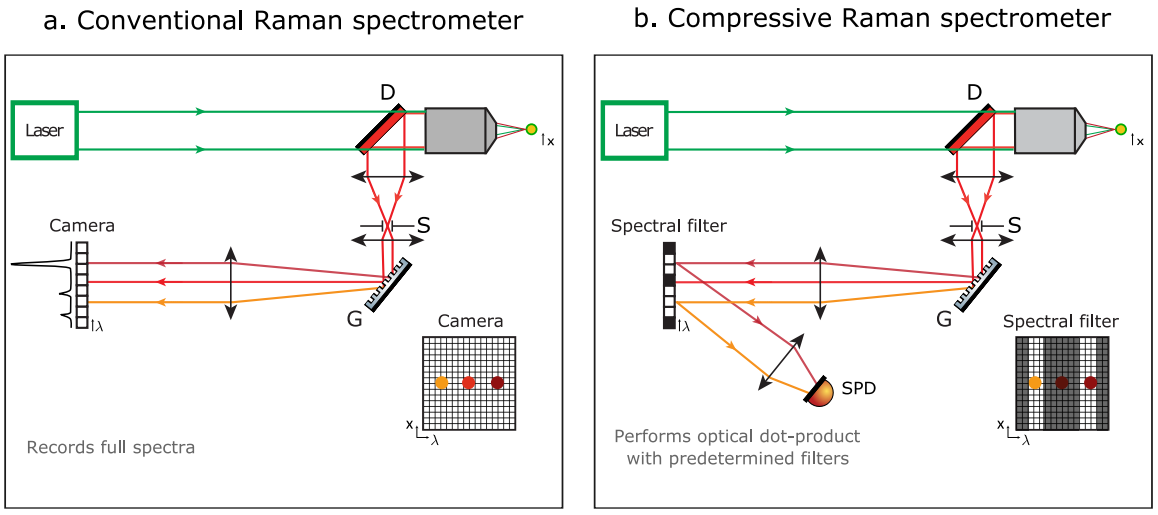


FIGURE 2.1: A compressive Raman spectrometer (b) is similar to a conventional spectrometer (a), in which the camera is replaced by a single-pixel-detector (SPD) combined with a spectral filter. While in (a), species proportions are extracted from the Raman spectrum, in (b) the knowledge of the chemical species is used to design the filters. An optical projection is performed, allowing to extract proportions information without recording a spectrum.

### 2.1.2 Previous (and on-going) work

The concept of multivariate optical computing dates back from 1986 [27]. In this paper, S. E. Bialkowski described 'a simple apparatus for optical spectroscopic signal processing' and set the basis of the signal processing framework. The idea was refined in 1991 in [104].
The first experimental demonstration of was reported in 1998 [28]. The multivariate optical computer was then based on interference filters, specifically designed to reproduce the eigenvectors obtained from chemometric techniques such as principal component analysis (PCA). This work was further developed by the same research group in [105–107]. This technique was subsequently exploited for fluorophores discrimination [108–110]. It started to be used, about 5 years ago, in the oil and gas industry for the detection of hydrocarbon composition in oil wells [111, 112]. Although interference filters make the devices compact, robust and stable, their relatively poor spectral resolution and inflexibility hinder their applicability, since the design and manufacture of a new interference filter is necessary for each new application.
To allow more flexibility, devices using liquid-crystal-based SLMs for were introduced in 2006 in [113] and 2011 in [114]. In [113], the instrument was used to estimate proportions of solvents from their Raman signal. In [114], the actual speed advantage of the technique for Raman imaging was shown: a distribution of sucrose and glucose crystals was mapped with a pixel-dwell time of a few ms. Such a device was also used for the classification of pharmaceutical components with integration times of a few tens of ms [115]. A similar instrument with 2 single-pixel-detectors was reported in 2014 [116]. However, SLMs require to operate on linearly polarized light, are expensive and relatively slow ($\approx$ 500 Hz update rates). In comparison, DMDs have faster switching rates (up to 22kHz) and are cheaper.
Although the first reported use of a DMD in spectroscopy dates back to 1995 [117], DMDs were

first used for multivariate optical computing in 2008 [29, 118], for Raman and fluorescence spectroscopy. From 2012, substantial work was carried by Wilcox et. al for Raman rapid imaging [119, 120]. The same group further developed the technique (i) in 2015, to take into account potential fluorescence background [121] and (ii) in 2017, to implement two single-pixel-detectors [122]. Other DMD-based compressive spectrometers include spectrally-resolved thermal cameras [123–125]. A NIR spectrometer has also been commercialized by Texas Instrument since 2014 [126].
In the past year, some work using compressive spectrometers were reported for fluorescence spectroscopy [127], for Raman imaging with time-gated fluorescence [128] and for stimulated Raman scattering [129]. A review (*Recent trends in compressive Raman spectroscopy using DMD-based binary detection*) has also been published [130].

### 2.1.3 Potential for Raman applications

In Chapter 1, we pointed out the main drawbacks of conventional Raman spectrometers, and saw that they seriously hinder the wider use of Raman technologies. Conversely, when pure constituents are known or accessible, compressive spectrometers present substantial potential for Raman applications, in terms of:

- Signal: Instead of being spectrally dispersed onto an array detector (Fig. 2.1 (a)), several wavelengths are multiplexed onto a single-pixel-detector (Fig. 2.1 (b)), leading to more signal. For example, if a uniform Raman spectrum of 1000 photons is distributed over 1000 pixels of a camera, the resulting signal of 1 photon per pixel leads to poor SNR in the best case, or to undetectable Raman photons in the presence of camera noise. On the contrary, if the compressive spectrometer selects half the spectral bases, more photons (500) are sent to a very low noise detector.
- Speed, in the acquisition: the readout speed of cameras no longer limits the acquisition rate in the high signal regime.
- Speed, in post-processing: the generated data is of very low dimension as compared to the hyperspectral datacube, and requires little post-treatment since part of the processing is performed optically
- Cost: the multivariate optical element and single-pixel-detector are together typically less expensive than a spectroscopic camera.

Nevertheless, it is only after the spectral filter functions have been established, through a training step or a calibration procedure, that the full speed advantages of this technique can be realized. It is therefore mostly useful for chemical analysis, when several experiments with the same kind of chemicals and same purpose are conducted.

All these advantages build strong motivation to use compressive spectrometers for some specific Raman applications: In particular, boosting the acquisition speed could ultimately enable wider industrial use, *in vivo* imaging or characterization of dynamic processes. However, despite recent advances in the field, the best performances shown so far in compressive spontaneous Raman imaging consist of images of simple chemical crystals (e.g. fructose and glucose [119]), with little scope for applications, except for some experiments on pharmaceutical components [115, 122]. In this context, our work constituted in further developing this technology, in better quantifying the mentioned advantages, and in exploiting it for some concrete problems.
In the following, we present the general formalism and some additional developments brought to the existing theory. We also demonstrated some proof-of-concept experiments that validate our implementation of compressive Raman.

## 2.2 Proportion estimation in Compressive Raman

*The results of this section arise from a work carried in collaboration with P. Réfrégier and F. Galland (Institut Fresnel). They have been published as a journal paper 'Precision of proportion estimation with binary compressed Raman spectrum' in [131].*

We place ourselves in the following framework: We suppose the sample is a mixture of pure chemical species with known Raman spectra. The aim is to estimate in which proportion the species are mixed, as accurately and precisely as possible.
Intuitively, we may understand that this problem entails two main difficulties: the measurement noise and the similarity between spectra: Even at high SNR, the estimation may be difficult if the pure spectra are highly correlated with each other. On the other hand, even if there are only two chemicals with orthogonal spectra, the estimation may still be difficult if the SNR is sufficiently low. To take into account these parameters, we need to model the system and consider the noise of the physical system.

Two major steps are implied in this problem. The first step is the design of relevant spectral filters, which are supposed to be binary. Naturally, one would choose the most prominent spectral peaks of each chemical species. Yet, most often, the problem is too complex for such a simple design. The second step is the choice of the estimation method, that allows one to estimate the proportions of the chemical species from the measurements.

### 2.2.1 Problem formulation

To begin with, we define the problem variables, visually presented in Fig. 2.2. We denote:

- $Q$ : number of pure chemical species present in the sample ($q = 1...Q$)
- $M$ : number of spectral filters, with $M \geq Q$ ($m = 1...M$)
- $L$ : number of energy bins along a Raman spectrum ($l = 1...L$)
- $\mathbf{y}$ : $L \times 1$ vector containing a Raman spectrum, mixture of $Q$ pure chemical species
- $\mathbf{S}$ : $L \times Q$ matrix of known Raman spectra. $\mathbf{s}_q$ of the spectrum of the $q^{th}$ pure chemical species. (in units of counts/s)
- $\mathbf{c}$ : $Q \times 1$ vector of unknown chemicals proportions to estimate
- $\mathbf{F}$ : $L \times M$ matrix of the $M$ binary spectral filters $\mathbf{f}_m$
- $\mathbf{b}$ : $M \times 1$ vector of noiseless measurements. Its $m^{th}$ element contains the projection of $\mathbf{f}_m$ on $\mathbf{y}$.
- $\mathbf{n}$ : $M \times 1$ vector of noisy measurements.
- $\tau$ : $M \times M$ diagonal matrix which elements contain the exposure time $\tau_m$ of filter $\mathbf{f}_m$.

For simplicity, other variables that might be relevant for the model (system transfer function, quantum efficiencies, etc) are directly incorporated into the matrix $\mathbf{S}$.

Suppose a sample consisting of a mixture of $Q$ chemical species. Each species Raman spectrum $\mathbf{s}$ is known. Each spectrum consists of $L$ spectral bases distributed over a certain frequency bandwidth, and is assumed to be positive ($s_{lq} \geq 0$). Furthermore, the chemical mixture is assumed to be linear with proportions $c_q$. The resulting Raman spectrum of the sample $\mathbf{y}$ reads:

$$\mathbf{y} = \mathbf{Sc} \tag{2.1}$$

In compressive Raman, combination of frequencies - selected by a binary spectral filter $\mathbf{f}_m$ - are summed onto a single-pixel-detector, leading to a measurement $b_m$. Formally, the filters $\mathbf{f}_m$ are projected, during time $\tau_m$, onto the pure spectrum $\mathbf{s_q}$ weighted with its relative proportion coefficient $c_q$. This optical projection of filters onto the Raman spectrum reads:

$$\mathbf{b} = \tau\mathbf{F}^T\mathbf{y} = \tau\mathbf{F}^T\mathbf{Sc} \tag{2.2}$$

Or, with $\mathbf{G} = \tau\mathbf{F}^T\mathbf{S}$:

$$\mathbf{b} = \mathbf{Gc} \tag{2.3}$$

The aim is to estimate the proportion vector $\mathbf{c}$ from this equation.

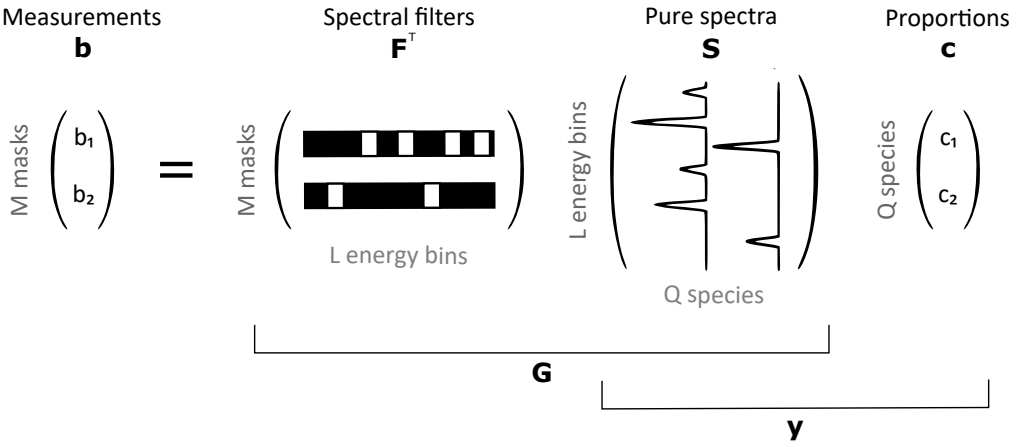


FIGURE 2.2: Visual representation of Eq. (2.3), with 2 pure chemical species and 2 spectral filters or 'masks'. The exposure times $\tau_m$ are not represented for clarity.

### 2.2.2 Noise and Precision

In reality, the ideal measurements $b_m$ are perturbed by noise. Its noisy counterparts are denoted $n_m$. When the single-pixel-detector dark noise is sufficiently low, the measurement can be assumed to be limited by photon-noise (2.3.1). Thus, the measured number of photons $n_m$ with filter number $m$ is a random variable, and its probability law can be modelled by a Poisson distribution, with mean $\langle n_m \rangle = b_m$. The probability to observe $n_m$ photons with filter $\mathbf{f}_m$ is then:

$$P_m(n_m) = e^{-b_m} \frac{b_m^{n_m}}{n_m!} \tag{2.4}$$

Given this noise, the aim is to estimate $\mathbf{c}$ from Eq. (2.3). Its estimate is denoted $\hat{\mathbf{c}}$, the estimation mean $\langle \hat{\mathbf{c}} \rangle$ and the error $\delta\hat{\mathbf{c}} = \hat{\mathbf{c}} - \mathbf{c}$. We consider an unbiased estimator, so $\langle \hat{\mathbf{c}} \rangle = \mathbf{c}$. The precision of an unbiased estimator can be characterized by its covariance matrix [132]:

$$\mathbf{\Gamma} = \langle \delta\hat{\mathbf{c}} \delta\hat{\mathbf{c}}^T \rangle \tag{2.5}$$

The diagonal elements of the covariance matrix represent the estimation variance of each component of $\hat{\mathbf{c}}$, while its off-diagonal elements represent correlations between its different components. Calculating $\mathbf{\Gamma}$ in general requires to choose a defined estimator to calculate $\hat{\mathbf{c}}$.
However, some knowledge about the diagonal elements of $\mathbf{\Gamma}$ can be deduced without choosing a specific estimator. Indeed, if an estimator is unbiased, its variance is bounded by a lower bound, called the Cramer-Rao lower bound (CRB) [132]. This property leads to:

$$\langle \delta\hat{c}_i^2 \rangle = [\mathbf{\Gamma}]_{ii} \geq [\mathbf{CRB}]_{ii} \tag{2.6}$$

where $\mathbf{CRB}$ is the CRB matrix. The CRB bound provides valuable information on the ultimate precision of an estimation problem that can be hoped for, independently of the chosen unbiased estimator. It is based on the model and the noise characteristics of the system and is defined

through the inverse of the Fisher Information matrix $\mathbf{I_F}$ [132]:

$$\mathbf{CRB} = {\mathbf{I_F}}^{-1} \tag{2.7}$$

$\mathbf{I_F}$ is obtained through $[\mathbf{I_F}]_{ij} = -\langle \partial_{c_i} \partial_{c_j} L(\mathbf{n}) \rangle$, where $L(\mathbf{n})$ is the log-likelihood derived from the Poisson distribution of Eq. (2.4). The derivation requires the measurements $n_m$ to be statistically independent. For the given problem, the derivation - detailed in Appendix A - leads to [131]:

$$[\mathbf{I_F}]_{ij} = \sum_{m=1}^{M} \frac{G_{mi} G_{mj}}{b_m} = \sum_{m=1}^{M} \frac{G_{mi} G_{mj}}{\sum_{k=1}^{Q} G_{mk} c_k} \tag{2.8}$$

Or, in the matrix form, with $\mathbf{B} = diag(\mathbf{b})$:

$$\mathbf{I_F} = \mathbf{G}^T \, \mathbf{B}^{-1} \, \mathbf{G} \tag{2.9}$$

The two above equations are only defined if : $\forall m, b_m \neq 0$. In other words, the denominator of Eq. (2.8) must be nonzero for each filter $m$. A null denominator could arise in general since we did not specify any positivity constraint for the proportions. Since $b_m \geq 0$, the denominator might be zero if a spectral filter is orthogonal to all species spectra, or if a proportion is zero. It is important to realize that the Fisher information matrix directly derives from the physical problem formalism (Eq. (2.3)) and from the noise associated with this physical problem (Eq. (A.1)). It shows that the estimation precision is a function of the species pure spectra and relative proportions, the integration times, and the binary filters. Since $\mathbf{G} = \tau \mathbf{F}^T \mathbf{S}$, it contains the pure Raman spectra (in units of counts/s) and its elements are in units of counts. Thus, the elements of $\mathbf{I_F}$ scale linearly with the number of counts, and the precision then improves linearly with the number of photons.

### 2.2.3 Estimation method

Now that we have an expression for a bound on the estimation variance, we wish to estimate $\mathbf{c}$ from a noisy measurement $\mathbf{n}$. The aim is to find an unbiased estimator with the best possible precision, i.e. which variance equals to the CRB. In general, it is not sure that such an estimator exists. In this section, we consider the common least-square estimator. It is the value of $\mathbf{c}$ which minimizes:

$$||\mathbf{n} - \mathbf{G}\mathbf{c}||_{l_2}^2. \tag{2.10}$$

#### General case

In general, if $(\mathbf{G}^T\mathbf{G})$ is not singular, the least-square solution reads:

$$\hat{\mathbf{c}} = (\mathbf{G}^T\mathbf{G})^{-1}\mathbf{G}^T\mathbf{n} \tag{2.11}$$

This solution is called the *pseudo-inverse* solution. The pseudo-inverse of $\mathbf{G}$ is: $\mathbf{G}^+ = (\mathbf{G}^T\mathbf{G})^{-1}\mathbf{G}^T$. Since $\langle \mathbf{n} \rangle = \mathbf{b}$ and $\mathbf{b} = \mathbf{G}\mathbf{c}$ (Eq. (2.3)) , the pseudo-inverse estimator is unbiased:

$$\langle \hat{\mathbf{c}} \rangle = (\mathbf{G}^T\mathbf{G})^{-1}\mathbf{G}^T\mathbf{b} \tag{2.12}$$

$$\langle \hat{\mathbf{c}} \rangle = \mathbf{c} \tag{2.13}$$

The covariance matrix defined in (2.5) derives from the error $\delta\hat{\mathbf{c}}$ :

$$\delta\hat{\mathbf{c}} = \hat{\mathbf{c}} - \mathbf{c} = \mathbf{G}^+\mathbf{n} - \mathbf{G}^+\mathbf{b} = \mathbf{G}^+\delta\mathbf{n} \tag{2.14}$$

with $\delta\mathbf{n} = \mathbf{n} - \mathbf{b}$. Thus, the covariance matrix reads:

$$\mathbf{\Gamma} = \langle \delta\hat{\mathbf{c}}\delta\hat{\mathbf{c}}^T \rangle = \mathbf{G}^+ \ \langle \delta\mathbf{n}\delta\mathbf{n}^T \rangle \ \mathbf{G}^{+T} \tag{2.15}$$

Since the components of $\mathbf{n}$ are independent and Poisson-distributed, the matrix $\langle \delta\mathbf{n}\delta\mathbf{n}^T \rangle$ is diagonal, and its elements are: $\langle \delta n_m^2 \rangle = \langle n_m \rangle = b_m$. Thus, the covariance matrix of the pseudo-inverse estimator becomes:

$$\mathbf{\Gamma} = \mathbf{G}^+ \ \mathbf{B} \ \mathbf{G}^{+T} \tag{2.16}$$

However, if the matrix $\mathbf{G}$ is not square and invertible, we cannot draw an equality with the **CRB**.

**Specific case** $M = Q$

When the number of filters equals the number of species ($M = Q$), the matrix $\mathbf{G}$ is square. If additionally $\mathbf{G}$ is not singular, the least-square solution from Eq. (2.12) simplifies to:

$$\hat{\mathbf{c}} = \mathbf{G}^{-1}\mathbf{n} \tag{2.17}$$

This estimator is also unbiased and its covariance matrix reads:

$$\mathbf{\Gamma} = \mathbf{G}^{-1} \ \mathbf{B} \ \mathbf{G}^{-T} \tag{2.18}$$

This time, since $\mathbf{G}$ is square and assumed not singular, the CRB matrix can be calculated from (2.9). This results in:

$$\mathbf{CRB} = \mathbf{G}^{-1} \ \mathbf{B} \ \mathbf{G}^{-T} = \mathbf{\Gamma} \tag{2.19}$$

Therefore, when the number of filters equals the number of species ($M = Q$), the least-square estimator is efficient, i.e. unbiased with minimal variance. This property is interesting, since performing a fast and simple linear operation leads to an efficient estimation of the species proportions when $M = Q$, which is often the case in practise. Furthermore, it shows that minimizing the mean square error (i.e. $tr(\mathbf{\Gamma})$) as in [133] is efficient with a Poisson noise model for the considered application, when $M = Q$ [131]. We note that these conclusions hold because no constraint was imposed on $\hat{\mathbf{c}}$ (see 2.2.5 and Chapter 6).

### 2.2.4 Filters optimization

In the above calculations, the spectral filters matrix **F** was fixed. It is clear from Eq. (2.9) that the estimation precision depends on **F**. The spectral filters should be calculated to maximize this precision. Thus, we choose to minimize the trace of the CRB matrix [131].
We constrain the relative exposure times $\tau_m$ of the binary filters to be equal and we fix a set of initial proportion. The implemented algorithm consists in a simple numerical optimization technique: a set of binary values $(m, l)$ is randomly chosen, and the value $f_{ml}$ is replaced by $1 - f_{ml}$ if $tr(\mathbf{CRB})$ is decreased. The process is then iterated for a given set of iterations or until no smaller value of $tr(\mathbf{CRB})$ is found. This simple algorithm does not always guarantee convergence to a global minimum, but simulations show that the precision reached with this method reaches values close to the CRB obtained with a complete Raman spectrum, at least in the considered cases [131](Chapter 3). More sophisticated optimisation algorithms could also be implemented to improve the convergence properties if necessary.
A similar approach is adopted in [119, 133], but the criterion minimized there is the mean square error instead of the trace of the CRB matrix. Eq. (2.19) shows that the two approaches are equivalent when $M = Q$. Our approach is easier to implement because it uses the analytical expression of the CRB matrix, while the optimization strategy used in [119] is based on the Matlab function*fmincon*. But none of the two optimization strategies guarantee convergence to a global minimum [131, 133].

#### Influence of filter exposure times $\tau_m$

The respective exposure times $\tau_m$ of the filters do not need to be constrained to be equal. In [119, 133], these exposure times are conjointly optimized with the filters. Optimizing each $\tau_m$ may result in a lower estimation precision than with constraining all $\tau_m$ equal ($\tau_m = T/Q$). In [131], the maximum loss of constraining the exposure times to be equal is quantified. It is shown that, when $M = Q$:

$$[\mathbf{CRB}]_{ii}^{\tau_{opt}} \geq \frac{1}{Q}[\mathbf{CRB}]_{ii}^{T/Q} \tag{2.20}$$

where the left-hand term represents the CRB when the exposure times are optimized and $T$ is the total exposure time. Therefore, optimising the $\tau_m$ can lead to a maximum precision gain of $Q$. It can therefore be interesting to optimize the exposure times of the filters, especially when the number of chemical species is large. Nevertheless, the loss is not bounded if an inappropriate choice of time is done.

#### Influence of initial proportion values $c_m$

It is important to note that the filters optimization is performed for a given initial proportion vector. The question on how do the filters depend on the latter thus arises. We do not properly examine this point here. However, we empirically noticed that the estimation precision seemed

relatively robust to the initial proportion choice, at least when $c_q = 1/Q$ , $M = Q$ and orthogonal filters (Chapter 3). Further details are given in [131].

#### Additional constraints on the filters

Additional constraints could easily be implemented into the filters design algorithm, such as filters orthogonality (3.1.2) or complementarity. Adding such constraints can be useful for some applications. Furthermore, the filters can also be designed to optimise the CRB of only a subset of chemical species, or to consider some others as nuisance parameters. This approach can for instance be helpful when some fluorescence background arises in the Raman spectra [121].

### 2.2.5 Conclusion

In this section, we presented the underlying estimation theory of CRT. We proposed a simple method to optimise the spectral binary filters, and showed that the least square estimation is efficient when the number of filters equals the number of species and when no constraint is imposed on the estimate $\hat{\mathbf{c}}$.

The search for an unbiased estimator allowed us to derive some interesting properties on the ultimate problem precision. Nevertheless, in practise, the estimate may be subject to physical constraints, such a positivity ($c_q \geq 0$). To take into account these constraints, other estimators could be used. They may also help reduce the variance of the estimation, at the potential cost of a bias. Then, a comparison with the CRB has a little relevance. More details on this point are provided in Chapter 6 and in [134].

Although there are sources of improvement, the method presented in the above section enabled us to experimentally implement CRT with success in a number of cases, as shown in the following.

## 2.3 Compressive Raman proof-of-concept experiments

A large part of this thesis has been dedicated to the experimental implementation of compressive Raman technology (CRT). This was first performed with a proof-of-concept experimental setup that allowed to validate our methodology. This was a necessary step to go any further in the technique or to concrete applications. In this part, we briefly describe the setup that was built, the experimental methodology, and show two experimental results that confirm the principle of CRT.

### 2.3.1 Experimental setup

#### Description of the setup

A simplified schematic of the setup is depicted in Fig.2.3. On the illumination side, a continuous wave laser operating at 532 nm (Verdi, Coherent Inc) is spectrally filtered and brought to a point-focus by an objective (Nikon X20 - 0.75). A piezoelectric stage scanner (P517, Physik Instrumente GmBH) holding the sample is used to scan the sample plane. On the detection side, the object is relayed onto a confocal slit to reject part of the out-of-focus light. A combination of a dichroic mirror and a notch filter ensures only the Raman signal is retained. The Raman signal is then dispersed by a blazed grating placed on the conjugate plane of the confocal slit. The spatially dispersed wavelength components of the Raman signal are imaged on a DMD. The DMD spectral axis ($\lambda-$axis), in conjunction with the grating, acts as a programmable spectral filter. Since the object is imaged onto the DMD, it can also be used as a virtual pinhole in its x$-$axis. When the DMD pixels are in the 'ON' state, the corresponding spectral components of the Raman signal are deflected into a photo-multiplier tube (PMT) operating in photon-counting mode, while the rest is sent into a beam dump. This is done by imaging the whole DMD surface onto the 5 mm detector active surface area. The PMT, DMD and Piezo-scanner are connected to an acquisition card (National Instruments) that ensures the connection with the computer. To verify the validity of the measured Raman spectra with our instrument, we also equip the setup with a commercial spectrometer (Horiba MicroHR) where the Raman signal can be sent. In addition, a 594 nm He-Ne beam-path is used for spectral calibration and alignment.

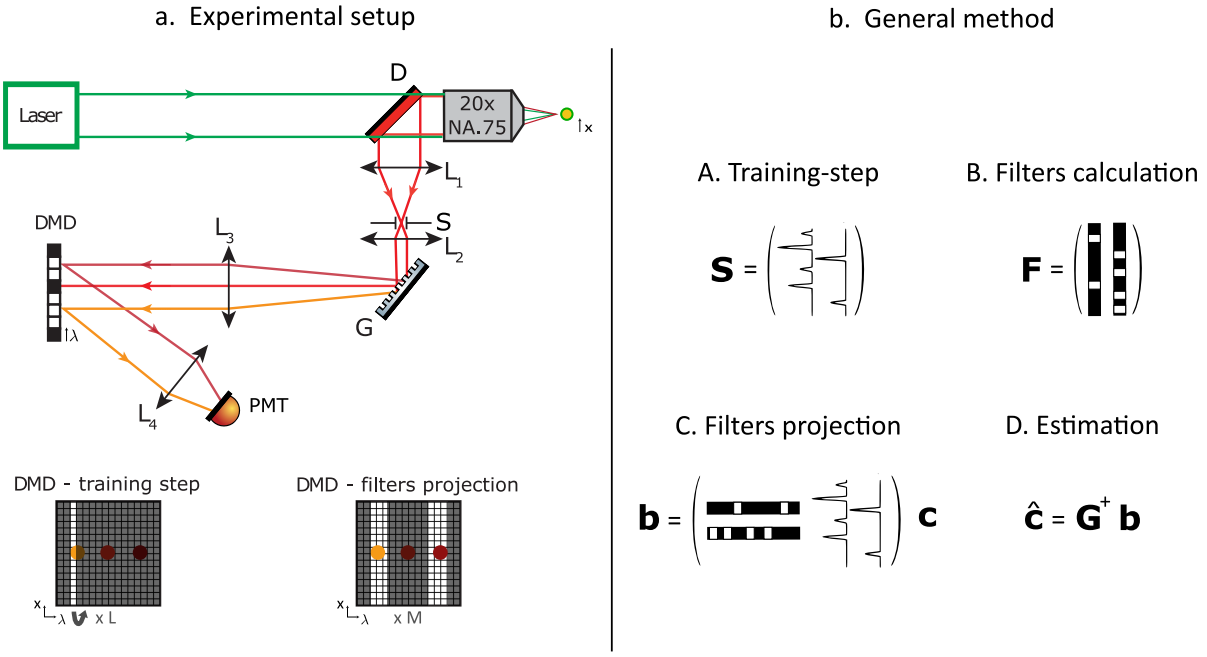


FIGURE 2.3: (a). Schematic of the experimental setup. $L_1 - L_3$ are achromatic doublets lenses with focal lengths 100, 100, 150 mm, respectively. $L_4$ is actually the combination of 2 achromatic lenses that image the DMD into the PMT with $\times$ 3 demagnification (Not represented for clarity). D: dichroic mirror; S: confocal slit; G: amplitude grating; DMD: digital micromirror device; PMT: photomultiplier tube. (b). General CRT method, consisting of (A) a training or calibration step to measure to pure Raman spectra, (B) a numerical optimisation step to generate the spectral filters (2.2.4), (C) an optical projection of the filters onto the Raman mixture, and (D) a final estimation step (Eq. (2.11)).

The compressive Raman spectrometer consists of three main elements, namely the grating, DMD and detector:

### Grating

The grating is a blazed grating (600 $mm^{-1}$, Thorlabs GR25-0608). In the given setup configuration, the grating, combined with the lens $L_3$, results in an inverse linear dispersion [1] of about 10.3 nm/mm. This corresponds to 0.14 nm per DMD mirror. The grating blazed wavelength (750nm) is not optimal for our application. Thus, in the targeted wavelength range of [540nm-630nm], its efficiency is only between $\approx$ 40% and 60%.

### DMD

The core component of the CRT setup is the DMD (V-7001, Vialux). A DMD is a micro-electronic mechanical system which consists of thousands of individually addressable moving micromirrors, controlled by underlying electronics. Each mirror can be individually rotated in

[1] Linear dispersion: $\frac{\partial L}{\partial \lambda} = \frac{f_3}{a cos(D)}$ , with $f_3 = 150$ mm focal length of $L_3$, $a \approx 5$ mm aperture radius, $D \approx 22°$ diffraction angle of the selected order) [135].

two states: $+12^\circ$ and $-12^\circ$, so the device in essence provides a binary modulation of light, although it can also be used to perform more complex modulations (eg.[136]). The DMD used here is composed of 768 $\times$ 1024 aluminium-coated mirrors of size 13.68$\mu$m $\times$ 13.68$\mu$m. The maximum switching rate of the mirrors is 22.7 kHz (44$\mu$s). In our setup, the DMD is mounted in normal incidence on a y$-$z stage to adjust its position in respect to the focus (z$-$axis) and to select the wavelength region of interest (y$-$axis). Furthermore, due to the mirrors axis of rotation, the device had to be mounted turned by $45^\circ$ about the x$-$axis. The DMD efficiency in reflection is $\approx$ 70% for the targeted wavelength range.

**Detector**

The detector is a photon-counting head from Hamamatsu (H7421-40). It is based on a GaAsP photocathode and a cooler. Its quantum efficiency for the wavelengths of interest is approximately constant around 40%. The photon counting process is linear up to 1.5 $10^6$ $s^{-1}$ [137] and its dark-noise is estimated to about 9 Hz (Fig. 2.4).

**Some characteristics of the setup**

In this section we briefly give a few characteristics of the setup. We mostly focus on the noise characteristics, since it constitutes one of the main assumptions of the underlying theoretical model (Eq. (2.4)).

**Spectral properties**

The accessible spectral range - limited by the $L_3$ lens aperture - is about 100 nm (3500 $cm^{-1}$). This wide spectral range allows to access the most of the full Raman spectrum at the same time. The spectrometer spectral resolution - measured with a 50 $\mu$m wide slit - is estimated to be about 40 $cm^{-1}$ (1.4nm), which is about 1.5 higher than the theoretical value [2]. This spectral resolution is poor but satisfactory for the present purposes.

**Spatial properties**

The microscope focal spot full-width-half-maximum is about 2 $\mu$m. Since the focal spot is fixed while the sample is scanned, the field-of-view is limited by the piezo-scanner travel range (200 $\mu$m).

**Spectrometer througput**

Because the efficiency of the PMT and grating are relatively poor, the spectrometer throughput is only about 15% at 600nm.

[2]The spectral resolution can be approximated by: $f_3(\frac{\lambda}{a} + \frac{b}{f_2})(\frac{\partial L}{\partial \lambda})^{-1}$, with $a$ the aperture size and $b$ the slit width [10].

**Noise properties**

The theoretical developments of (2.2) assume that the measurements are shot-noise limited. We therefore need to check experimentally that our measurements are indeed limited by photon noise. Let $n$ be the number of counted photoelectrons by the detector. We hypothesise it follows Poisson statistics. The measurement variance should then be equal to its mean: $\langle \delta n^2 \rangle = \langle n \rangle$. To check if the above hypothesis is reasonable, we measure the photons detected through the system. We use a solution of dimethyl sulfoxide as a sample, and a spectral filter that selects its main peaks. The laser power is fixed to 100 mW and the spectral filter exposure time is varied between 50 $\mu$s and 10 ms. Each measurement is repeated 3000 times. We found the mean number of counts $\langle n \rangle$ to be equal to its variance $\langle \delta n^2 \rangle$ (Fig. 2.4 (a)). The same experiment with fixed exposure time and varying laser power led to the same relationship (not shown).

In addition, we measure the detector dark-noise (thermally generated electrons), to ensure it is negligible compared to the signal count-rates faced in usual experimental conditions. Fig. 2.4 (b) shows the histogram of 1000 dark-counts measurements (1 s integration time per measurement). It can be fitted with a Poisson probability density function of mean $\approx 9$, which means the dark-count of our detector is about of 9 photoelectrons per second. This value is low enough to ensure a negligible influence of the dark noise on our measurements. In all, we can consider that the CRT experiments are indeed operated in the shot-noise limited regime.

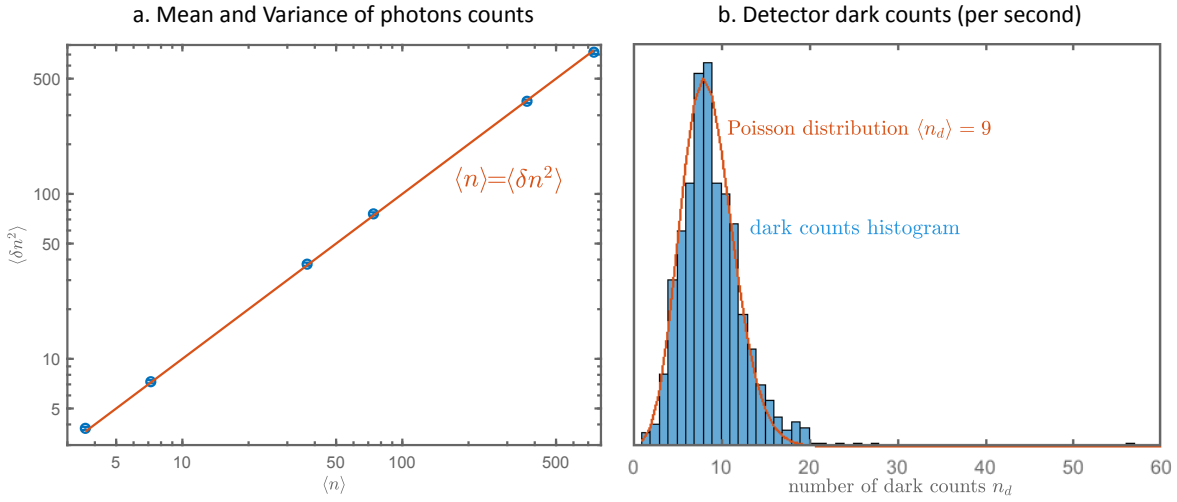


FIGURE 2.4: (a) Mean and variance of 3000 measurements for different integration times. (b) Detector dark-count rate: histogram of 1000 measurements.

### 2.3.2 Experimental method

The general method for performing compressive Raman experiments in summarised is Fig. 2.3 (b). It includes the following stages.

**A. Training step**

The aim of the training step is to measure or determine the spectral library **S**. It can be performed in different ways.

When the pure chemical species present in the sample are known, their theoretical Raman spectra can generally be found on various databases or handbooks. These theoretical spectra could then be fitted with the spectrometer transfer function. This approach is nevertheless subject to imperfections in the spectral calibration and in the estimation of the spectral transfer function. Rather, we directly incorporate the instrument parameters into the model by performing an *in situ* training step: We measure the spectra of the pure chemical species (on an available pure solution, piece of pure material, etc), by raster-scanning the DMD. Since each DMD column corresponds to one spectral basis, raster-scanning it along the $\lambda-$axis builds a spectrum (Fig. 2.3 (a)). Alternatively, positive Hadamard patterns could be used and the data demultiplexed to obtain a spectrum [52]. Such an approach can be interesting in certain cases, but its advantage over raster-scanning is not trivial because of the shot-noise limited nature of the measurements (Chapter 6).

**B. Filters calculation**

Once the matrix **S** is known, the filters can be optimised with the procedure described in 2.2.4. In practise, the algorithm is executed for about 50 random initial filters. If the filters are not all identical, the filter set leading to the smallest $tr(\mathbf{CRB})$ is selected. In most practical cases, we use as many filters as chemical species $M = Q$. Simulations are also performed to verify the validity of the filters.

**C. Projections**

The sample of interest is placed in the focal plane of the microscope. The $M$ filters are sequentially projected onto the DMD, with equal exposure times $\tau_m = T/M$, resulting in a measurement vector **n**. When the sample is imaged, the DMD pattern is fixed while the image pixels are scanned along x and y. Alternatively, all the filters may be projected before another spatial pixel is probed. This second approach may be necessary in the case of unstable samples.

**D. Estimation**

Finally, the species proportions are estimated using the linear estimation given in Eq. (2.11) or Eq. (2.17) if $M = Q$.

### 2.3.3 Experimental demonstration on solutions

As a first demonstration example, we show results on mixed liquid solvents: Dimethyl-Sulfoxide (DMSO, 99.9%, Sigma-Aldrich) and chloroform (99.9%, Sigma-Aldrich). Along this experiment, the laser power at the sample plane is $\approx 25$ mW and the slit is 100 $\mu$m wide. The DMD pixels are binned 4-by-4 along the $\lambda-$axis, and fully binned along the x$-$axis. Each pure solvent is placed into a cuvette (Hellma), and their spectra are measured by raster-scanning the DMD (Fig. 2.5

(a)). The DMD is placed to only select the fingerprint region. The measured pure spectra are consistent with the spectra found on data bases. The spectral overlap of the measured spectra is 0.79. It is defined as: We define the spectral overlap $r_{ij}$, between species $i$ and $j$, through:

$$r_{ij} = \frac{\sum_{l=1}^{L}(s_{li}s_{lj})}{\sqrt{(\sum_{l=1}^{L} s_{li}^2)(\sum_{l=1}^{L} s_{li}^2)}} \tag{2.21}$$

The two solvents are then mixed with 70% of chloroform and 30% of DMSO: the resulting measured spectrum with our spectrometer is found to approximately match the simulated mixture spectrum - obtained by summing the weighted pure spectra (Fig. 2.5 (b)).

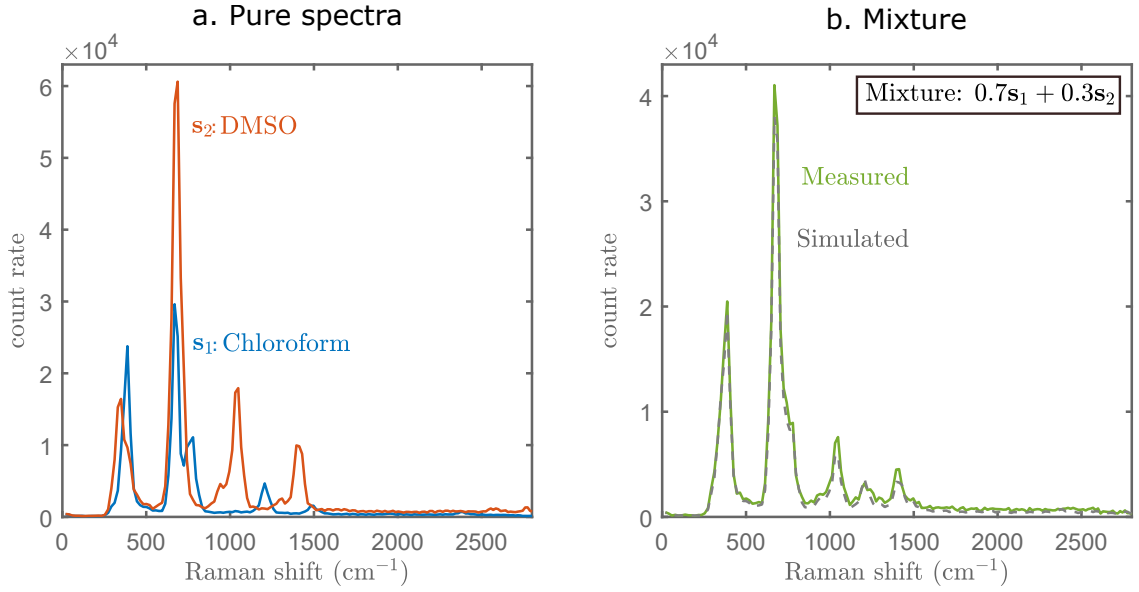


FIGURE 2.5: (a) Spectra of the pure solvents measured by raster-scanning the DMD. The spectral overlap in the selected spectral region is 0.79. (b) Simulated and measured spectra of the mixture of solvents.

**Filters optimization: two models**

In the following, we perform experiments on this specific solvent mixture to retrieve the theoretical proportions of 70% of chloroform and 30% of DMSO. To illustrate the importance of the accurate modelling of the physical problem on CRT performances, we present the results obtained with two different models (Fig. 2.6). The two filter model (a) only takes into account the two pure spectra. The three filter model (b) takes into account the two pure spectra and an additional constant Raman background - modelling Raman signal arising from optics. To generate the filters, the initial proportions are set to $c_1 = c_2 = 0.5$ for (a) and to $c_1 = c_2 = 0.495$, $c_3 = 0.01$ for (b). In the two cases, the spectral filters obtained with the algorithm are found identical for 50 random initial trials, respectively. We notice that the filter $\mathbf{f}_1$ mainly selects chloroform peaks, while $\mathbf{f}_2$ mainly selects DMSO peaks.

For these spectral filters, the CRB matrices evaluated at (70% - 30%) are calculated. The **CRB**

first diagonal element relates to the chloroform estimation precision, the second diagonal element to DMSO, and the third diagonal element to the background. Thus, only the two first diagonal elements are of interest. The trace of the **CRB** of model (a) and (b) are found to be approximately equal. Thus, the model (b) is not expected to improve the estimation precision in this specific case.

We note that the CRB matrix element related to chloroform is larger than the DMSO. This is relevant since the chloroform spectrum is dimmer than the chloroform. Although the number of counts associated to the background is very small compared to the solvent species, its associated CRB is small since it is weighted with a small proportion of 1% (Eq. (2.8)).

In addition, we simulate the expected values of the matrix $\mathbf{G}$ (with $\tau_m = 1$s). In cases (a) and (b), the two matrices comparable elements have similar values. The highest number of counts arises from the projection of the filter $\mathbf{f}_2$ onto the DMSO spectrum. Although the spectral correlation is relatively high, the matrix $\mathbf{G}$ off-diagonal elements are relatively small as compared to the diagonal elements: this reveals the degree of spectral selectivity performed by the filters $\mathbf{f}_m$.

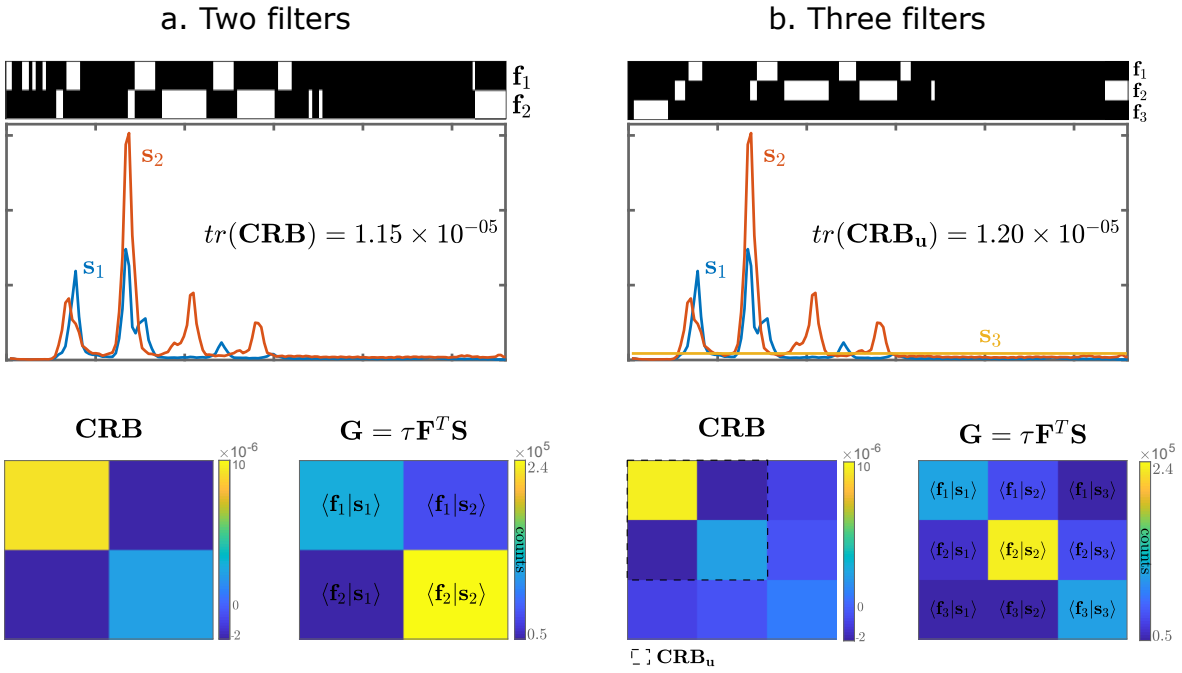


FIGURE 2.6: (a) Model with no additional background spectrum (b) Model with a small additional background spectrum. The spectra and the associated filters obtained by the algorithm are shown. The CRB matrices first diagonal element relates to $\mathbf{s}_1$ (chloroform), the second diagonal element $\mathbf{s}_2$ (DMSO), (and the third to $\mathbf{s}_3$ (background). Thus, in (b), only the top-left 2-by-2 block matrix is of interest. $\mathbf{G}$ represents the degree of spectral selectivity performed by the filters. The traces of the two considered CRB matrices are similar for (a) and (b): no expected gain in precision is expected from using this background spectrum.

**Experimental results**

We now show the results of experiments performed with the filters of model (a) and model (b). We analyse the influence of these two models on the estimation proportions bias and variance. We also analyse the influence of the number of photons.
The filters are sequentially displayed onto the DMD, for equal exposure times $\tau_m$, and 1000 times each. Experiments are conducted with $\tau_m$ = 50, 75, 100, 500, 1000 and 5000 $\mu$s. These exposure times lead to different measured signal levels. As an example, for the model (b) with $\tau_m$ = 5 ms, the average number of counts measured with filters $\mathbf{f}_1$, $\mathbf{f}_2$ and $\mathbf{f}_3$ are respectively $b_1 = 488$ counts, $b_2 = 527$ counts and $b_3 = 9$ counts. The resulting total number of counts is then: $\sum b_m = 1025$. These total number of counts are represented on the abscissa of Fig. 2.7.

The proportion ground truth is estimated from the full spectrum measurement (Fig. 2.5 (b)). This leads to 'ground truth' proportions of 70.98% for chloroform, 33.75% for DMSO (and 11.74% for the background). Note that we do not constrain the sum of proportions to be equal to 1. To evaluate the estimation bias, the means of the 1000 estimated proportions are shown in Fig. 2.7 (a-b). For both models (a) and (b), the CRT estimation shows a bias. The bias decreases with an increasing signal level, and is larger for chloroform than for DMSO. Model (b) helps to reduce the bias for the solvents proportion estimation, at the expense of a bias for the background (negative estimated proportion is found in this case).

To evaluate the estimation precision, the variance of the estimated proportions $\langle \delta \hat{c}_q^2 \rangle$ is shown in Fig. 2.7 (c-d). It matches the calculated CRB (evaluated at the estimated proportions from Fig. 2.7 (a-b)). The predictions of Fig. 2.6 are also verified: the two models lead to very similar estimation precisions. We note that the variances are found to be slightly higher than the CRB of the full Raman spectrum, to which it can be compared because the filters are orthogonal (3.1.2). We come back on this point in Chapter 3.

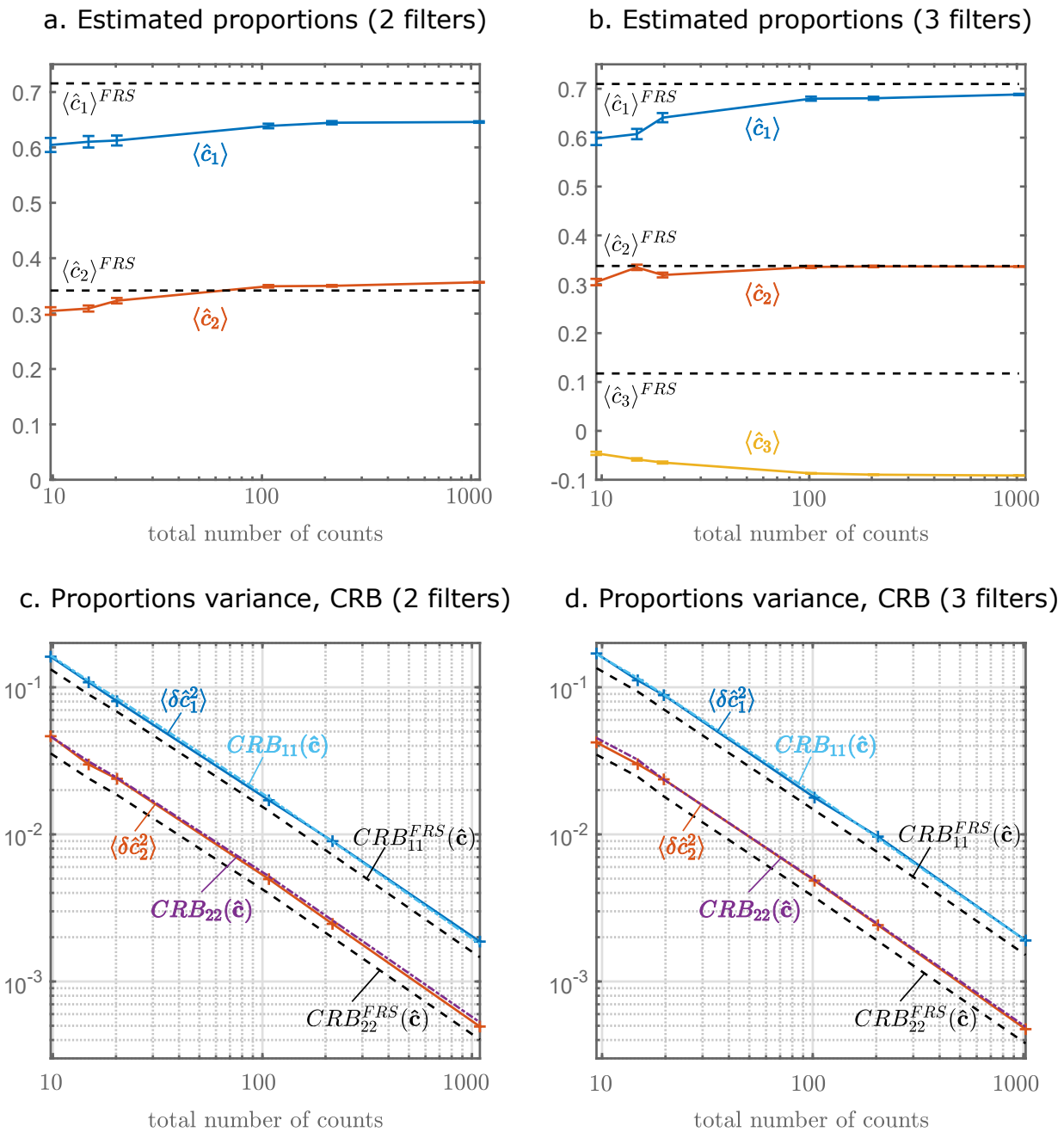


FIGURE 2.7: (a-b) Mean of the proportions estimations, as compared to the proportions found from measuring the full Raman spectrum (FRS) of the mixture, considered as the 'ground truth'. The model (b) seems to reduce the bias for the solvents proportions. The error bar is at $1\sigma$. (c-d) Variance of the proportions estimations, as compared to the theoretical CRB evaluated at the proportions means found in (a-b), and to the CRB associated with the full Raman spectrum. Number of measurements: 1000. Abscissa: sum of the measured counts after applying all the filters (10, 100 and 1000 counts correspond to individual filters exposure times $\tau_m$ of 50, 500 and 5000 $\mu$s, respectively).

In all, on this example, we compared two simple models. We showed that the two models lead to the same estimation precision, and that in both cases, the variance of the estimations matches

the theoretical value (CRB). Although the least square estimator is not biased (Eq. (2.13)), the estimation exhibits a bias, which could be reduced by taking a background spectrum in our model. We surmise these biases to arise from a model mismatch.

### 2.3.4 Experimental demonstration for imaging

As a second demonstration example, we show CRT results on polymer beads images. Two different types of beads (Sigma Aldrich) - 30 $\mu$m polystyrene beads (PS) and 12 $\mu$m melamine resin (MR) - are displayed on a $CaF_2$ coverslip (Crystran). For this experiment, the laser power at the sample plane is $\approx 4$ mW, and the slit is 100 $\mu$m wide. The DMD pixels are binned 4-by-4 along the $\lambda-$axis, and fully binned along the x$-$axis. The reference spectra (Fig. 2.8 (a)) are obtained by averaging 3 spectra measured at different spatial positions of the sample, for an integration time of 1 s per spectral pixel. Their spectral overlap (Eq. (2.21)) is equal to 0.72. The calculated spectral filters are shown in (Fig. 2.8 (a)).

The image scan is performed while a fixed filter is displayed on the DMD. The images are acquired with scanning steps of 0.65 $\mu$m in x and y directions, and with a pixel dwell-time of 4 ms. The resulting images are shown on Fig. 2.8 (b). $\mathbf{f}_2$ mainly selects PS resonances so more signal is detected on the PS beads. $\mathbf{f}_1$ mainly selects MR resonances, but since MR gives lower Raman signal than PS and since their spectra partially overlap, no noticeable difference in photon counts can be seen in the raw measurement. The subsequent estimated proportion maps (Fig. 2.8 (c)) are obtained through Eq. (2.17). Note that since this sample consists of pure species, the true proportion coefficients are either 0 or 1. We clearly see on the top map that on the PS pixels, the estimated proportions are close to 100%, whereas MR pixels have proportions close to 0%. The opposite case is observed on the bottom map. Here again, a slight bias is observed (PS seems to be slightly underestimated, to about 0.8 instead of 1).
Combining these two estimation maps and normalizing them to their brightest pixel leads to a composite RBG map (Fig. 2.8 (d-left)). To obtain the average number of detected counts per spatial pixel, we simply sum the numbers of counts detected with the two filters and average over the species pixels. This way, we obtain an average of 120 counts on MR pixels and 320 counts on PS pixels. Experiments with less laser power were conducted, and RGB maps allowing visual discrimination of the two species could be obtained down to $\approx 5$ counts on MR pixels and 15 counts on PS pixels (Fig. 2.8 (d-right)).

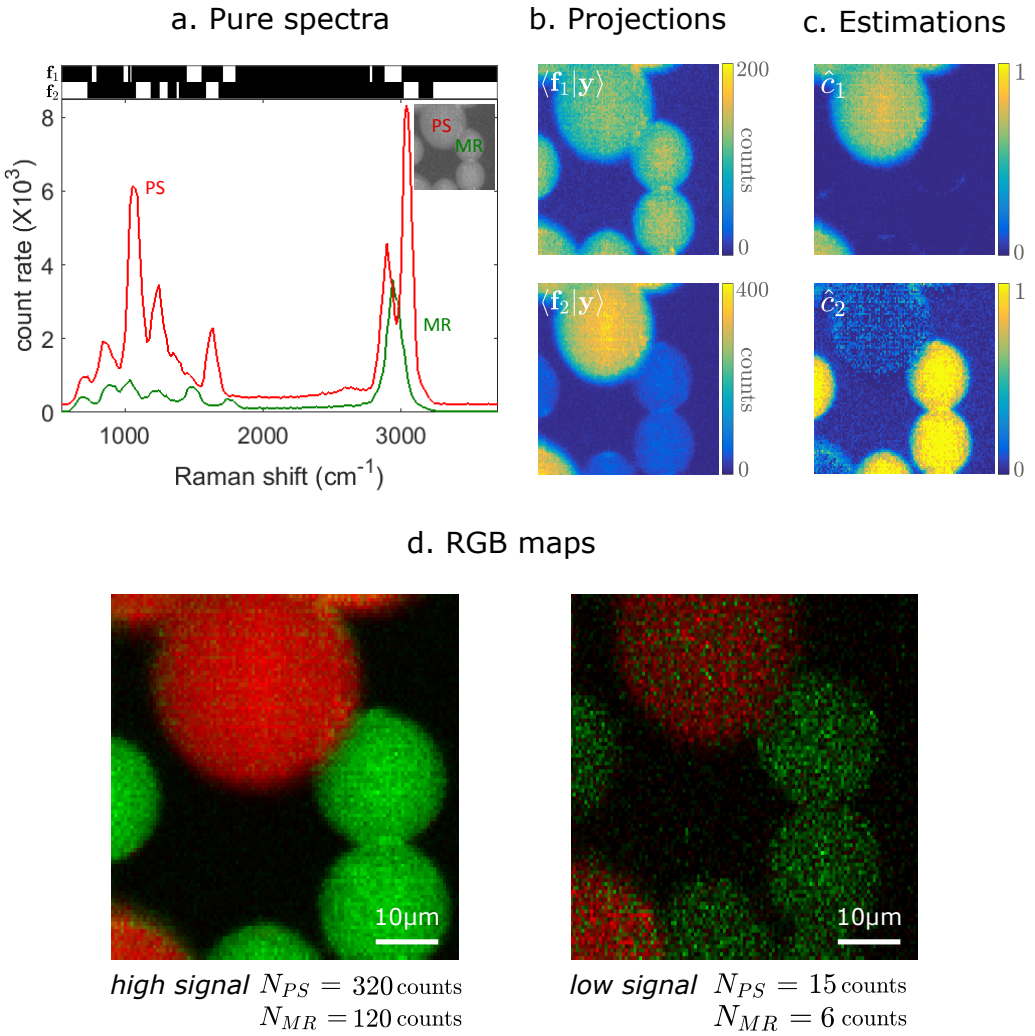


FIGURE 2.8: (a) Reference spectra of polystyrene (PS), melamine resin (MR), and their associated spectral filters. (b) Projection maps with exposure time per pixel per filter of 4 ms. (c) Estimated proportion maps of PS (top) and MR (bottom). (d) Associated RGB image with same (left) and less (right) laser power. $N_{PS}$: average total number of counts on PS pixels. $N_{MR}$: average total number of counts on MR pixels.

## 2.4 Conclusion

In this chapter, we highlighted the main principles of compressive Raman. It uses *a priori* information (spectra of pure chemical species) to directly probe the information of interest without generating a highly dimensional hyperspectral datacube. As compared to conventional Raman imaging, the technique promises decisive advantages in terms of speed and therefore has a great potential for Raman imaging, when some knowledge about the sample chemical species is held or accessible.

In a first part, we introduced the general formalism and underlying estimation theory. Based on the physical model and noise properties, a lower bound on the proportion estimation variance was derived. It represents the intrinsic best achievable precision of any unbiased estimator. When the number of spectral filters is equal to the number of pure chemical species, and when no constraint is imposed on the estimate $\hat{\mathbf{c}}$, the simple least square estimation of $\mathbf{c}$ was shown to be efficient (i.e. unbiased with minimal variance). This result is interesting, since it means that this simple estimation - that is fast and has low computational cost - is efficient. Furthermore, we described the optimisation procedure to calculate the spectral filters: although it has some limitations, it is simple and is based on analytical calculations of the CRB matrix. More complex filters optimization could be implemented, but we keep this simple approach in this thesis.

In a second part, we illustrated the performances of CRT on two simple experimental examples. The experiments were realized on a simple experimental setup designed for the purpose. First, we showed that our measurements were shot-noise limited, allowing the theoretical conclusions to apply. We showed that we could perform proportion estimations on binary mixtures of solvents, with an experimental estimation precision that matches the theoretical bound. However, we noticed some bias in the estimation that could probably be reduced with a better modelling of the system. We also demonstrated that our CRT system was adequate for imaging, and that it could perform successful estimation down to $\approx 10$ detected counts.

These experimental results do confirm the technique to some extent, but both the presented theoretical and experimental work leave many open questions that are still to investigate. We elaborate on the technique's limitations and improvements ideas in the final discussion of the manuscript. Nevertheless, as we will show in the two following chapters, the presented compressive Raman technique already demonstrates interesting performances as compared state-of-the-art Raman instruments (Chapter 3), and on samples relevant for some concrete applications (Chapter 4).

# Chapter 3

# Comparison of Compressive Raman with Conventional Raman

**Contents**



Compressive Raman has some interesting potential as compared to conventional Raman hyperspectral imaging. In particular, it is expected to bring considerable advantages in speed and cost. Although results from previous studies (2.1.2) strongly suggest the capability of CRT to surpass conventional Raman for some applications, no actual comparison of the techniques is available. In this chapter, we propose to assess some of the performances of CRT, as compared to conventional Raman. First, based on some theoretical considerations, we attempt to compare the achievable estimation precision of the two techniques. In a second part, we experimentally compare our CRT system with two state-of-the-art commercial instruments, and assess the techniques limits in terms of sensitivity and acquisition speeds.

## 3.1 Comparison in terms of estimation precision

*This section is based on the publication 'Precision of proportion estimation with binary compressed Raman spectrum' [131]*

In the previous chapter, we derived a lower bound (CRB) on the ultimate estimation precision potentially achievable with CRT. We saw that the implemented methodology allowed to reach precisions close to this bound in a number of cases. Yet, the fact that only a subset of spectral bases of the complete Raman spectrum is selected may worsen the estimation precision. This potential loss of precision, as compared to cases when the complete Raman spectrum is available, should be quantified. In this section, we provide some keys to compare the CRB obtained when measuring a full Raman spectrum (FRS) with the CRB obtained when applying CRT with orthogonal filters.

### 3.1.1 Precision bounds with a full Raman spectrum (FRS)

To begin with, we derive a lower bound on the estimation precision of a conventional Raman system, i.e. when a full Raman spectrum is acquired in parallel onto an array detector. A similar model can be found in [134]. We denote:

- $Q$ : number of pure chemical species present in the sample ($q = 1...Q$)
- $L$ : number of energy bins along a Raman spectrum ($l = 1...L$)
- $\mathbf{S}$: $L \times Q$ matrix of known Raman spectra. $\mathbf{s}_q$ of the spectrum of the $q^{th}$ pure chemical species. (units of counts/s)
- $\mathbf{c}$ : $Q \times 1$ vector of unknown proportions to estimate
- $\mathbf{y}$ : $L \times 1$ vector containing a Raman spectrum, linear mixture of $Q$ pure chemical species.
- $\mathbf{n}$: $L \times 1$ vector containing the noisy measurement of a Raman spectrum $\mathbf{y}$.
- $\mathbf{T}$: $L \times L$ diagonal matrix which elements contain the same detector exposure time $T$ since the measurements are parallel.

We assume that the measurements are shot-noise limited. This is the most favourable case for a conventional system, since other noises arising from the cameras may affect the signal, especially under low signal conditions (Appendix B). Under this assumption, the probability to observe $n_l$ photons in energy bin $l$ with mean $y_l = \langle n_l \rangle$ is:

$$P_l(n_l) = e^{-y_l} \frac{y_l^{n_l}}{n_l!} \tag{3.1}$$

Applying the same derivation as in Appendix A, with the joint probability function $P(\mathbf{n}) = \prod_{l=1}^{L} e^{-y_l} \frac{y_l^{n_l}}{n_l!}$ and $\mathbf{y} = \mathbf{Sc}$, we obtain the Fisher information matrix:

$$[\mathbf{I_F}^{FRS}]_{ij} = T \sum_{l=1}^{L} \frac{S_{li} S_{lj}}{y_l} \tag{3.2}$$

Or, in the matrix form, with $\mathbf{Y} = diag(\mathbf{y})$:

$$\mathbf{I_F}^{FRS} = T\ \mathbf{S}^T\ \mathbf{Y}^{-1}\ \mathbf{S} \tag{3.3}$$

The two above equations are only defined if : $\forall l, y_l \neq 0$. In theory, $y_l \geq 0$, but is likely to be null on the spectral bases that do not correspond to any vibrational transition. In practise, there is often some baseline and/or additional noise arising from the array detector, so the number of counts at extremely low light levels is rarely zero. Under these conditions, the CRB full Raman spectrum (FRS) is defined through:

$$\mathbf{CRB}^{FRS} = [\mathbf{I_F}^{FRS}]^{-1} \tag{3.4}$$

Similarly to CRT (Eq. (2.11)), the proportion estimation can be performed with a least-square estimation, if $(\mathbf{S}^T\mathbf{S})$ is not singular:

$$\hat{\mathbf{c}} = (\mathbf{S}^T\mathbf{S})^{-1}\mathbf{S}^T\mathbf{n} \tag{3.5}$$

### 3.1.2 Comparison of FRS and CRT precision bounds

The CRBs obtained with a full Raman spectrum can be compared with the CRBs obtained with binary filters, provided that:

- The measuring times for each binary filter $f_m$ are equal. In the following, we consider that the filters are virtually applied in parallel with $\tau_m = T$.
- The binary filters are orthogonal ($\sum_{m=1}^{M} f_{ml} \leq 1$). This means that each spectral basis can be selected by at most one filter. Such filters are called Orthogonal binary filters (OBF).

Intuitively, we can understand the necessity of orthogonality for the comparison. Indeed, the FRS measurements are parallel, thus they allow only one spectral basis to be selected at a time. Conversely, in CRT, multiple filters may select the same spectral basis: this would lead to more detected photons, at the advantage of CRT. In addition, to be able to draw a comparison, we would like to think as CRT as virtually applying spectral filters onto a full Raman spectrum, after the later has been acquired. Yet, when doing so, it is not guaranteed that the resulting measurements are statistically independent if the filters are not orthogonal. In other words, $\langle \mathbf{f}_m | \mathbf{n} \rangle$ - the measurement $m$ resulting from the projection of filter $\mathbf{f}_m$ onto the noisy Raman spectrum $\mathbf{n}$ - is not statistically independent from $\langle \mathbf{f}_{m'} | \mathbf{n} \rangle$, unless the filters are orthogonal. This

statistical independence is a necessary condition for the **CRB** to be given by Eq. (2.9).
With these considerations, the OBF approach is thus equivalent to perform the estimation on the numerically filtered full Raman spectrum. OBF can thus be considered as a subset of the FRS approach. In these conditions, and considering the OBF applied in parallel with exposure time $T$:

$$[\mathbf{CRB}]_{ii}^{OBF,T} \geq [\mathbf{CRB}]_{ii}^{FRS,T} \tag{3.6}$$

Therefore, the CRB with OBF cannot be smaller than the CRB obtained when measuring a complete Raman spectrum (under the same noise conditions). This is somehow intuitive since only a subset of the complete available spectral information is selected with the filters. We emphasize that the above property is not shown if the filters are not orthogonal.

In practice, the orthogonality constraint can be incorporated into the filters design algorithm described in chapter 2 (2.2.4). We note that this constraint leads to higher or equal CRBs as compared to the unconstrained minimization procedure. In some cases, the increase could be substantial. In the cases encountered so far, the increase is limited [131], and we empirically observed that the unconstrained minimization procedure often leads to filters which are already orthogonal (see for example Fig. 2.6 and Fig. 2.8).

The inequality of Eq. (3.6) is certainly interesting, but the subsequent matter is to quantify the loss of precision due to OBFs. Evidently, the goal is to design OBFs that lead to an estimation precision as close as to the precision obtained when measuring a complete Raman spectrum; to ultimately reach a CRB with OBF as close as possible to the CRB with FRS. One can quantify the precision loss by calculating the CRB obtained with OBF and FRS via the analytical expressions of with Eq. (2.9) and Eq. (3.3), respectively. The loss in precision is expressed through:

$$\sqrt{\frac{[\mathbf{CRB}]_{ii}^{OBF,T}}{[\mathbf{CRB}]_{ii}^{FRS,T}}} \tag{3.7}$$

We note that if the filters are applied sequentially with $\tau_m = T/M$, a similar analysis can be conducted, but only if the total measuring time for the OBF approach is $M$ times the one of the FRS approach.

As an illustrative example, we consider the same mixture of chloroform and DMSO as in Fig. 2.5. In this case, even without specifying constraints in the filters optimisation algorithm, the binary filters were found to be orthogonal (Fig. 2.6). Here, we only consider the model with only two filters. The initial proportion for the optimisation are set $c_1 = c_2 = 0.5$. In chapter 2, we found that the experimental proportions variances matched the theoretical CRB. The later are higher that the CRB of FRS CRB by a factor of about 1.25 (Fig. 3.1 (a)). This corresponds to a ratio of Eq. (3.7) of 1.12 and therefore to a loss in precision of about 10%. Note that here, the two filters are applied sequentially, therefore twice more time was spent in the CRT approach.

Fig. 3.1 (b) shows the ratio of (3.7) for simulated mixtures of DMSO and chloroform with various proportions. We find that for most proportions, the precision loss is $\leq 20\%$. It illustrates a certain robustness of the filters to the chosen initial proportions. More detailed examples of the precision loss quantification are given in [131], for three chemical species with variable spectral overlap. For most proportion values, the precision loss was found to be less than 1% for spectra with correlations coefficients under 16%, less than 20% for spectra with correlations coefficients under 50%, and less than 35% for spectra with correlations coefficients (Eq. (2.21)) under 65%. These examples are not representative of all possible situations, and an extensive study should be carried to identify some general conclusions. Nevertheless, the proposed methodology allows one to quantify the proportion loss for their specific cases.

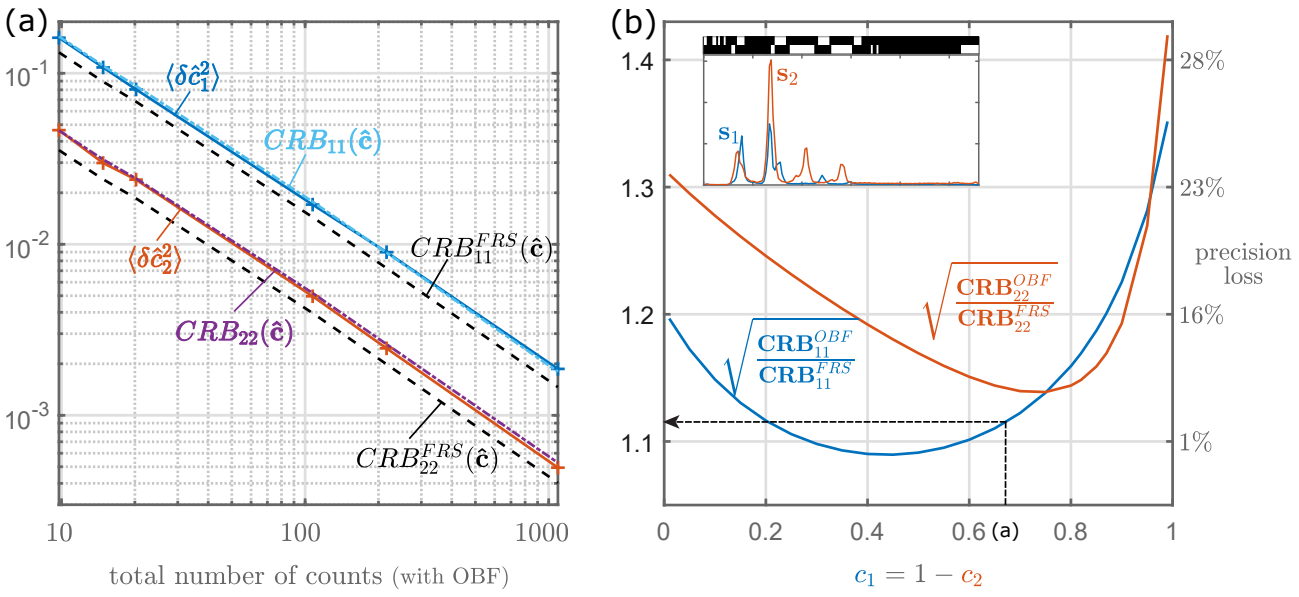


FIGURE 3.1: (a) Estimated proportions variance, CRB for OBF and for FRS, for proportions $c_1 \approx 0.65$ and $c_2 \approx 0.3$). The CRB of OBF is 1.25 times larger than the CRB of FRS. Experimental details are given in (2.3.3). (b) Square-root of the ratios of CRBs, corresponding to mixtures with different proportions of chloroform and DMSO. The proportions of (a) are indicated with a dashed line. $\mathbf{s}_1$: chloroform; $\mathbf{s}_2$: DMSO.

### 3.1.3 Discussion and conclusion

The above short analysis highlights a few points concerning the ultimate precision of CRT as compared to a full spectrum acquisition. We saw that the CRB associated with both methods could be compared if the spectral filters are orthogonal and their exposure times are equal. In this case, the CRT estimation precision cannot surpass the precision estimation obtained with a full spectrum. We proposed a general methodology to quantify potential losses in estimation precision due to the use of CRT. However, this comparison only holds in the mentioned context,

and only considers the most favourable noise scenario for the full Raman approach.

The quantification of the achievable estimation precisions allowed by the two methods is an essential point, and further analysis should be conducted. In particular, more realistic noise models of the cameras of conventional Raman system should be taken into account (Appendix B). Such an analysis has not been conducted in this work. Instead, in the following, we attempt to gain intuition on the performances of two techniques, with a more technological approach: we experimentally compare our CRT system with two state-of-the-art conventional Raman systems. This allows us to assess performances such as speed, and to face realistic experimental conditions and noises.

## 3.2 Comparison with state-of-the-art instruments

*This section is based on the publication 'Assessment of compressive Raman versus hyperspectral Raman for microcalcification chemical imaging' [138]. The conventional hyperspectral Raman experiments were conducted in the University of Exeter (UK), with P. Bouzy and E.M. Green, and in Horiba Scientific (Villeneuve d'Acsq, France) with S. Vergnole.*

To assess the relevance of CRT compared to conventional hyperspectral imaging, we choose to adopt an engineer-oriented approach. We compare our custom-built CRT system with two conventional state-of-the-art Raman hyperspectral imaging systems, on samples mimicking microcalcifications relevant for breast cancer diagnosis. We compare the systems in terms of acquisition speed and limit of detection.

### 3.2.1 Experimental context

#### Instrumentation

We conduct hyperspectral Raman experiments on two conventional hyperspectral systems, commercialised by two reference companies in the field, namely WITec and Horiba. We choose one of the instruments to be equipped with a CCD and the other with a EMCCD camera. In all cases, the excitation source is a 532 nm CW laser. Other experimental details differ, such as spatial and spectral resolutions, which are chosen according to the available systems settings. The main specifications of the three systems and their respective sensors are listed in Table 3.1. In Appendix B, we give more details about the noise properties of the cameras, as well as the experimental characterisation of their noise.

The first Raman system (Alpha300R - WITec) is equipped with a CCD (DV401A-BV, Andor). CCDs equip many Raman systems to date. On this system, the experiments are conducted with

a rate that minimizes the camera readout noise (Appendix B). In this regime, the minimum achievable integration time per spectra is 43 ms, regardless of the signal level.

The second system (LabRAM HR Evolution - Horiba) is equipped with an EMCCD (Synapse EM, Horiba). These detectors are replacing CCDs since they outperform their performances (Appendix B). This system is used in one of the fastest scanning modes, so that one spectrum is acquired in about 2 ms at best.

The third system is the proof-of-concept CRT system described in (2.3.1). All images are acquired with an exposure time of 4 ms per spatial pixel per spectral filter. The pixel dwell time for imaging is limited by the piezo-electric scanning system.


FIGURE 3.2: The two commercial Raman hyperspectral systems and the custom-built CRT system.

| | WITec (+ CCD) | Horiba (+ EMCCD) | CRT (+ PMT) |
|---|---|---|---|
| Spectral resolution | 10 $cm^{-1}$ | 20 $cm^{-1}$ | 40 $cm^{-1}$ |
| Spatial resolution | 0.4 $\mu$m | 0.4 $\mu$m | 1.4 $\mu$m |
| Spatial sampling | 0.5 $\mu$m | 0.6 $\mu$m | 0.75 $\mu$m |
| Objective | 50X / NA=0.7 | 50X / NA=0.75 | 20X / NA=0.75 |
| Detector max. $QE$ | 95% | 90% | 40% |
| Pixel dwell time (in chosen mode) | 43 ms limited by camera | 2 ms limited by camera | 4 ms limited by scanning |
| Readout noise (in chosen mode) (e-/pixel) | 6.1 (2.25 counts) | $\leq$ 1 (34 counts) | – |
| Dark noise (e-/pixel/s) | 0.006 | $\leq$ 0.01 | 9 |
| Detector mode | Full vertical binning | Full vertical binning | – |
| A/D rate | 33 kHz | 3 MHz | – |
| Vertical clock speed | 16 $\mu$s | 4.6 $\mu$s | – |
| Conversion factor $g$ (e-/count) | 2.7 | 3.36 | – |
| EM gain $g_{EM}$ (counts/e-) | – | 999 | – |

TABLE 3.1: Main specifications of the three instruments and their respective sensors. (Top) Spectral and spatial parameters (Middle) Detector main characteristics under the chosen mode of operation (Bottom) Details on the chosen modes of operation. $QE$: detector quantum efficiency; e-: electrons; A/D rate: horizontal readout speed, Vertical clock speed: speed of vertical electrons transfer; –: not applicable.

### Samples

The samples are two types of synthetic powders: calcium oxalate monohydrate (COM) and hydroxyapatite (HAP), dispersed on a $CaF_2$ coverslip. Their composition mimic microcalcifications that can be found in human breast. More details about these samples are given in Chapter 4 (4.2.1). Since the experiments were conducted at different times and in different places, they could not be performed on the same region of the sample. Yet, this was not a major problem since these synthetic samples are relatively homogeneous.
Fig. 3.3 shows the spectra of each pure species, averaged over 20 (a, b) and 4 (c) different spatial positions. The acquisition times per spectra are 43 ms, 2 ms and 25 s (100 ms per spectral basis), for the WITec, Horiba and CRT systems, respectively. We note that the resolution and signal-to-background ratio obtained with our spectrometer are much poorer than the commercial spectrometers, but sufficient for the considered problem. Our wide spectral range (2.3.1) is not useful for this sample, thus we only represent the spectra on the same spectral range as in (a-b).

### General method

The aim of all the experiments is to estimate the species proportions in each pixel of the image, to finally discriminate them. For the hyperspectral images, we first subtract the baseline level from all spectra. The camera baseline levels are assessed from dark frame measurements (Fig. B.3). Secondly, we perform proportion estimation on the entire datacube, using Eq. (3.5). This leads to proportion maps and subsequent composite RGB maps, as shown in Fig. 3.3. For CRT, the same method as in Chapter 2 (Fig.2.3) is applied, also resulting in proportions maps and composite RGB maps.
The experiments on each system are performed with fixed pixel dwell times (43 ms, 2 ms and 8 ms (2×4 ms), respectively). First, we performed experiments with full laser power (4 mW, 40 mW and 60 mW at the sample plane, respectively), that resulted in the proportion maps shown in Fig. 3.3. The laser powers are then progressively decrease to evaluate the limits of detection of the three systems.

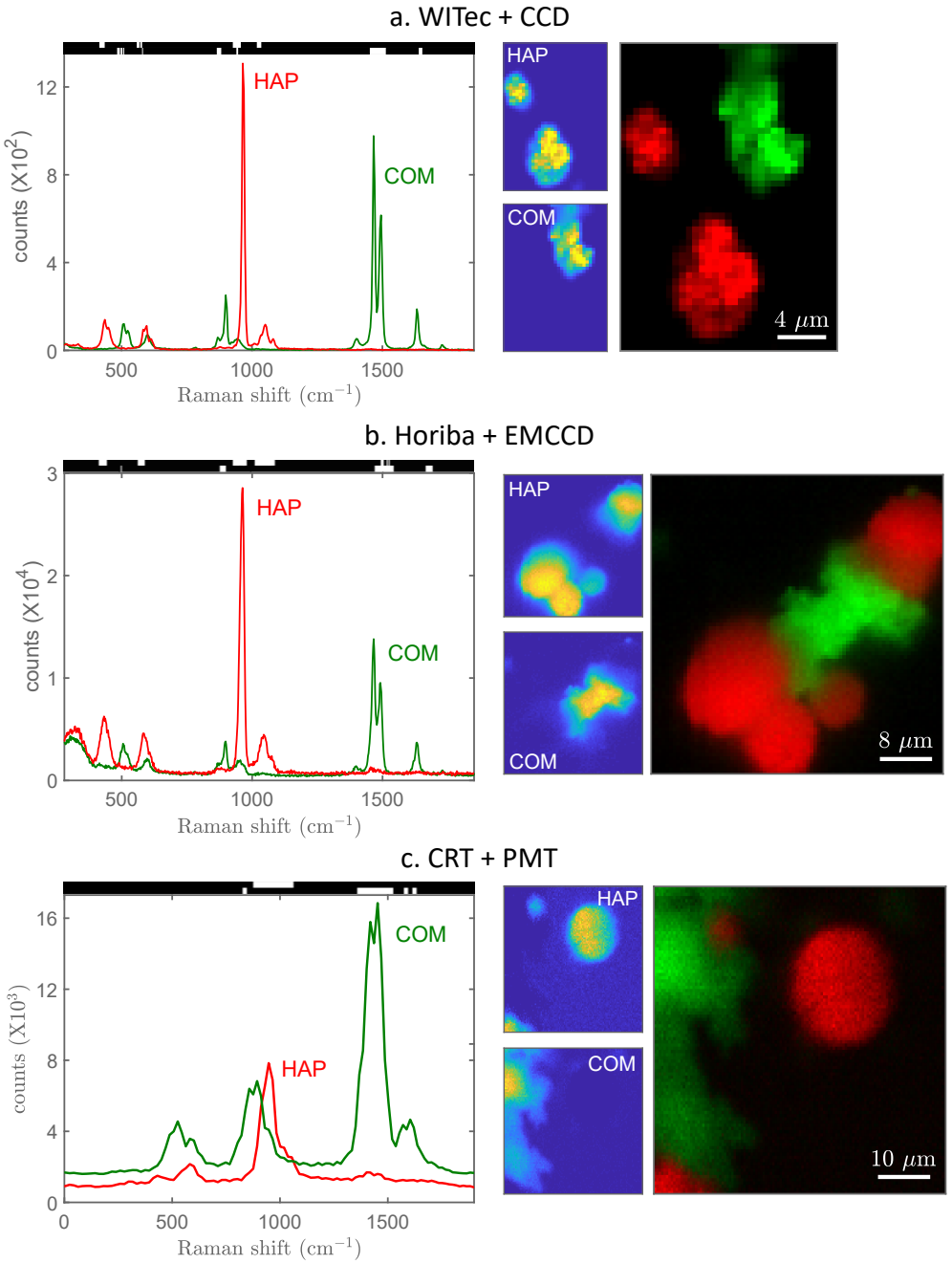


FIGURE 3.3: (Right) Spectra of HAP and COM acquired with the three systems. In (a) and (b), the spectral filters generated from these spectra are only used to estimate the systems limit of detection (3.2.2). (Left) Proportion maps and composite RGB images, for pixel dwell times of 43 ms (a), 2 ms (b) and 8 ms (c), with laser powers at the sample plane of 24 mW (a), 40 mW (b) and 60 mW (c).

### 3.2.2 Assessment of the systems limits

Since many parameters of the systems differ, one of the main difficulties lies in finding relevant figures of merit to compare. Especially, the conclusions should have as little dependence as possible on these multiple parameters - especially the throughputs variations. To bypass this

problem, we place ourselves at the detector level: we compare their SNR, and the detected minimum number of photons necessary to perform successful proportion estimation (limit of detection). We also give insight on their intrinsic speeds limits.

**Comparison of detectors SNR**

To begin with, it is important to specify the noise characteristics of the detectors that equip each of the systems. This allows us to know which potential noise sources may limit the measurements SNR. As mentioned in chapter 2 (2.4), the measurements on the CRT system are shot-noise limited. This is generally not the case of cameras: they exhibit more complex noise properties than single-pixel-detectors, and the measurements may not be shot-noise limited (Appendix B). Table B.1 and Fig. B.2 show that for a CCD camera, the measurements are typically limited by the camera readout noise in the low signal regime, and by the shot-noise in the high signal regime. EMCCDs exhibit a near shot-noise behaviour at all signal regimes, though they can often be used as CCDs in the high signal regime.
The three detectors of this study are intrinsically different, since the two cameras have millions of pixels, while the PMT has only one. We therefore choose to examine their SNR per detector pixel: using Table B.1 and the detectors respective parameters of Table 3.1, we calculate the theoretical SNR per detector pixel as a function of the number of photons (Fig. 3.4). It differs from Fig. B.2 because of differences in $QE$ between the three detectors. Since our PMT has a $QE$ of only 40%, while the two cameras reach 90 to 95%, the shot-noise limit advantage of CRT is somewhat hindered. The CCD shows an advantage over CRT in the high signal regime, while CRT and EMCCD exhibit similar SNR per pixel at all signal regimes. It is then clear that CRT would benefit from a single-pixel-detector with higher quantum efficiency (e.g. an avalanche photodiode).

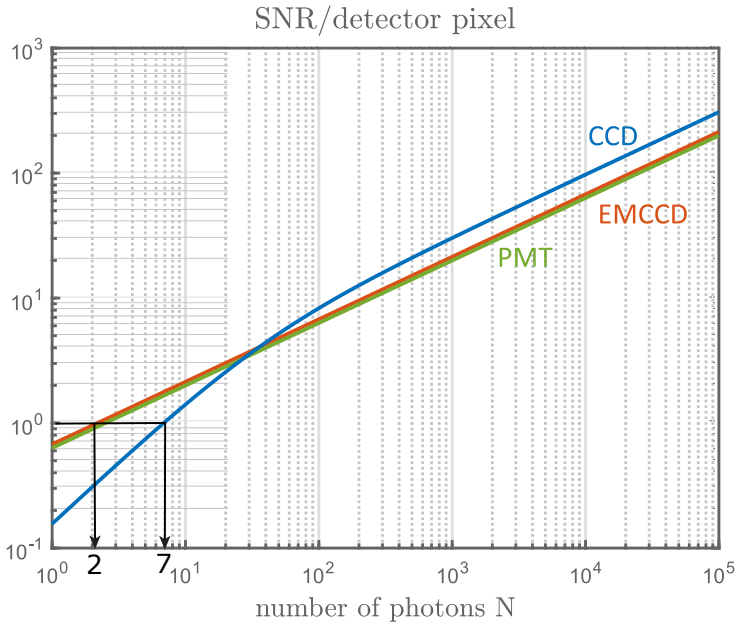


FIGURE 3.4: SNR per detector pixel as a function of the number of photons (Table. B.1), considering the specifications of the three systems detectors. In particular, the CCD, EMCCD and PMT quantum efficiency are 95%, 90%, 40%, respectively.

The above analysis shows the three detectors SNR per pixel. However, it is not sufficient, since it does not take into account the fundamentally different detection schemes of the three systems. In the camera-based systems, the signal is distributed over the cameras pixels, whereas CRT combines relevant spectral components into a single pixel. For instance, consider a hypothetical signal dispersed over 20 spectral pixels of interest. From Fig. 3.4, we see that to reach a SNR per pixel of 1, the number of photons per spectral pixel is about 7 for the CCD, 2 for the EMCCD and 3 for the PMT. Then, to reach a SNR per pixel of 1 in all the 20 spectral pixels of interest, the CCD needs a total of 140 photons (7x20), the EMCCD 40 photons (2x20), and the CRT 3 photons (because it recombines all the wavelengths into one pixel). Therefore, in the low signal regime, we rather choose to compare the systems limits of detection (LOD), i.e. the minimal photon budget necessary to achieve proportion estimation in the context of our experiments.

### Comparison of the systems limits of detection (LOD)

In chapter 2, we saw that the estimation precision depends on the number of detected photons (Eq. (2.8), Fig. 2.7). We recall that $n_m$ is the number of photons detected with filter $\mathbf{f}_m$. Applying $M$ filters thus involves $N$ photons, with:

$$N = \sum_{m=1}^{M} n_m \tag{3.8}$$

When $N$ decreases, the estimation variance increases, resulting in noise in the subsequent images (Fig. 2.8. When this noise becomes large, the estimations are not precise enough to differentiate between the present chemical species: visually, we cannot distinguish the two species from each other. Here, we define the LOD as the minimal number of Raman photons $N$ that we must detect so that the proportion estimation variance is low enough to distinguish one chemical species from the other (on proportion maps and composite RBG images). This definition is questionable, but complies with experimental constraints and gives an idea of the minimal photon budget necessary to achieve successful proportion estimation in the context of our experiments. It also has the advantage of being independent of the respective systems throughputs.

For the two hyperspectral systems, this photon budget is distributed over the cameras pixels, while for CRT, it is combined into a single pixel detector. The number of photons at the LOD are estimated as followed. We denote $N_{tot}$ the average number of photons detected per spatial pixel $i$ (pixels corresponding to chemical species of interest).

$$N_{tot} = \langle N_i \rangle \tag{3.9}$$

For CRT, we obtain $N_{tot}$ by summing the numbers of photons $N_i$ detected after each filter projection. For hyperspectral images, we do not integrate the full spectrum on each pixel, but only consider some relevant spectral bases. To do so, we generate binary filters using the reference spectra acquired with each system (Fig. 3.3). We then project those filters onto the hyperspectral data cube. We again obtain $N_{tot}$ via Eq. (3.8) and Eq. (3.9).
Finally, the number of counts $N_i^c$ detected on the detector is related to the number of photons $N_i$, through the detectors quantum efficiencies $QE$ and conversions factors $g$, $g_{EM}$ (Table 3.1). For each detector, the relationship between the number of counts and number of photons are:

- $N_i = (N_i^c g)/QE$, for the CCD
- $N_i = (N_i^c g)/(QE\ g_{EM})$, for the EMCCD
- $N_i = N_i^c/QE$, for the PMT.

In practice, we perform experiments by gradually decreasing the laser power onto the sample. An upper bound on the LOD can be predicted from the last experiment before the noise is too high for the species to be distinguished. The laser powers at the sample plane at these limits were 0.3 mW (WITec), 0.4 mW (Horiba) and 2 mW (CRT). A lower bound corresponds to the experiment in which the species cannot be distinguished anymore. Fig. 3.5 (a) shows the proportion maps and composite RGB maps obtained at the LOD upper bound. Evaluating the number of photons $N_{tot}$ as described above leads to LOD upper bounds of approximately 450 photons and 40 photons, for the CCD and EMCCD systems, respectively. Lower bounds of the LOD are found to be of about 150 and 25 photons, respectively. For CRT, the LOD upper bound is estimated to be $\approx 15$ photons. Unfortunately we did not perform the experiment to assess a lower bound.

Fig. 3.5 (b) shows the spectra (averaged over 20) of the two hyperspectral images at the LOD upper bound. We note that the highest value of these spectra are of about 10 counts ($\approx$ 30 photons) for the CCD-based system, and 250 counts ($\approx$ 1 photon) for the EMCCD-based system.

These results are summed up in Table 3.2. They show that, on this sample, successful quantitation is possible with a few hundreds of photons with the CCD-based system, and a few tens of photons with the EMCCD and CRT systems. This analysis is subject to some limitations. For example, there is a difference in signal-to-background ratio on the above images. There is also some imprecision in the EMCCD $N_{tot}$ assessment, that comes from the probabilistic nature of the multiplication stage (Appendix B). Yet, in view of the imprecisions discussed in (3.2.3), we conclude that, on this example, the CRT limit of detection seems similar to the EMCCD-based system, and one order of magnitude lower than the CCD-based system.

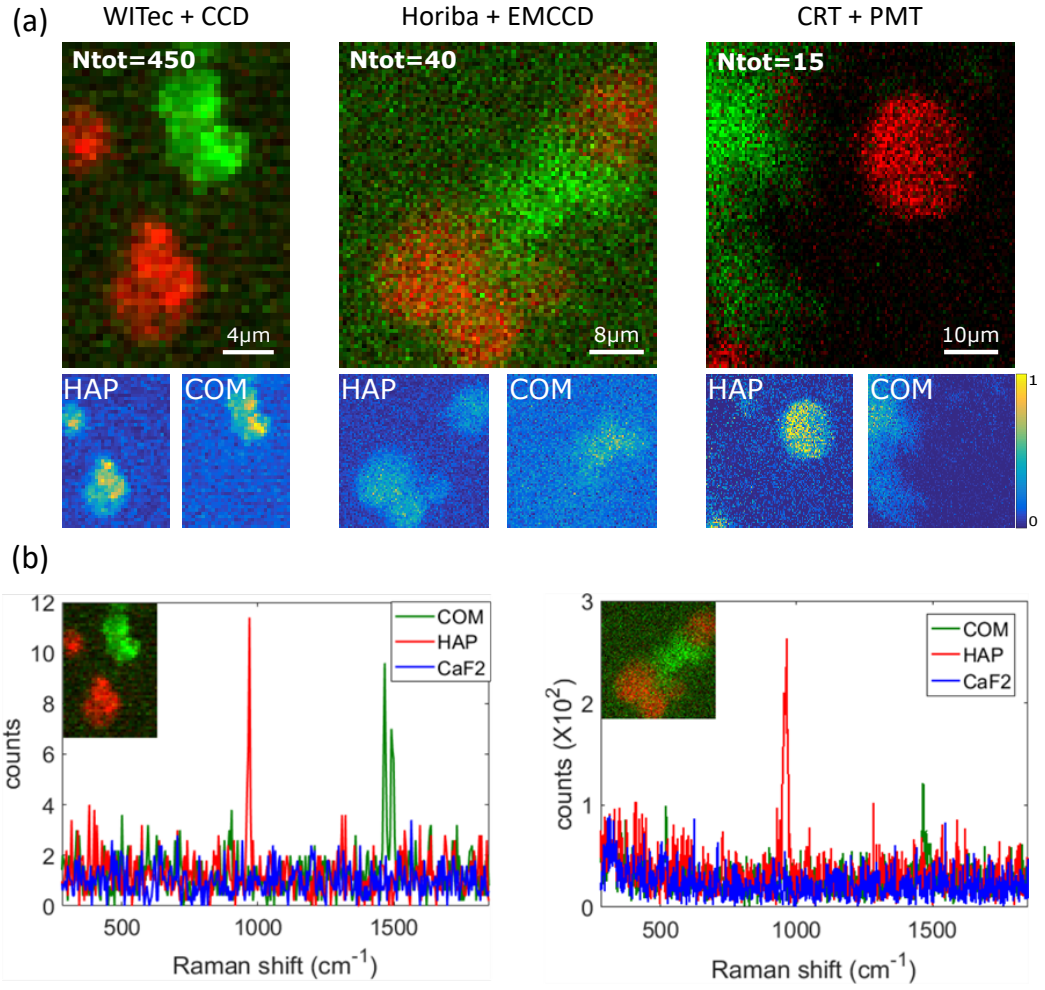


FIGURE 3.5: (a) Proportion maps and composite RGB maps obtained at the estimated LOD upper bound ($N_{tot}$). (b) Spectra of the two species and the substrate (averaged over 20) at this limit.

**Comparison of the systems acquisition speeds**

Last, we attempt to compare the speed performances of the systems. Because the CRT system is limited by the scanning speed of the scanning stage, the above study does not allow us to provide a direct experimental comparison of the systems acquisition speed. Nevertheless, we can extrapolate an equivalent acquisition speed from the results of Fig. 3.5. As previously mentioned, the two cameras systems are already ran close to their maximum readout rate. Thus, the above LOD results could not have been acquired with faster speeds than 43 ms/pixel and 2 ms/pixel, respectively. However, this is not the case for CRT. Indeed, the result of Fig. 3.5 necessitated to decrease the initial laser power (used for Fig. 3.3 (c)) by a 20 times: we thus surmise that the same image could have been acquired with a 20 times smaller pixel dwell time, resulting in 200$\mu$s per pixel per spectral filter, thus in 400$\mu$s per pixel in total. This is 100 times faster than the CCD-based system and 5 times faster that the EMCCD-based system.

Furthermore, we can give order of magnitudes of the fundamental speeds limits of the three systems when the measurements are not limited by the SNR. At the expense of more noise or less signal, slightly faster speeds can be reached by both cameras. The maximum achievable with the WITec + CCD system is 12 ms/spectrum. This speed, twice faster than chosen mode (Table 3.1), leads to twice higher readout noise. On the Horiba + EMCCD system, only a small portion of the camera rows can be readout, thus improving the total readout rate. Reading only 20 rows out of the 400 camera rows allows speeds of about 700 $\mu$s/spectrum. But this will generally be at the expense of spectra with poorer SNR. In these fastest modes, one image of $100 \times 100$ pixels can then be acquired, at best, in about 2 min for the CCD-based system, 7 s for the EMCCD-based system.
In CRT, the single-pixel-detector readout speed does not limit for the acquisition speed. Rather, the acquisition speed is only fundamentally limited by the maximum count rate of the detector ($\approx 10^6$ Hz). In practice, in a scanning microscope, it is usually limited by the scanning system speed ($\approx 1$ $\mu$s per pixel for galvanometric mirrors). In all, in high signal regime, we surmise the CRT to reach pixel dwell times per spectral filter of the order of 10 $\mu$s to 100 $\mu$s. These expectations are confirmed in chapter 4. The mentioned speeds for CRT should then be multiplied by the number of spectral filters $M$. Thus, the advantage of CRT would be more pronounced as the number of species to estimate in the sample is small.

| | WITec (+ CCD) | Horiba (+ EMCCD) | CRT (+ PMT) |
|---|---|---|---|
| SNR limitation | readout noise | excess noise | photon noise |
| LOD bounds ($N_{tot}$ photons) | $150 < LOD < 450$ | $25 < LOD < 40$ | $LOD < 15$ |
| Speed limitation | camera readout rate | camera readout rate | detector max. count rate / scanning system |
| Min. pixel dwell time (LOD experiment) | 43 ms | 2 ms | 400 $\mu$s (*) |
| Min. pixel dwell time (high SNR) | 12 ms | 700 $\mu$s | 10-100 $\mu$s $\times$ $M$ |

TABLE 3.2: LOD bounds and intrinsic speed limits of the systems. Minimum speeds achievable for the LOD experiments, and potential achievable speeds when the SNR can be considered as 'infinite'. (*): extrapolated speed from the experimental data at the LOD (Fig 3.5). Expected speeds, shown experimentally in Chapter 4. $M$: number of spectral filters.

### 3.2.3 Discussion and conclusion

From the above analysis, the advantage of CRT over the CCD-based system appears clear. On the given example, we found the limit of detection of CRT to be 10 times smaller and expect its acquisition speed to be about 100 times faster. However, the comparison with the EMCCD-based system is less straightforward, and a more precise analysis would be required to draw conclusions. The limits of detection were found to be similar. For a given SNR, we expect CRT to bring a interesting speed advantage, that would be less substantial as the number of species in the sample increases. Naturally, the CRT speed advantage holds once the reference spectra are learnt and the spectral filters calculated. These results are encouraging for CRT. Indeed, we compared state-of-the-art instruments with our suboptimal CRT custom-build spectrometer. In particular, CRT performances suffer from the poor PMT quantum efficiency (twice as worse as the cameras). Thus, we anticipate CRT to show greater advantage when further improved and equipped with a higher quantum efficiency detector.

This study tempted to benchmark the technology against state-of-the-art instruments. Although the conclusions seem relatively consistent, more analyses should be carried out to mitigate the

limitations of the present study. The main difficulty of this comparison lied in the many specific parameters of the three systems. Essentially, everything was different, apart from the sample and the excitation wavelength. This is why we tried to compare the systems by looking at the signal at the detectors, to draw conclusions with as little dependence as possible on the throughputs and focusing quality. Other relevant figures of merit could surely be considered, such as signal-to-background ratio, etc.
Other imprecisions that may modify the final results include (i) the differences in spectra quality (Fig. 3.3), (ii) the differences in signal-to-background ratio for the evaluation of the limit of detection (Fig. 3.5), (iii) the fact that we arbitrary decided to use the same algorithm as for CRT to select relevant spectral bases for the full Raman measurements. Nevertheless, we do not expect these imprecisions to strongly modify the conclusions and the given orders of magnitudes.
Yet, one of the main problems of the study - that could clearly be improved - is its lack of reproducibility and statistical relevance. First, although the samples are synthetic samples, they are not reference samples commonly used in Raman imaging. Second, the experiments were conducted on different regions of these samples, which may lead to some variability. Third, the results are derived from only a single experiment. To remedy these problems in a easy way, the study should be conducted on the same region of a reference sample (e.g. latex beads) and results derived from multiple identical experiments. A complementary study could be carried, for example in pure spectroscopy on a mixture of liquid solutions, to assess the proportion estimations performances in terms of speed and sensitivity.

## 3.3 Conclusion

Overall, in this chapter, we tried to provide a quantitative comparison of compressive Raman and conventional hyperspectral imaging. In general, the estimation precision of CRT may surpass the precision obtained when acquiring a full Raman spectrum, but the precision could only be compared when the spectral filters are orthogonal and exposure times are equal. In this case, the CRT estimation precision cannot surpass the precision estimation obtained with a full spectrum. We proposed a general methodology to quantify this difference in estimation precision.
The conclusions from the experimental comparison with state-of-the-art instruments suggest a clear advantage of CRT over CCD-based system, in terms of limit-of-detection and speed. The advantages over EMCCD-based system is slighter, but is expected to be substantial with a further improved CRT device, for small-scaled estimation problems. Yet, the gain in cost as compared to these systems is considerable.

# Chapter 4

# Applications

## Contents



As compared to state-of-the-art Raman imaging, compressive Raman presents some key advantages that strongly motivates its use for concrete applications. Sub-milliseconds acquisition speeds could enable rapid characterisation processes, in research and industry, or even ultimately allow the study of *in vivo* or dynamic processes. Yet, despite recent advances in the field, the best performances of compressive Raman shown so far consist of images of simple chemical crystals [119], with little concrete purpose, except for some results reported on pharmaceutical compounds [115, 122]. Thus, there is some incentive to apply compressive Raman to fields where it could bring substantial improvement.

In this chapter, we illustrate the usefulness of CRT for some applications related to biomedical imaging, pharmaceutical industry and environmental studies. Most of these results were obtained on a new CRT setup dedicated to applications: it was designed to operate in spectral region relevant for biological samples, to be more stable and capable to perform faster image scanning than the previous setup (Chapter 2). The design, development and characterisation of this setup

constituted a major part of this thesis work. In the following, we describe the setup and show its performances on samples relevant for concrete applications.

## 4.1 Application-oriented setup

### 4.1.1 Motivation

Originally, our main motivation was to use CRT for biomedical applications, which are often photon-starved, and for which acquisition speed is most important. The proof-of-concept setup, described in Chapter 2, has several critical drawbacks which made its operation impractical, even impossible, for realistic biomedical applications in tissue. The primary issue is its excitation wavelength at 532 nm. Although it gives rise to relatively high Raman signal (Eq. (1.28)), it also leads to strong tissue absorption and scattering [139–141], which greatly limits the light penetration depth, thus making imaging into tissue essentially impossible (Fig. 4.1). In addition, its relatively high energy is likely to give rise to tissue autofluorescence and may damage tissue. Conversely, choosing an excitation wavelength in the NIR mitigates these disadvantages, at the expense of lower Raman signal. We select the standard excitation at 785 nm, which gives rise to a Stokes-shifted Raman signal between about 800 nm and 1.1 $\mu$m, i.e. in a spectral region with low tissue absorption (Fig. 4.1). This standard wavelength enables us to buy conventional optics and to use a silicon-based detector. This allows us to stay in the shot-noise limited regime (A longer excitation wavelength would have implied to use a noisy IR detector).
Another flaw of the proof-of-concept setup is its scanning mechanism based on a piezo-electric scanner, which prevents us from exploiting the full speed capacities of CRT. On the new setup, we thus implement a scanning-system based on galvanometric mirrors than can perform precision scanning down to about 1 $\mu$s per pixel. We also use a commercial microscope for better stability. The setup design had to be compatible with requirements such as spatial/spectral resolution and compactness. In the following, we describe the developed setup and its main components.

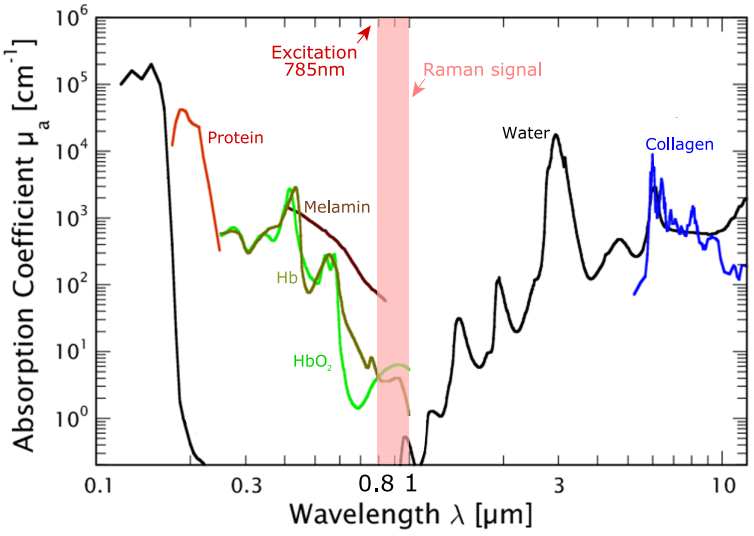


FIGURE 4.1: Absorption spectra of main tissue absorbers. Adapted from [139]

### 4.1.2 Setup description

The setup is depicted in Fig. 4.2. The excitation source is a continuous wave laser operating at 785 nm. The laser beam can be scanned in x and y with two galvanometric mirrors (GM) and scanning lenses ($L_2$). Inside the microscope, a prism (P) redirects the light into a tube lens ($L_1$) and an objective. The collected backscattered signal is de-scanned through the same optical path, and relayed onto a confocal slit (S) to reject part of the out-of-focus light. A combination of dichroic mirror (D) and notch filter ensures only the Raman signal is retained. A grating (G) spatially disperses the Raman wavelengths, which can be selected with the DMD. In this setup, we can collect the light from both the 'ON' and 'OFF' orders of the DMD. On each side, the selected spectral components are spatially recombined using a second grating that cancels out the first grating dispersion. This allows the collection of the signal onto a small area single-photon avalanche photodiode (SPAD). For the spectrometer alignment, we used a laser diode operating at 846.8 nm (CPS850 - Thorlabs). This allows alignment at a corresponding Raman signal at 927 $cm^{-1}$, i.e. approximately in the middle of the fingerprint region (Table.4.1).

| 785 nm | 800 nm | 850 nm | 900 nm | 950 nm | 1000 nm | 1050 nm | 1100 nm |
|---|---|---|---|---|---|---|---|
| 0 $cm^{-1}$ | 239 $cm^{-1}$ | 974 $cm^{-1}$ | 1628 $cm^{-1}$ | 2213 $cm^{-1}$ | 2739 $cm^{-1}$ | 3215 $cm^{-1}$ | 3648 $cm^{-1}$ |

TABLE 4.1: Match between the Stokes Raman signal wavelength (top) and the Raman shift (bottom), for an excitation wavelength of 785 nm. The fingerprint region is approximately comprised between 200 $cm^{-1}$ and 2000 $cm^{-1}$.

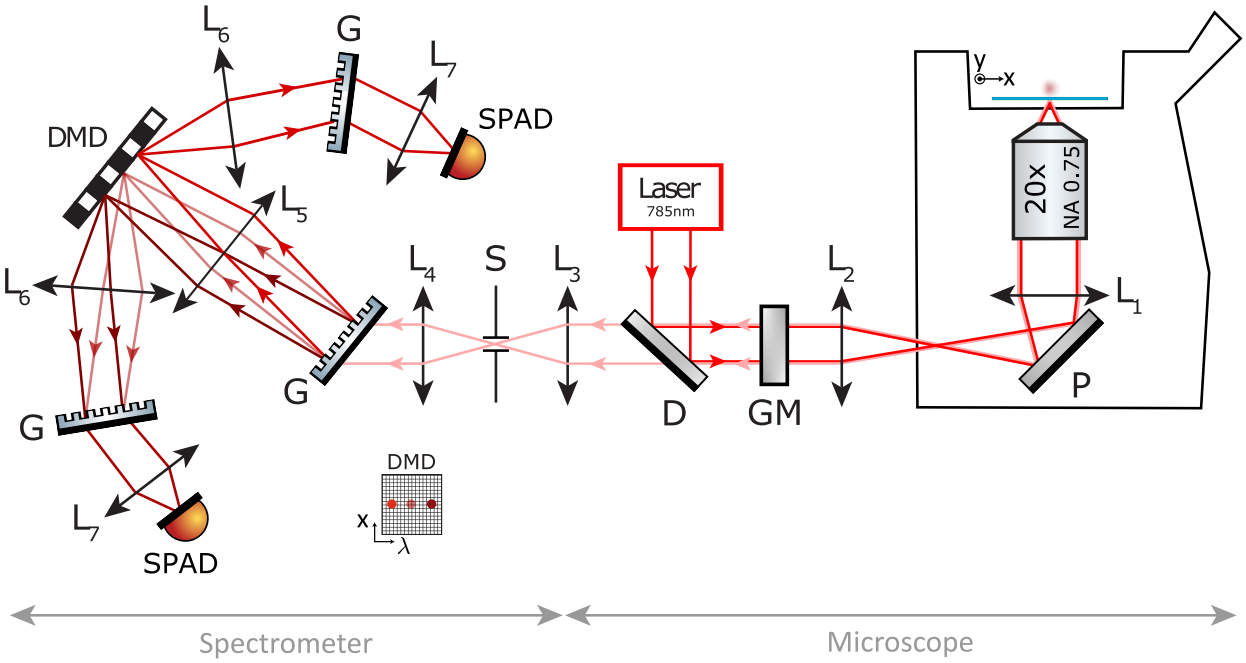


FIGURE 4.2: Schematic of the experimental setup, built around a commercial microscope. P: prism, GM: galvanometric-mirrors, D: Dichroic mirror, S: slit, G: grating, SPAD: single-photon avalanche photodiode. $L_1$: tube lens (200 mm), $L_2$: scanning lens (50 mm), $L_3 - L_7$: achromatic doublets with focal lengths 100, 125, 100, 100, 75 mm, respectively.

In the following, we describe main components of the system and elaborate on some of their characteristics. Since Raman applications are typically photon-starved, each component had to be chosen with care to maximize the instrument throughput.

### Laser

We choose a laser diode module from IPS (Innovative Photonic Solutions) that commonly equips commercial Raman spectrometers. Its output wavelength is meant to be stable and narrow, as well as robust to temperature changes, vibrations and back reflections.
The laser (L2K0785SD0090B-IS-TH-L) operates at 785nm. Its integrated laser line filter reduces the bandwidth down to 0.02 nm ($\leq$ 0.3 cm$^{-1}$). The output power is 100 mW and should vary by less than 1%, according to the specifications. The beam, vertically polarized, has a single spatial mode. However, the beam quality is relatively poor. It exhibits a square-like shape, a slight ellipticity (1.1) and $M^2 = 1.25$.

### Scanning system

The (x, y) scanning system comprises a pair of galvanometric mirrors and a lens ($L_2$). The silver-coated galvanometric mirrors (Cambridge Technology) are controlled with a driver designed for

high accuracy positioning. They are conjugated with the back focal plane of the objective with a $\times$ 4 magnification. The scanning lens is actually a pair of 2" identical achromatric doublets, with their crown glass facing each other (equivalent to a Plössl system),to make the scanning system telecentric. The equivalent focal length of $L_2$ (50 mm) is chosen to obtain a FOV of about 120 $\mu$m at the sample plane. The scanning system is calibrated by setting up the right voltage to scan known distances onto a calibration target.

**Microscope and objective**

The microscope assembly is an inverted microscope (Eclipse TE2000U - Nikon). We use the microscope port with the highest transmission to the sample plane. On this port, a prism redirects the light vertically towards the objective, with a transmission efficiency of 91%. Together with the tube lens, the microscope assembly transmission efficiency is 83% (Fig. 4.4). For alignment and characterisation purposes, we also equip the microscope with a CMOS camera (DCC1545M - Thorlabs) and a NIR LED.
The objective is a Nikon air objective (CFI Plan Apochromat Lambda - $\times$20 - NA 0.75). It is chosen for its relatively high NA and high transmission in the NIR region (above 80% between 800 nm and 1000 nm - Fig. 4.4). In the excitation pathway, the pupil of the objective is slightly underfiled, but we make full use of the NA for the collection.

**Notch filter and dichroic mirror**

The dichroic mirror (LPD02-785RU - Semrock) is a long-pass filter that reflects the laser beam and transmits the Stokes-shifted Raman signal. It reflects more than 94% of the light below 785 nm and transmits more than 93% above 795.2 nm, with a quite sharp transition (7.9 nm, or 126 $cm^{-1}$ width). Its transmission spectrum is relatively constant between 795.2 nm and 1200 nm (Fig. 4.4).
The holographic notch filter (HSPF785.0 - Kaiser), placed at the spectrometer entrance in normal incidence, rejects most of the remaining laser and Rayleigh light at 785 nm (optical density $\geq$ 6). Its spectral bandwidth is $\leq$ 10 nm (162 $cm^{-1}$).

**Relay optics**

All mirrors are broadband dielectric mirrors (Thorlabs) that ensure a transmission efficiency $\geq$ 99%. All lenses are achromatic doublets (Thorlabs) to limit chromatic aberrations. The focal lengths of $L_3 - L_5$ were chosen to comply with constraints such as available space, collection efficiency and spectral resolution. Ideally, to ensure high collection angles and completely cancel chromatic aberrations, 2" parabolic mirrors should be used in the spectrometer, instead of 1" lenses. However, the relatively small DMD reflection angles, the size of the two detectors and the limited available space did not make it possible to use such optics in our setup, while keeping its symmetry.

### Gratings

The gratings are transmission gratings (T-1200-850s - Lightsmyth) with a groove density of 1200 $mm^{-1}$. They are chosen for their high transmission efficiency ($\geq 94\%$ for the polarisation parallel to the grating lines). However, this efficiency drops for the opposite polarization, resulting in an average transmission efficiency of $\approx 85\%$ at 850 nm. The efficiency is acceptable but the setup would benefit from gratings with higher transmission efficiencies for both polarizations (Fig. 4.4).
The first grating of the spectrometer is placed in Littrow configuration (same incidence angle and diffracted angle at 850 nm), to reach its maximum diffraction efficiency. This is achieved by rotating the grating until the highest power in the first diffraction angle was found.
The grating placed after the DMD is identical to the first grating. It has to be aligned carefully to correctly cancel the first grating dispersion. To align it, we make the two lasers sources (at 785 nm and 850 nm) overlap spatially at the spectrometer entrance. First, the grating has to be placed at the plane where the two dispersed beams recombine after $L_6$. Since the system is not perfectly symmetrical and the DMD induces additional phase delay between the different wavelengths, the spectrum does not exactly recombines at the focal plane of $L_6$ [142]. Secondly, the grating incident angle has to be tuned so that the two wavelengths recombine into the same spatial point. The overlap is verified on a camera (distance between the two laser spots well smaller than the SPAD active area (500 $\mu$m)). As an additional verification, we translate the detector to verify that the spectrum is comprised within its active area.
Besides alignment difficulties, the thinness of the gratings ($\approx 0.6$ mm) caused some problems. The mounts were not sufficient to place the gratings in a stable way without applying strong mechanical constraints. At first, some solid gel was applied on the grating edges, and this greatly improved the stability. Yet, overtime this gel diffused into the grating grooves, thereby dramatically reducing their transmission efficiency, and thereby the spectrometer throughput. The gratings could be cleaned by immersion into chemical baths of alcohols and acetone, and their original efficiency retrieved. Finally, some Blu-Tack was used to stabilize them in a way that diffusion into the grooves could not happen.

### DMD

We use the same DMD as in the previous setup (2.3.1). It is made of 768 $\times$ 1024 aluminium-coated mirrors of size 13.68 $\mu$m $\times$ 13.68 $\mu$m. The reflection efficiency of aluminium in the wavelengths of interest is about 85%. Combined with other losses, the total DMD efficiency in this window is about 60% (Fig. 4.4). The DMD is mounted on a y$-$z stage to adjust its position in respect to the focus (z$-$axis) and to select the wavelength region of interest (y$-$axis). Since there are two detectors on each side of the DMD, we mount the DMD in normal incidence to preserve the system symmetry. Yet, the DMD intrinsic structure makes it act as a blazed grating [143–145]. Therefore, on the reflected light, orders of diffraction are present. The spatial position of these diffraction orders may be shifted compared to the optical axis, depending on

the DMD pixel pitch, wavelength and incident angle. For the wavelengths matching the blazed condition, most energy lies in a central order. In the opposite case, the energy is split into orders of diffraction. In our case, we collect all the signal onto a single-pixel-detector. Therefore, this behaviour is only a concern for the wavelengths already subject to vignetting, due to their proximity to the edge of the collecting lens $L_6$. In our case, the wavelengths at the edge of $L_6$ are 800 nm and 1 $\mu$m (Fig. 4.3). Since the total system efficiency is extremely low at 1 $\mu$m (Fig. 4.4), we would like to match the blazed condition for 1 $\mu$m, so that no further light is lost in vignetting.

To verify that the normal incidence configuration is indeed a consistent choice for our setup, we perform simulations using the code available in [145]. We found that the normal incidence configuration leads to blazed conditions around 800 nm and 1 $\mu$m, while the blazed condition is not matched for central wavelengths around 850-900 nm (Fig. 4.3 (a)). This is most appropriate regarding the setup design, since the central wavelengths impinge onto the detector regardless (Fig. 4.3 (a)). On the contrary, for wavelengths that fall on the optics borders, it is more important that the energy is concentrated into one spot so that we can detect them. Pictures of the orders of diffraction, obtained experimentally at 785 nm and 850 nm, qualitatively confirm the simulations validity (Fig. 4.3 (b)). We also note that the DMD OFF order of diffraction (residual light in the OFF order when all mirrors are ON) could contribute to some noise and degrade the spectral resolution to some extent. We estimated this OFF order to a few %, but its effect should be further investigated.

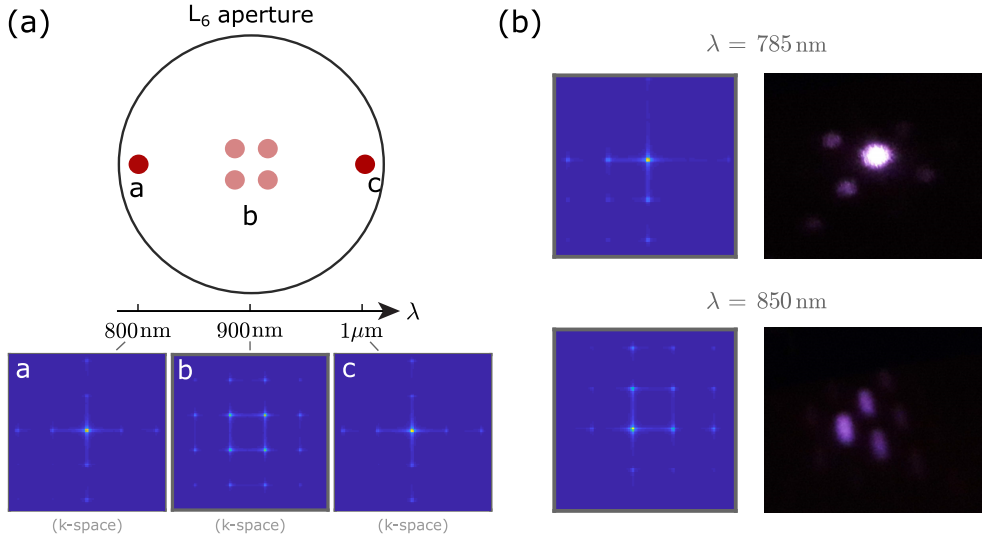


FIGURE 4.3: (a) Simulated orders of diffraction obtained with normal incidence onto the DMD, at three different wavelengths (k-space). The blazed condition is matched for wavelengths that are typically at the edge of our spectral range (800 nm and 1 $\mu$m). Conversely, the energy is split in between four orders around 900 nm. (b) Simulations and experiments with the two available light sources at 785 nm and 850 nm.

#### Detector (SPAD)

The detector specifications are decisive in the overall performance of the instrument. The detector needs to be a low noise and high quantum-efficiency photon-counting device. Yet, the excitation wavelength at 785 nm implies that the Raman Stokes-shifted signal lies between about 800 nm and 1.1 $\mu$m (Fig. 4.1), which is at the limit of the sensitivity region of silicon-based detectors. We chose the detector with the highest quantum efficiency that we were able to find: a single-photon avalanche photodiode (ID120) from IDQ (ID Quantique). Its quantum efficiency similar to the best silicon-based (EM)CCDs (e.g. Andor iXon): it reaches 75% at 800 nm, but drops to less than 5% at 1050 nm (Fig. 4.4). Thus, although the sensitivity region of this detector should allow us to measure Raman signal up to 3200 $cm^{-1}$, it is mostly sensitive in the fingerprint region (Table 4.1). As compared to the PMT of our previous setup (2.3.1), the detector quantum efficiency is twice better for low wavelengths, but varies a lot across the Raman spectrum. Another drawback is the relatively low available dynamic range, since the counting process is only linear until about $10^5$ counts/s. The detector dark-count rate is below 200 Hz and its active area of 500 $\mu$m.

### 4.1.3 Setup characterisation

In this section, we give some characteristics of the setup, in terms of throughput, spectral properties and spatial properties. We also assess its performances on a simple test sample.

#### System transfer function and throughput

The characteristics of the optical elements described above enables us to estimate the spectral transfer function of our instrument. Fig. 4.4 (a) represents the efficiency of the main optical elements through which the Raman signal passes, from emission to detection. These considerations are purely derived from the material themselves and ignore numerical apertures and vignetting. Combining these efficiencies results in a maximum efficiency of the collected Raman signal of $\approx$ 18% at 800 nm (Fig. 4.4 (b-c)). This efficiency decays fast to $\approx$ 0% above 1000 nm. The bottleneck clearly lies in the detector quantum-efficiency. In addition, due to the filters characteristics, no Raman signal can be detected below $\approx$ 795 nm (160 $cm^{-1}$). The efficiency curve (Fig. 4.4 (b-c) was not measured experimentally, but this could be done by measuring a constant intensity spectrum or a spectrum with a commercial spectrometer with known transfer function. We also note that, although the maximum available laser power is of 100 mW, the elements transmission on the excitation path lead to a laser power at the sample plane of only $\approx$ 55 mW.

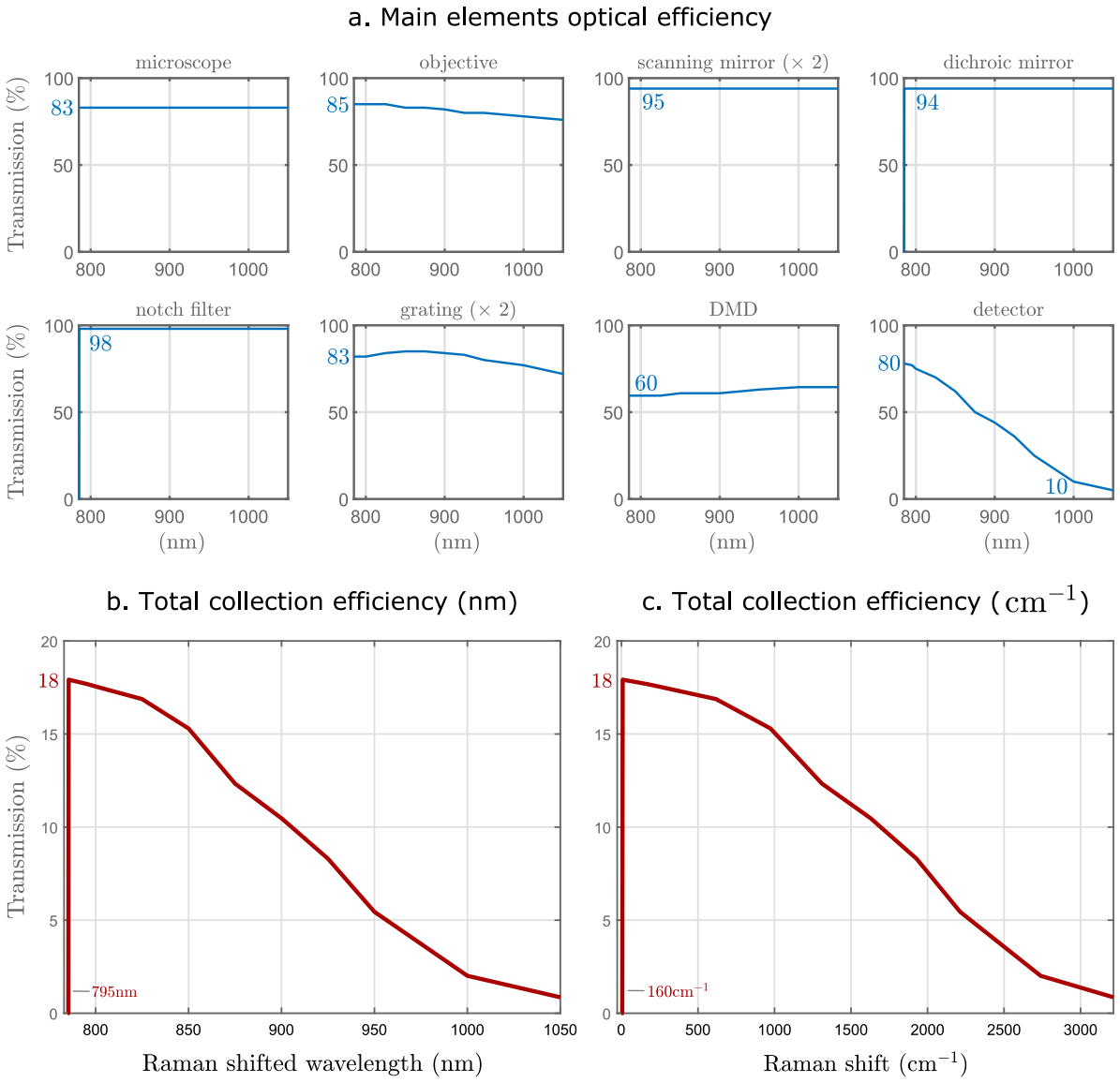


FIGURE 4.4: (a) Transmission, reflection or quantum efficiency of the main elements of the setup. Elements where the signal passes twice are indicated by (× 2). Efficiencies are relatively constant over the full spectrum, except for the detector. (b) Simulated total collection efficiency of the Raman signal.

### Spectral properties

The spectral resolution of the system can be approximated through [10]:

$$\delta\lambda = f_5\left(\frac{\lambda}{a} + \frac{b}{f_4}\right)\left(\frac{\partial L}{\partial \lambda}\right)^{-1} \tag{4.1}$$

where $f_5$ is the focal length of $L_5$, $f_4$ is the focal length of $L_4$, $a$ is the beam size , $b$ is the slit width, and $\frac{\partial L}{\partial \lambda}$ is the linear dispersion given by:

$$\frac{\partial L}{\partial \lambda} = \frac{f_5}{l\ cos(D)} \tag{4.2}$$

with $l$ the groove density (1200 mm$^{-1}$) and $D \approx 30.7°$ the diffraction angle at 850 nm. In the given setup configuration, at 850 nm, the inverse linear dispersion is estimated at 7.2 nm/mm. This corresponds to about 0.098 nm (1.36 cm$^{-1}$) per DMD mirror. The spectral resolution is estimated at $\delta\lambda \approx 12$ cm$^{-1}$. Thus, DMD mirrors can be binned 8-by-8 in the spectral direction $\lambda-$ without compromising the resolution. The accessible spectral range, limited by the size of the DMD, is about 95 nm. (1300 cm$^{-1}$). It allows to access the majority of the fingerprint region (Table 4.1). As previously mentioned, the targeted spectral window can be chosen by translating the DMD along the $\lambda-$axis (2.3.1). To assess the spectral properties, we measure the spectrum of a silicon (Si) sample, which is often used for calibration purposes in Raman spectrometers. Its sharp Raman peak at 520.7 cm$^{-1}$ is wider than gas laser lines, but is narrow enough for the predicted relatively large spectral resolution. Measuring the Si spectrum (with a slit width of 100 $\mu$m), and fitting its peak with a Lorentzian curve leads to a FWHM of about 17 cm$^{-1}$ (Fig. 4.5 (a)). In addition, evaluating the Si peak position allows to calibrate the spectrometer (i.e. to match one DMD pixel to a Raman shift with Eq. (4.2)).

The spectral resolution of our setup is relatively poor as compared to commercial Raman spectrometers, which commonly attain resolution of a few cm$^{-1}$. Such resolutions may be necessary for some applications. It could for instance be improved by choosing longer focal lengths, or a finer grating. Yet, this would come at the expense of spectral range or compactness.

**Spatial properties**

The laser beam does not fill the pupil of the objective, resulting in an effective NA of 0.37 in excitation. The FWHM of the excitation PSF ($\lambda$/ (2 NA)) should thus theoretically measure about 1 $\mu$m.

To confirm this estimation, we acquire Raman images of a resolution target provided by Horiba Scientific. This target is made of thin gold patterns (40 nm) deposited onto a silicon substrate (inset Fig. 4.5 (a)). The images are acquired by designing a DMD filter that only selects the silicon peak, and thus rejects any light reflected by the gold surfaces. Fig. 4.5 (c) shows the image of a zone where the space between two lines is the same than the width of the line. The sampling is 0.26 $\mu$m. We clearly resolve the lines in the 1.5 $\mu$m zone, hardly the lines in the 1 $\mu$m zone, and we do not resolve the lines 0.5 $\mu$m zone. This confirms the approximation of the spatial resolution of 1 $\mu$m.

Furthermore, we measure the Raman signal from an homogeneous silicon zone of the target, to experimentally estimate the FOV. It is found to be about 100 $\mu$m, which is slightly smaller than the 120 $\mu$m expected from the optical design (Fig. 4.5 (b)).

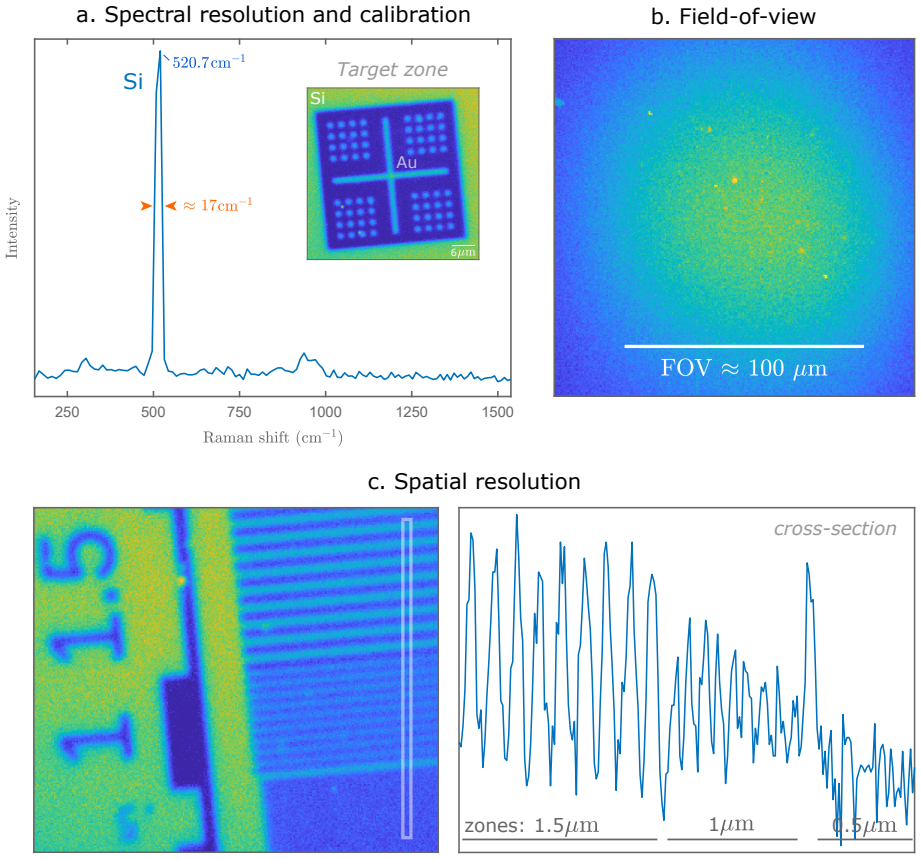


FIGURE 4.5: (a) Raman spectrum of silicon: the peak location permits to calibrate wavelength position on the spectrometer DMD pixels, and its FWHM gives an estimation of the spectral resolution. Inset: One zone of the resolution target, made of gold deposited on silicon. (b) Signal from a scanned homogeneous silicon zone, resulting in an estimation of the FOV. (c) Spatial resolution estimation measurement. On the target zone, the line spacing = lines width).

### System performances on a test sample

Last, we demonstrate the ability of the instrument to perform rapid imaging of latex beads, with the same method as described in chapter 2. We only use one of the detectors, the use of two detectors is not covered in this thesis.

Two different types of beads (Sigma Aldrich) - 30 $\mu$m polystyrene beads (PS) and 20 $\mu$m poly(methyl methacrylate)) (PMMA) - are displayed on a $CaF_2$ coverslip (Crystran). The laser power at the sample plane is set to 55 mW, and the slit is 100 $\mu$m wide. The DMD pixels are binned 8-by-8 along the $\lambda-$axis, and fully binned along the x$-$axis. The reference spectra (Fig. 4.6 (a)) are obtained by averaging 4 spectra measured at different spatial positions of the sample, for an integration time of 100 ms per spectral pixel.

Each filter $\mathbf{f}_m$ projection results in the images of Fig. 4.6 (b), with $n_m$ the number of counts per pixel. These images are acquired with scanning steps of 0.5 $\mu$m, and with a pixel dwell-time of 200 $\mu$s. The subsequent estimated proportion maps (Fig. 4.6 (c)) allow to clearly distinguish the species. Combining these proportion maps and normalizing them to their brightest pixel leads to the composite RBG map of Fig. 4.6 (d-left). To obtain the average number of detected

counts per spatial pixel, we sum the numbers of counts from the projection maps and average over each species pixels. This way, we obtain an average of 100 counts on PS pixels and 50 counts on PMMA pixels. Experiments with faster pixel dwell time are conducted, down to 12 $\mu$s per pixel per filter. This results on a total acquisition time of 36 $\mu$s per pixel for the three filters projection. At such speeds, only about 6 and 3 counts are measured on the pixels corresponding to PS and PMMA, respectively (averages on each species pixels, see Eq. (3.8)-3.9). Thus, on this simple example, we show our instrument ability to perform a CRT experiment with acquisition speeds of the order of 10$\mu$s per pixel per filter.

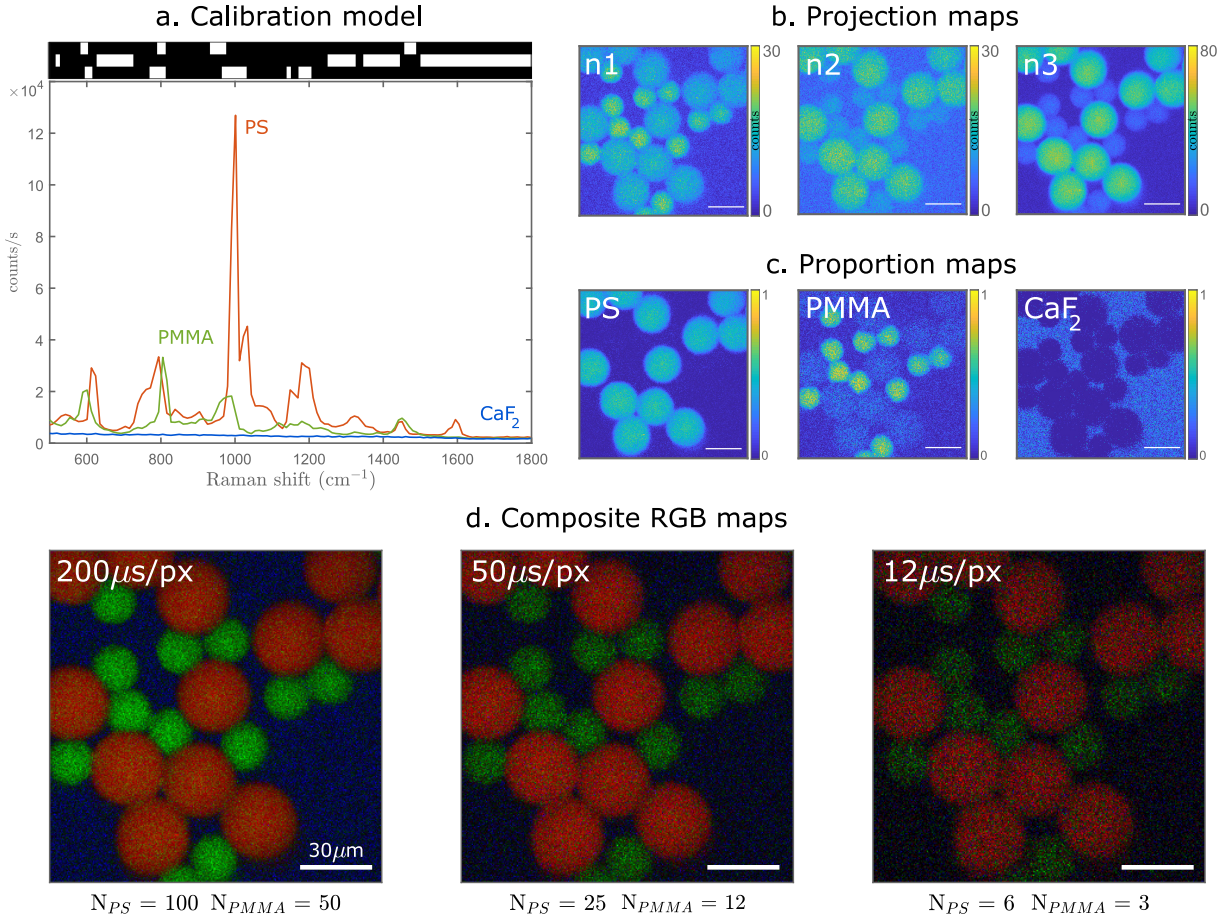


FIGURE 4.6: (a) Reference spectra of polystyrene (PS), poly(methyl methacrylate) (PMMA), $CaF_2$ , and their associated spectral filters. (b) Projection maps with exposure time per pixel per filter of 200 $\mu$s. (c) Estimated proportion maps of the three species. (d) Associated composite RGB image with same exposure time (left), and less exposure time (middle and right). $N_{PS}$: detected total number of counts, averaged on PS pixels, $N_{PMMA}$: detected total number of counts, averaged on PMMA pixels. Scale bars: 30 $\mu$m.

## 4.2 Applications

In the above section, we described the developed setup and showed compressive Raman results on a simple test sample. From now on, we test the ability of CRT on more complex samples. We applied CRT to some fields that, in our sense, could benefit from its use. The following results are early stage results and could be improved in the future. They are a necessary step before more conclusive results can be shown. First, we show one set of results obtained with the proof-of-concept setup. Next, we demonstrate results obtained with the setup described above.

### 4.2.1 Breast microcalcifications

*The results in this part arise from a collaboration with the group of N. Stone (University of Exeter, UK). Samples were provided by A. Ghita. These compressive Raman experiments were performed on the proof-of-concept setup operating at 532 nm. This work led to the publication 'Assessment of compressive Raman versus hyperspectral Raman for microcalcification chemical imaging' [138]*

Microcalcifications are important indicators of disease in breast tissue, and are often considered in diagnosis [146]. Although the current breast cancer diagnostic techniques are not chemically specific, several studies suggest that the chemical composition of microcalcifications reflects the physiological state of surrounding tissue, and is related to cancer development [146–148]. In the breast, two types of microcalcifications are frequently found. Type I microcalcifications are composed of calcium oxalate $CaC_2O_4$, for instance in a monohydrate form (COM). Type I microcalcifications seem to be mostly associated with benign breast disease [146, 147]. Type II microcalcifications consist of hydroxyapatite (HAP), a mineral form of calcium apatite with lattice unit cell $Ca_{10}(PO_4)_6(OH)_2$. In some conditions, a phosphate group of HAP can be substituted by carbonate group, thereby forming carbonated hydroxyapatite (CHAP) [146–149]. Studies have demonstrated that the carbonate content in CHAP is an indicator for the malignancy of the breast cancer [146–149]. It has been shown that Raman spectroscopy can be particularly useful to distinguish between different types of microcalcifications and to assess their carbonate content [149]. For example, the carbonate substitution in CHAP has a Raman spectroscopic signature, manifested by a shift of the resonance at 1048 $cm^{-1}$ to 1071 $cm^{-1}$ [149] (Fig. 4.7 (b)). In this context, we apply CRT on samples mimicking microcalcifications commonly found in human breast.

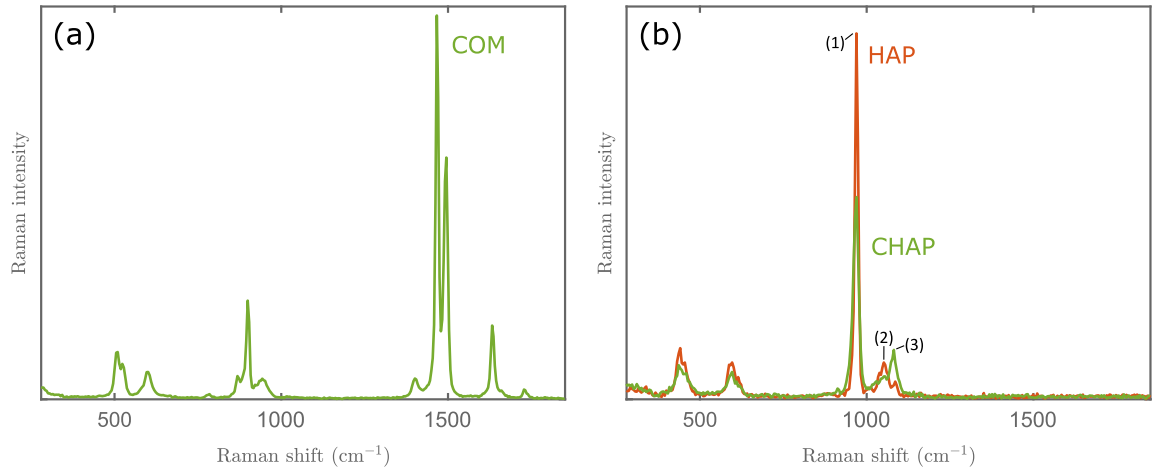


FIGURE 4.7: Raman spectrum of (a) Monohydrate calcium oxalate (COM) (b) Hydroxyapatite (HAP) and carbonated hydroxyapatite with 8.12% carbonate substitution (CHAP). In HAP and CHAP, the peak (1) is a signature of the phosphate group ($\approx$ 960 cm$^{-1}$). The carbonate content leads to a Raman red shift of the peak at 1048 cm$^{-1}$ (2) to 1071 cm$^{-1}$ (3). The spectra were acquired with the WITec system described in Chapter 3.

### Method

In this work, we used three synthetic powders mimicking the chemical composition of breast microcalcifications: COM (Alfa Aesar), HAP (Sigma-Aldrich), and CHAP, i.e. HAP with 8.12% carbonate substitution (Sigma-Aldrich). Such highly concentrated CHAP is not believed to be found in the breast but exhibits the same spectral peaks as less concentrated CHAP, with a more pronounced carbonate peak at 1071 cm$^{-1}$. Experiments focused on discriminating HAP from COM, and HAP from CHAP. They were conducted on the CRT setup operating at 532 nm described in chapter 2. The laser power at the sample plane was 60 mW, the spatial sampling of 0.75 $\mu$m, and the exposure time of 4 ms per pixel per spectral filter.

### Results

Experiments were conducted with the powder samples dispersed onto $CaF_2$ coverslips. In a first experiment, we imaged a sample composed of HAP and COM. The reference spectra were acquired with 100 ms integration time per spectral basis (4 binned DMD mirrors), and averaged over 4 different spatial points. A simple calibration model with only two spectral filters allowed an accurate estimation of the two species proportions (Fig. 4.8 (a-b)). The same experiment was conducted on a sample composed of HAP and CHAP. These two species spectra are quite similar (spectral overlap Eq. (2.21) of 0.85). Their reference spectra were acquired with 500 ms integration time per spectral basis and averaged over 4 different spatial points. The signal-to-background ratio of the CHAP spectrum is poor as compared to the HAP spectrum. This time, a simple two filters model failed at estimating the two species. We included the $CaF_2$ spectrum in the model, as well as a constant background that models the offset difference between HAP

and CHAP spectra. This calibration model allows for the species to be accurately estimated (Fig. 4.8 (c-d)). These images were obtained with about 100 counts in total on HAP and CHAP pixels. Estimation could be performed down to 8 counts.

A third experiment was conducted in the presence of tissue background. For this, we placed a $\approx$ 1 mm piece of chicken breast on a glass coverslip. We acquired the Raman spectrum of the tissue (Fig. 4.9 (c)), and sprinkled sample powders (HAP and COM) onto the chicken tissue. We could not image the powders inside the tissue due to the very high scattering of tissue at the laser wavelength (532 nm). To assess the influence of the background on the model in this specific example, we performed the experiment with three different calibration models (Fig. 4.9):

- (a) No background is included in the model. The estimation performs relatively well on HAP and COM, but the tissue part is estimated as being HAP. This is expected since we wish to discriminate three species with only two filters.
- (b) The $CaF_2$ spectrum is included in the calibration model. The estimation performs better, but the tissue is still partially considered as HAP.
- (c) The tissue spectrum is included in the calibration model. There is a neat improvement in the estimation. HAP, COM and the tissue are well estimated. More details are also captured: On the top right of the field of view, there seems to be a HAP particle hidden below the tissue.

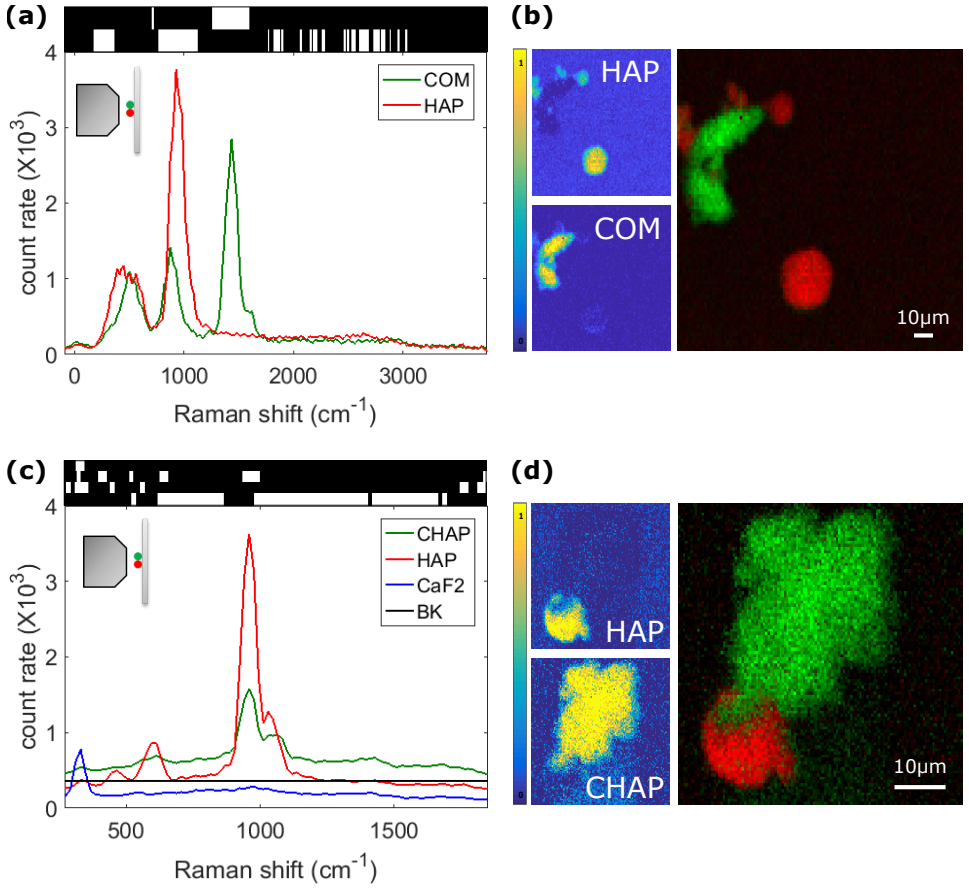


FIGURE 4.8: (a) Reference spectra and filters for HAP and COM estimation. (b) Proportion maps and composite RGB image. (c) Reference spectra and filters for HAP and CHAP estimation. Only the spectral range of interest in shown, and only the proportion maps of CHAP and HAP (d).

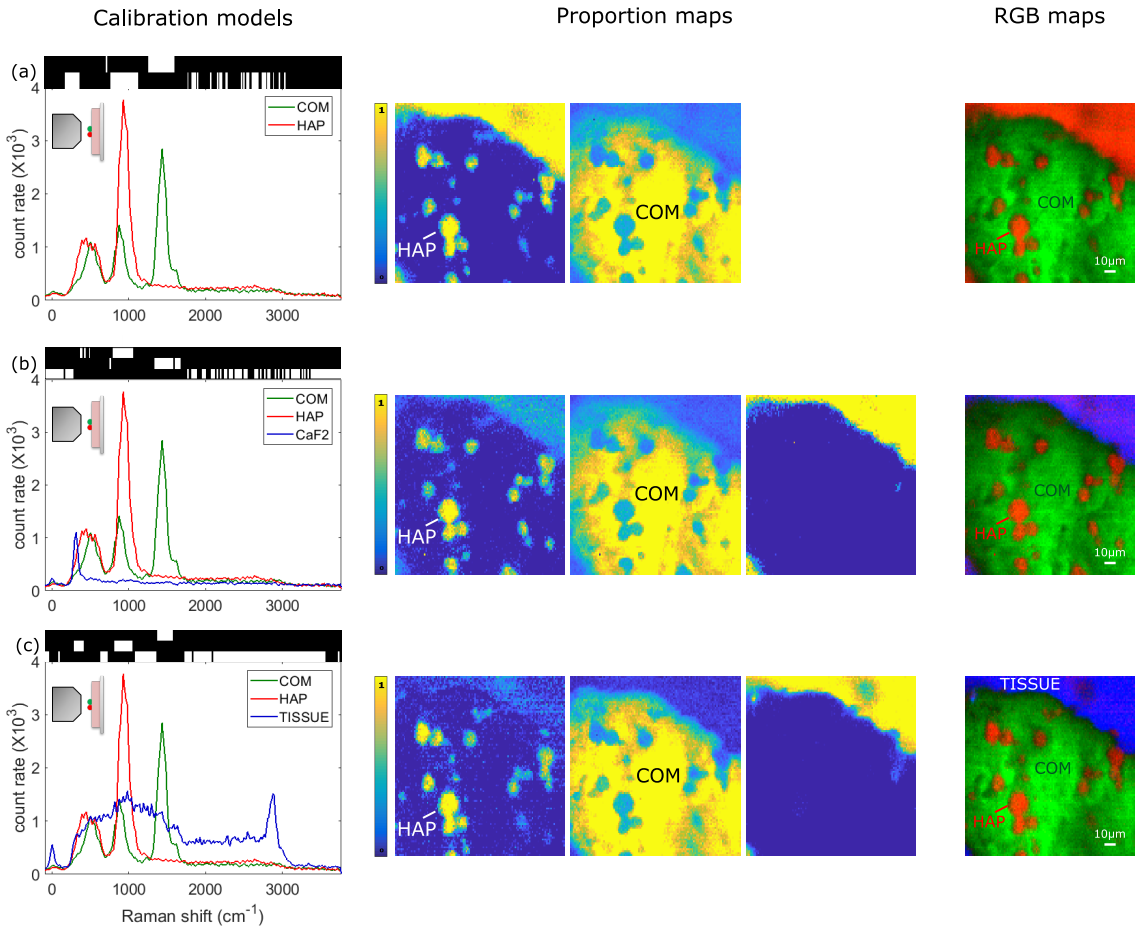


FIGURE 4.9: Experimental results in the presence of tissue background, with three different calibration models (a) with only two filters, (b) with an inappropriate background spectrum, and (c) with taking into account the spectrum of tissue.

### Discussion and conclusion

We demonstrated preliminary results of compressive Raman on samples of biomedical interest. Experiments were realised on powders mimicking microcalcifications that can be found in human breast. Results allowing to dicriminate between different types of microcalcification types are shown. We also show results in the presence of tissue background. Although this experiment is simplistic and does not reflect a real sample, it highlights that CRT is a background adaptable technique. The filters can be optimized in a different way depending on the background. This is an interesting advantage over conventional hyperspectral Raman imaging, in which the same information is measured whatever the background, and in which the background presence can only be post-processed. In this example, we considered the background as a chemical species. But for further improvement, we could also consider it as a nuisance parameter [121].
Theses experiments were realised early in the thesis, therefore on the proof-of-concept setup operating at 532 nm. Experiments on the same samples should now be conducted on the NIR setup, with the microcalcification powders embedded in tissue [150]. In the following, all experiments were performed on the NIR applicative setup.

### 4.2.2 Pharmaceutical compounds

*The samples in this part were provided by Sanofi (Sanofi Recherche Développement, Montpellier, France). This works follows the work of B. Sarri [151] and X. Audier [41] performed on the same samples, using Stimulated Raman Scattering (SRS).*

In the pharmaceutical industry, it is common that the drug production process leads to the formation of pharmaceutical compounds under different polymorphic forms [152, 153]. It means that these compounds have the ability to crystallize in more than one form. Polymorphs have the same chemical composition but their arrangement and/or conformation differ: This leads to differences in physico-chemical properties, such as solubility, stability, or compactibility [152–154]. Therefore, the control of polymorphs is critical for the pharmaceutical industry, in order to provide the more efficient form of medicines. Polymorphs screening is mandatory when developing a drug; different techniques are used for this purpose, such as thermal analysis, differential scanning calorimetry, X-ray powder diffraction, or electron microscopy [153]. Vibrational spectroscopy is also widely used, since it allows non-destructive control [153]. In this context, Raman spectroscopy is particularly interesting, and would benefit from faster imaging capabilities. Recent work reported the use of SRS to assess polymorph distributions in tablets [41, 151]. In this section we evaluate the performances of CRT for mapping the distribution of some pharmaceutical compounds.

#### Method

The experiments were performed on powders samples, provided by Sanofi. The active pharmaceutical compound - Clopidogrel - is known to have two polymorphic forms [151, 155], denoted here C1 and C2. In pharmaceutical tablets, the active compounds are generally found is small proportion. Most of the tablet volume is made of functional excipients that ensure tablet integrity, taste, conservation, stabilization, delivery, etc. To mimic real pharmaceutical tablets, we also image three common excipients in the form of powders, namely mannitol (MAN), polyethylene glycol (PEG), and corn starch (AMI).
In our experiments, the reference spectra were measured by placing a small portion of each chemical powder on distinct areas of a $CaF_2$ coverslip. The integration time per spectral basis (8 binned DMD mirrors) was 100 ms, and spectra from 5 different spatial locations were averaged to obtain the reference spectra. For mapping the chemical distribution, the five different powders were then mixed together onto a $CaF_2$ coverslip. The laser power at the sample plane for all experiments was 55 mW.

#### Calibration

Fig. 4.10 (a-b) shows the Raman spectra, in the fingerprint region, of the two pharmaceutical compounds and three excipients. These Raman spectra were provided by Sanofi. We measured

on our setup the spectra of each chemical species. We found a good match with the expected spectra (Fig. 4.10 (c-d)), but our spectral resolution is lower and lesser signal is obtained at higher wavenumbers, due to the transfer function of our system (Fig. 4.4). While the compounds particles seem morphologically alike, the morphology of the three excipients is sufficiently different to make the experiments easier. AMI appeared in the form of circular particles, while MAN and PEG exhibit distinct crystals shapes (Fig. 4.10 (d)).
Together with the $CaF_2$ slide spectrum, these measured spectra constitute the calibration model from which the spectral filters were calculated (Fig. 4.11 (a)). We note that this estimation problem is relatively complex as compared to the previously presented experiments, since it includes six chemical species, among which two (C1, C2) have a high spectral overlap (0.86). The correlations between all spectra is represented in Fig. 4.11 (b).

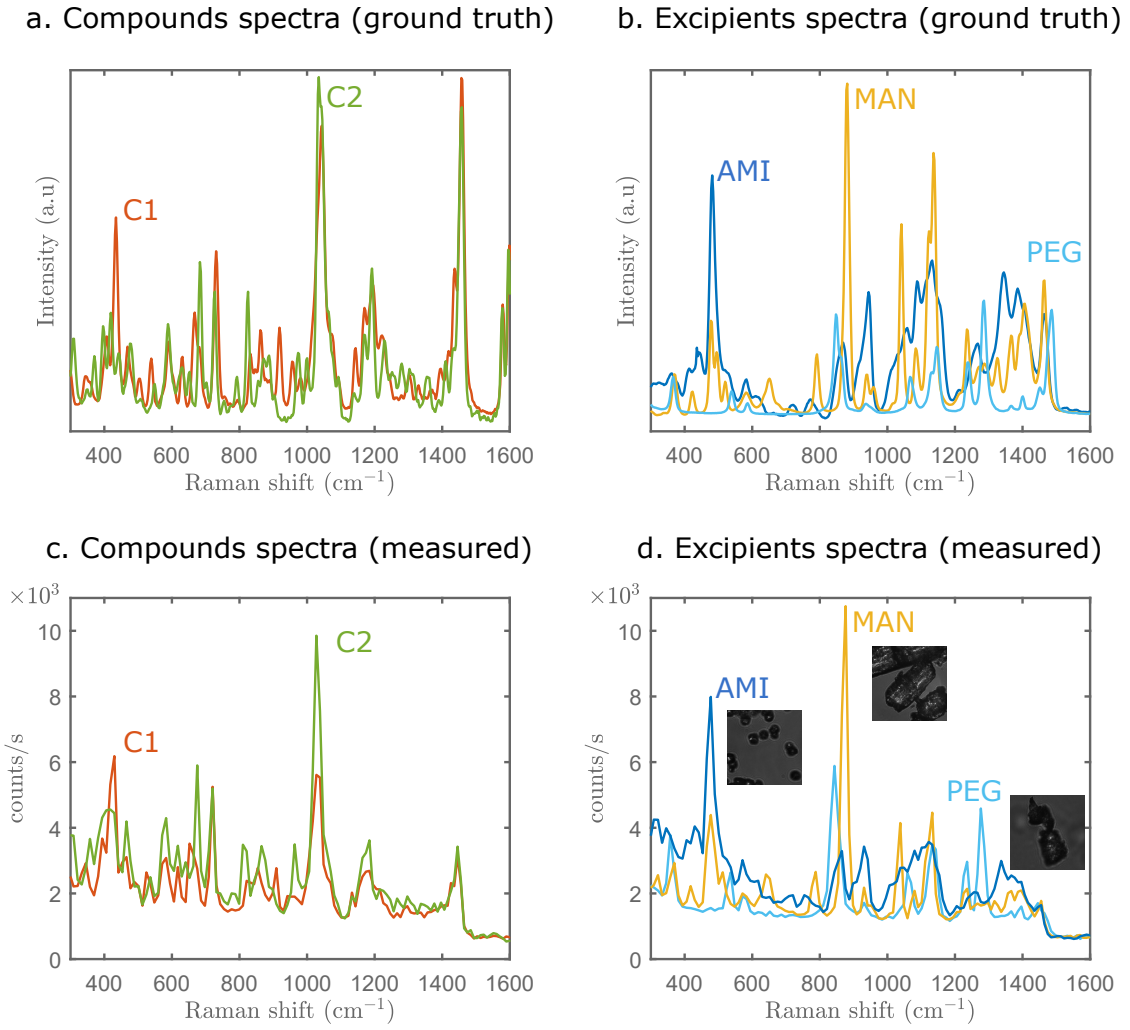


FIGURE 4.10: Raman spectra of pharmaceutical compounds and excipients provided by Sanofi (a-b), and measured on the Compressive Raman spectrometer (c-d). Unlike the two polymorphic compounds C1 and C2, the excipients crystals have low spectral overlap and distinct morphologies

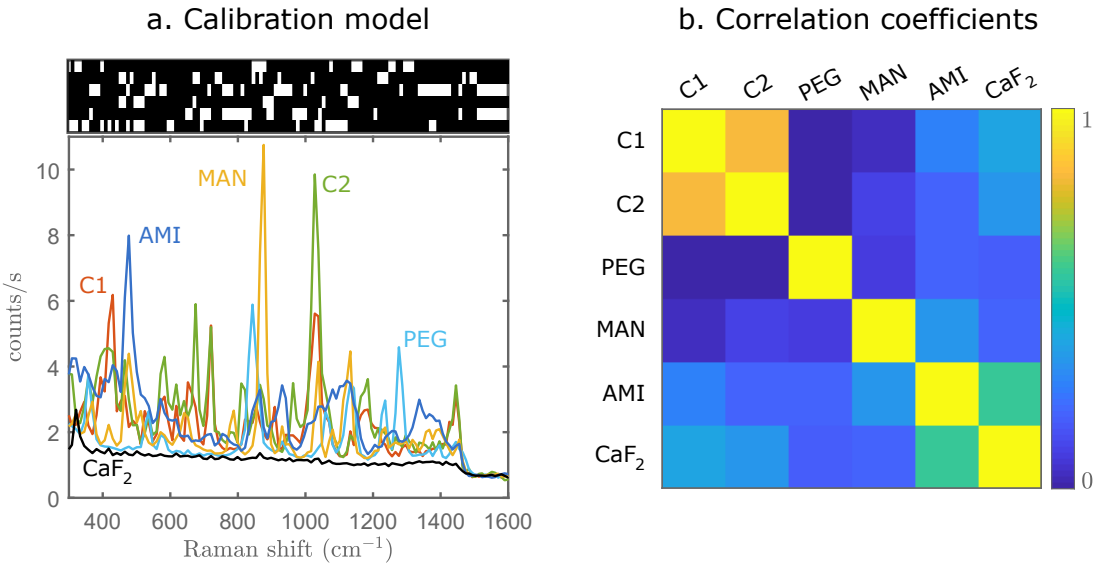


FIGURE 4.11: (a) Reference spectra of the compounds, excipients and $CaF_2$; and the associated spectral filters. (b) Spectral correlation coefficients: The highest spectral overlap Eq. (2.21) is between C1 and C2 (86%).

### Species mapping

We then mixed the five different powders onto a $CaF_2$ coverslip. The spatial sampling is set to 0.5$\mu$m, and the exposure time to 1 ms per spatial pixel per spectral filter. The obtained estimated proportion maps show limited crosstalk (Fig. 4.12 (a)). To obtain the fake colors images, a threshold was applied on these proportion maps (all proportion values lower than 7% are set to zero), and they were normalised to the brightest pixel of each map. Combining these images (except the $CaF_2$ map) resulted on composite maps Fig. 4.12 (b). In total, acquiring this 120 $\mu$m $\times$ 120$\mu$m composite image necessitated 5.7 min. Images allowing visual species discrimination could be acquired with exposure times down to 100 $\mu$s / pixel / filter (34 s in total). For this exposure time, each spectral filter led to the detection of less than 5 counts on particles pixels. In a last step, we acquired spectra on some pixels corresponding to C1 and C2 on the Fig. 4.12 and confirmed the validity of the estimates. The same procedure was applied to image a larger region of 480 $\mu$m $\times$ 480$\mu$m, by stitching several FOV (Fig. 4.13 (a-b). The spatial sampling of 1 $\mu$m. Images acquired with 1 ms and 100 $\mu$s / pixel / filter could be obtained.

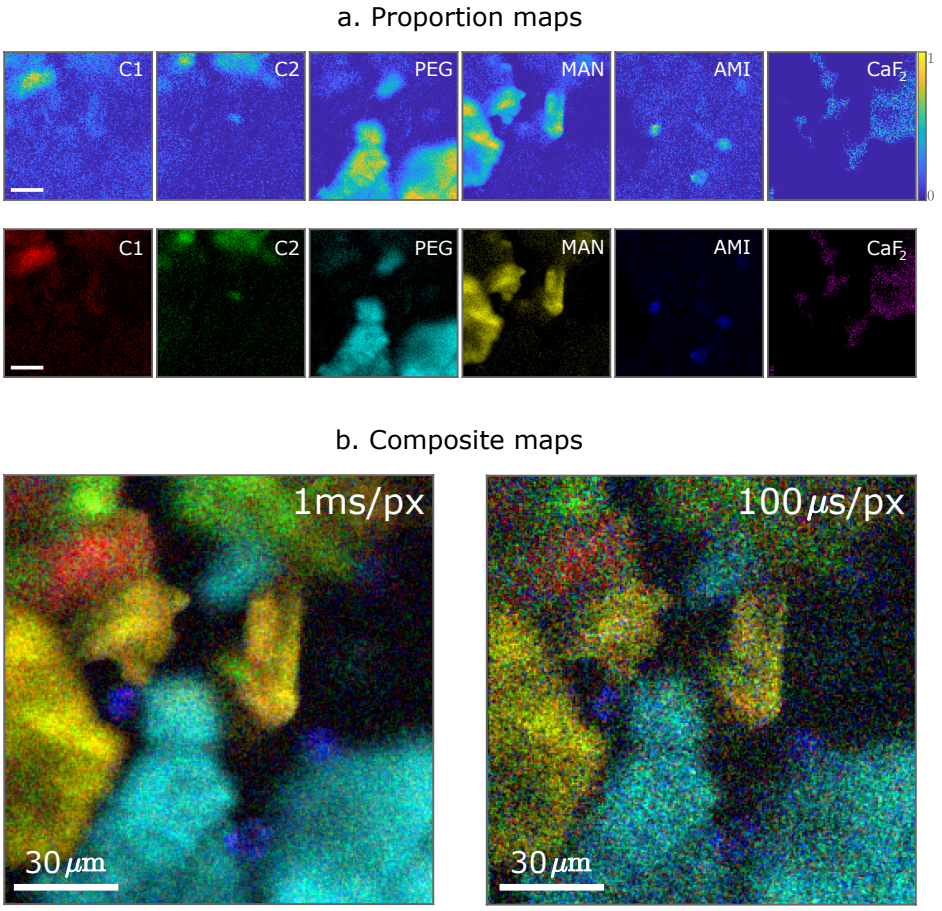


FIGURE 4.12: (a) Raw proportion maps (top), and after thresholding and normalisation, with associated fake colors (bottom). (b) Composite map obtained by combining all proportion maps except $CaF_2$. The pixel dwell times are given per spectral filter. Scale bars: 30 $\mu$m.

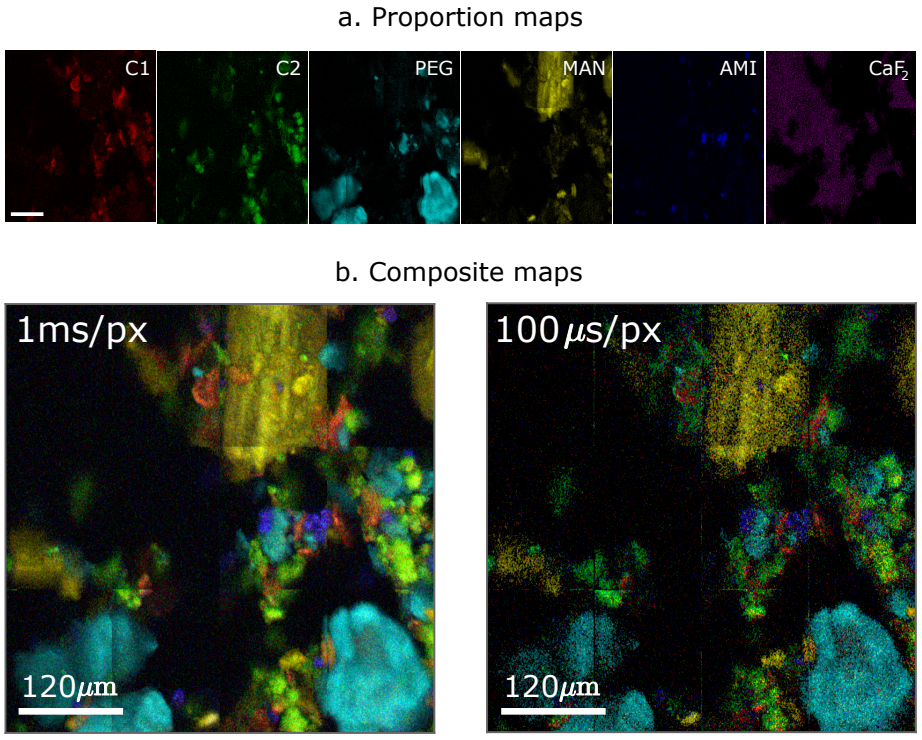


FIGURE 4.13: (a) Proportion maps after thresholding and normalisation, with associated fake colors, obtained by stitching several FOV (b) Composite map obtained by combining all proportion maps except CaF−2. The pixel dwell times are given per spectral filter. Scale bars: 120 $\mu$m.

**Discussion and conclusion**

We showed preliminary results that demonstrate the usefulness of CRT for mapping the distribution of five pharmaceutical powders, mimicking a pharmaceutical tablet. We were able to distinguish between the two spectrally-similar polymorphs and three commonly used excipients, with total pixel dwell times of 600 $\mu$s. This could be compared with recent results obtained with SRS in [151], which necessitated a total pixel dwell time of 2 ms to obtain similar images on tablets. Experiments on large areas of pharmaceutical tablets were not performed by lack of time, but should be performed for more convincing proof. We also note that these experiments could not be performed with the setup operating at 532 nm, due to the presence of a high fluorescence background in the Raman spectra. In conclusion, these results are encouraging for the suitability of compressive Raman for this type of application.

### 4.2.3 SERS reporters

*The results in this part arise from a collaboration with the group of N. Stone (University of Exeter, UK). The samples were provided by B. Gardner and A. Ghita.*

One method to amplify weak Raman signals is to employ surface-enhanced Raman scattering (SERS) [156–159]. Typically, molecules are attached to nanometer sized metallic structures. When the exciting light field matches the resonance of the structure surface charges, highly localized plasmonic fields can be created in the structure vicinity. This results in strongly increased Raman signals, since both the exciting field and the resulting Raman field undergo enhancement [160, 161]. The enhancement factor can be as much as $10^{10}$-$10^{11}$ [160, 161], thereby rendering SERS useful to detect single molecules [158]. Nevertheless, the SERS process is complex, and does not just provide spontaneous Raman spectra with simply enhanced signals. For example, the enhancement is not equal for all frequencies along the spectrum, since its strength depends on the field frequency with respect to the plasmon frequency. In addition, although the modes present in SERS and Raman spectra are often similar, some modes may differ, because the SERS process modifies the Raman selection rules. Indeed, when molecules are adsorbed to a surface, the symmetry of the system can change, slightly modifying the symmetry of molecules, which can lead to differences in modes selection [162].

The group of N. Stone, with which we collaborated for this project, aims at using SERS for theranostics [163–166]. Theranostics is the combination of diagnosis and therapy. It aims to identify diseases and treat them in a single non-surgical procedure. Typically, nanoparticles are coated with Raman active molecules (Fig. 4.14). In turn, recognising agents such as antibodies are attached onto this molecular layer, so that the whole structure binds to some specific targets. The whole structure can thus be seen as a Raman label for specific targets in the body: the Raman signature is specific to the target, and may be used for diagnosis [166]. Afterwards, the metallic particles plasmon resonance can further be exploited to create large temperature fields in their vicinity, thus favouring the target heating and destruction [166]. The advantage of using Raman labels instead of fluorescence labels is that they can be excited with NIR light that penetrates in tissue. Another advantage is that many molecules are Raman active so a large number of materials can be chosen to satisfy particular constraints, such as biocompatibility, etc. In this context, compressive Raman could be interesting. Since the SERS spectra of the Raman labels can be measured in a calibration step, CRT could be a useful tool for rapid identification of the different Raman labels.

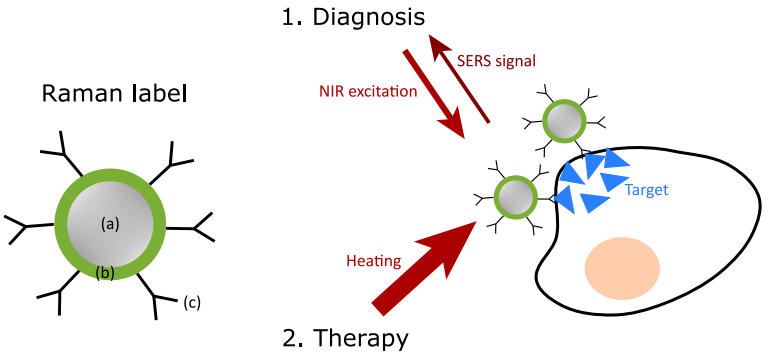


FIGURE 4.14: Schematic Raman label composed of (a) a metallic nanoparticle, (b) a layer of Raman active molecules, (c) recognising agents. This label binds to a specific target which can be identified through its SERS signal. Therapy can then be realised by heating the target.

### Calibration

In this study, we focused on the coated nanoparticles, without the recognising agent. The samples were prepared from 100 nm nanoparticles with resonance at 785nm. They were labelled with 4-Mercaptobenzoic acid (MBA) or 2-Naphthalenetiol (NAP) (Fig. 4.15 (b)). For calibration, we acquired the spectra of isolated beads from each type. Samples coated with MBA were found to be unstable: different spectra were measured on different particles and on slightly different positions of the focus (Fig. 4.16 (a)). On the contrary, samples coated with NAP were found to be relatively stable ((Fig. 4.16 (b)). We nevertheless proceeded to a CRT experiment. The calibration model (Fig. 4.15 (a)) was obtained by averaging some MBA spectra that seemed to be occurring the most often, and that matched best the spectra measured by the sample providers. The spectra were acquired with about 3 mW of laser power at the focus, and in 100 ms per spectral basis (8 binned DMD mirrors).

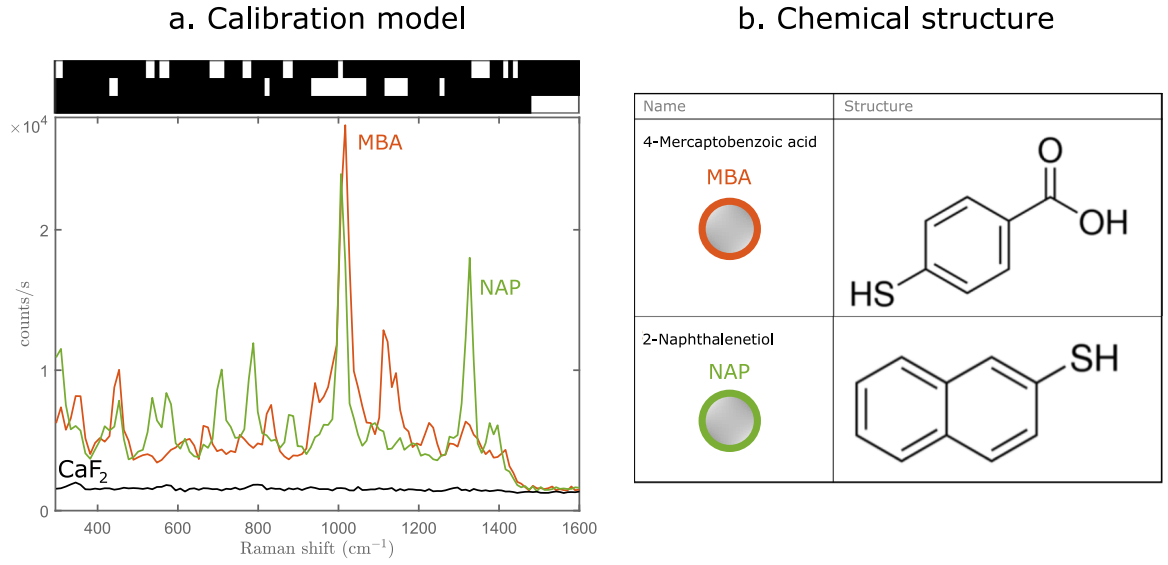


FIGURE 4.15: (a) Reference SERS spectra of the coated nanoparticles, and associated spectral filters. (b) Nanoparticles coating chemical structure.

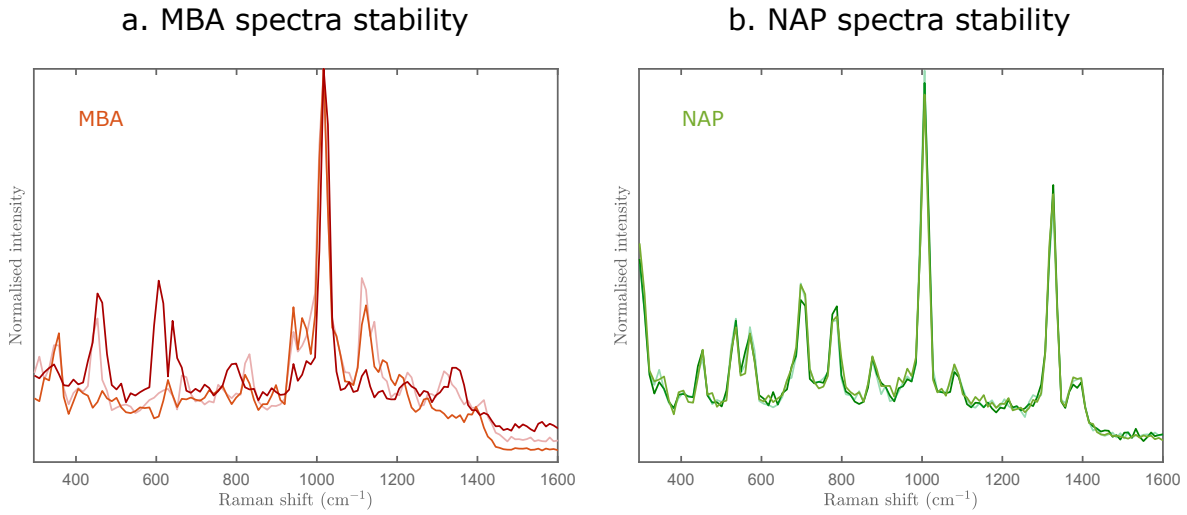


FIGURE 4.16: Examples of spectra recorded on (a) three random MBA-coated particles and (b) three random NAP-coated particles.

### Species mapping

An example of obtained proportion and composite map is given in Fig. 4.17 (a). The FOV was $50 \times 50$ $\mu$m, the spatial sampling 0.3 $\mu$m, the laser power at the sample plane 12 mW and the exposure time of 200 $\mu$s per pixel per filter. On this FOV, the estimation seemed to perform relatively well with respect to the model. We unsurprisingly noticed a wrong estimation for one of the particles, denoted A. It was estimated to account for about 50% of NAP and MBA. When recording the SERS spectra of this particle, they were found to be different for every acquisition. Three examples of these spectra acquired on A are shown on Fig. 4.17 (b). We note that the Raman signal from the particles was indeed very strong due to the SERS effect. Nevertheless, the laser power was greatly reduced to avoid burning, leading to these pixel dwell-times of a few hundreds of $\mu$s.

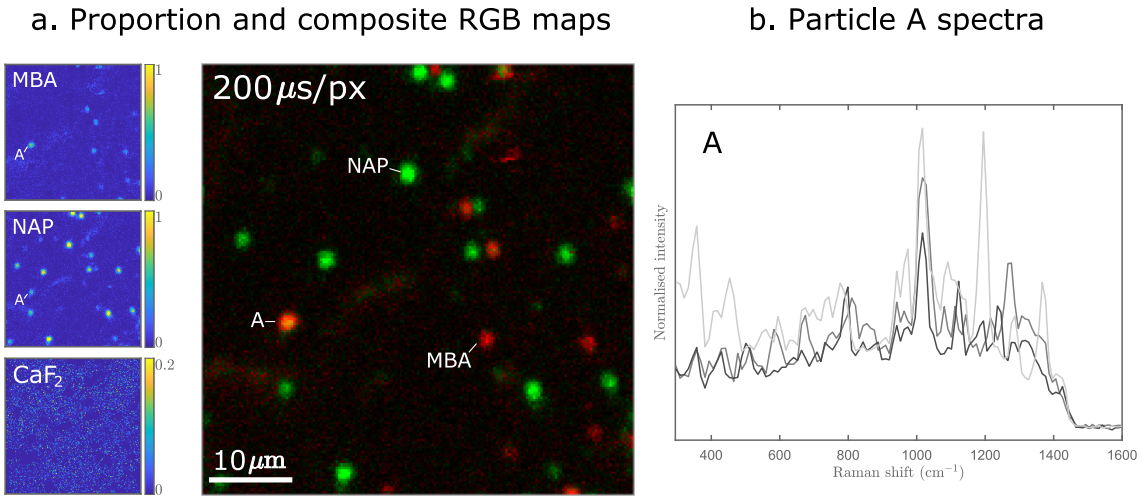


FIGURE 4.17: (a) Proportion maps and composite RGB map (form MBA and NAP proportion maps). Exposure time: 200 $\mu$s / pixel / filter. Most particles are clearly identified, but particle A is seen as a mixture of two species. (b) Three recorded spectra, in a raw, on A show instability. We surmise A to be a MBA-coated particle.

**Discussion and conclusion**

Although CRT could be very interesting for the kind of theranostics applications mentioned above, the results obtained so far are not very conclusive. The samples are very bright, but seem to exhibit some instability. However, we do not know if this instability is intrinsic to the particles or if it arises when focusing for too long on a particle.
Intrinsic instability could arise from the sample preparation. For instance, if the coating is formed around an aggregate of 2 nanoparticles instead of 1 nanoparticle, the SERS signal may be modified. Our spatial resolution is not sufficient to detect such aggregates.
Instability may also arise from a power excess when recording spectra. We noticed that, when raster-scanning an image during 10 min, with laser power 12 mW and a pixel dwell time of 200 $\mu$s, the level of signal was stable over time. However, acquiring a spectrum requires to keep the laser focused on a fixed point at least for a few seconds per spectrum. This may result in consequent heating, and we observed burning when acquiring consecutively a few spectra on the same focal spot. In addition, we cannot perform calibration by measuring the Raman spectra of the pure materials without the nanoparticles, since the Raman and SERS spectra may differ . Therefore, other methods of calibration should be thought of to improve the results.

### 4.2.4 Microplastics

*The results of this part arise from a collaboration with L. Zada (VU Amsterdam, The Netherlands). L. Zada works on SRS for microplastics identification [167]. He provided samples and shared ideas of experiments.*

The abundance of plastic products has resulted in a proliferation of small plastic particles - called 'microplastics' - in the environment. Although public awareness is rising and research is growing on the subject [168–170], little is known yet regarding their their toxicity and impact on the environment. A better identification and quantification of these particles is of upmost importance, in order to evaluate the environmental impact and potentially mitigate the resulting pollution.
The term of microplastics generally designates plastics fragments of less than 5 mm diameter, with no lower limit [171]. These small size polymer particles have diverse origins and compositions. They constitute a wide range of polymers, which chemical, mechanical or aesthetic properties were often modified with additives. Their diversity in size and chemical composition makes them difficult to detect and categorise. These tasks are even more challenging since they are often embedded in complex environmental matrices.

Currently, the identification of microplastics is often performed with spectroscopic techniques such as Fourier-transform infrared spectroscopy (FTIR) and conventional spontaneous Raman spectroscopy [172–177]. Recent advances in Raman spectroscopy for the identification of microplastics can be found in [174]. Yet, both FTIR and Raman spectroscopy are very time-consuming methods. As a result, these techniques often rely on visual inspection to preselect the particles suspected as microplastics for spectroscopic confirmation [178, 179]. Recently, microplastics identification with stimulated Raman scattering (SRS) has been demonstrated [167], with acquisition speeds of a few hundreds of $\mu$s per spatial pixel: this is more than 100 times faster than conventional Raman mapping of the same samples [167]. This shows that SRS could be an efficient method for monitoring microplastics in the environment. However, implementing SRS requires expensive equipment, and environmental studies may benefit from a cheaper and simpler tool. In this context, we propose to use CRT for microplastic mapping. We show preliminary results on different types of polymer powders (same samples than in [167]).

### Method

Artificial polymer powders were provided by L. Zada. The powders were obtained by grinding with sandpaper each type of polymer (high production-volume polymers). We performed experiments on powders of polypropylene (PP), polyethylene (PE) and polyethylene terephthalate (PET).
The particles sizes were relatively unequal, comprised between a few $\mu$m and a few hundreds of $\mu$m. For calibration, each polymer powder was placed onto a separated area of a $CaF_2$ coverslip. Several spectra were acquired in each zone, for an integration time of 100 ms per spectral basis. The reference spectra result from averaging 5 spectra. Afterwards, several powder types were mixed and displayed onto a $CaF_2$ coverslip. We acquired images over larger areas by stitching several FOVs. The sampling was set to $2\mu$m. For these experiments, the laser power at the sample plane was 55 mW.

### Mapping of PP and PE

One of the experiments consisted in imaging a mixture of PP and PE powders. Fig. 4.18 (a) shows the obtained reference spectra and the spectral filters. The acquisition time was 250 $\mu$s per spatial pixel per spectral filter. This corresponds to the acquisition of a FOV of 0.7 mm $\times$ 0.7 mm with three filters in about 1.5 min. Fig. 4.18 (b-c) shows the obtained proportion maps after estimation and the composite RGB image: Some particles seem to be clearly identified as being PE or PP, while others lead to high proportions on the three maps. To verify the validity of these estimations, some spectra were acquired after the filters projection was completed. The spectra acquired in particles A and B (Fig. 4.19) validate their composition as being PP and PE, respectively. The spectrum obtained on particle C does not correspond to any spectrum taken into account by the model, with brighter spectral signature. This explain why the considered model (Fig. 4.18 (a)) does not lead to a correct estimation of these particles. These spectra may result from some fluorescence of this particle. The Raman image (with no spectral selectivity) of the same FOV supports this: the particles which proportions are misestimated correspond to brightest particles of the image (Fig. 4.19 (b)).

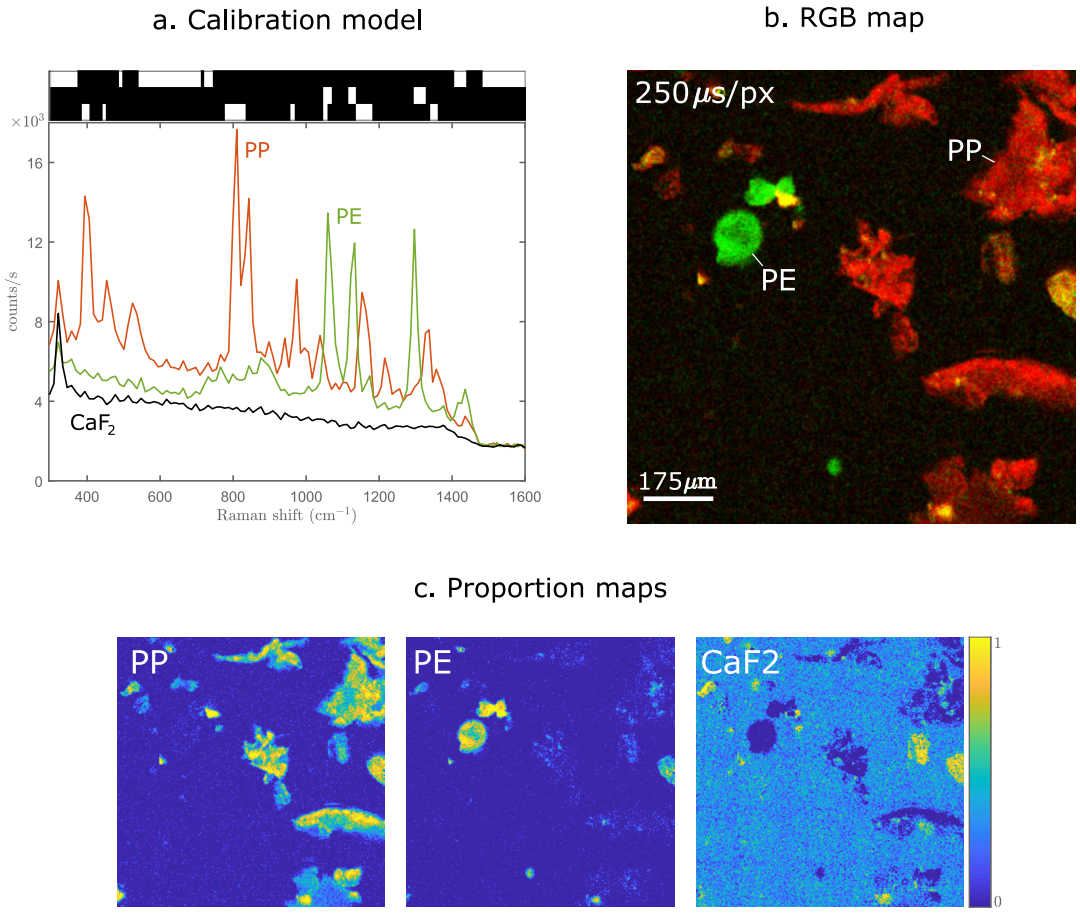


FIGURE 4.18: (a) Reference spectra and associated spectral filters. (b) Composite RGB map of the two first proportions maps of (c). The estimation fails on the particles in yellow: they are be found to have close to 100% proportion on the three proportion maps (c). Images exposure time = 250$\mu$s / pixel / filter. PE: Polyethylene. PP: Polypropylene.

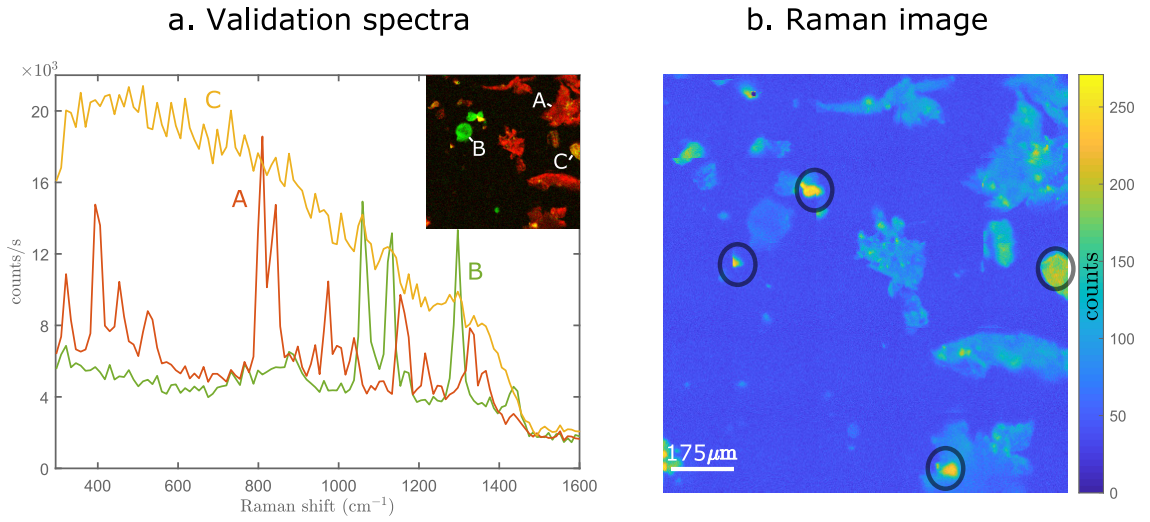


FIGURE 4.19: (a) Partial validation: After the filters projection, spectra are acquired on some points on the image. Spectra acquired in position A and B are found to match the PP and PE reference spectra, respectively (Fig. 4.18). The spectrum acquired in C may arise from fluorescence with high signal. (b) Raman image (no spectral selectivity) of the same area: the poorly estimated particles exhibit stronger signal that the others. Exposure time = 250$\mu$s / pixel.

### Mapping of PP, PE and PET

Another experiment consisted in imaging a mixture of PP, PE and PET powders. Already during the calibration step, we encountered difficulties to measure the PET reference spectra, since some strong background was arising from many PET particles. Thus, included an additional background spectrum into the model. Fig. 4.20 (a) shows the reference spectra and the spectral filters. The acquisition time was 330 $\mu$s per spatial pixel per spectral filter. This corresponds to the acquisition of a FOV of 0.87 mm × 0.7 mm with three filters in about 4.2 min. Fig. 4.20 (b-c) shows the obtained proportion maps after estimation and the composite RGB image (from PET, PE and PP proportion maps): Some particles seem to be clearly identified as being PE, PP or PET, while others lead to high proportions on the three maps and appear in white on the RGB image. On the background map (BK), we note that low proportions are estimated for most particles, except on particles that appear in white onto the RGB map. As opposed to Fig. 4.18 (c), here the $CaF_2$ map does not contain other chemical species than $CaF_2$, although its proportion is underestimated. Fig. 4.21 shows examples of spectra acquired on two particles. Spectra acquired on two positions of what seems to be a PET particle exhibit some strong background (Fig. 4.21 (a)). On the region A, some peaks on the reference PET spectrum can be identified but sit on a high background. The same is observed for region B, but with an even worse signal- to-background ratio: the peaks hardly stand-out of the background. Fig. 4.21 (b) shows spectra acquired on a 'white' particle. Three spectra were consecutively acquired: we notice a decrease in intensity of these spectra, which could be a signature of fluorescence bleaching.

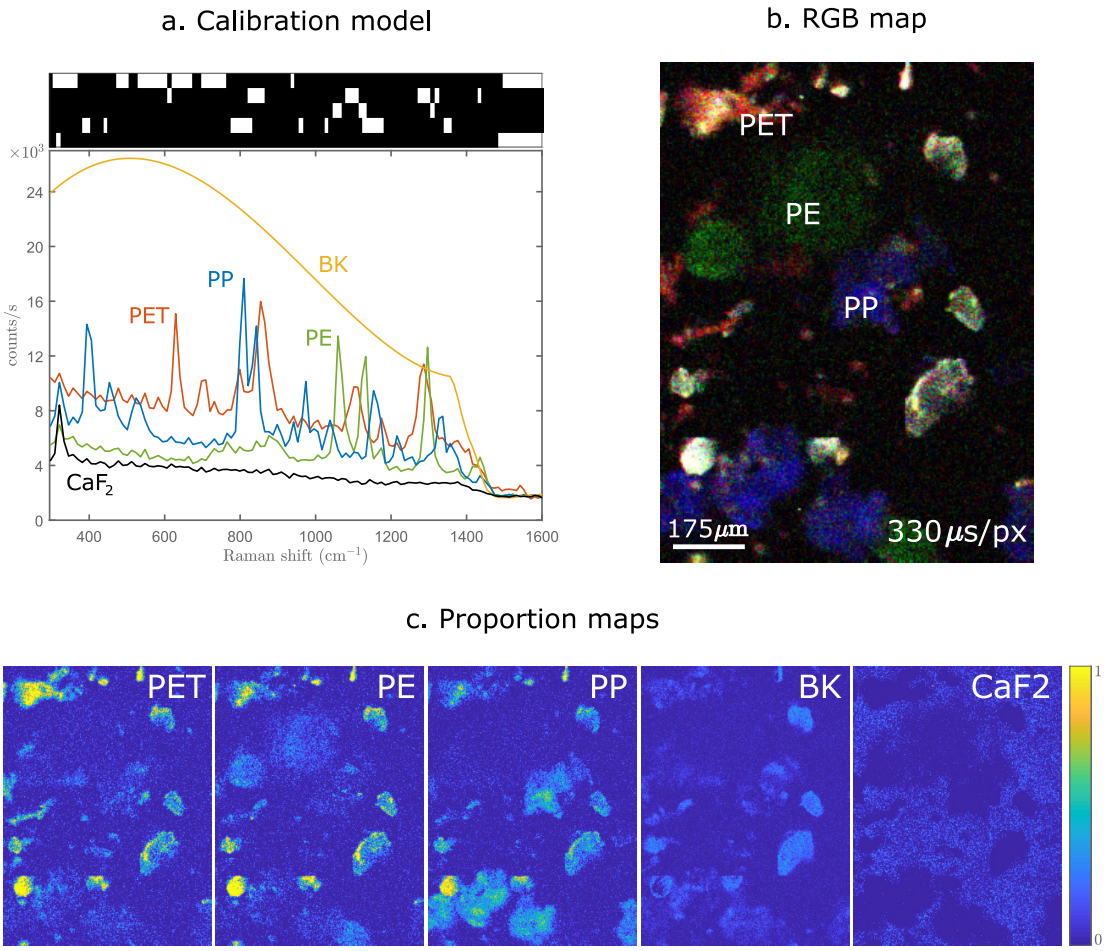


FIGURE 4.20: (a) Reference spectra and associated spectral filters, taking into account a modelled fluorescent background (b) Composite RGB map of the three first proportions maps of (c). The estimation fails on the particles in white: they are found to have high proportions on the four first proportion maps of (c). Images exposure time = 330$\mu$s / pixel / filter. PE: Polyethylene. PP: Polypropylene. PET: Polyethylene terephthalate. BK: modelled background.

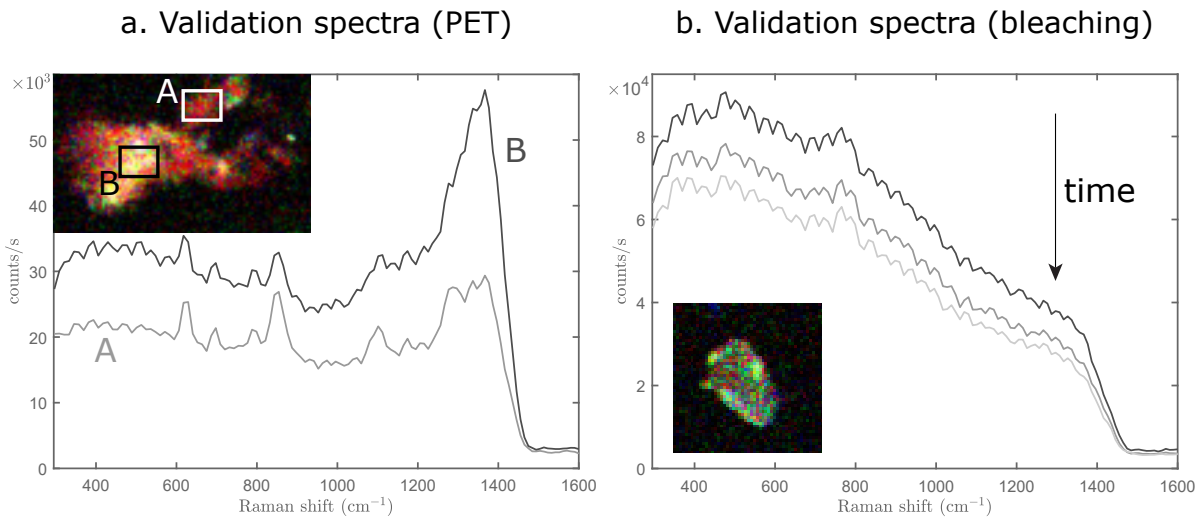


FIGURE 4.21: Partial validation: After the filters projection, spectra are acquired on some points on the image. (a) Spectra acquired in position A and B are found to partially match the PET reference spectra (Fig. 4.20) but with a high background. (b) Evolution of the spectrum acquired on a white particle at the same spatial position. The signal seems to bleach.

### Discussion and conclusion

In this section, we reported some preliminary results on artificial microplastics samples. The estimations were successful to some degree, with pixel dwell times of a few hundreds of $\mu$s. As a comparison, SRS experiments on the same samples performed about 2 to 3 times faster [167]. However, the results quality is limited by high background signal arising from some particles. We surmise this background to be some fluorescence signal, that may come from additives. This is supported by the fact that the samples are not transparent but white. Differences between reference spectra from pure materials and measured Raman spectra on microplastics are often reported in the literature [174, 180]. Often, these differences are due to fluorescence arising from impurities such as additives, organic particles, etc [174]. To overcome this problem, we tried to model the fluorescent background, or to consider it as a nuisance parameter (like in [121]) but with limited success. The problem is that the fluorescent background sometimes completely overshadows the Raman spectrum. Other solutions include time-gating the fluorescence [128], or to use a non-linear contrast such as SRS.

Another problem we faced was the very different sizes of the particles. It was hard to find the right focus, but this will be facilitated by mounting an automated translation stage along the optical axis. Additional experiments were performed on residual microplastics contained in water bottles [175], but we came across similar difficulties.

## 4.3 Conclusion and discussion

In this chapter, we described the optical setup developed for application-oriented experiments. Its NIR excitation wavelength makes it particularly useful in a biomedical context, but also for applications where scattering or fluorescence may be problematic. With this setup, we demonstrated Raman imaging on a simple sample made of polymer beads, with acquisition speeds down to $\approx 10\mu$s per pixel per spectral filter. This confirms the capability of CRT for Raman fast imaging.

We also showed results on samples having real applicative interest, for instance for biomedical imaging. First, the results obtain on synthetic microcalcification samples constitute a conclusive first step. Further experiments with the same samples embedded in tissue, and with *ex vivo* samples, would bring stronger proof of the usefulness of CRT for this specific application. Secondly, we showed preliminary results on SERS reporters. However, more work should be performed - on the sample itself and on the calibration procedure - to prove the consistency of CRT for this application.
The results obtained on pharmaceutical compounds are encouraging. They show the performances of CRT in a system of six chemical species, among which two have highly overlapping spectra. The acquisition speeds, on the order of a few hundreds of $\mu$s, are of the same order of magnitude than SRS on the same samples [151]. The ability of CRT to map the species distribution on bulk pharmaceutical tablets should now be shown.
Last, we showed preliminary results for microplastics identification. The acquisition speeds are here again comparable with SRS speeds obtained on the same samples [167]. Yet, the fluorescence that seems to arise from some samples constitutes a severe obstacle. Therefore, adopting methods to mitigate this fluorescence background is crucial if one wants to apply CRT to this problem. For example, we could time-gate the fluorescence [128] and combine it with a fluorescent-robust calibration model [121].
Although all these results are preliminary, they give concrete examples of applications that could benefit from CRT. The conducted experiments allowed us to identify some problems related to the samples themselves or to the experimental procedure. They also gave ideas of improvements that could be brought to the setup or the model. Thereby, they pave the way for future experimental work that would potentially give rise to more conclusive results.

In general, CRT performances would benefit from additional improvements brought to the setup and/or to the model. For example, the low collection efficiency of our system could be enhanced. Although the detector efficiency is the bottleneck, not a lot of improvements can be brought on this side, since its quantum efficiency is related to the intrinsic properties of silicon. Nevertheless, some enhancement of the collection efficiency could be obtained with more efficient gratings and a DMD with a coating dedicated to the NIR region. We also note that for a given application, the use of the DMD is not necessary. Although the DMD allows versatility, it also introduces other problems and has a relatively low efficiency. Instead, for a system dedicated to one specific

application, in-built binary spectral masks with combinations of absorptive/reflective coatings could for instance be designed.
Other potential improvements could be brought to the dynamic range and signal-to-background ratio of our system, which are both relatively poor. First, the SPAD we use saturates only slightly above $10^5$ counts/s. Second, there is a relatively high Raman background that arises from some optics, that we have not managed to suppress yet.
Other ameliorations could arise from the use of two detectors (Fig. 4.2). Indeed, in all the presented experiments, only one of the two detectors were used. The use of two detectors is not covered in this thesis, but we simply mention that, applying complementary filters onto the DMD potentially allows faster acquisition speeds [122]. For example, for a case of two chemical species and two spectral filters, with $f_1 = 1 - f_2$, the measurements can be performed in parallel (signal from $\mathbf{f}_1$ to one detector and signal $\mathbf{f}_2$ to the other detector).
Other improvements could be brought to the model itself. For instance, the model could be made more robust by considering background as a nuisance parameter [121]. In addition, we note that, although we use an estimation model, the final purpose of all above experiments is, *in fine*, species discrimination. Therefore, a model based on classification theory is expected to bring some improvements [181, 182].

All the sources of improvement mentioned above are not developed in this thesis and reported to future work. Rather, in the following, we decide to focus on one particular change that could potentially improve CRT acquisition speed. We propose to further multiplex the Raman signal by implementing a line-scan modality to CRT (Chapter 5), and we question its utility as compared to point-scanning (Chapter 6).

# Chapter 5

# Line-Scan Compressive-Raman

**Contents**



While conventional hyperspectral Raman imaging can exploit both dimensions of cameras to perform line-scanning of the sample, or widefield imaging with spatial and/or spectral encoding (1.2.2-1.2.3), CRT, so far, only permits a raster-scanning imaging modality. The work presented until now only exploited the system adaptability in the spectral dimension, to measure Raman spectra and to display sample-dependant optimal spectral filters. Yet, the system single-pixel architecture and the 2 dimensions of the DMD makes it exploitable also in the spatial dimension.

In this chapter, we give an overview of some spatio-spectral acquisition strategies enabled by the system versatility. We take further advantage of our system to supplement CRT with spatial domain multiplexing, for potential speed up. We also suggest to exploit together the spatio-spectral information to offer the possibility of unsupervised fast-imaging.

## 5.1 Spatio-spectral acquisition modalities

### 5.1.1 General description of the acquisition modalities

Up to this point, in CRT, all the images were acquired with a point-focus, and all experiments made use of the $\lambda-$axis of the DMD only (Fig. 5.1 (a)). The setup was designed so that the focal spot is imaged onto the slit, which in turn is imaged onto the DMD. In this configuration, only a few pixels DMD along the x$-$axis are actually used. The rest can be binned along the x$-$axis or turned OFF to define a virtual pinhole.
Instead of point-scanning the sample, it may be interesting to line-scan it to potentially speed up the image acquisition: A line-focus is formed with a cylindrical lens and its image is formed along the DMD x$-$axis. The spatial information along this line can be probed with various strategies. One of them makes use of spatial frequency-modulated illumination imaging techniques (SPIFI) [183, 184]. It consists in modulating the illumination with chirped cosine patterns imprinted on a rotating disk. The sample 1D-spatial information is encoded into the temporal signal sent to a single pixel detector (Fig. 5.1 (b)). Alternatively, the spatial information along x can be read from the DMD itself (Fig. 5.1 (c)). Using the DMD pixels along the x$-$axis, the line can be raster-scanned or modulated with various patterns.
Then, spectral and spatial dimensions can be combined in various manners. The possibilities for the 3 presented architectures are presented in Fig. 5.1 (d). Only the configuration (c) allows to exploit all the possibilities at the same time: The configuration (a) only allows spatial raster-scanning, while (b) does not allow spatial raster-scanning along x. The last line of the table corresponds to CRT, which original configuration is shown on the extreme bottom-left DMD panel.

### 5.1.2 General system characteristics

For simplicity, we implemented the line-scanning modality on the proof-of-concept setup described in chapter 2 (2.3.1). In this section, we simply provide a quick reminder of the setup characteristics that are common to the various modalities. Simplified schematics of the three setup configurations are depicted in Fig. 5.1.
On the illumination side, a continuous wave laser operating at 532 nm is spectrally filtered, expanded, and brought to a point-focus (a) or line-focus (b-c). A piezoelectric stage scanner holding the sample is used to scan either the sample plane (a) or the y$-$axis only (b-c). On the detection side, the object is relayed onto a confocal slit to reject part of the out-of-focus light. A combination of dichroic mirror and notch filter ensures only the Raman signal is retained. Next, it is dispersed by a blazed grating placed on the conjugate plane of the confocal slit. The spatially dispersed wavelength components of the Raman signal are imaged on a DMD. The DMD $\lambda-$axis, in conjunction with the grating, acts as a programmable spectral filter. Since the object is imaged onto the DMD, its x$-$axis offer controls over the corresponding spatial dimension of the object. When the DMD pixels are in the 'ON' state, the signal impinging of

these pixels is deflected into a PMT, while the rest is sent into a beam dump.
Experimentally, the configurations (a), (b) and (c) depicted in Fig. 5.1 are implemented. The setup is designed and pre-aligned so that switching from one imaging modality to the other is simple. In all the configurations, the y− spatial dimension is scanned with the piezoelectric stage scanner.

### 5.1.3 General model

Mathematically, the acquisition of signal with the different configurations can be modelled in a similar manner. The spatial and spectral dimensions being formally equivalent, we consider the same model when the unknown of the problem is either a spectrum or an object intensity distribution of along the illumination line. We consider the following simple linear model: An 'object' $\mathbf{x}$ (spectrum or 1D object) is measured through a matrix $\mathbf{A}$, leading to an ideal noiseless measurement $\mathbf{b_0}$:

$$\mathbf{b_0} = \mathbf{A}\mathbf{x} \tag{5.1}$$

where $\mathbf{x}$ is a $N \times 1$ vector, $\mathbf{A}$ a $M$x$N$ matrix and $\mathbf{b_0}$ a $M \times 1$ vector. In the case of raster-scanning, $\mathbf{A}$ is the identity matrix $\mathbf{I}$ and each element of $\mathbf{b}$ is $b_{0i} = x_i$ $(i = 1...N)$. In the case of multiplexing, the matrix $\mathbf{A}$ is a weighting matrix that can be designed by the user (e.g. cosine-transform matrix, Hadamard matrix, Random matrix, etc).

When the unknowns of the problem are proportions $\mathbf{c}$ of chemical species with known pure Raman spectra $\mathbf{s}_q$, the CRT model applies (Eq. (2.3)). The patterns projected onto the DMD are the designed spectral filters $\mathbf{f}_m$ and the ideal noiseless measurement writes :

$$\mathbf{b_0} = \mathbf{F^T S c} \tag{5.2}$$

The unknowns can also be both spectral and spatial. In the following, we focus on CRT with a line-illumination: we want to estimate both the chemical proportions and the sample spatial profile along the illumination line.

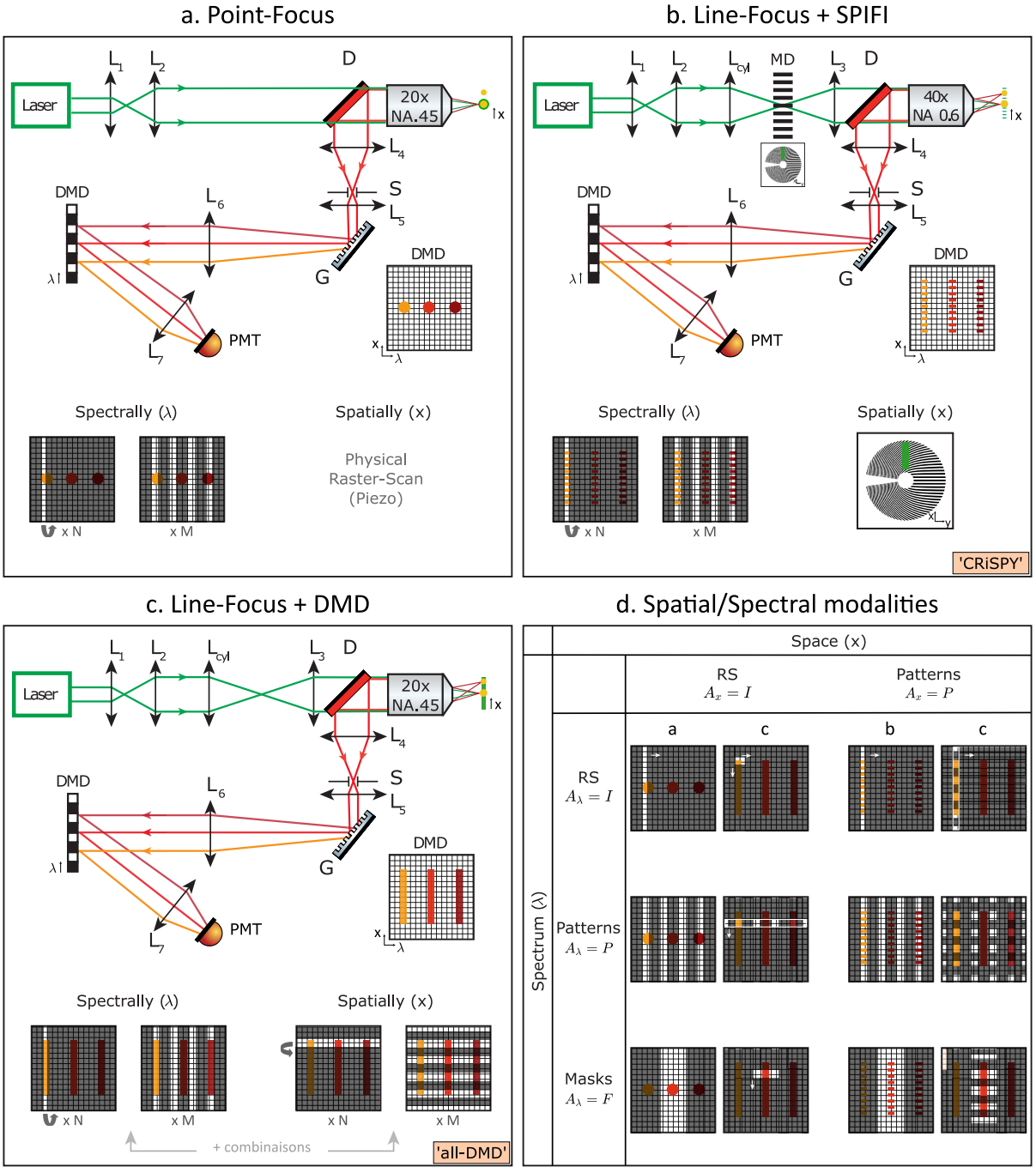


FIGURE 5.1: (a-c) Schematics of the experimental setup in its different acquisition modalities. $L_1 - L_6$ are convex lenses with focal lengths 50, 150, 150, 100 (a-b) or 150 (c), 150. $L_7$ is actually the combination of 2 lenses which image the DMD into the PMT with $\times 3$ demagnification (Not represented for clarity). $L_{cyl}$: cylindrical lens with focal length 150 mm; D: dichroic mirror; S: confocal slit; G: amplitude grating; DMD: digital micromirror device; PMT: photomultiplier tube. (d) Combinations of spatio-spectral acquisition strategies for the 3 configurations : raster-scanning and multiplexing. Line-scan CRT corresponds to the last row of the table.

## 5.2 Line-Scan Compressive Raman : two implementations

In this thesis, we demonstrate two experimental implementations of line-scan CRT: first with spatial modulation of the illumination beam (Fig. 5.1 (b)) and second with spatial modulation of the Raman signal (Fig. 5.1 (c)). The model for line-scanning CRT combines Eq. (5.1) and (5.2). We denote :

- $P$ : number of spatially varying patterns: illumination patterns or DMD x− patterns. ($p = 1...P$)
- $Q$ : number of pure chemical species present in the sample ($q = 1...Q$)
- $M$ : number of spectral filters $\mathbf{f}_m$ ($m = 1...M$)
- $L$ : number of energy bins along a Raman spectrum ($l = 1...L$)
- $\mathbf{A}$ : $P \times N$ matrix of the $P$ spatially varying patterns along the line of $N$ resolved points.
- $\mathbf{C}$ : $N \times Q$ matrix of unknown chemicals proportions to estimate along the line
- $\mathbf{S}$ : $Q \times L$ matrix of known Raman spectra of pure chemical species (each of its row contains the known Raman spectrum of the pure $q^{th}$ chemical species).
- $\mathbf{F}$ : $L \times M$ matrix containing the $M$ spectral filters $\mathbf{f_m}$
- $\mathbf{H}$ : $P \times M$ matrix containing the noiseless measurements of the spatio-spectral projections.

We seek to generate a spatial map of the distribution of $Q$ molecular species with known Raman spectra and estimate their proportions in each of the $N$ resolved points of the illumination line. The unknown proportions to estimate are gathered in the matrix $\mathbf{C}$. Each of its rows specifies the proportions of pure chemical species contained in the resolved point $x_n$ of the illumination line. The modulation is done spatially along the x−axis and spectrally along the $\lambda$−axis. The spatial modulation (through $\mathbf{A}$) and spectral modulation (through $\mathbf{F}$) lead to the detection of photons on the single pixel detector. The mean [1] of these measurements are gathered in a matrix $\mathbf{H}$. Each of its element $h_{pm}$ contains the mean number of counts obtained for one given spatio-spectral projection (one spatial pattern with one spectral filter). Assuming the generated signal is linear to the excitation intensity and ignoring constant terms and exposure times, this translates to:

$$\mathbf{H} = \mathbf{ACSF} \tag{5.3}$$

Then, with $\mathbf{G^T} = \mathbf{SF}$, Eq. (5.3) reads:

$$\mathbf{H} = \mathbf{ACG}^T \tag{5.4}$$

[1] Each measurement is polluted by photon-noise. $\langle h_{pm}^{noisy} \rangle = h_{pm}$

or, as : $\mathbf{H} = (\mathbf{A} \otimes \mathbf{G})\mathbf{C}$ ($\otimes$ denotes the Kronecker product).

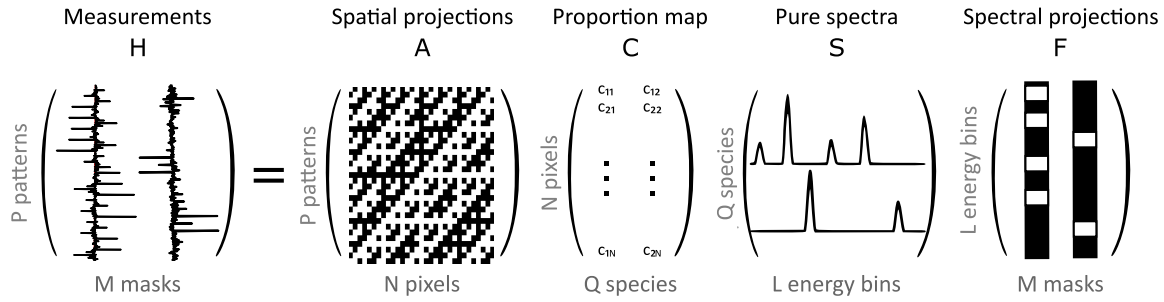


FIGURE 5.2: Visual representation of Eq. (5.3), with two pure chemical species and two spectral masks.

The spatio-spectral filters could be conjointly optimised and $\mathbf{C}$ estimated with various strategies, but for now we handle the spatial and spectral dimensions distinctly. The estimation is performed in two steps. First, we estimate a spatial line image of Raman intensities, for each spectral filter $\mathbf{f_m}$. In a second step, we estimate the relative proportions of the $Q$ species. The Raman intensity in each pixel $x_n$, for the spectral filter $\mathbf{f_m}$, is estimated through least square estimation [2] and denoted as $\hat{\eta}_m(x_n)$. Then, the estimation of the species proportions reduces to a 1D CRT problem :

$$\hat{\boldsymbol{\eta}}(x_n) = \mathbf{G}\mathbf{c}(x_n) \tag{5.5}$$

With $\hat{\boldsymbol{\eta}}(x_n) = (\hat{\eta}_1(x_n), ..., \hat{\eta}_M(x_n))^T$ and $\mathbf{c}(x_n) = (c_1(x_n), ..., c_Q(x_n))^T$. If $\mathbf{G}^T\mathbf{G}$ is not singular, the proportions $c_q(x_n)$ can be estimated with a simple least square estimation 2.11:

$$\hat{\mathbf{c}}(x_n) = \left[\mathbf{G}^\intercal\mathbf{G}\right]^{-1}\mathbf{G}^\intercal\hat{\boldsymbol{\eta}}(x_n) \tag{5.6}$$

### 5.2.1 Line modulation of the illumination beam

*The work of this section led to the publication of the paper 'Compressive Raman imaging with spatial frequency modulated illumination' [185]. It was carried together with S. Sivankutty (Institut Fresnel) and with P. Stockton and R.Bartels (Colorado State University).*

In this section we demonstrate an experimental implementation of line-scan CRT using spatial modulation of the illumination beam (Fig. 5.1 (b)). It makes use of spatial frequency-modulated illumination imaging techniques (SPIFI) [183, 184]. While similar encoding schemes were developed in spectrometry in the 1960's [186–188], the method was demonstrated in imaging by [183], and then developed and theorised by [184]. SPIFI imaging was demonstrated on absorptive and fluorescent objects [184, 189–192], but had never been used for Raman imaging. Here,

[2] We elaborate on other estimation strategies in chapter 6

we combine SPIFI and CRT to perform compressive Raman imaging with spatial frequency modulated illumination (CRiSPY). It corresponds to the configuration depicted in Fig. 5.1 (b).

### Principle

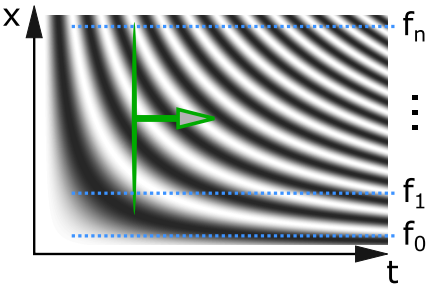


FIGURE 5.3: Modulation pattern printed on a rotating disc (Fig. 5.1 (b)). The linear modulation chirp leads to different modulation frequencies $f_i$ along the x position of the sample.

In SPIFI, the illumination beam is modulated by a time-varying illumination pattern. The beam is modulated with a circular modulator on which an amplitude grating is imprinted (Eq. (5.7))[Disc of Fig. 5.1 (b)].The modulator is swept with a constant rotation speed, and the illumination beam is continuously modulated with a chirp cosine. The modulated line illumination is imaged onto the object and produces a temporal modulation of the signal, $\eta_m(t_p)$, that encodes the representation of the object in the spatial frequency domain. Each object spatial point experiences a unique temporal modulation pattern and frequency. Hence, a line image can be obtained with a cosine transform or Fourier transform of the temporal signal [184]. Those measurements are gathered in matrix H, in which each column contains the time trace (sampled every $t_p$), recorded when applying one spectral filter $\mathbf{f_m}$ onto the DMD. The matrix $\mathbf{A}$ can be seen as the discrete version of the cosine transform.

### Experimental implementation

Experimentally, the laser beam is brought to a line focus on the amplitude modulator with a cylindrical lens. This modulator is a glass disk on which an aluminium modulation pattern is imprinted (Inlight Gobos) [Inset Fig. 5.1 (b)]. This pattern takes the form (in polar coordinates)

$$w(R,\phi) = \frac{1}{2} + \frac{1}{2}\mathrm{sgn}\big[\cos(\Delta k R\phi)\big] \tag{5.7}$$

where the sign function, $sgn$, accounts for the binary nature of the grating and $\Delta k = 10\ mm^{-1}$ is the finest spatial frequency on the disc. The pattern of the disc is re-imaged on to the object with $\approx 33$ de-magnification, in a $4f-$ configuration (combination of lenses and a microscope objective (40x, 0.6 NA)). The disc finest spatial frequency, $\Delta k$, and the $4f-$ imaging system limit the lateral resolution of the system to about 3 $\mu$m. The resolution can be improved by either increasing $\Delta k$ of the modulator disc and/or increasing the NA of the imaging system. Likewise, the line length limits the field of view along x to 120 $\mu$m. The disk is mounted on a

stepper motor (MCL-3006, Faulhaber) and is rotated at a constant velocity, $v_r$. The resulting sweep, in local spatial frequency of the modulated beam, is given by:

$$k(x,t) = 2\pi\Delta k v_r t = 2\pi\kappa t \tag{5.8}$$

where $\kappa$ is the chirp parameter that relates the temporal modulation frequency to the lateral position in the object space. In all our experiments, $v_r = 2400$ rpm, thereby achieving line scans at a rate of 40 Hz. The resulting time trace is sampled every 16 $\mu$s.
In the detection path, the slit is 100$\mu$m wide and the effective pixel of the DMD is obtained by binning 8 mirrors along the $\lambda-$axis. All mirrors along the spatial axis x to mitigate spurious diffraction effects.

### Method and Results

#### Intensity-only Raman imaging

The first step in CRiSPY is to calibrate the imaging system, i.e. measure the mapping between temporal modulation frequency and space - given by the scaling factor $\kappa$. This parameter is obtained by recording a time trace while translating an isolated 12 $\mu$m melamine resin (MR) bead through the line focus and tracking the centroid of the positive sideband of the Raman signal Fourier transform as in [191]. The resulting gradient of the modulation frequency with respect to the spatial position leads to $\kappa = 12.8$ Hz $\mu$m$^{-1}$ [Fig. 5.4(c)]. Additionally, the signal intensity from the same bead plotted versus the relative $x-$ position confirms the 120 $\mu$m FOV estimate. Line images, along the x$-$ dimension, are obtained with a Fourier transform of the temporal signal $h_m(t_p)$ recorded by the PMT and isolating its positive sidebands. Fig. 5.4(a) is a representative time trace of a Raman signal of a 30 $\mu$m polystyrene bead (red) and the background from the $CaF_2$ slide (black). Fig. 5.4(b) shows one isolated sideband of the Fourier transformed time trace from panel (a).
A spontaneous Raman image (with no spectral selectivity) of a mixture of beads (Sigma Aldrich) - 30 $\mu$m polystyrene beads (PS), 20 $\mu$m polymethylmethacrylate (PMMA) and 12 $\mu$m melamin resin (MR) on a $CaF_2$ coverslip (Crystran) - was obtained with spatial frequency projections [Fig. 5.4(d)]. Each time trace was Fourier transformed, and then the sideband corresponding to the field of view was isolated and scaled by the $\kappa$ parameter to generate a line image. In this way, the 2D Raman image was reconstructed line-by-line.

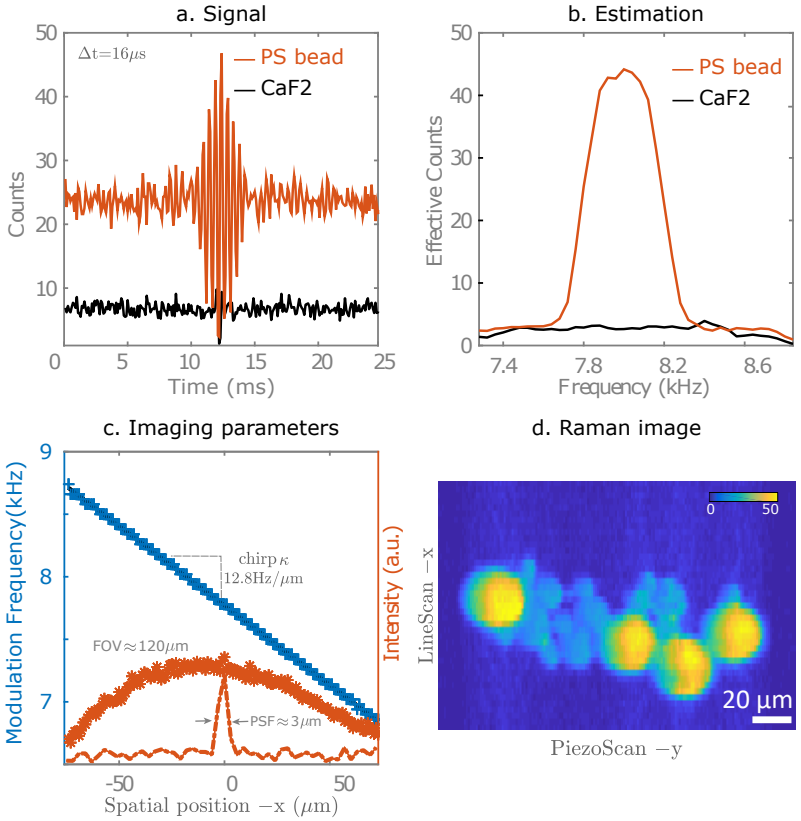


FIGURE 5.4: (a) Time trace of Raman signal of a 30 $\mu$m PS bead (red) and of the $CaF_2$ slide background (black) (16 $\mu$s sampling time). (b) Corresponding isolated sidebands of the Fourier transformed time traces (10x averaged). (c) In blue, the calibration between temporal modulation frequency and space - measured by translating an isolated 12 $\mu$m MR bead. In red, imaging system parameters - PSF and field of view (sample - MR beads). (d) Line scanned Raman image of a beads mixture (PS, PMMA, MR) on a $CaF_2$ slide with no spectral filtering.

### CRT imaging

CRT assumes the Raman spectra of the pure chemical species present in the sample are known. We thus measure the reference spectra $\mathbf{s_q}$ of the species present in the sample. The calibration spectra are acquired by using the DMD as a virtual pinhole along the spatial dimension. This is a crucial step, since the line focus of the illumination patterns might also include signal emanating from the substrate or other chemicals present along this line. Fig. 5.5(a) shows the reference spectra $\mathbf{s_q}$ (averaged on 10 spatial positions) and the associated computed filters $\mathbf{f_m}$. The line images for filters $\mathbf{f_1}$, $\mathbf{f_2}$ and $\mathbf{f_3}$ obtained via spatial frequency projections are shown in Fig. 5.5(b).

First, we imaged a sample composed of beads with distinct chemical compositions and distinct sizes. The proportion maps estimated via Eq. (5.6) are shown in Fig. 5.5(a). The proportions were normalized and thresholded to [0 1]. The classification of the beads is clearly verified in the images depicted in Fig. 5.5(b-c). The total laser power along the line in this experiment was about 65 mW (irradiation $= 0.24 \times 10^{-3}$ W/$\mu m^2$ ). Images (b) were obtained by averaging 10

recorded time traces (corresponding to 10 sweeps of all the spatial frequencies from the SPIFI modulator), resulting in an effective dwell time 6.6 ms per pixel. Image (c) was obtained without averaging (one single sweep) corresponding to a dwell time of 0.66 ms. We note the high fidelity classification of the four different chemical species in the case of spatially indistinguishable beads (having the same size) in Fig. 5.5(d), with no further calibration (i.e. using the same spectral filters as in (b-c)). We also demonstrate the application of CRiSPY by imaging two powders mimicking microcalcifications (e) : hydroxyapatite (HAP - green) and monohydrate calcium oxalate (COM - red), as in (4.2.1). The laser irradiation for the experiments in (d,e) is $0.48 \times 10^{-3}$ W/$\mu m^2$.

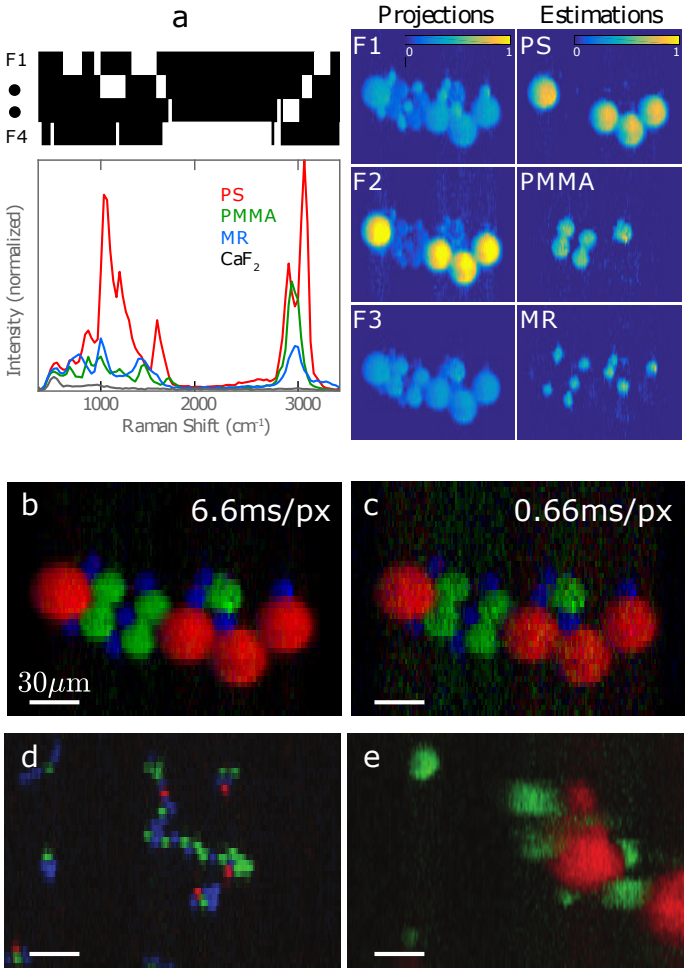


FIGURE 5.5: (a) Reference Raman spectra of the three beads and background (10 averages - 100 ms integration time per spectral bin) and representative spectral filters. Images for filters $F_1$, $F_2$ and $F_3$ are obtained via spatial frequency projections (normalized to the maximum intensity of the 3 images) and their proportions are estimated. (c-d) Composite estimated proportion maps RGB for pixel dwell time of 6.6 ms and 0.66 ms. (d) Visualization of proportion maps of PS (red), PMMA (green) and MR (blue) beads of identifical sizes (5 $\mu$m) (e) Same for microcalcifications synthetic powders of HAP (green) and COM (red).

### 5.2.2 Line modulation of the collected signal

In this section, we do not modulate the illumination. Rather, we modulate the the collected signal on the spatial dimension of the DMD. We refer to this method as the 'all-DMD' line-scan CRT (Fig. 5.1(c)).

#### Principle

As explained previously, the DMD holds spatial information about the sample, since the line-focus is imaged onto the DMD x−axis. Here, the line illumination is not modulated by an external disc, but the signal is modulated by patterns projected onto the DMD itself. To access the spatial information along the line, we implement two methods (Fig. 5.1(c)):

- Raster-scan the DMD along its x−axis, by turning each mirror 'ON' one-by-one. This directly builds the sample spatial distribution along the line. In Eq. (5.1), $\mathbf{A} = \mathbf{I}$.
- Multiplex the acquisition along x. We choose to use positive Hadamard patterns ('S-patterns', see chapter 6 and Fig. 6.2). In this case, half of the x DMD pixels are 'ON' in each measurement, thus the total measured number of photons is much higher than with raster-scanning. The sample spatial distribution is then estimated with a least square estimation. In Eq. (5.1), $\mathbf{A} = \mathbf{S}$.

#### Experimental implementation

The laser beam is brought to a line focus onto the sample plane with a combination of cylindrical lens, plano-convex lens and microscope objective (Nikon 20x, 0.5 NA). This line focus is imaged onto the DMD in a $4f-$ configuration with a de-magnification of $\approx 22.5$. The DMD physical pixel size and the imaging system limit the spatial resolution along the x−axis to $\approx 0.6$ $\mu$m. The line length, together with cropping from diverse optical elements in the spectrometer, limit the field of view along x−axis to about 220 $\mu$m. The spatial resolution along the y−axis is about 1.5$\mu$m. The pixel dwell time along x is in theory limited by the DMD frame rate (22 kHz) but in practise can be limited by the SNR. The line-scan rate then depends on the number of effective DMD pixels along x within the FOV (thus on the pixel binning / desired spatial resolution).
In the detection path, the slit is 50$\mu$m wide, and the effective pixel of the DMD is obtained by binning 8 mirrors along the spectral axis $\lambda-$. In the following we consider two samples that consist of three types polymer beads (30 $\mu$m polystyrene (PS), 20 $\mu$m polymethylmethacrylate (PMMA), and 12 $\mu$m melamine resin (MR)), displayed in two different manners :

- A: a sparse sample (Fig. 5.6 (A)) that consists of a few beads of each type displayed onto a CaF2 coverslip (Crystran). The coverslip hardly gives any Raman signal and only a few beads are present along the x−axis.

- B: a denser sample (Fig. 5.6 (B)) that consists of more beads displayed onto a glass coverslip. The glass exhibits little Raman signal and more beads are present along a multiplexed line.

### Method and Results

#### Intensity-only Raman imaging

The spatial calibration is performed by scanning a bead of known size and matching it to its profile onto the DMD. The effective FOV along x is estimated by scanning with the DMD a spatially homogeneous Raman sample (a microscope glass slide), and found to be $\approx 220$ $\mu$m. On the DMD plane, it only represents 1/3 of the entire DMD size. We however multiplex or raster-scan over the whole DMD x−axis (6.5.3). The DMD pixels are binned 2-by-2 along x−axis: this results in an equivalent spatial resolution along x of $\approx 1.2$ $\mu$m and in $P = 511$ measurements. The laser power 3.6 mW ($1.1 \times 10^{-5}$ W/$\mu m^2$) is chosen so that, when projecting S-patterns, the total count rate lies in the linearity regime of the detector ($1.5 \times 10^6$ Hz). Then, the integration time (10 ms per measurement) is chosen to achieve sufficient SNR with raster-scanning measurements. The line rate is thus long (0.2 Hz) but is purely limited by the dynamic range of the detector, and to preserve the same power irradiance for both S-patterns and raster-scanning measurements.

Fig. 5.6 represents raw measurements and estimation when performing measurements with S-patterns. The results are averaged over 50 realisations. We see that the signal from sample B is higher due to the higher density of beads. We note that raster-scanning the same sample would give a maximum number of counts of about 50 (on the brightest image pixels), while it reaches more than 1000 counts for S-patterns.

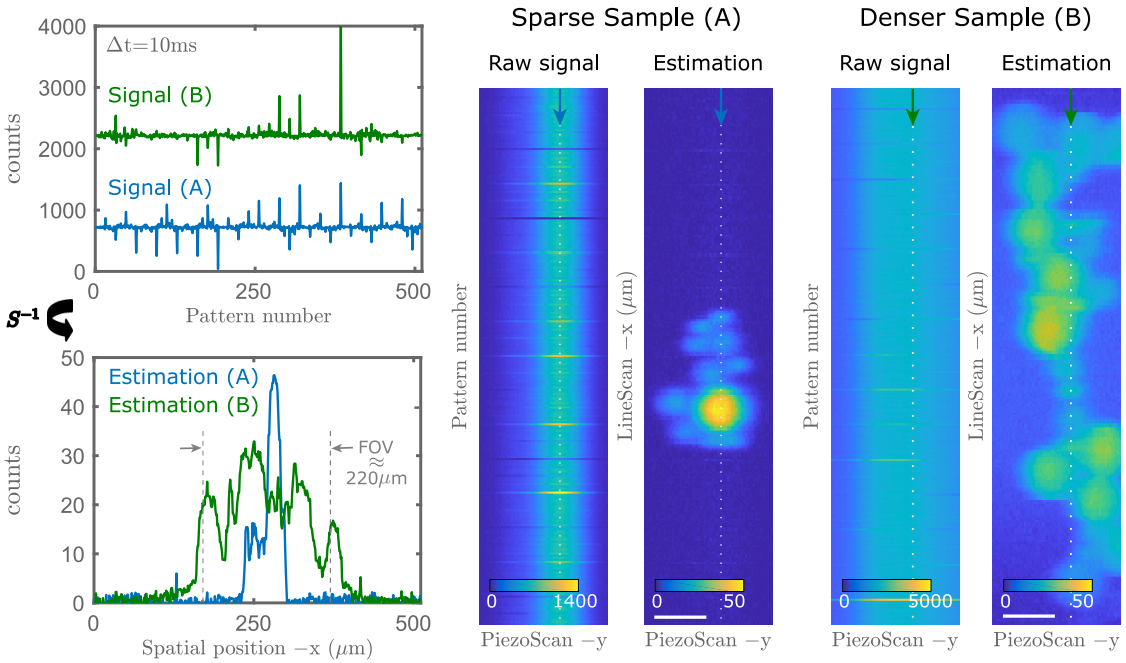


FIGURE 5.6: (Top-Left) Raw Raman signal acquired with S-patterns, along a given line for samples A and B. The integration time per pattern is 10 ms and the signal is averaged over 50 measurements. (Bottom-Left) Corresponding Raman intensities. The effective FOV represents less than half of the probed space. (Left) Raw Raman signal acquired with S-patterns and the corresponding estimations, over 65 $\mu$m along the y−axis, and cropped on 250 $\mu$m on the x−axis, for samples A and B. The dotted lines reference to the cross-sections represented on the left. Scale bars: 30$\mu$m.

### CRT imaging

For CRT, the calibration spectra are acquired by using the DMD as a virtual pinhole along the spatial dimension. Fig. 5.7(a) shows the reference spectra $\mathbf{s_q}$ of the 2 samples (averaged on 10 spatial positions) and the associated computed filters $\mathbf{f_m}$.

We image each sample with S-patterns projections and with raster-scanning. The total laser power along the line in this experiment was about 10.6 mW (irradiance $3.34 \times 10^{-5}$ W/$\mu m^2$ ) and effective dwell time 10ms per pixel. No averaging was performed. The proportion maps estimated via Eq. (5.6) are shown in Fig. 5.7. The classification of the beads is clearly verified. For sample A, the proportion map obtained with S-patterns has clearly a better SNR that the one acquired with raster-scanning. For sample B, the difference in SNR is more subtle. We will extensively discuss this point in the next chapter. We note that the long integration time here is due to the limited linearity range of the detector for S-patterns projection. With S-patterns and same power-density, images with sufficient SNR could be obtained down to 1 ms pixel dwell time. When raster-scanning, at least 20 times more laser power can be used without saturating the detector, lowering by the same amount the integration time necessary to obtain a comparable SNR (thereby easily reaching pixel dwell times of 500 $\mu$s).

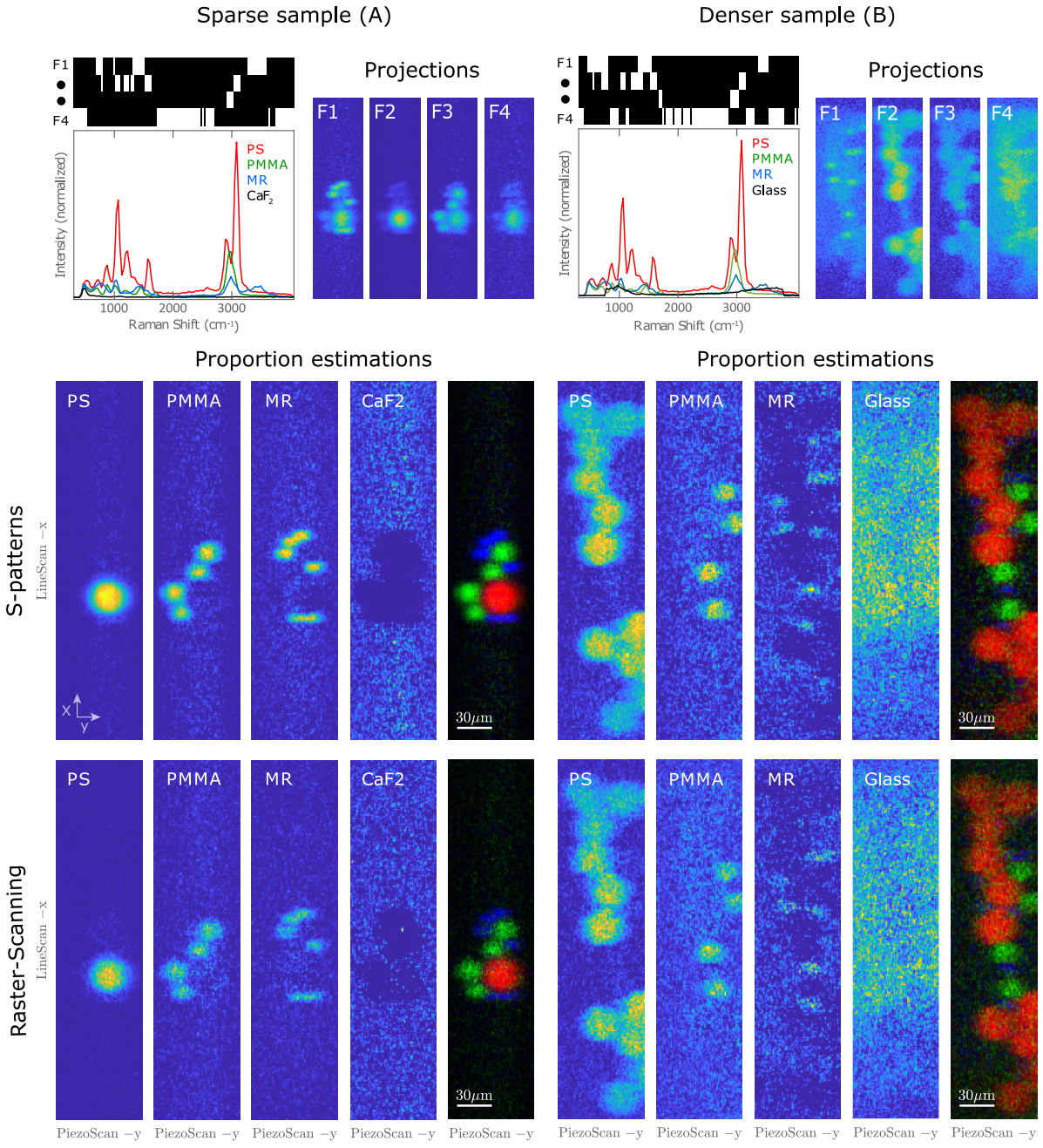


FIGURE 5.7: (Top) Reference Raman spectra of the four species (10 averages) and representative spectral filters. Estimated line images after one set of S-patterns projections, for the 4 spectral masks. Colorbars in counts. (Middle-Bottom) Estimated proportions thresholded to [0 1] and composite RGB map, for integration time of 10 ms and for S-patterns projections and raster-scanning. Images are cropped on 250 $\mu$m on the x−axis.

### 5.2.3 Conclusion and Discussion

We demonstrated two experimental implementations of line-scan CRT and showed proof-of-concept results demonstrating the capability of the setup for line-scan imaging. The first strategy (CRiSPY) exploits spatial-frequency modulated illumination and uses an external modulator.

The second strategy ('all-DMD') makes use of the spatial dimension of the DMD and does not required an additional modulator. It is based on the projection of discrete patterns onto the DMD spatial axis, which can result in raster-scanned or multiplexed measurements.

Each strategy presents advantages and drawbacks. In CRiSPY, the modulation is performed in the illumination path. The detection is thus less at risk of being affected by undesired effects such as diffraction from the DMD (4.1.2). However, it requires an external modulator. A major advantage of the 'all-DMD' method is its versatility. User defined projection patterns can be displayed and might even be optimised for specific applications (as CRT does in the spectral domain). For a given imaging configuration, the spatial resolution is more easily adaptable (within a defined range): it indeed simply requires a different DMD pixels binning, while in CRiSPY it requires to change the modulator disk or associated optics. The techniques could be compared on the same samples, and SPIFI-like modulation implemented on the DMD.

The results in this chapter show the capability of line-scan CRT. However, they would only be of interest for further implementation if line-scan CRT actually leads to faster acquisition speeds or to better SNR than a conventional point-scanning CRT.

**Speed**

In terms of speed, CRiSPY results in images acquired at best with a line rate of 40 Hz, which is equivalent to a pixel dwell-time of about 660 $\mu$s. This speed is intrinsically limited by the motor-disc technology. Line rates of 100 Hz (250 $\mu$s equivalent pixel dwell time) have been reported in SPIFI. We note that in the performed experiments, the count rate was actually slightly outside the linearity range of the detector: Fig. 5.4 (a) shows a max count rate of about 2.5 $\times$ $10^6$ counts/s while the PMT is linear until 1.5 $10^6$ counts/s. In the 'all-DMD' experiments, the chosen illumination power was much lower than for CRiSPY, in order to comply with this linearity range (5 $\times$ $10^5$ counts/s maximum count rate). The displayed results were obtained with pixel dwell times of 10 ms. With the same power density, S-patterns display could lead to good SNR images down to about 1 ms integration time. For raster-scanning, much fewer photons are detected, but pixel dwell times of 500 $\mu$s could be obtained with an increased laser power. For an infinite SNR, the speed of the 'all-DMD' stategy is intrinsically limited by the DMD frame rate, i.e. about 50 $\mu$s pixel dwell time (for binary patterns).

Nevertheless, the intrinsic speed limits of the two above systems do not compete with the speeds attained in conventional raster-scanned CRT on the same samples (a few 10 $\mu$s, Fig. 4.6). Thus, in terms of pure speed and technology, the currently implemented line-scan CRT technology does not outperform point-scanned CRT. Yet, faster line-rates could be obtained with faster modulators or with compressive-sensing strategies (5.3.2).

**SNR**

Although it is a crucial point, in this chapter we did not discuss SNR advantages of the techniques. Instead, we choose to only elaborate in depth on this point in a more general context in chapter 6. Still, we provide here some remarks and anticipated conclusions.

Since in practise, the acquisition speed is often limited by the SNR, one would think that the higher photons flux brought by multiplexing (through SPIFI or S-patterns) would result in higher SNR and thus faster speeds than raster-scanning. Nevertheless, this intuition is not always true when the measurements are limited by the photon-noise. In chapter 6 we will see that, under these noise conditions, some types of multiplexing can bring substantial SNR improvement for sparse samples and in regions of high signal, as compared to raster-scanning. This can already be seen in Fig. 5.7(A). However, it has some limitations. For instance, if two species of different brightness lie in the same line-focus, the signal of the dim species may be buried into the shot-noise of the bright one: In the estimation, noise spreads along the line, and thus more noise is present on the lines containing bright beads [Fig. 5.4 (d) , Fig. 5.5 (a-F2 Projection)]. However, the masks spectral selectivity plays in favour of multiplexing since they render the sample more sparse, in the sense that the potential noise from beads of different species along the line is not very likely to pollute the others if the masks do not probe the same spectral signature.

In all, the results of Chap.6, strengthened by the above line-scan CRT data, lead us to surmise line-scan CRT with S-patterns to bring a SNR improvement over raster-scan CRT, when the sample is sufficiently sparse along the line focus. It may bring drastic improvement on bright regions when the sample is sparse (sample A), although the proportion estimation of the background would be worsen. As compared to images with no spectral selectivity ('spatial only multiplexing'), the fact that CRT adds spectral filtering can mitigate potential noise spreading due to multiplexing, at least to some extent. Furthermore, the spectral selectivity makes it harder to bury dim species into the shot-noise of bright ones as long as their spectral signatures are different.

Overall, the conclusions of when line-scan multiplexing CRT is advantageous over point-scanning CRT are the same than the conclusions of chapter 6, with an additional spectral selectivity. Therefore, when (i) the species spectral overlap is relatively small (ii) no extremely dim species with spectral overlap with others is present, (iii) no significant background or fluorescent signal are present, (iv) if the background estimation precision is not of interest, we surmise line-scan multiplexing CRT to bring, in general, a SNR advantage over raster-scanning, and thus be faster. The SNR and speed gain will depend on the spatial and spectral structure of the sample. We refer the reader to (6.6) for more details.

## 5.3 Perspectives

The results in this chapter show the capability of line-scan CRT. Together with the results of chapter 6, they inform on its potential advantages over point-scanning CRT. However, the results are preliminary: the conclusions on the usefulness of line-scan CRT are not definitive because there are still many improvements to be brought to this technology. In this section we describe some improvements that are postponed to future work.

### 5.3.1 Perspectives for high-speed line-scan CRT

Until now, line-scan CRT makes use of *a priori* knowledge in the spectral dimension only. If some *a priori* knowledge is also held in the spatial dimension, line-scan CRT could be improved in different ways.
Firstly, positivity or sparsity constraints could be implemented to improve the estimations, instead of only using least square estimation. They were not implemented in this chapter to keep the main message clear. We refer the reader to chapter 6 for a further description (6.2.5) and effect of some of these estimators.
Secondly, if the sample is known to be spatially sparse in some basis, this sparsity *a priori* knowledge should be exploited by using compressive-sensing [25, 85–88]. Indeed, if the sample is sufficiently sparse in some basis, one could design a projection matrix that would enable to acquire data with sub-Nyquist sampling; thereby speeding up the acquisition. In CRiSPY, this is not easily implementable because the modulator disc patterns are not programmable, but it could be implemented on the fully-sampled data for proof-of-concept [193]. The acquisition could actually already be twice faster since the disc architecture leads to twice the same information. In the 'all-DMD' modulation, compressive sensing could be implemented. Reconstructing the object spatial profile with $M = 0.01N$, as commonly reported in the literature (e.g.[92, 93]) would improve the acquisition speed by the same amount. Nevertheless, the shot-noise model of our system should be considered to apply compressive sensing [194]. Overall, for sparse objects, multiplexed line-scan CRT could bring a speed improvement over raster-scanning CRT.
Last, *a priori* knowledge in the spatial dimension could be used for spatio-spectral masks co-optimisation: one could optimise spatio-spectral masks to directly probe the necessary information in both the spatial and spectral dimension, thereby fastening the acquisition.

### 5.3.2 Perspectives for high-speed hyperspectral-imaging

So far in this thesis we have assumed that the Raman spectra of the pure chemical species contained the sample are known. This assumption has led to interesting results for a number of applications. However, the spatio-spectral encoding modalities offered by the setup in the line-scan configuration [Fig. 5.1 (c-d)] now open interesting perspectives for unsupervised problems (i.e. with no *a priori* knowledge about the sample). When the spectra are not *a*

*priori* known, the problem falls in the class of hyperspectral imaging: both spatial distribution and species spectra are unknown and are to be estimated. As described in chapter 1 (1.2.3), some recent techniques use the compressibility of the hyperspectral datacube. Often, they are based on a camera and use compressive strategies by multiplexing one of the dimensions (space - via encoded apertures, or spectra - via FT spectroscopy for instance). Studies include [68, 70, 78, 79, 81, 82, 92, 96, 195, 196].

Our line-scan system architecture enables to probe together spatial and spectral information. It can be considered as similar to the above strategies. Instead, the camera is replaced by a single-pixel detector, and instead of multiplexing the whole 2D space, we multiplex only one of the two spatial dimensions (x−axis) and the spectral dimension ($\lambda$-axis). The other spatial dimension (y−axis) is raster-scanned with the piezo-scanner. One perspective would be to mix the complete 2D spatial information (with a diffuser for instance) and send the complete spatio-spectral information to the detector [100]. The resulting problem is then of higher dimension than when using CRT: we now wish to retrieve the hyperspectral matrix (along each line) $\mathbf{U}$ of size $N \times L$. Each row of this matrix represents the Raman spectrum of the species in pixel n. Then, Eq. (5.3) becomes :

$$\mathbf{H} = \mathbf{A_x} \mathbf{U} \mathbf{A}_\lambda \tag{5.9}$$

Where $\mathbf{A_x}$ is the $P \times N$ matrix of the $P$ spatial patterns and $\mathbf{A}_\lambda$ the $L \times P'$ matrix of the $P'$ spectral patterns. $\mathbf{A_x}$ and $\mathbf{A}_\lambda$ can be programmed at will with the DMD. The projected patterns could for instance be random patterns in both dimensions, or could be designed to raster-scan both dimensions in a random way, etc. Any combination can be designed.

Implementing compressive strategies can be done in different ways. One of them is to use compressive sensing in both the spatial and spectral domain. This is refer to as Kronecker compressive sensing [197]. Other strategies based on non-negative matrix factorisation (NMF) could also be implemented [23, 198].
Other strategies are based on matrix completion, with which it is possible to perfectly recover most low-rank matrices from an incomplete set of entries [22, 90, 199]. This theory is perfectly fitted to hyperspectral imaging where the data is highly redundant and therefore low-rank. If the number of measurements is sufficiently large and the matrix entries sufficiently uniformly distributed, one can in practice find the matrix with minimal rank with these entries. The rank minimization problem being NP-hard, the problem can be relaxed into the form of a convex-optimisation problem [200], which minimizes the nuclear norm i.e. the sum of the matrix singular values (rank = number of non-zero singular values). The problem aims to find, among all matrices consistent with the observed entries, that with minimum nuclear norm. It was shown that the number of samples needed to recover most $N$-by-$N$ matrices of rank $r$ was on the order of $Nrlog(N)$ [22, 90].

These potential strategies are reported to future work. In the past year, two papers have reported the use of matrix completion for Raman hyperspectral imaging, one in SRS [99] and one in spontaneous Raman [101]. Both are based on spatial point-scanning. The same approach with our setup would bring a complementary approach by exploring more sampling modalities.

## 5.4 Conclusion

To conclude, in this chapter we demonstrated proof-of-concept results of line-scan CRT. The first strategy (CRiSPY) exploits spatial-frequency modulated illumination and modulates the illumination beam with a chirp cosine. The second strategy ('all-DMD') makes use of the spatial dimension of the DMD and modulates the Raman signal with discrete patterns projection onto the DMD spatial axis.
The presented preliminary results do not show speed improvement as compared to point-scanning CRT - which was shown in the preceding chapters to attain minimal speeds of few tens of $\mu$s. Yet, the presented line-scan CRT is a versatile technology that is now ready to use of compressive sensing strategies: the latter are likely to fasten the acquisition and make line-scan CRT compete or surpass point-scanning CRT speeds. It also offers the possibility to easily implement compressive hyperspectral imaging, thereby opening doors to unsupervised approaches.
The potential usefulness of line-scan CRT also - and importantly - resides in the potential SNR improvement over point-scanning CRT. Since line-scan CRT uses spatial multiplexing and leads to the detection of more photons, the common sense expects the estimation precision to improve over point-scanning CRT. However, the shot-noise limited regime in which this whole thesis operates renders the SNR study less trivial than it may seem. I elaborate on this point, in a more general framework, in the forthcoming chapter.

# Chapter 6

# Multiplexing in the shot-noise limited regime: a SNR study

## Contents

Throughout this thesis, we have studied several ways of combining spectral and/or spatial information into a single-channel detector. In the spectral domain, CRT uses *a priori* knowledge to multiplex the spectral information with optimized filters. In the spatial domain, generic patterns were used to combine the information. The use of multiplexing was clearly motivated: instead of collecting the information from different points separately, combining it permits to bypass some noise and speed limits of array detectors. Multiplexing allowed us to collect more signal on high-speed and low-noise single-pixel-detectors. One consequence of detecting signals with these high performances detectors is that the measurements are often shot-noise limited: the physical measure is only perturbed by the photon noise itself. Nevertheless, in this noise regime, higher flux also means higher noise, and the question of the impact of multiplexing on signal-to-noise ratio arises.
In the case of CRT, we have examined this question in details in Chapter 2 and 3. In the present chapter, we now study a more general type of multiplexing based on binary Hadamard matrices. We investigate its implications on SNR when the measurements are shot-noise limited. In this chapter, we propose some new insights on this vast subject and try to provide a clearer view on which practical situations could multiplexing provide advantages. Within a given framework, we examine both with simulations and experiments how multiple factors, such as object sparsity or brightness, play a role in determining if multiplexing is advantageous or not.

## 6.1 Context and motivation

Multiplexing is used in numerous fields, such as in telecommunications or computer networks. It relies on *information mixing*. Many times, it consists in combining multiple signals from different channels into a single one (Fig. 1.11). Thus, instead of collecting information from each channel separately or sequentially, the information from many different channels is combined into one receiver. As a result, each measurement contains partial information from several channels. The full detected signal then has to be demultiplexed to retrieve the original signal information. The error in the retrieved signal information, as compared to the ground-truth, can then be quantified with quantities such as SNR (Eq. (6.4)), to estimate how 'well' the object is estimated after demultiplexing the raw measurements. A high SNR means small error and thus good reconstruction 'quality'.

### 6.1.1 The Multiplexing advantage

Historically, some major work on the multiplexing impact on SNR was performed in the early days of fourier-transform infrared spectroscopy (FTIR). In infrared spectroscopy, the measurements are often overwhelmed by considerable detector noise. In the 1960s, it was realised that, instead of dispersing the signal, multiplexing the signal through interferometric measurements could bring substantial SNR advantage. The theoretical advantages of FT spectroscopy were studied in details by Jacquinot [201], Roland [202], P. Connes [203] and Fellgett [204], among others. It is the later who really brought to light this multiplexing advantage, also called Fellgett's advantage, defined as an improvement in SNR when taking multiplexed measurements rather than raster scanned measurements. In this scenario where the limiting noise comes from the detector (additive signal-independent noise), multiplexing $N$ channels with Fourier or Hadamard bases was demonstrated to bring a considerable SNR advantage of the order of $\sqrt{N}$. This was confirmed experimentally both in spectroscopy [52, 205–209] and imaging [210, 211]. Latter, with the advent of spatial light modulators, multiplexing has become extremely popular in numerous fields. Countless work have been reported in microscopy and in the framework of single-pixel cameras (e.g. [100, 212–223]).

Intuitively, the origin of the multiplexing advantage can be easily understood: When the detector noise is high, the signal may easily be buried into it: therefore, it is better to multiplex the signal in order to detect large intensities that are well above the detector noise. Fig. 6.1 illustrates the signal measured from an object when raster-scanning its pixels one-by-one (a), or when multiplexing with a binary matrix - called 'S-matrix' (Fig. 6.2) - containing 50% of 1s and 50% of 0s (b). Since about half the whole object is integrated onto the detector each time, it is clear that multiplexing leads to overwhelmingly larger signal level. Since in the considered scenario the noise is additive and signal-independent of the signal, the same error is added independently of the signal level, and the relative error is much smaller when multiplexing than when raster-scanning the object. For example, consider a constant object with intensity 100 on each of its 50 pixel. Consider it is contaminated by electronic noise only (zero mean and standard deviation $\sigma = 10$). Raster-scanning this object leads to relative signal fluctuations of 10%. In multiplexing with a S-matrix, half of the total signal from the entire object is detected per measurement : each measurement consists of 2500 photons in average. Since the error ($\sigma = 10$) is constant, the relative signal fluctuations are only of 0.4%. Since the multiplexed signal has a better SNR than the raster-scanned signal, and since the error is constant, it seems reasonable to think that the respective objects SNR (after estimation) is also better.

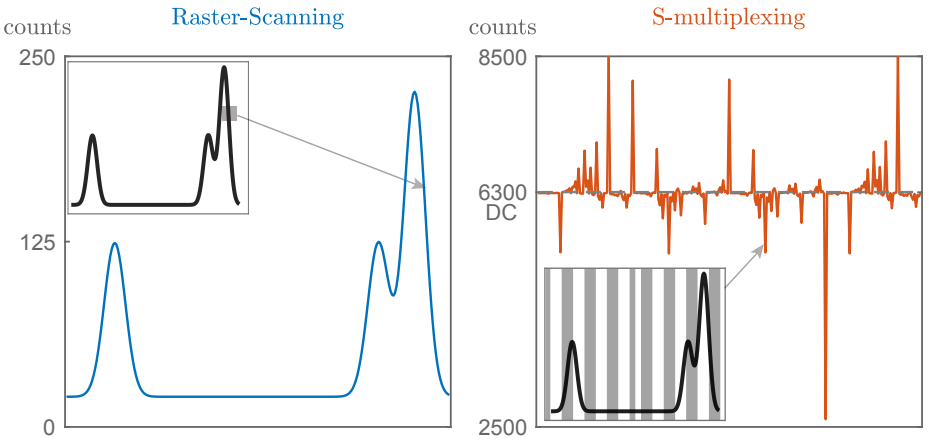


FIGURE 6.1: Illustration of noiseless raster-scanning and S-multiplexing measurements, for an object showing three peaked features. Multiplexing with S-matrix leads to higher signal levels than raster scanning. Measurements oscillate around a DC component equal to half the object integral.

### 6.1.2 Photon noise: a Multiplexing disadvantage ?

Nevertheless, one should keep in mind that the above advantage holds in a specific noise regime when noise arises from the detector. Already in the 1960s, some authors of the early days of FTIR warned that the multiplexing advantage may vanish when the measurements are shot-noise limited. For instance, Jacquinot [201] wrote in 1964: *Cet avantage, connu sous le nom de Fellgett's advantage n'existe que si l'origine du bruit est seulement dans le détecteur, ce qui est le cas pour l'infrarouge. Dans le visible, l'avantage Fellgett est perdu car les récepteurs ont une efficacité quantique telle que le bruit provient uniquement de la lumière et non du récepteur.* When the measurements are shot-noise limited, several studies [205, 224–231] have reported what they call a 'multiplexing disadvantage', i.e. a deterioration of SNR due to multiplexing, as compared to raster scanning.

The physical intuition for this disadvantage is not as easy to grasp as in the previous case. When the data is shot-noise limited, the noise is signal dependant. Thus, the error is not constant any more but depends on the measured signal levels, and more photons also means more noise. The same constant object as above is now contaminated with photon-noise only. In raster-scanning, the noise standard deviation is $\sigma = \sqrt{100} = 10$. The relative signal fluctuations are of 10%. In multiplexing with a S-matrix, the error increases : $\sigma = \sqrt{2500} = 50$. The resulting signal relative fluctuations are now of 2%. Once again, the multiplexed signal has a better SNR than the raster-scanned signal, but the fact that the error is signal dependent brings some subtleties. When multiplexing under photon noise, information is mixed and so is the noise. Since multiplexing with a S-matrix selects half on the object pixels at each measurements, each the measurement oscillates around a DC value equal to half the object integral (Fig. 6.1). When demultiplexing, the noise associated to this DC component spreads equally over the whole object: The object regions of low signal become more noisy than with raster-scanning, while the

regions with high signal become less noisy. For example, if an object does not emit any photon at some position, the associated raster-scan shot-noise is also zero and no noise is associated to this position. But after multiplexing and estimation, some noise from the whole object spreads and the noise associated to this position is non-zero. Another example would consist of an object with a very intense peak and a very dim peak: in raster-scanning, each peak is associated with a photon noise associated to its own brightness. But with the signal mixing due to multiplexing, the signal of the dim peak could be buried in the photon-noise of the intense peak. In a sense, the disadvantage also lies in the multiplexing matrix and the estimation step: While under signal-independent noise, one can design an optimum multiplexing matrix (in the sense of the SNR), doing so with shot-noise limited data would imply to know at least partially the object (as in CRT).

In a context of increasing use of single-pixel-detectors in the framework of compressive sensing [86, 87], single pixel cameras [91, 223] or ghost imaging [232, 233]; and with progress in detectors technology that tends to make measurements more and more likely to be limited by photon-noise only, it seems relevant to seriously consider this multiplexing disadvantage reported in the literature. Yet, in this noise regime, much less work has been investigating this question than for the multiplexing advantage. Though the conclusions of studies considering shot-noise limited data [205, 224–231] converge to a multiplexing disadvantage, in my opinion they have several limitations and lack some clear conclusions.
Firstly, the studies show a global loss in SNR when the latter is averaged over the whole object of interest. Only a few studies mentioned that this disadvantage may depend on the structure of the object [202, 205, 234–236], but with no extensive analysis. In a noise regime where the noise is signal-dependant noise regime, the SNR is just a global figure of merit and varies with the signal of interest. Yet, no study shows how the SNR is distributed over the object and how does it compare to raster-scanning. The two later points are key points in my opinion since it can help clarify when to use multiplexing or not. Secondly, most of the derivations and simulations were carried using one type of estimation method (least-square-based methods) to demultiplex the signal. While Poisson noise-based estimation strategies may mitigate the multiplexing disadvantage in some cases, they are considered in only a few papers [230, 231, 237]. Last, the reported studies are based on theoretical work and/or simulations: no experimental study has been reported to our knowledge.

In all, when the noise only comes from the photon-counting process, no study has made it clear, to our knowledge, when to use - or not - multiplexing techniques, and with which estimation strategy. Therefore, in this chapter, we theoretically and experimentally study more extensively multiplexing under the shot-noise regime, investigate its implications in terms of SNR, and try to provide some insights and rule of thumbs for experimentalists. We want to clarify under which circumstances multiplexing may bring an advantage, for shot-noise limited data, for a given system architecture. In this study, we will mostly focus on one type of multiplexing based on the Hadamard matrix and on quantitative estimation.

## 6.2 Methodology

Let us take the example of imaging an apple. Imagine we want to image a perfect apple (ground-truth) through a given imaging system. We image the apple in two ways : we raster-scan it - so that each measurement targets a point of the apple, or perform multiplexing measurements - so that many parts of the apple are measured at each time. Experimentally, the image is noisy. Despite the noise, we want to obtain the best quantitative image: it means that not only we want to know where is the apple and its shape, but we also wish to know the right color tones and associated brightnesses, and all this as close to the perfect apple as possible. We want to know which of the 2 imaging strategies allow to retrieve the apple with the least error (as compared to the perfect apple).

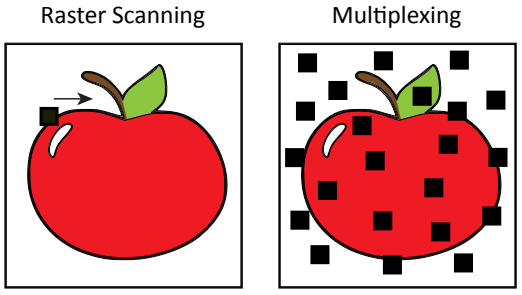


Before conducting such a study, we need to:

- Define the study framework and assumptions (6.2.1)
- Define a multiplexing strategy (6.2.3)
- Model the measurement system with its associated noise (6.2.2)
- Define the figures of merit that evaluate the estimation performances (6.2.4)
- Present the estimation strategies and the associated algorithms (6.2.5)

### 6.2.1 Framework and assumptions

The problem under study is wide, and many directions could be investigated. In this report, we restrict our study to a simplified physical model and to the following framework:

- We focus on the comparison between the previously presented raster-scanning and multiplexing strategies
- We consider shot-noise limited measurements: the main source of noise is the signal photons intrinsic noise.
- We mainly focus on one type of multiplexing with the S-matrix (6.2.3).

- We assume that the resolution (spatial or spectral) is infinitely smaller than the finest details of the considered structures. We thus ignore resolution effects.
- We restrict ourselves to cases where the signal is linear in intensity (e.g. Fluorescence, Raman)
- We work at constant irradiance and integration time. For example, if in raster-scanning a 10 mW focused laser beam stays for 1 ms in each pixel, then, in multiplexing each targeted pixel also sees 10 mW of power, and each pattern is displayed for 1 ms. Multiplexing thus results in much higher measured signal.
- We mainly focus on signal quantitative estimation: the principal criterion we wish to minimize is the mean-square-error (MSE), i.e. the error of our estimation compared to the ground truth. We study which of raster-scanning or multiplexing leads to the smallest MSE. We do not study localisation though some conclusions may be relevant for localisation as well.
- We use several estimators to estimate the object, some of them are more complex (e.g. estimator based on the Poisson-noise models) than others (simple least-square estimation). We also assume our object is positive. We report the use of further *a priori* knowledge about the object (e.g sparsity) to future work.
- The study context is common to spectroscopy and imaging: we thus speak independently of spectrum or object. We restrict ourselves to 1D-multiplexing (spectra or 1D-profile of 2D objects), but conclusions can be extended to 2D.

### 6.2.2 Model

The main variables are defined below :

- $\mathbf{x}$: vector of $N$ object pixels - ground truth ($\mathbf{x} \in \mathbb{R}_N^+$)
- $\mathbf{b_0}$: vector of $M$ noiseless measures
- $\mathbf{b}$ : vector of $M$ noisy measures
- $\mathbf{g}$ : vector of $M$ background counts - assumed known
- $\mathbf{A}$ : $M$x$N$ measurement matrix

We consider the following simple linear model. An object $\mathbf{x}$ is measured through a matrix $\mathbf{A}$, leading to an ideal noiseless measurement $\mathbf{b_0}$:

$$\mathbf{b_0} = \mathbf{A}\mathbf{x} + \mathbf{g} \tag{6.1}$$

Shot-noise limited measurements are given by $\mathbf{b}$:

$$\mathbf{b} = Poisson(\mathbf{Ax} + \mathbf{g}) \tag{6.2}$$

In the case of raster-scanning, $\mathbf{A}$ is the identity matrix $\mathbf{I}$ and each element of $\mathbf{b_0}$ is $b_{0i} = x_i + g_i$ $(i = 1...N)$). In the case of multiplexing, $\mathbf{A}$ is a weighting matrix that can be designed by the user. Each element of $\mathbf{b_0}$ is a linear combination derived from the object : $b_{0i} = a_{i1}x_1 + ... + a_{iN}x_N + g_i$. The aim is to estimate $\mathbf{x}$ as precisely and accurately as possible from the noisy measurements $\mathbf{b}$. $\mathbf{g}$ is a small constant vector which accounts for some possible background that does not experience $\mathbf{A}$. It is assumed to follow a Poisson distribution and to be signal independent. In the study simulations and experiments, it is negligible, but we take it into account in the algorithms to avoid singularities.

### 6.2.3 Choice of the multiplexing matrix

Multiplexing can be implemented in many different ways. In principle, any mixing technique, discrete or continuous, binary or not could be used to multiplex the data. But both technological and mathematical constraints restrict the choices. In imaging and spectroscopy, two main hardware multiplexing techniques are used. The first technique uses interference techniques (e.g. FTIR): the multiplexing is performed continuously with an interferometer and the estimation via a Fourier-transform. The second techniques are based on modulating or blocking parts of the light with encoding patterns. This can be achieved with simple elements such as simple absorptive pattern imprinted on mirror [52], or with a light modulator device (e.g. SLM, DMD). In general, the current technologies make it easier, cheaper and faster to implement binary patterns into the hardware, and thus makes the binary matrices generally preferred over other solutions. Secondly, the chosen matrix needs to ensure easy and efficient demultiplexing of the data. Amongst the binary matrices, the S-matrix (modified Hadamard matrix with positive coefficients) is widely used in the optics community. Its deterministic and well-conditioned nature makes it preferable over binary random matrices in a number of cases. We can note that, under additive white Gaussian noise (AWGN), the Hadamard matrix was shown to minimize the MSE [52], and the S-matrix was proved to be minimize it for odd dimensions [238, 239]. In the shot-noise limited case, the error is object-dependent, therefore the multiplexing matrix may only be optimal with certain *a priori* knowledge on the object. Research on optimal encoding strategies for photon noise include [229, 240, 241], but this is beyond the scope of our work.

This chapter mainly focuses on multiplexing with the S-matrix (*S-multiplexing*), which is a modified Hadamard matrix with positive coefficients. The S-matrix of size (N-1) is built from removing the first row and column of a N-Hadamard matrix, and changing its ones to zeros and minus ones to ones. It is invertible. Some of its properties are described in Appendix C.

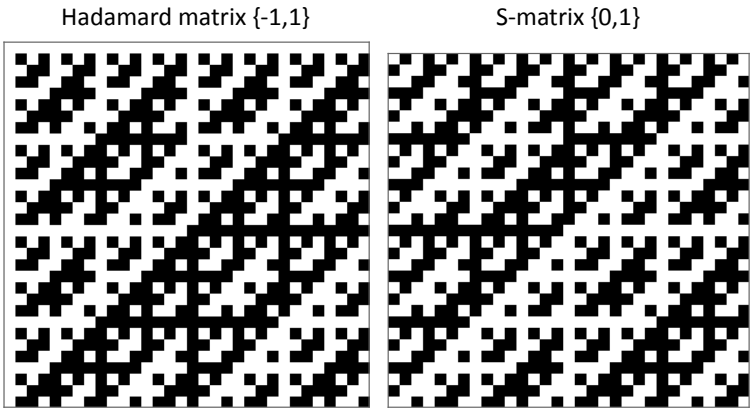


FIGURE 6.2: Hadamard matrix (32×32), white: 1 , black: -1. Corresponding S-matrix (31×31), white: 1 , black: 0.

### 6.2.4 Figures of Merit

For the quantitative estimation of the signal, the principal criterion we wish to minimize is the mean-square-error (MSE). It indicates the error between the estimate $\hat{\mathbf{x}}$ and the ground truth $\mathbf{x}$. The MSE in each object pixel $i$ is defined as:

$$MSE_i = E((\hat{x}_i - x_i)^2) \tag{6.3}$$

The SNR directly relates to the MSE through :

$$SNR_i = \frac{x_i}{\sqrt{MSE}} = \frac{x_i}{\sqrt{E((\hat{x}_i - x_i)^2)}} \tag{6.4}$$

We call 'average MSE' the MSE averaged over all the object pixels.

$$\overline{MSE} = \frac{1}{N} \sum_i E((\hat{x}_i - x_i)^2) \tag{6.5}$$

We also define a ratio that directly compares the error due to raster-scanning to multiplexing :

$$G = \sqrt{\frac{\overline{MSE}_{rs}}{\overline{MSE}_{multiplex}}} \tag{6.6}$$

G relates to the gain or loss in object SNR : if $G > 1$, multiplexing improves the average SNR compared to raster-scanning, while if $G < 1$, multiplexing degrades the average SNR compared to point-scanning.

### 6.2.5 Estimators and algorithms

To minimize the MSE, various estimators can be used. Under AWGN, the least-square (LS) estimate is efficient and optimal in the sense of the maximum-likelihood estimator (MLE). In Chapter 2, we saw that under Poisson noise with no constraint on the estimate, the LS estimate

is also efficient, if $\mathbf{A}$ is invertible (Eq. (2.19)). In this study, the objects of interest are positive intensities and the measurements number of photons counts. We thus include estimators that consider positivity constraints. Although they may add a bias, they may still reduce the MSE.

#### Least-square (LS)

The LS solution minimizes $||\mathbf{b} - \mathbf{b_0}||^2$. Assuming $\mathbf{g}$ known, it reads :

$$\hat{\mathbf{x}} = \mathbf{A}^{+}(\mathbf{b} - \mathbf{g}) \tag{6.7}$$

It is the only unbiased estimator used in this chapter.

#### Least-square with negative values removal (LS-clip)

The simplest method to take into account the positivity of the object is to set to zero all the negative values of $\hat{\mathbf{x}}$ after performing the LS estimation of Eq. (6.7). I call this method LS-clip. I include it because it reflects the commonly applied positive threshold on experimental results.

#### Non-negative Least-square (NNLS)

The NNLS takes into account the positivity of the object by solving the LS problem with positivity constraints:

$$||\mathbf{b} - \mathbf{b_0}||_{l2} \; subject \; to \; \mathbf{x} \geq 0 \tag{6.8}$$

For simplicity I use the function *lsqnonneg* of Matlab (checked to behave $\approx$ as FISTA with positivity constraint on the studied objects).

#### Expectation-maximization algorithm (EM)

To find maximum likelihood estimates (Appendix A) of a Poisson-distribution under positivity constraints, we use an expectation–maximization (EM) algorithm, also known as Richardson-Lucy algorithm. This algorithm was described in the 1970s by Richardson [242] and Lucy [243], and in 1982 by Shepp and Vardi in the context of Emission Tomography [244]. It searches for the parameter $x_k$ that maximizes the likelihood to obtain $b_i$ photons, therefore to minimize the equivalent of Eq. (A.5) for the present model, which in the matrix form reads:

$$\mathbf{A}^T diag(\mathbf{A}\mathbf{x} + \mathbf{g})^{-1}\mathbf{b} - \mathbf{A}^T\mathbf{1} = \mathbf{0} \tag{6.9}$$

The EM algorithm solves this non-linear equation iteratively through:

$$\mathbf{x}^{q+1} = \frac{\mathbf{A}^T diag(\mathbf{A}\mathbf{x}^q + \mathbf{g})^{-1}\mathbf{b}}{\mathbf{A}^T\mathbf{1}}.\mathbf{x}^q \tag{6.10}$$

where the division symbolizes term-by-term division and the . term-by-term multiplication. The EM iteration alternates between performing an expectation (E) step, which evaluates the log-likelihood using the current estimate for the parameters, and a maximization (M) step, which computes parameters maximizing the expected log-likelihood found on the E step. At every iteration, a value of the estimated parameter is computed so that the likelihood function cannot decrease. The algorithm was shown to converge but there is no guarantee that the maximum is a global maximum [245].
We decided to use this algorithm because it is well-established, widely used and simple to implement. It is also used in some work relative to the present study [230, 231, 246]. Although it is slow, it is not very problematic so far.

#### Sparse Poisson Intensity Reconstruction ALgorithms: SPIRAL-TAP (ST)

We use a second method to find the maximum likelihood estimate of a Poisson-distribution under positivity constraints. We use the SPIRAL-TAP developed by Harmany et al. [247]. The equation solved is:

$$maximize\ L(\mathbf{x}) + \tau pen(\mathbf{x})\ subject\ to\ \mathbf{x} \geq 0 \tag{6.11}$$

Where $L$ is the Poisson log-likelihood (Appendix A) and $pen$ is a finite, usually non-smooth and potentially non-convex penalty term. This algorithm was shown to be stable and converge [247]. We use this algorithm because it is open-access, cited in numerous work and offers the possibility to include sparsity constraints (e.g. $l1$, $TV$). Though we do not use them much in this study ($\tau = 0$), they will be considered in future work. We also use SPIRAL-TAP to verify that the EM-algorithm I implemented gives the same results. Thus, results from SPIRAL-TAP are only included in the following when they differ from the EM results.

In the following, we derive theoretical expressions of the MSE, and present simulations and experiments.

## 6.3 Theoretical expressions of the MSE

To begin with, we derive a theoretical expression for the MSE, for S-multiplexing and LS-estimation, when the measurements are limited by detector noise or photon-noise. It is interesting because it explains the Multiplexing advantage and disadvantage mentioned in (6.1.1) and (6.1.2).
In the following, the multiplexing matrix $\mathbf{A}$ is square ($N = M$) and invertible, and we consider independent measurements. The object, power-densities and integration times are supposed identical for raster-scanning and multiplexing. For clarity, we also neglect the background counts of Eq. (6.1) ($\mathbf{g} = \mathbf{0}$). Last, we remind that the covariance matrix related to the estimate error $\delta\hat{\mathbf{x}}$ is defined by $\mathbf{\Gamma} = E(\delta\hat{\mathbf{x}}\delta\hat{\mathbf{x}}^{\mathbf{T}})$.

Detector noise (AWGN)

Detector noise can often be modelled with additive i.i.d. Gaussian noise with zero-mean and uniform variance (AWGN). This noise is assumed to be signal independent. Then, Eq. (6.1) reads:

$$\mathbf{b} = \mathbf{A}\mathbf{x} + \mathbf{e} \tag{6.12}$$

where, $\forall i \neq j$, $E(e_i) = 0$, $E(e_i e_j) = 0$, $E(e_i^2) = \sigma^2$, with $\sigma$ the noise standard deviation.

The LS estimate leads to :

$$\hat{\mathbf{x}} = \mathbf{A}^{-1}\mathbf{b} \tag{6.14}$$

The error $\delta\hat{\mathbf{x}} = \hat{\mathbf{x}} - \mathbf{x}$ reads :

$$\delta\hat{\mathbf{x}} = \mathbf{A}^{-1}\mathbf{e} \tag{6.16}$$

It leads to the covariance matrix:

$$\mathbf{\Gamma} = \sigma^2(\mathbf{A}^T\mathbf{A})^{-1} \tag{6.18}$$

The errors are uncorrelated and the estimator is unbiased. We define the average MSE as:

$$\overline{MSE} = \frac{\sigma^2}{N} tr((\mathbf{A^T A})^{-1}) \tag{6.20}$$

Thus, for AWGN, the average MSE only depends on the noise variance $\sigma^2$, and on the multiplexing matrix $\mathbf{A}$. It is object independent.

Shot-noise

When the detector noise and all other noise sources are negligible, the measurements are limited by photon noise. The error depends on the detected signal. (6.1) reads:

$$\mathbf{b} = Poisson(\mathbf{A}\mathbf{x}) \tag{6.13}$$

where, $\forall i$, $E(b_i) = E(\delta b_i^2) = b_{0i}$, with $\delta b_i = b_i - b_{0i}$

The LS estimate leads to :

$$\hat{\mathbf{x}} = \mathbf{A}^{-1}\mathbf{b} \tag{6.15}$$

The error $\delta\hat{\mathbf{x}} = \hat{\mathbf{x}} - \mathbf{x}$ reads:

$$\delta\hat{\mathbf{x}} = \mathbf{A^{-1}}(\mathbf{b} - \mathbf{b_0}) = \mathbf{A^{-1}}\delta\mathbf{b}. \tag{6.17}$$

With $\mathbf{B} = diag(\mathbf{A}\mathbf{x})$, the covariance matrix reads:

$$\mathbf{\Gamma} = \mathbf{A}^{-1}\mathbf{B}\mathbf{A}^{-T} \tag{6.19}$$

Although the errors might be correlated, we also define an average MSE:

$$\overline{MSE} = \frac{1}{N} tr(\mathbf{B}(\mathbf{A}\mathbf{A}^T)^{-1}) = \frac{(\mathbf{A}\mathbf{x})^T}{N} diag((\mathbf{A}\mathbf{A}^T)^{-1} \tag{6.21}$$

Thus, for shot-noise limited data, the average MSE depends on the multiplexing matrix $\mathbf{A}$ and on the object itself. It is object dependent.

For the shot-noise case, we note that we find an equivalent expression for $\mathbf{\Gamma}$ as in Eq. (2.19), and

thus when $\mathbf{A}$ is square, $\mathbf{\Gamma} = \mathbf{CRB}$. Using the above average MSE expressions, we can derive the theoretical values for raster-scanning and S-multiplexing:

Detector noise (AWGN)

Using Eq. (6.20) and Eq. (C.4), we obtain, for raster-scanning ($\mathbf{A} = \mathbf{I}$) :

$$\overline{MSE}_{rs} = \sigma^2 \tag{6.22}$$

And S-multiplexing (for $N >> 1$)

$$\overline{MSE}_{mult} = \frac{4\sigma^2}{N} \tag{6.24}$$

Thus, the SNR gain reads

$$G = \sqrt{N}/2 \tag{6.26}$$

Thus, with LS estimation, S-multiplexing leads to an average MSE $4/N$ times smaller than with raster-scanning. This corresponds to a gain in object SNR of $\sqrt{N}/2$. This is referred to as the *Multiplexing advantage*

Shot-noise

From Eq. (6.21) and Eq. (C.3), we obtain, for raster-scanning :

$$\overline{MSE}_{rs} = \frac{\sum_i x_i}{N} = \bar{x} \tag{6.23}$$

And for S-multiplexing (for $N >> 1$):

$$\overline{MSE}_{mult} = \frac{2\sum_i x_i}{N} = 2\bar{x} \tag{6.25}$$

Thus, the SNR gain reads:

$$G = 1/\sqrt{2} \tag{6.27}$$

Thus, with LS estimation, S-multiplexing leads to an average MSE twice larger than with raster-scanning. This corresponds to a moderated disadvantage in SNR of $1/\sqrt{2}$. This is referred to as the *Multiplexing disadvantage*

It is important to note that the factors 2 in the derivations arise from the S-matrix properties and positive coefficients. The same derivation with the 'true' Hadamard matrix (with $+1$ and $-1$) leads to $G = \sqrt{N}$ for AWGN and $G = 1$ for shot-noise. In the latter case, this means that there is no average MSE advantage or disadvantage due to Hadamard multiplexing (over raster-scanning). Therefore, the S-multiplexing disadvantage on the *average* MSE arises from the positive DC component of the measurements.

We stress that in the above calculations, the fact that the noise is signal-dependent is the key hypothesis rather than the noise probability distribution. If the Gaussian noise error properties now depend on the signal ($E(e_i) = (\mathbf{Ax})_i$, $Var(e_i^2) = E(e_i)$), the covariance matrix of Eq. (6.18) becomes $\mathbf{\Gamma} = \mathbf{A}^{-1} < \mathbf{ee^T} > \mathbf{A}^{-T}$. Then the average MSE equals to the MSE of the shot-noise limited case (Eq. (6.25)), showing a disadvantage of S-multiplexing. This is consistent with the fact that the Poisson distribution can be well estimated by a Gaussian distribution for sufficient

photon rate.

Fig. 6.3 illustrates with a simple example the above derivations. In the presence of AWGN only, the error in the estimated object after S-multiplexing is clearly lower than for the raster-scanned measurement. When averaging the error over all the object pixels, we indeed find a SNR gain $G$ of $\sqrt{N}/2$. In the presence of photon-noise only, the background of the raster-scanned object clearly appear less noisy than in the case of multiplexing, but it seems to be the opposite on the object peaks. When averaging the error over all the object pixels, we find the expected SNR loss $G$ of $1/\sqrt{2}$.

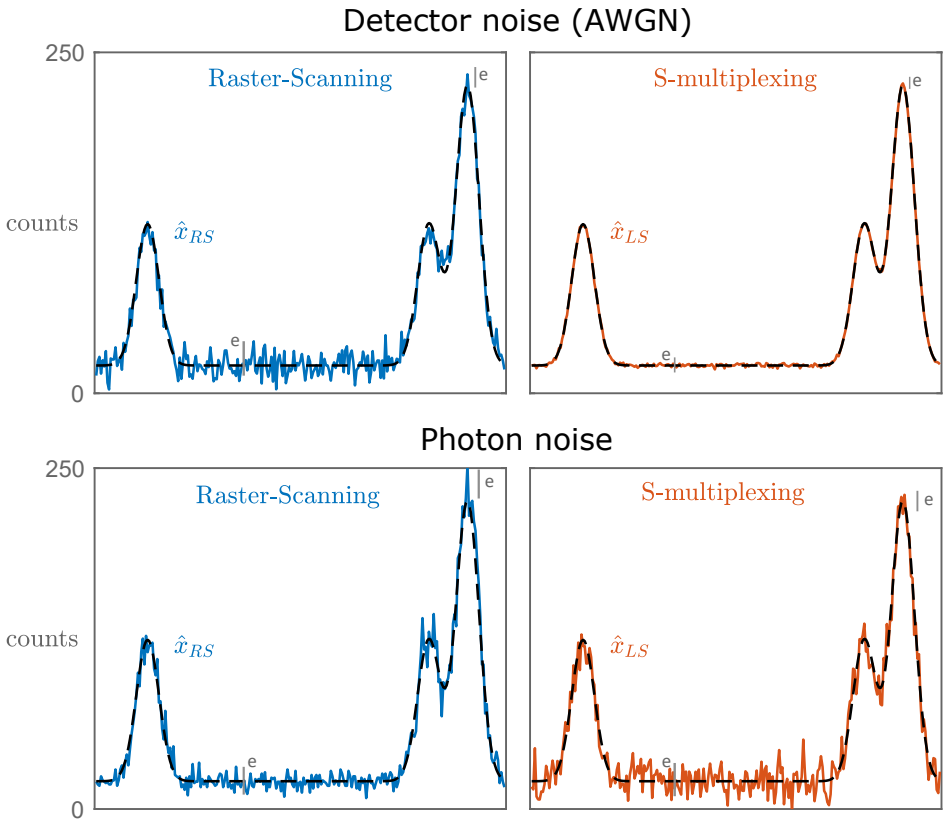


FIGURE 6.3: (Top) In the AWGN case (zero-mean, $\sigma = 10$) S-multiplexing seems to bring a clear advantage. (Bottom) In the shot-noise case, S-multiplexing seems to increase the error in the low signal regions and increase it on the higher signal regions.

Overall, when the measurements are limited by signal independent detector noise, the average MSE theoretical derivations show a clear S-multiplexing advantage: An object is much better estimated if the measurements are S-multiplexed. However, in the shot-noise limit, the derivations show a mitigated disadvantage for S-multiplexing. These derivations are informative, but average MSE does not encompass the object structure, so has a limited significance. Nevertheless, it indicates that if S-multiplexing decreases the error on some parts of the object; it would automatically degrade it on other places, since the error overall should increase by a factor 2.

In the following, we investigate in more details the dependence of the error on the object structure in the shot-noise limit, using LS estimations as well as other estimators.

## 6.4 MSE dependence on the object structure: Simulation results

In this section, we study the influence of the object structure on the MSE. We reproduce some results of the literature concerning the average MSE, and add (i) an analysis of the MSE per object pixel, (ii) a comparison to raster-scanning, (iii) the use of NNLS estimator, (iv) a rule-of-thumb and insights for when S-multiplexing may be useful or not.

Simulations are performed on 4 different 1D-objects (Fig. 6.4): a broad object (A), an object with localised peaks and positive background (B), an object with localised peaks and zero background (C), and a sparse object (D). The brightness of the objects is varied, resulting in different numbers of photons. This would physically be changed with the incident laser power and is numerically implemented by multiplying the whole object by a constant. The numbers of photons we refer to are mean numbers of photon per object pixel. Simulations are performed for 500 Poisson-noise realisations, and with the background counts set to $g_i = 5 \times 10^{-3}$ (e.g. modelling a detector with mean dark counts of 50 counts/s for an integration times of 0.1 ms). As already mentioned, the model is simplified: No PSF is considered for generality. We work at a fixed sampling and the number of object pixels is equal to the number of rows of the S-matrix and thus to the number of measurement ($N = M = 255$). Last, I choose to conduct the analysis in terms of $MSE$ eq.(6.5) instead of *object SNR* (6.4) because I find the plots more informative, but one could conduct the same analysis with $SNR$ - bearing in mind that higher $MSE$ means lower $SNR$.

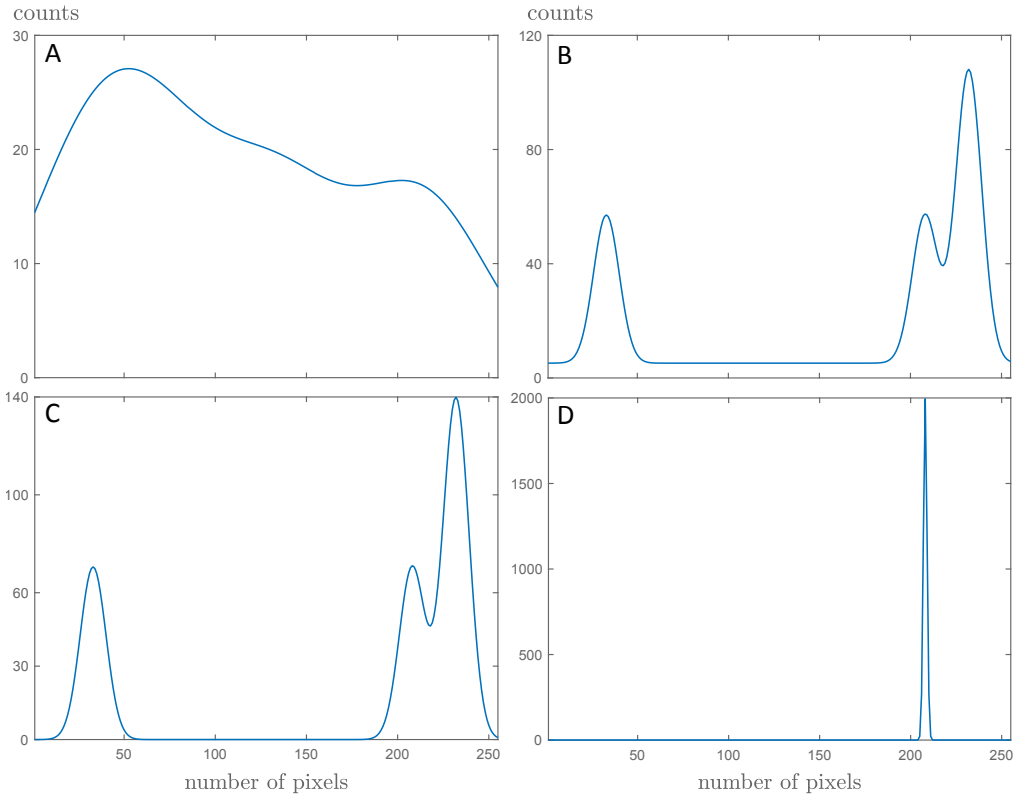


FIGURE 6.4: Ground truth objects: (A) Broad object, (B) Object with localised peaks and positive background, (C) Object with localised peaks and zero background, (D) Sparse object. Mean number of counts / pixel = 20

### 6.4.1 Average MSE

To begin with, we study the effect of the proposed algorithms on the average MSE given, for LS estimation, by Eq. (6.25). Each plot (Fig. 6.5) represents the relative averaged MSE ($\overline{MSER} = \sqrt{\overline{MSE}}/\bar{x}$) as a function of the number of photons (mean number of photon / object pixel), for each object. The dotted dark lines relate to raster-scanning, and the other colors to S-multiplexing coupled to different estimation methods. The ticks represent errorbars. A relative averaged MSE curve above the raster-scanning curve means that S-multiplexing represents a *global* (averaged over the whole object) disadvantage as compared to raster-scanning. Conversely, any estimation method leading to curve below the raster-scanning curve implies a global advantage of S-multiplexing. The ratio of the relative averaged MSE is equal to $G$ (Eq. (6.6)).

For the 4 objects, the results of raster-scanning and LS-estimation are consistent with the theoretical predictions from Eq. (6.23), (6.25) and (6.26): S-multiplexing associated to LS-estimation leads to an average $MSE$ twice as large as compared to raster-scanning.

The effects of the other estimators depend on the object structure. For objects A and B, some estimation methods seem to improve the LS-estimation at low number of photons. EM and NNLS seem to even slightly outperform raster-scanning at extremely low flux. However, this advantage should be considered with care and we expect that raster-scanning would still be

preferred (Fig. 6.9-6.12). Above a certain signal level, all the estimation methods give similar $\overline{MSER}$: S-multiplexing is then disadvantageous.
When the objects exhibit many zero values (C and D), things are different. For object C, S-multiplexing with the EM-algorithm slightly outperforms raster-scanning ($1 \leq G \leq 1.2$). We also note that a simple NNLS can greatly reduce the error as compared to LS. The last object (D) is sparse. It is interesting to see that multiplexing can bring a great advantage in terms of average MSE if used with NNLS ($G \approx 2$) or EM ($G \approx 4$). We only notice a difference in the estimations of ST (SPIRAL-TAP) and EM in this extremely sparse case. These $\overline{MSE}$ results are consistent with [230, 231, 237]

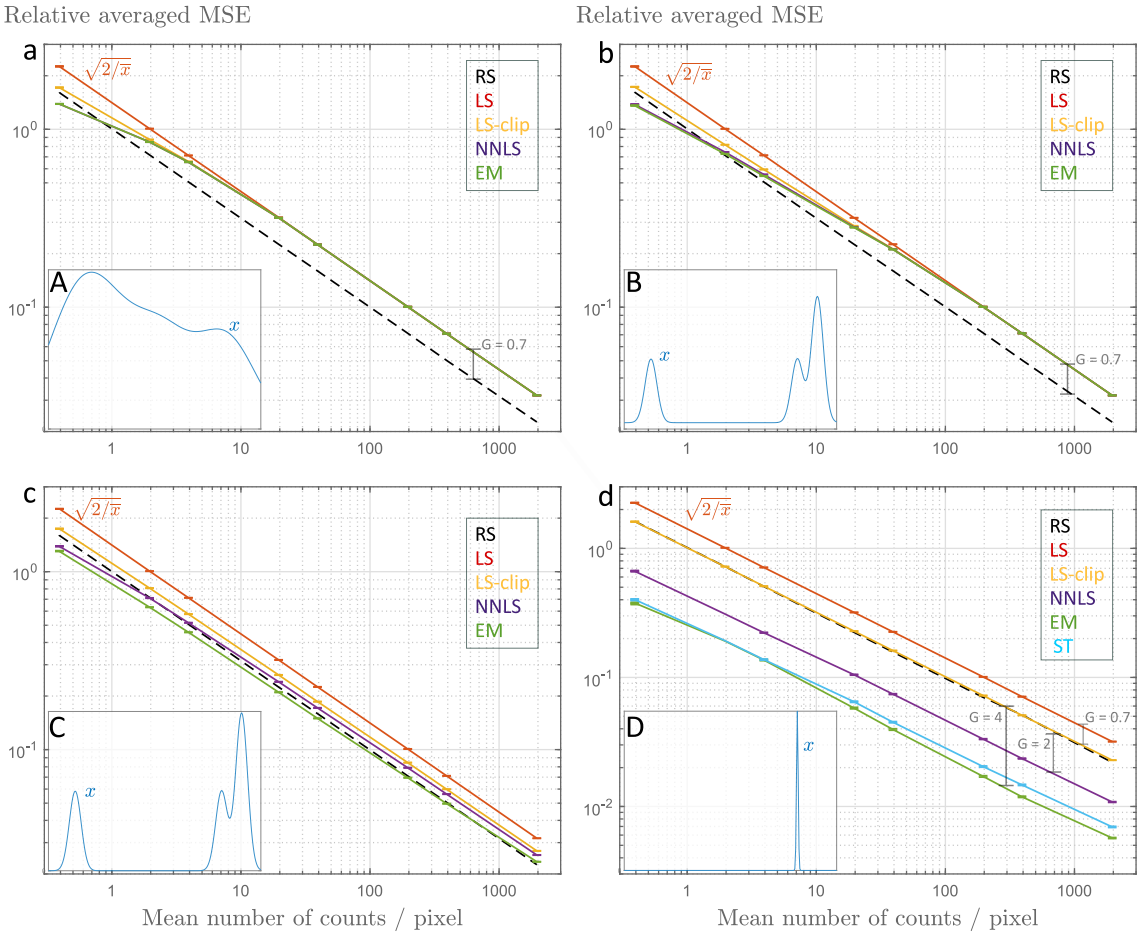


FIGURE 6.5: Average relative MSE as a function of the signal (mean number of counts / pixel), for the 4 objects. Estimations are performed with least-square (LS), least-square with clipping negative values (LSclip), non-negative least-square (NNLS), Poisson-Likelihood Expectation-minimisation algorithm (EM), and Poisson-Likelihood SPIRAL-TAP algorithm (ST). ST results are slightly different than EM only for object D so are only shown for object D. In (a), the NNLS and EM curves overlap

### 6.4.2 MSE per pixel

The above $\overline{MSE}$ analysis is interesting to a certain extent but not sufficient to draw conclusions. Indeed, since the noise depends on the signal, an analysis of the MSE per pixel ($MSE_i$) should be included to gain insights of S-multiplexing effects. Fig. 6.6 shows the MSE / pixel for the 4 objects at a fixed number of photons (mean number of counts / pixel = 4), that corresponds to the third data point on the curves of Fig. 6.5. We see that, while the MSE due to raster-scanning follows the object shapes (consistent for photon-noise), the MSE due to S-multiplexing spreads over all the object pixels. When using LS-estimation, the error is constant over the whole object: it behaves like a white-noise of mean $2\overline{x}$. The other estimation methods may act on this error depending on the object structure and signal level.
For object A, raster-scanning leads to the least MSE on every pixel: S-multiplexing degrades the estimation for all tested algorithms, although LS-clip, NNLS and EM slightly improve the MSE compared to LS. Object B and C show similar behaviour: The MSE associated with S-multiplexing is higher on most of the pixels, but is smaller on the object peaks. On the brightest pixel of object C, S-multiplexing decreases the MSE by more than 3 times as compared to raster-scanning. S-multiplexing thus seems to perform better than raster-scanning on the regions of highest signal, but worse on the low signal regions and background. On the peaks, all estimators seem to perform approximately the same, while some (LSclip, NNLS, EM) help reducing the error on the background. Object D is sparse: the effect observed for object C is more pronounced. On the brightest pixel, S-multiplexing decreases the MSE by more than 50 times as compared to raster-scanning. However, it leads to a MSE worsened by 7 times on all other pixels (for LS-estimation). NNLS, EM and ST help to greatly reduce the error on the background and so the average MSE (Fig. 6.5 (d)). On the object peak, all estimators, except NNLS, seem to perform approximately the same. On the null pixels, all the algorithms reduce the MSE as compared to LS (but may increase the bias, see (6.4.5)). We emphasize that these algorithms do not include a sparsity-prior. The error reduction is just due to the positivity constraint.

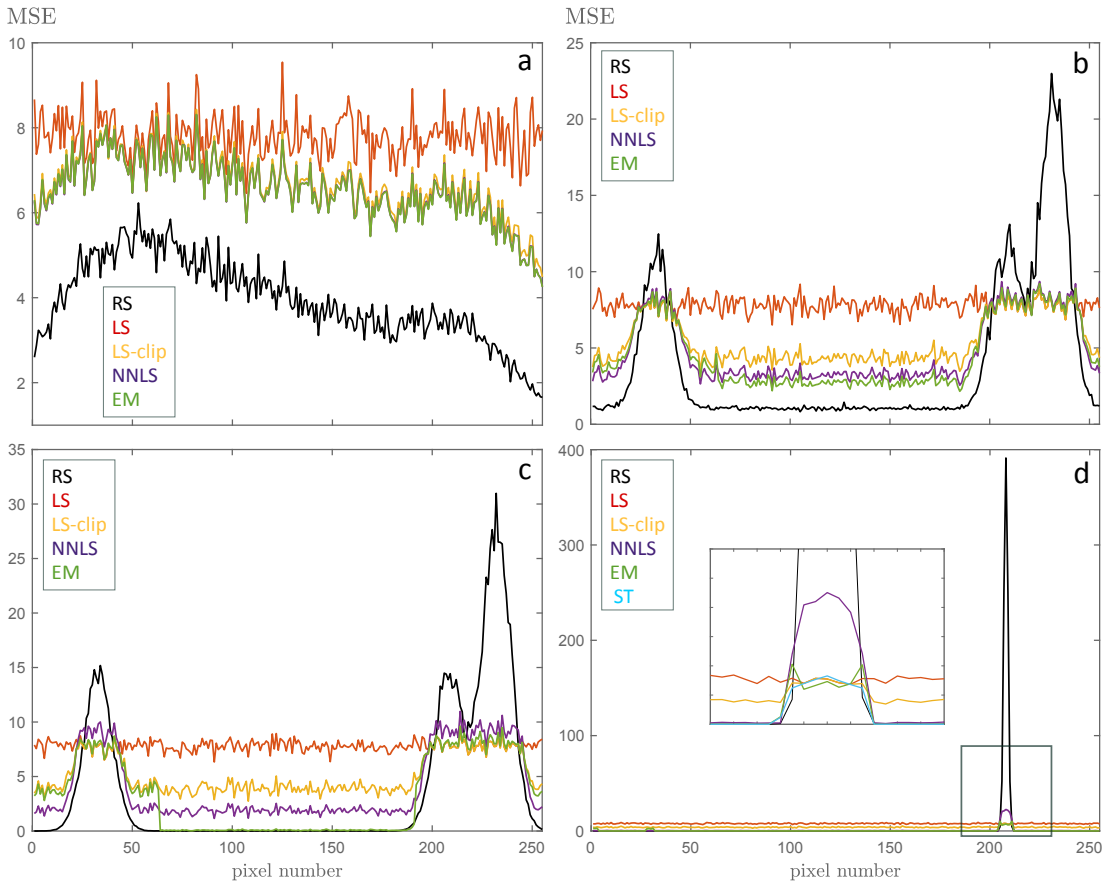


FIGURE 6.6: MSE per object pixel for a fixed signal level (mean number of counts / pixel = 4). With S-multiplexing, the MSE is higher over the whole object when it is relatively homogeneous (a). Conversely, S-multiplexing decreases the MSE on object peaks above a certain threshold value (b,c,d). The error reduction on the peak is drastic when the object is sparse (d).

Fig. 6.7 shows the MSE per pixel for object B at 4 fixed signal levels. It shows that LS-clip, NNLS and EM mainly have an effect at low signals, and on the object background. They bring an improvement over LS-estimation at low flux but their advantage decreases as the flux increases. This is simply because at low signal, the LS estimation may lead to estimated negative values on the background pixels. Thus, adding a positivity constraint simply reduces the associated variance. At high flux, even the background counts are large enough so the LS-estimate does not lead to any negative values: all estimations seem equivalent to the simple LS-estimation.

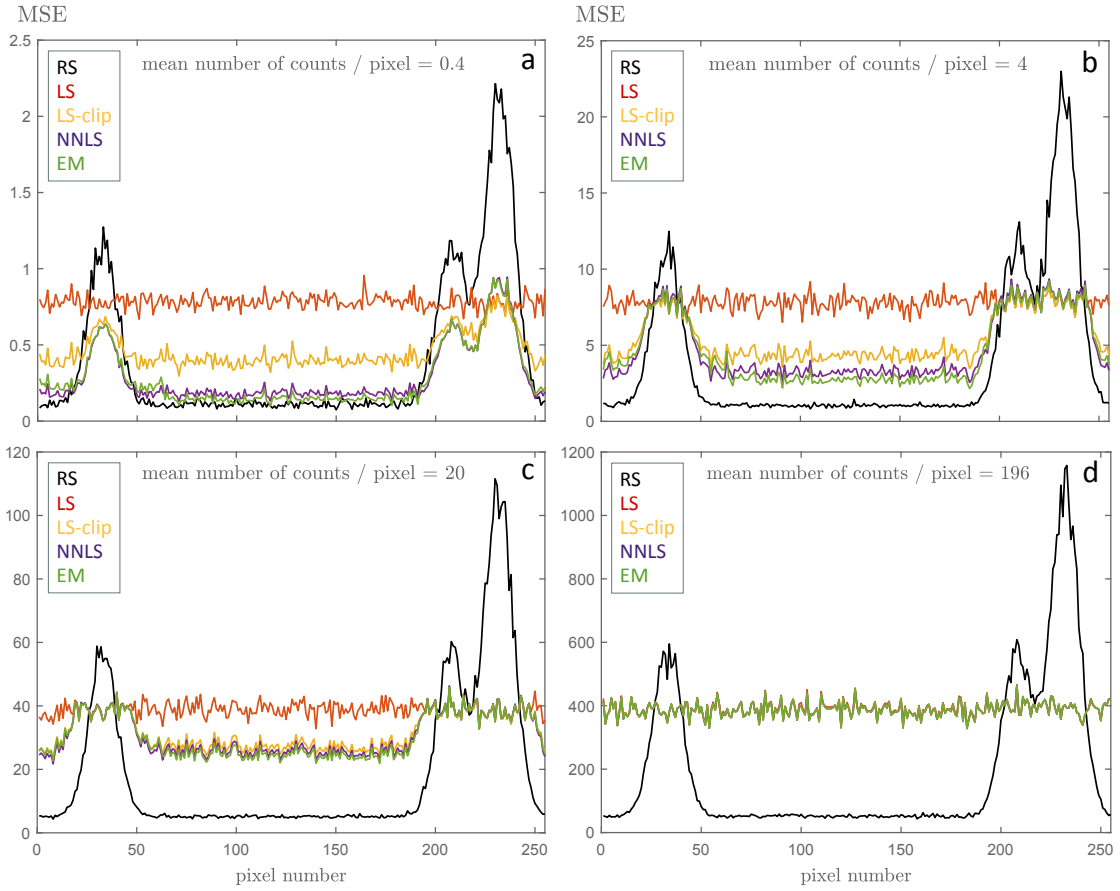


FIGURE 6.7: MSE per object pixel for object B and different signal levels. At low signal levels (a,b), the object background is close to zero so the least-square estimation leads to negative values and alternative algorithms improve the MSE on the background (compared to LS). At high flux, all estimators give similar MSE (d).

### 6.4.3 MSE per pixel: Rule of thumb

Overall, we see that S-multiplexing reduces the MSE on bright object regions while it increases it on dimmer parts. Since the S-multiplexing advantage / disadvantage appears to be dependent on the object structure, we seek in this section a structure-independent rule of thumb to know on which pixels the MSE is improved or worsen.

We know theoretically from Eq. (6.23) and Eq. (6.25) the MSE per pixel $i$ for raster-scanning is:

$$MSE_{i,rs} = x_i \tag{6.28}$$

For S-multiplexing, the error associated with LS estimation equally spreads all over the spectrum :

$$MSE_{i,ls} = \overline{MSE}_{ls} = \ 2\bar{x} \tag{6.29}$$

Therefore, the SNR gain per pixel writes : $G_{i,ls} = \sqrt{x_i/2\bar{x}}$. As a rule of thumb, we thus expect an improvement in SNR of S-multiplexing over raster-scanning on pixels $i$ for which :

$$x_i \geq 2\bar{x} \tag{6.30}$$

Therefore, S-multiplexing is expected to decrease the MSE on pixels for which the signal value is greater than twice the mean signal across the object ($\bar{x}$). Since the other estimators seem to mostly bring an SNR improvement on the background (where the positivity constraint may actually act), we surmise this threshold value to be independent of the estimation strategy used.

To illustrate this behaviour, we simulate an object with peaks of different intensities Fig. 6.8). The object mean number of counts is $\approx 10$. As expected, we observe that S-multiplexing decreases the MSE as compared to raster-scanning on peaks more intense than $\approx 20$ counts (Fig. 6.8). The advantage is more striking as the peaks are brighter. Conversely, any pixel with lower number of counts sees its error increase due to S-multiplexing. The bottom panels of Fig. 6.8 shows estimates for one Poisson realisation : We see that (i) the smallest peak is clearly distinguishable in raster-scanning, while it is quasi-buried into noise with S-multiplexing, (ii) the noise spreads in between the peaks with S-multiplexing.

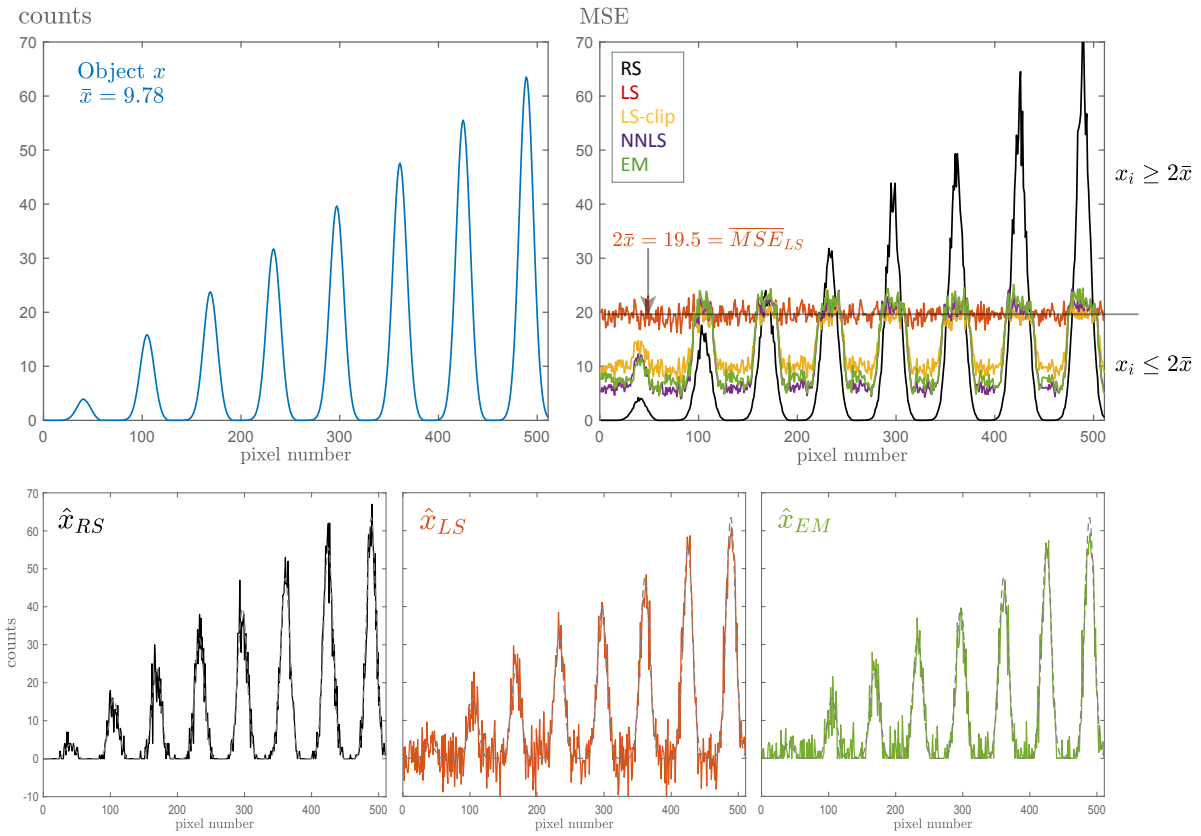


FIGURE 6.8: Simulated object (top left) and associated MSE per pixel (top right). S-multiplexing improves the MSE on pixels higher than twice the object average. Bottom: Examples of estimated objects for raster-scanning (RS), least-square estimation (LS) and Poisson-likelihood based algorithm (EM)

Therefore, the potential benefit of S-multiplexing is related to the object mean signal. S-multiplexing improves the MSE on object regions at least twice as bright as the average object brightness and degrades it on regions dimmer than this value. Dim signals could be easily buried in the noise if bright species were present.

### 6.4.4 Examples of reconstructions

To gain intuition on the consequences of S-multiplexing together with the different estimation strategies, this section gives examples of estimated objects (for one Poisson realisation). We show results on four 1-D objects, for three levels of signal and for RS, LS, NNLS and EM. The ground truth object is represented with a dotted gray line. The plots can be related to Fig. 6.5 - 6.6

For Object A (Fig. 6.9), a slight improvement due to EM over raster-scanning was suggested by Fig. 6.5 (a) at very low flux ($< counts >= 0.4$). But the estimated objects below do not show tangible improvement even when looking at many realisations. However, at higher flux ($< counts >= 40$), the degradation in average MSE suggested on Fig. 6.5 (a) clearly appears: raster-scanning leads to the least fluctuations. S-multiplexing degrades the estimation error and

the effect of other estimators seems limited. For Object B (Fig. 6.10), a slight improvement due to EM over raster-scanning was also suggested (Fig. 6.5 (b)) at very low flux ($< counts >= 0.4$). But here again it seems that this potential 'advantage' in average MSE should be considered with care. Quite the opposite, since at these extremely low flux, nearly no photons are detected on the background in raster-scanning, we surmise that to detect only peaks, raster-scanning should be preferred to S-multiplexing. When the number of counts gets higher, S-multiplexing clearly decreases the noise on the peaks while increasing it on the background (consistent with Fig. 6.6 (b)). The effect of using other estimators than LS-clip appears to be limited. For object C (Fig. 6.11), the same conclusions as for object B hold for low flux. However, at higher flux, EM clearly improves the estimation as compared to NNLS or LS-clip (consistent with Fig. 6.5 (c)). It decreases the background variance by removing the zeros. Here again, S-multiplexing leads to a better estimation of the object peaks. Similar statements hold for object D.

Furthermore, for object types similar to object B (distinct peaks and no-zero background), it can be relevant to define another figure of merit. The peak-signal-to-background ratio (SBR) relates the maximum object value to the fluctuations of the background ($\sigma_{bck}$):

$$SBR = \frac{max(x)}{\sigma_{bck}} \tag{6.31}$$

Although the peaks are better estimated with S-multiplexing, the spread of the error on the background leads to a worse SBR (Fig. 6.11). NNLS and EM slightly improve the SBR compared to LS-clip but the effect is limited. One could plot a similar figure than Fig. 6.5 for different objects of this class, and observe a worsening of SBR due to S-multiplexing, independently on the photon flux. Thus, if interested in SBR rather than in quantitative estimation, one should be aware of this disadvantage of S-multiplexing.

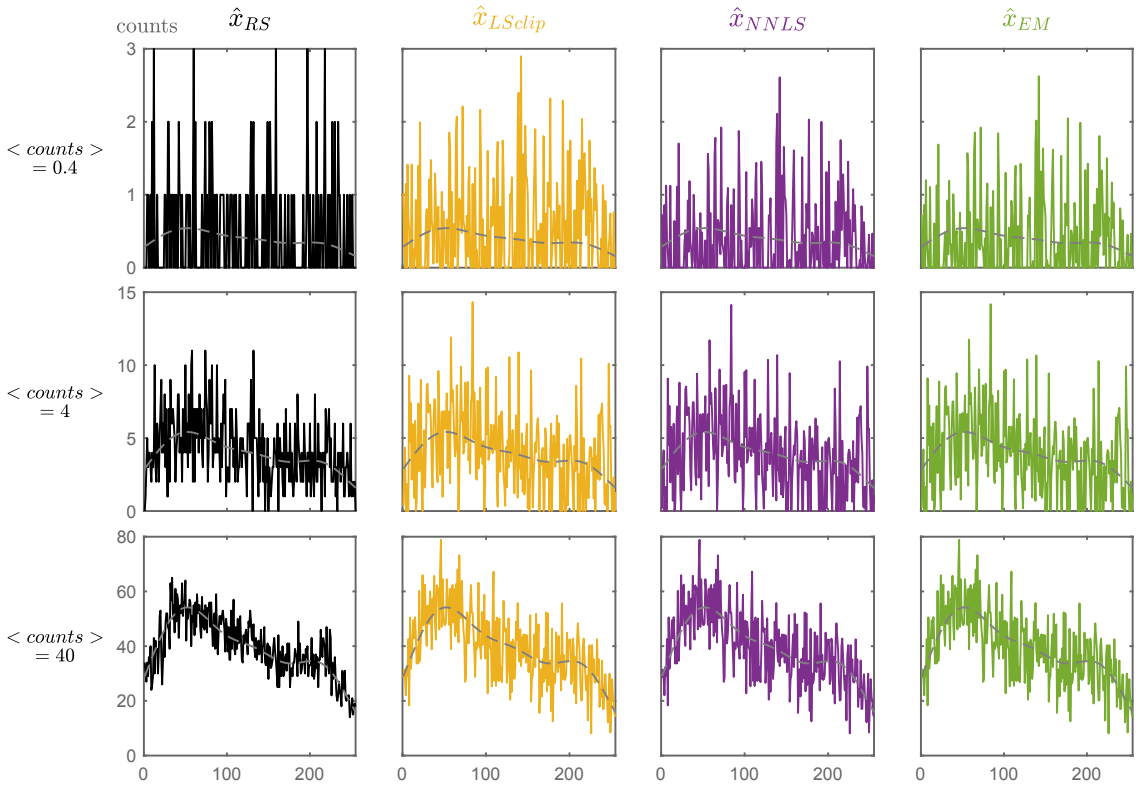


FIGURE 6.9: Examples of estimations for object A for three signal levels and different estimations.

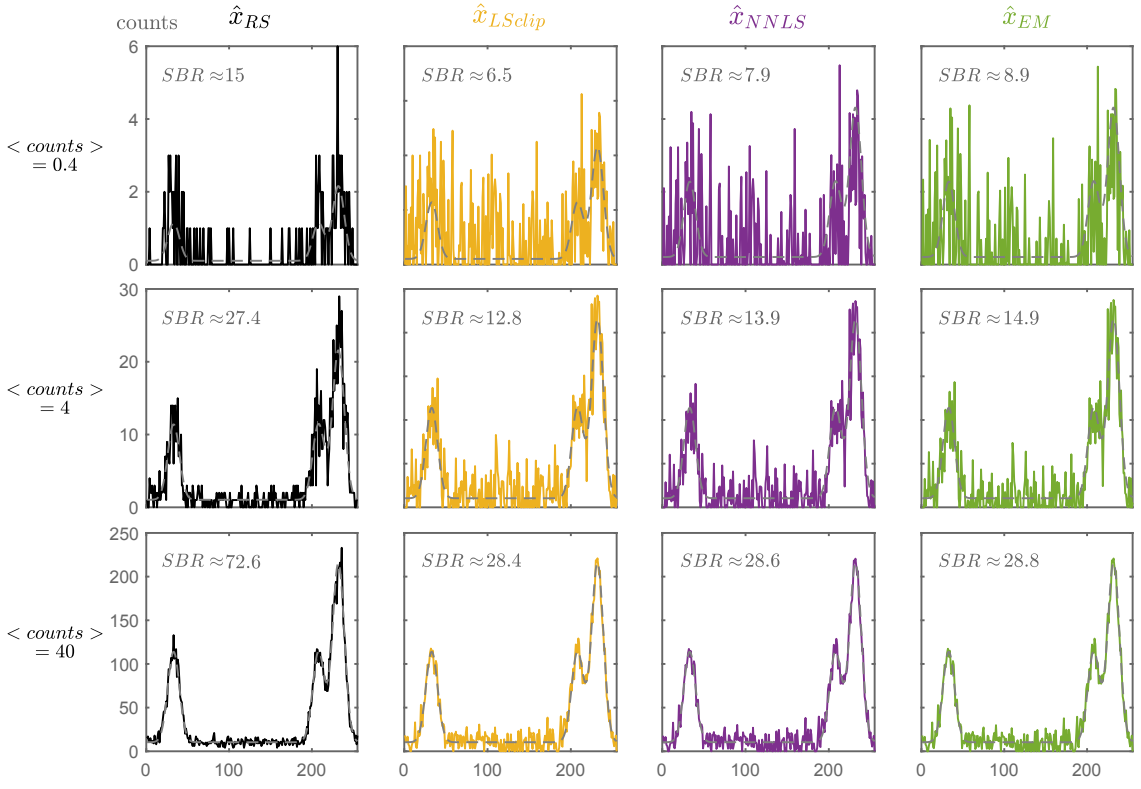


FIGURE 6.10: Examples of estimations for object B for three signal levels and different estimations.

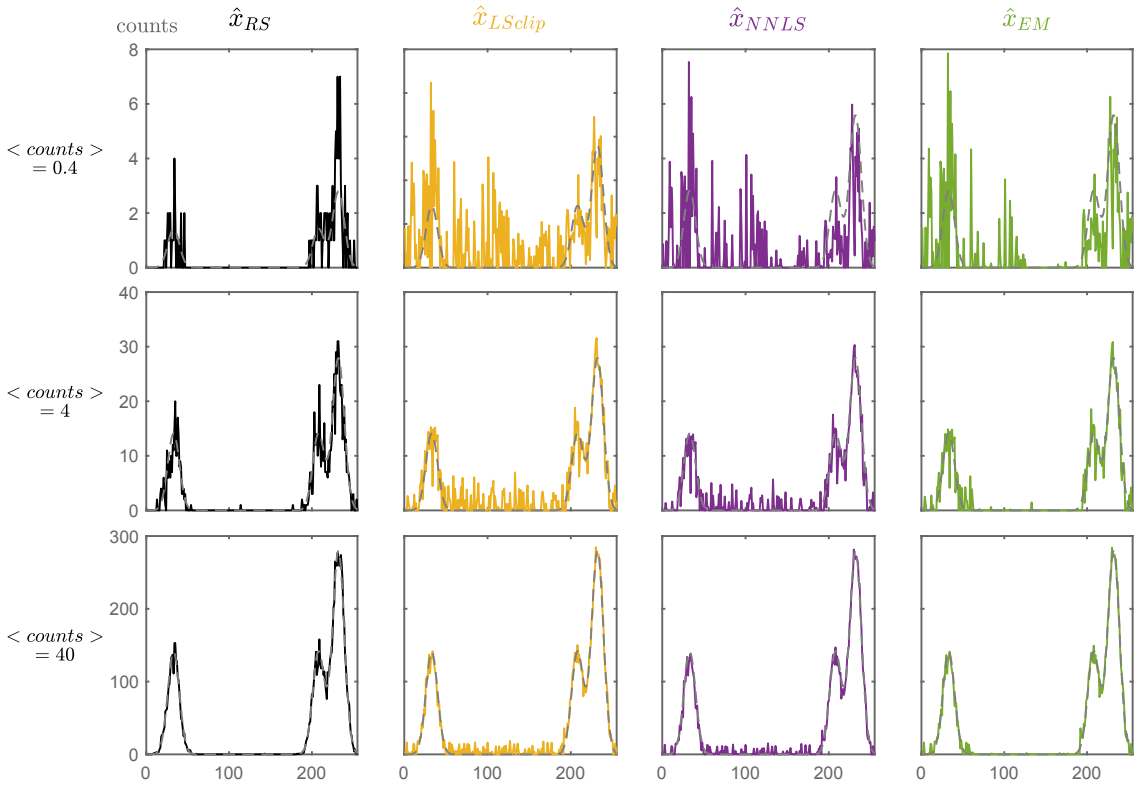


FIGURE 6.11: Examples of estimations for object C for three signal levels and different estimations.

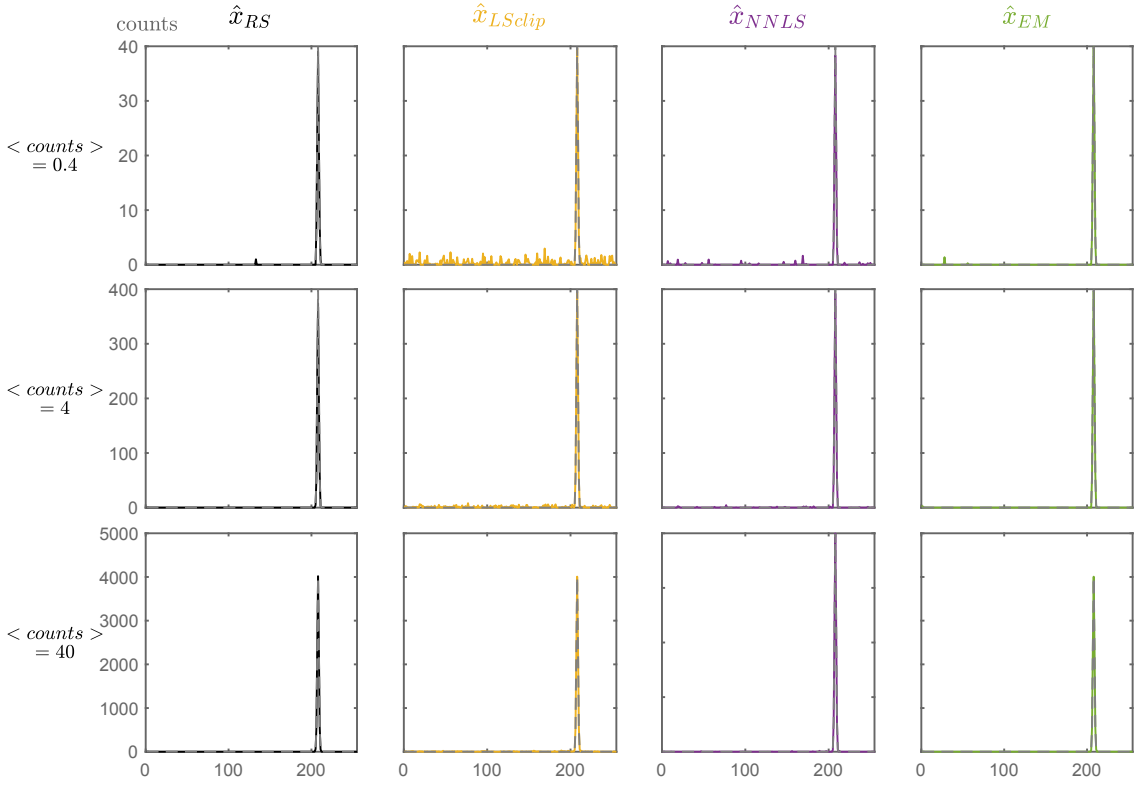


FIGURE 6.12: Examples of estimations for object D for three signal levels and different estimations.

### 6.4.5 Effect of the estimation algorithms on the variance and bias

Last, we investigate the effects of the mentioned estimators on the variance and bias. The MSE combines both variance and bias ($MSE = var + bias^2$). We saw that the variance could be reduced through the use of positivity constraints, but this can be at the expense of an additional bias.

Fig. 6.13 illustrates the effect of all the estimators for the 4 objects at an average flux of 4 counts per pixel. At this low flux, the estimators reduce the variance as compared to LS by acting on the potential estimated negative values, but do not act on the brightest regions of the object. For sparse objects C and D, more negative values are likely to be estimated, and the estimators EM and ST perform best at reducing the variance on the zero-valued pixels. Concerning the absolute value of the bias, it is in general increased as compared to LS. LS-clip increases the bias on the background pixels while maintaining it low on the peaks (Fig. 6.13 (b, c, d)). NNLS reduces even more the bias on the background pixels but leads to an increase of the bias on the peaks : this effect is mostly noticeable on Fig. 6.13 (d).

In all, simply removing negative values (LS-clip) obviously increases the bias on the background but does not bias the estimation on object peaks. Conversely, as compared to LS-clip, NNLS, EM and ST show a limited bias increase on the background but add bias on object peaks. For sparse objects, we notice a higher bias due to NNLS, but this should be investigated more, and expect EM/ST to perform better. Finally, EM and ST seem to offer the best compromise when the object is sparse, but at the expense of computational complexity.

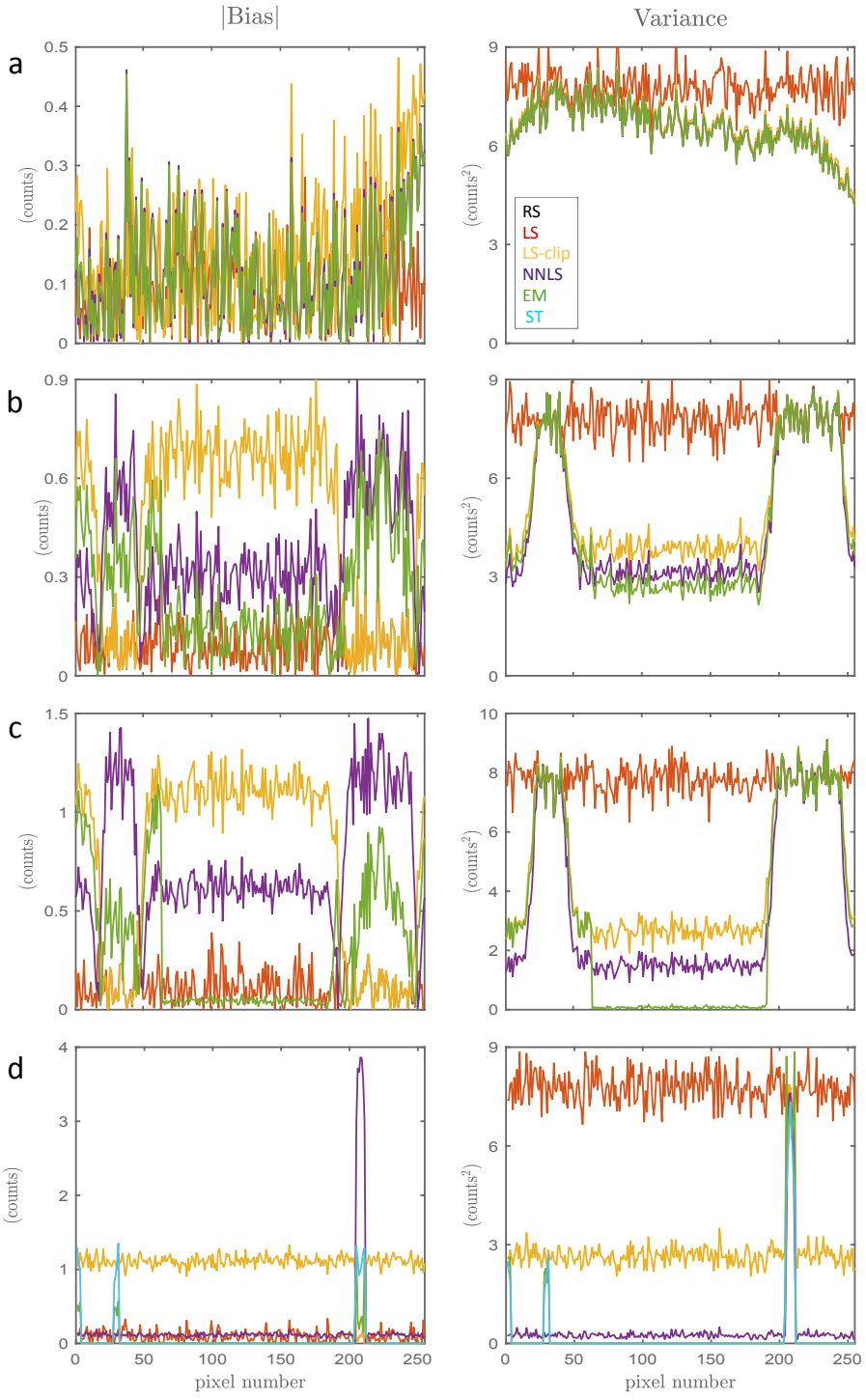


FIGURE 6.13: Effect of the estimators on the absolute bias and variance for the 4 objects (mean number counts / pixel = 4). Alternative estimators reduce the variance as compared to LS (right) but may introduce some bias. LSclip leads to a significant bias increase on the background. NNLS moderately increases the bias on the background but seems to increase it a lot on the peaks when the object is sparse (d). EM probably leads to the best compromise.

### 6.4.6 Conclusions of the simulations

In this section, we simulated the effect of S-multiplexing as compared to raster-scanning, when the measurements are shot-noise limited and in the context of quantitative estimation. Simple simulations considering a simple physical model and fixed sampling were performed. They were carried on 4 types of 1D-objects exhibiting various structures.
The simulations confirm the theoretical derivations which suggested a global S-multiplexing disadvantage - when the error is averaged over the whole object: S-multiplexing leads to an average MSE twice as worse as with raster-scanning, regardless of the object. This corresponds to a loss in estimation SNR of $\sqrt{2}$. This is due to an error spread arising from the shot-noise properties, the multiplexing matrix and the estimation. A more detailed analysis of the distribution of the MSE over the object indicates that S-multiplexing actually reduces the error on object regions at least twice as bright as the object mean signal, and degrades it on regions dimmer than this value.
The effect of alternative estimators to least-square estimation was also studied. It seems limited when the object is not sparse or background-free. However, for sparse objects, the alternative estimators can bring a substantial reduction of the error on the null pixels and thus help mitigate the S-multiplexing disadvantage. Yet, while the LS-estimator is unbiased, the others may bring a bias. When the object is relatively sparse, we surmise the algorithms based on the Poisson noise model to offer the best compromise.

## 6.5 Experimental results

In the following, we present experimental results that confirm the above simulations. Experiments are performed on the setup described in Chapter 2 which is well-suited for the purpose. We exploit the setup versatility (Fig. 5.1) to compare raster-scanning and S-multiplexing:

- In the Spectral Domain (Fig. 5.1 (a)). The Compressive Raman spectrometer can raster-scan or multiplex Raman spectra. When raster-scanning the spectrum with the DMD, it is equivalent to a monochromator with a moving exit slit: each wavelength bin is measured sequentially onto the detector. The width of the exit slit is defined by the pixel binning along the DMD spectral axis. When S-multiplexing the Raman spectrum, it is equivalent to a monochromator with a coded-aperture, which sequentially measures combinations of wavelengths.
- In the Spatial Domain (Fig. 5.1 (c)). A line illumination is formed at the sample plane to line-scan the sample. The line focus is imaged onto the DMD and raster-scanned or multiplexed onto the DMD plane.

### 6.5.1 General methodology

In each of the two dimensions (spatial and spectral), we compare raster-scanning and S-multiplexing. Raster-scanning is performed by turning on each DMD pixel one-by-one, and S-multiplexing is performed by displaying each S-matrix row sequentially onto the DMD.

**Excitation power and integration time**

The experiments are carried at constant integration time and irradiance for raster-scanning and S-multiplexing. The maximum excitation intensity we can use is limited by the linearity of the detector response: The PMT is linear to approximately $10^6$ counts/s. To ensure the counts linearity, we set the maximum count-rate to about $5\times10^5$ counts/s. Since multiplexing leads to much higher count rates than raster-scanning, it is the multiplexing experiment that limits the maximal excitation power. Once the later is set, the integration time is chosen to have enough counts in raster-scanning: considering the low powers used, the integration times in this sections are relatively long, of the order of 10 ms per pixel.

**Number of measurements**

The experiments are carried at constant sampling: data is acquired with same number of measurements for raster-scanning and S-multiplexing. The number of measurements is dictated by the binning of the DMD mirrors. In the spectral domain, we choose the binning to match the spectral resolution: the 1024 mirrors are binned 8-by-8, which results in 128 effective pixels. The Identity matrix and S-matrix are thus of size $127\times127$ ($M = 127$). In the spatial domain, we choose $M = 511$ to reach a spatial resolution along the line of $\approx 1.2$ $\mu$m.

All the measurements are repeated a number of times in the exact same configurations, to be able to calculate means and variances. Regarding the long integration times, the number of realizations is relatively low (between 10 and 50 realizations).

Theoretical derivations and simulations mainly focused on the MSE as a figure-of-merit (6.2.4). Experimentally, we consider that we do not have access to the ground-truth seeing the small number of realizations. Since we expect the differences between raster-scanning and S-multiplexing performances to be subtle, we do not want to favour one or the other with some potential experimental bias. We thus exclusively present variance results in this section, which we believe are informative enough for the purpose. Actually, even when considering an imperfect ground-truth, the experimental MSE results are consistent with the simulation results and no detectable bias seems to arise.

**Noise model**

We already verified in 2 that, in the considered experimental system, the measurements follow Poisson statistics (Fig. 2.4). In these experiments, the system was slightly modified and the objective different, so we have to make sure that the experimental physical model matches the theoretical model used (6.2.2).

Controllable sources of spurious noise are cancelled (computer screen, LEDs from the DMD, etc). In addition to the detector dark-noise, we measured some noise that does not arise from the sample: there is Raman signal coming from the objective. It arises in both line-focus and point-focus setup configurations. It is linear with the excitation intensity and integration time: this unwanted Raman signal follows the same statistics and dependence as the photon-noise coming from the sample. It also experiences the multiplexing matrix. A more realistic experimental model thus writes :

$$\mathbf{b} = Poisson(\mathbf{A}(\mathbf{x} + \mathbf{r}) + \mathbf{g}) \tag{6.32}$$

where $\mathbf{A}$ is the multiplexing matrix to be displayed on the DMD (S-matrix), $\mathbf{x}$ is the object, $\mathbf{r}$ is the Raman background present along the optical path mainly arising from the objective, and $\mathbf{g}$ accounts for the detector dark noise ($\approx 10$ counts/s). These sources of noise are measured and taken into account. Yet, in the experimental conditions of the present study, they are relatively negligible ($r_i \leq 1$ count per pixel, and $g_i \approx 0.01$ count).
We additionally performed preliminary simulations to study the influence of such a relatively homogeneous background source $\mathbf{r}$: the results seem to follow the same general trends as for pure shot-noise limited data, but the threshold values (6.4.3) of advantage/disadvantage of S-multiplexing over raster-scanning will be modified, at the expense of S-multiplexing. Indeed, in our setup configuration, the background-noise is multiplexed, so each S-multiplexing measurement is polluted with approximately half of the total background noise. The simulations are not shown because the results are too preliminary.

### 6.5.2 Spectral Multiplexing

In this section, 1D S-multiplexing is performed to measure the Raman spectra of two types of liquid samples.

#### Method

We use a point-focus to illuminate a static sample (Fig. 5.1 (a)). In this configuration, there is no spatial selectivity: only the spectral axis $\lambda-$axis of the DMD is used. The DMD pixels are fully binned along its spatial axis (x$-$axis). We measure the Raman spectra of two different samples based on DMSO (Dimethyl Sulfoxide - 99.9%, Sigma-Aldrich):

- Pure DMSO (Fig. 6.14 (a)) placed in a spectroscopic cuvette. The laser power at the sample plane is about 1.2 mW (irradiance $\approx 3.3 \times 10^{-3}$ W/$\mu$m$^2$). The exposure times are set to 5 ms per measurement. Each measurement was repeated 10 times.
- Polluted DMSO (Fig. 6.14 (c)): Pure DMSO placed on a glass coverslip and surrounded by a latex spacer : after some time, the spacer content slowly diffuses into the solvent. This results in polluted spectrum with high background. The laser power at the sample

plane is about 0.2 mW (irradiance $\approx 5.8 \times 10^{-4}$ W/$\mu$m$^2$). The exposure times are set to 10 ms per measurement. Each measurement was repeated 10 times.

The Raman spectra of these two samples (Fig. 6.14) correspond to simulated objects of types B, and mixed A/B, respectively (Fig. 6.4). Since the simulations indicated that, for these non-sparse objects, the 4 estimators gave similar results to the least-square estimator (LS), we only show results with LS estimation.

**Results**

Fig. 6.14 shows the mean of 10 acquired spectra of Pure DMSO and Polluted DMSO. The pure DMSO spectrum (a) exhibits 5 peaks of different brightness and a positive background. The polluted DMSO spectrum exhibits the same peaks but a stronger background: the peaks stand out less clearly from the background. The spectra acquired with raster-scanning and S-multiplexing are in good agreement. For both RS and LS, the mean number of counts per spectral basis ($\overline{<\hat{x}>}$) is $\approx 10$ for Pure DMSO and $\approx 23$ for polluted DMSO.

The variances results (Fig. 6.14 (b),(d)) are in agreement with the MSE theoretical predictions and simulations. We do not have access to the MSE but raster-scanning and least-square should not introduce bias. The variances corresponding to raster-scanning follow the object shape and its average is equal to the mean. The variances corresponding to S-multiplexing with LS are approximately uniform and their averages are equal to twice the objects means (within the error bar at $3\sigma$). This is consistent with the predicted degradation of the average MSE by a factor of 2 when S-multiplexing (Eq. (6.23) - (6.25)).

The rule of thumb results (6.4.3) are also confirmed by these experiments. For Pure DMSO, the S-multiplexing variance (Fig. 6.14 (b)) is clearly lower than the RS variance on the 3 brightest peaks (brighter than $\approx 20$ counts), while it is similar or higher on the rest of the spectrum. Similarly, for polluted DMSO, the variance seems degraded on the dimmest peaks, more realizations should be done for clearer results.
These results clearly translate when superimposing the 10 estimates (Fig. 6.15). The brightest peak of Pure DMSO appears more noisy in raster-scanning (a) than in S-multiplexing (b). Conversely, S-multiplexing distinctly introduces more noise in the background. The results on the dim peaks are not so clear due to the small number of realizations. We note that S-multiplexing undoubtedly degrades the SBR. For polluted DMSO, the three dimmest peaks are distinguishable in the raster-scanned version, while quasi-embedded into the noise with S-multiplexing.

Thus, although these results could be improved with stronger statistics, they are consistent with the theoretical predictions and the simulations. They also help to realize that, even though S-multiplexing is slightly disadvantageous when averaged over the whole object, it can lead to

non-negligible improvement on bright regions as well as critical degradation on dim regions, embedding peaks of interest into noise. It also leads to a SBR deterioration.

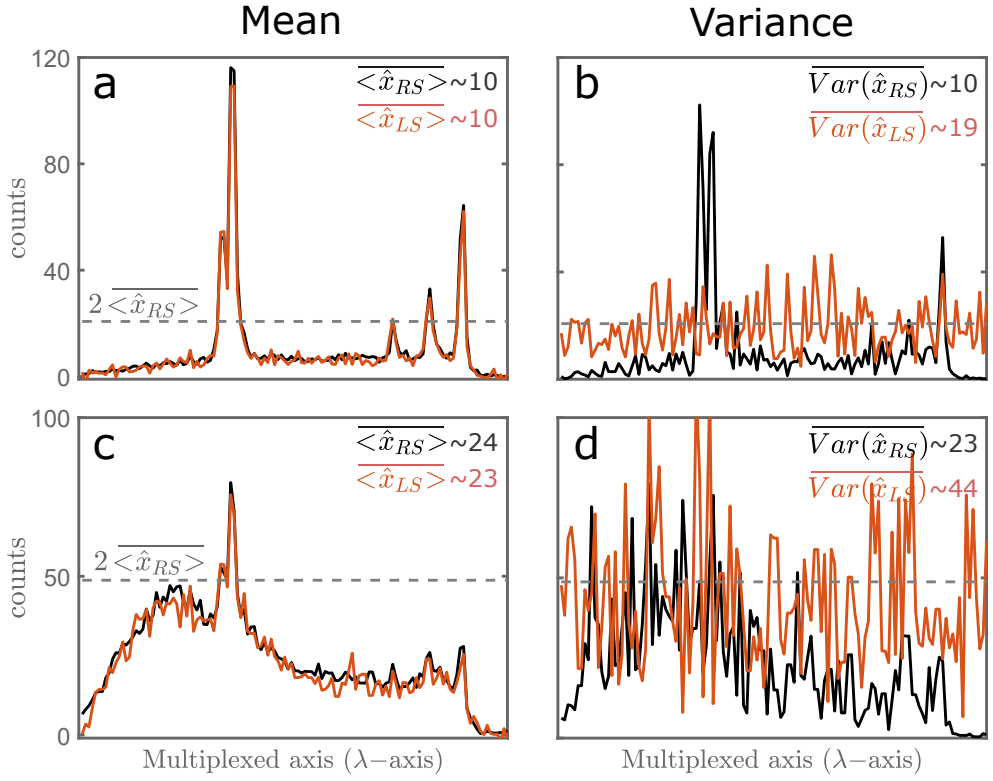


FIGURE 6.14: Mean spectra of pure DMSO (a) and polluted DMSO (c), and their respective variances. The average S-multiplexing (with LS) estimation variance is twice higher than the raster-scanning variance, but is lower on the brightest regions of the spectra. Results are based on 10 realizations.

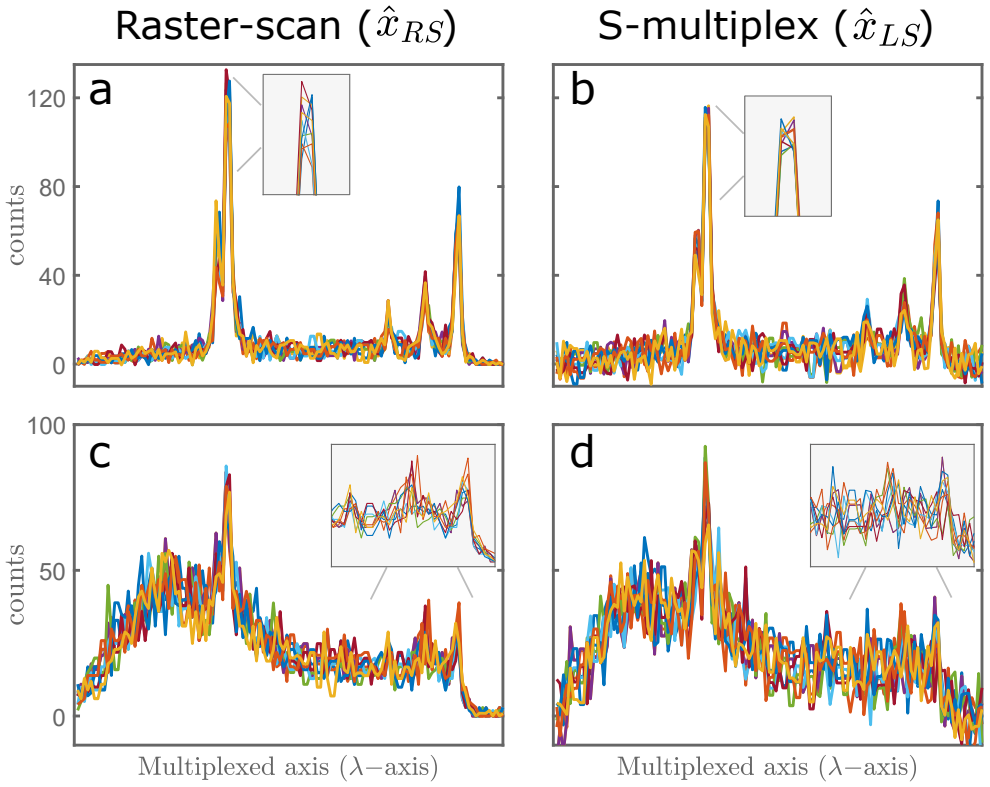


FIGURE 6.15: Superposition of the 10 realizations of raster-scanning and S-multiplexing with least-square estimation, for pure DMSO (a,b) and polluted DMSO (c,d). High intensity spectral bases are less noisy with S-multiplexing (b) while the background noise is enhanced. S-multiplexing embeds the dimmest peaks of polluted DMSO into the background noise (d), whereas they were distinguishable in the raster-scanning results. Furthermore, S-multiplexing degrades the SBR in both cases.

### 6.5.3 Spatial Multiplexing

In this section, 1D S-multiplexing is performed to measure Raman line images (with no spectral selectivity) of two types of samples.

#### Method

We use a line-focus to illuminate a sample (Fig. 5.1 (c)). The line illumination is imaged onto the DMD plane, along the DMD x$-$axis. We acquire Raman images with no spectral selectivity: all the Raman wavelengths are integrated onto the detector. The DMD pixels are thus fully binned along its spectral axis ($\lambda$-axis). The sample is mounted onto a piezoelectric stage scanner which scans the object y$-$axis, yielding 2D images.
The two samples consist of three types polymer beads (30 $\mu$m polystyrene (PS), 20 $\mu$m polymethylmethacrylate (PMMA), and 12 $\mu$m melamine resin (MR)) displayed in two different manners:

- The sparse sample (Fig. 6.16 (a)) consists of a few beads of each type displayed onto a $CaF_2$ coverslip. Since the coverslip hardly gives any Raman signal and since only a few beads are present along the multiplexed line, the sample is considered as relatively sparse.
- The denser sample (Fig. 6.16 (b)) consists of more beads displayed onto a glass coverslip. The glass exhibits Raman signal and more beads are present along a multiplexed line.

The total laser power along the line at the sample plane is about 3.6 mW (irradiance $\approx 1.1 \times 10^{-5}$ W/$\mu$m$^2$) and the integration time 10 ms per measurement. Each measurement is repeated 50 times. The spatial resolution along the scan axis is $\approx 1.4$ $\mu$m, and the piezo-scanner scans this axis by steps of 1 $\mu$m, over 65 $\mu$m. The DMD pixels along the x$-$axis are binned 2-by-2, which corresponds to a spatial resolution of about 1.2 $\mu$ along the line. The effective FOV along the line is about 220 $\mu$m, which on the DMD plane only represents 1/3 of the entire DMD size. We should have used only the DMD height corresponding to this FOV, but we used the whole DMD height instead. This requires more measurements but also artificially favours multiplexing by lowering the effective object mean. In this configuration, the sparse sample contains a maximum of 70 non-zero pixels (out of 511 pixels) along its multiplex axis; while the denser sample contains a maximum of 240 non-zero pixels. In the figures below, we crop zeros at the top and bottom of the images for visualisation purposes, but one should keep in mind that the samples are more sparse than what is suggested by the images.
In this section, we show the results for raster-scanning and S-multiplexing with estimations based on LS-clip, NNLS and EM. Indeed, (i) we already showed experimental LS results in the spectral domain and (ii) simulations suggested that these other algorithms could bring improvement over LS-estimation for sparse objects or objects containing zeros, which is the case here.

**Results**

Fig. 6.16 shows the estimated images from one single measurement. For the sparse sample (a), S-multiplexing clearly reduces the noise on the beads as compared to the raster-scanned measurement. However, the LS-clip estimation results in a noise spread along the multiplexed axis. As expected, this noise is higher on the denser lines than on the lines where there is a single bead. The use of the positivity constraint reduces this noise, with more efficacy for EM than NNLS. The EM estimation of the background even seems slightly better than raster-scanning (even if it is extremely low, at these very small number of counts the DMD OFF-order probably contributes to this small noise - less than 1 count - on the raster-scan measurements). For the denser sample (b), the interpretation of this single measurement is not trivial. The brightest beads seem slightly more noisy in raster-scanning than with S-multiplexing, and the results of the three estimators seem comparable. The signal in between the beads is the Raman signal from the glass coverslip. These results are also confirmed by Fig. 6.17, which shows cross-sections of the 2D images at two positions along the y$-$axis.

Fig. 6.18 shows the variance of the estimations. The variance of the raster-scanned measurements follows the objects shapes. For the sparse sample (a), the variance associated with S-multiplexing is smaller on the beads while it is higher on the background. Again, NNLS and EM help reducing the variance on the zero-background. This appear more clearly in the cross-section variance figures (Fig. 6.19 (a-b)): The raster-scanning variance is considerably higher than with S-multiplexing on the beads, and this difference is higher as the number of beads along the multiplexed line decreases (Fig. 6.19 (a-b)). The variance associated with LS is not shown but again found to be uniform along each line. For the denser sample, the variance associated with S-multiplexing is quasi-uniform over the sample, and NNLS or EM lead to a variance reduction on null pixels. The cross-section plots (Fig. 6.19 (b-c)) show S-multiplexing leads to a slight variance reduction on bright pixels and to a slight variance increase on the glass background.

Overall, these results in the spatial domain are consistent with the previous conclusions. They confirm that for sparse objects, great improvement can be obtained with S-multiplexing on bright pixels, and that the background noise can be considerably reduced by including positivity constraints in the estimation. For denser objects, the advantage is limited and depends on the different species brightness and on the sample composition along the multiplexed line. We note that the presented results tend to favour multiplexing since we do not multiplex only the DMD pixels corresponding to the effective FOV but rather the entire DMD, thereby introducing more zeros and rendering the samples more sparse.

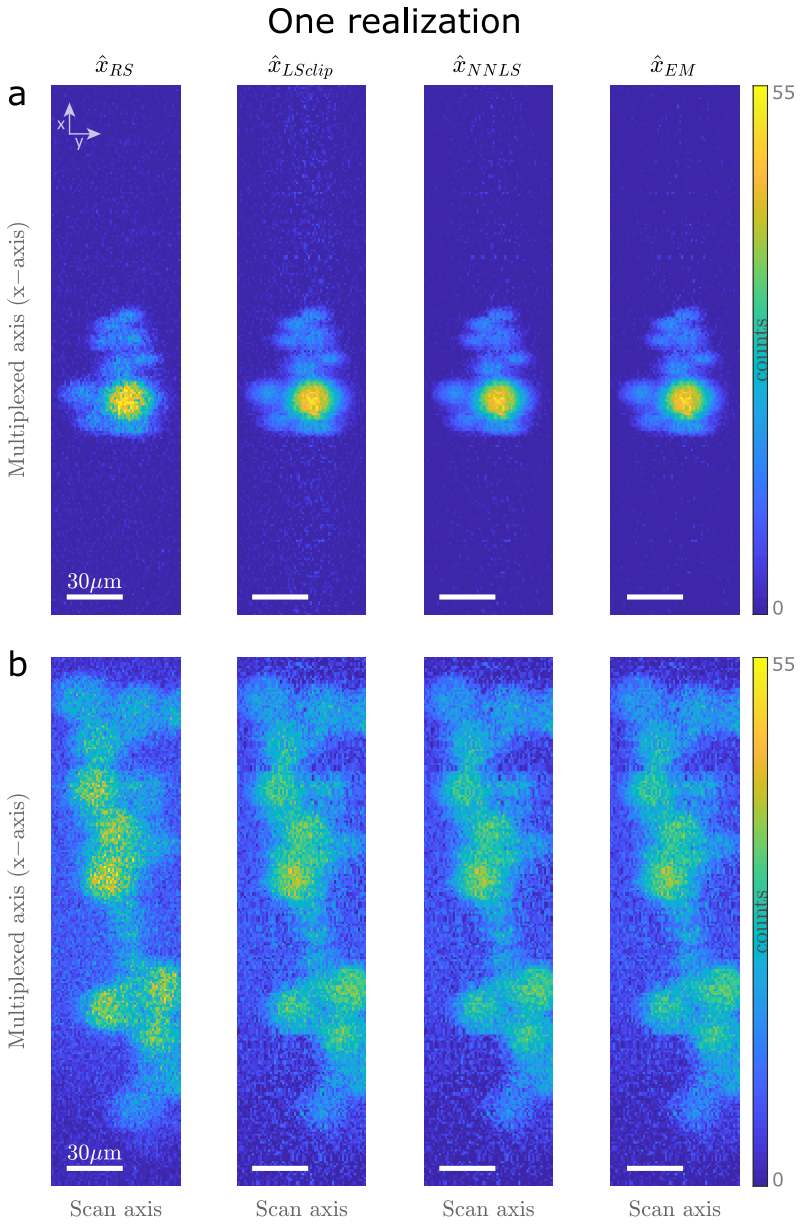


FIGURE 6.16: Estimated objects after one measurement, in raster-scanning and S-multiplexing with different estimators. Only 270 $\mu$m out of 511 are shown along the multiplexed axis. (Top - sparse sample): S-multiplexing decreases the noise on the beads and LS estimation spreads the noise along the multiplexing axis. Estimators with positivity constraints mitigate this noise spread. (Bottom - denser sample): The effect of S-multiplexing is not as neat as for the sparse sample.

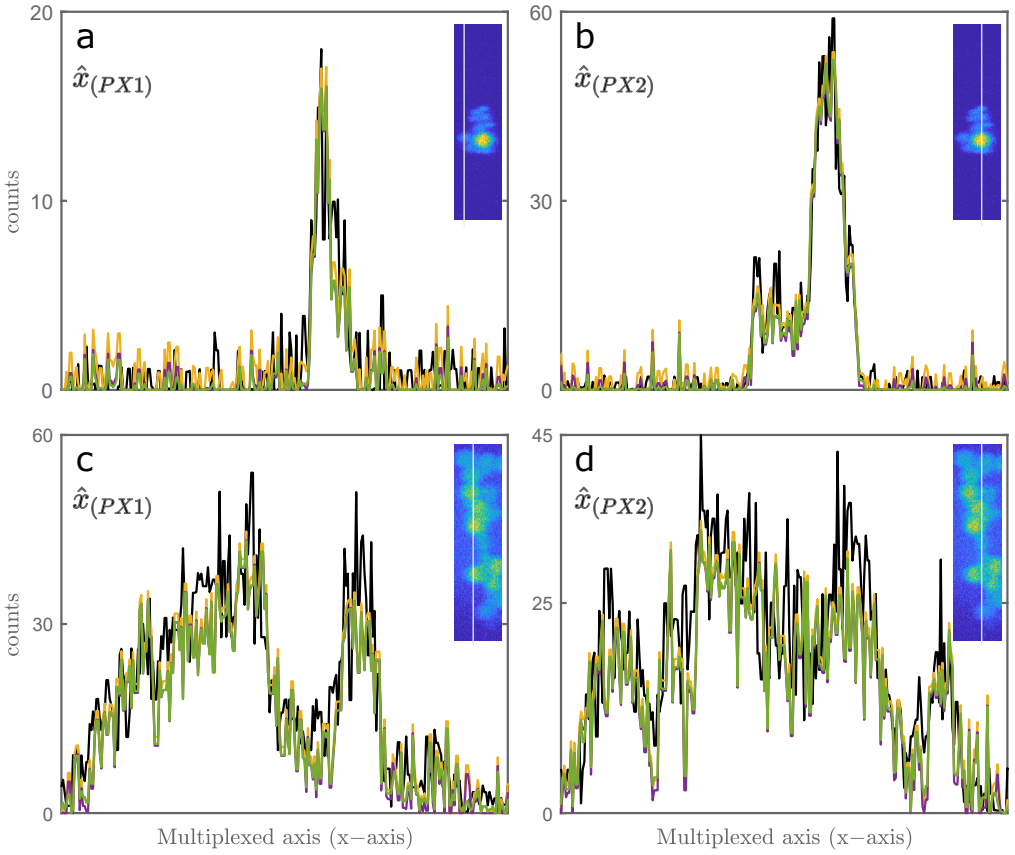


FIGURE 6.17: Cross-sections along the multiplexed axis of the estimated objects after one measurement (Top - sparse sample, Bottom - denser sample). The estimations from S-multiplexing retrieve the raster-scanning estimation. The same color code as in the rest of the chapter is used for the estimators : RS, LSclip, NNLS, EM.

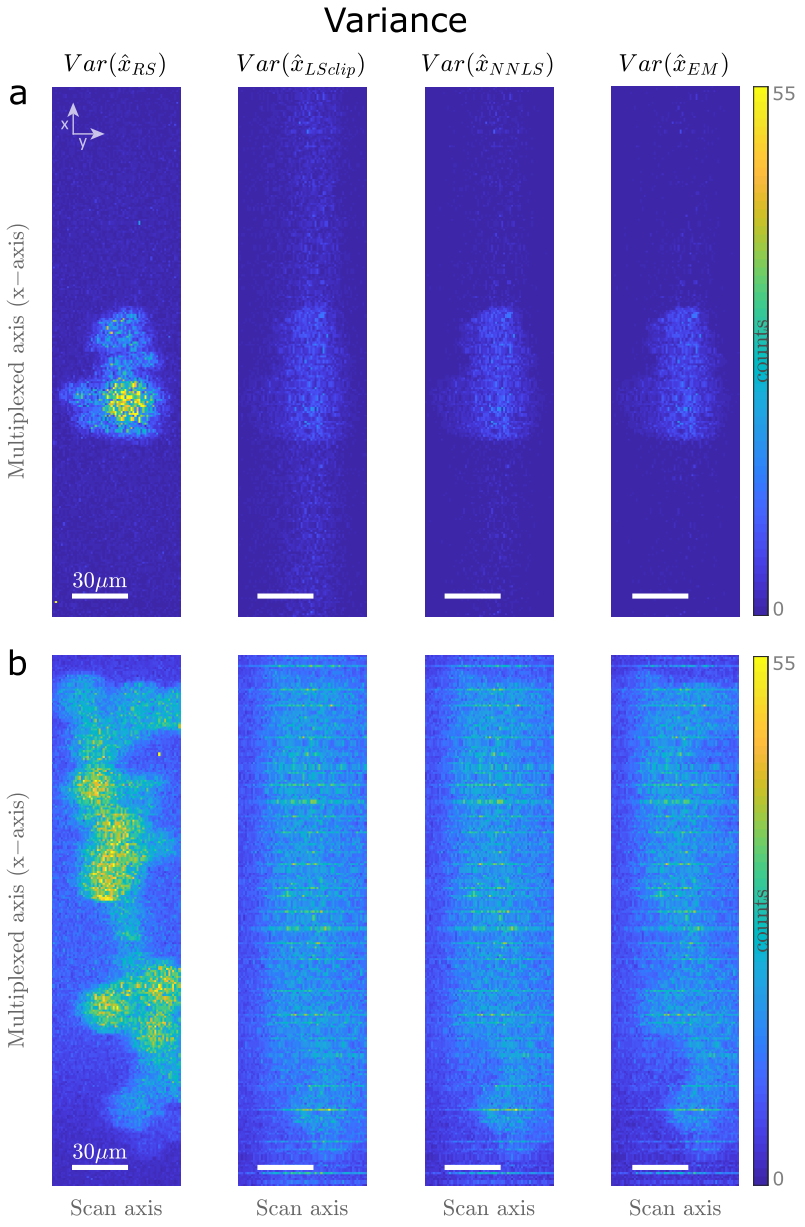


FIGURE 6.18: Estimation variances calculated from 50 measurements. Only 270 $\mu$m out of 511 are shown along the multiplexed axis. (Top - sparse sample): S-multiplexing decreases the variance on the beads and LS estimation spreads the noise along the multiplexing axis. The object shape is slightly retrieved with LS-clip because the zeros are removed, but we retrieve a uniform variance along each multiplexed line with pure LS estimation (not shown). Estimators with positivity constraints mitigate this effect. (Bottom - denser sample): The variance is quasi-uniform though NNLS and EM help reducing it on null pixels at the object borders.

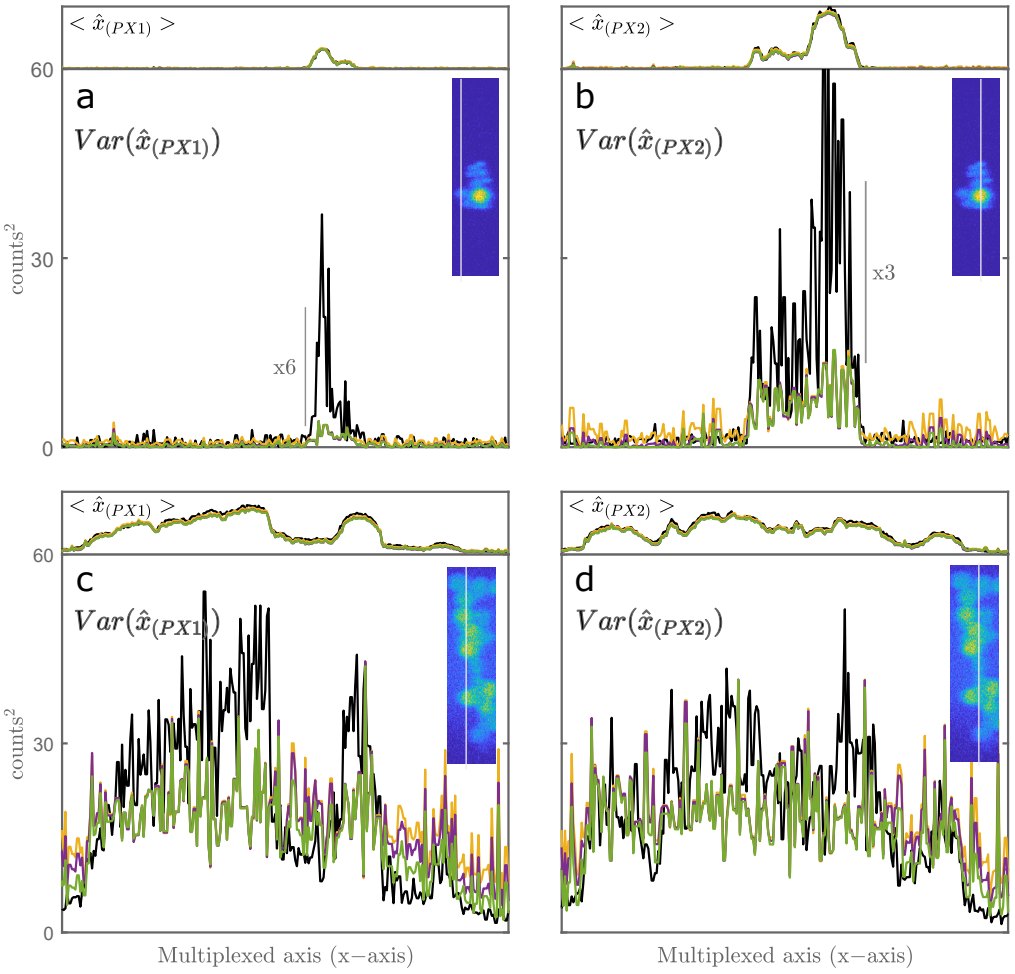


FIGURE 6.19: Cross-sections along the multiplexed axis of the estimation variances. (Top - sparse sample): S-multiplexing decreases the variance by ≈ 6 times on the brightest pixels of the line containing only one bead (a). When the line is denser (b), it decreases the variance by ≈ 3 times on the brightest pixels and increases it on the background. (Bottom - denser sample): Any change in the variances are limited due to the denser nature of the sample. It is slightly improved on bright beads and slightly degraded on the glass background or on very dim beads. The same color code as in the rest of the chapter is used for the estimators: RS, LSclip, NNLS, EM.

### 6.5.4 Conclusion of the experimental results

The results from 1D raster-scanning and S-multiplexing experiments, performed in both the spectral and spatial domain, are in agreement with the theoretical derivations and simulations. They show cases where S-multiplexing is advantageous, not particularly useful, or even disadvantageous, as compared to raster-scanning. They are to our knowledge the only available experimental results for shot-noise limited data, at least in this community.
Yet, they could be improved for instance by: (i) increasing the number of realisations for more statistical robustness, (ii) using the DMD only over a relevant FOV, (iii) including a comparison with a spatially focused beam instead of artificially raster-scanning a line-focus. In addition, we

noticed some systematic and periodic artefacts on the images and spectra, probably due to some model mismatch and yet unidentified technical issues. So far, this was removed in a processing step but should be better studied in the future.

## 6.6 Conclusion and discussion

### 6.6.1 Conclusion

In this chapter, the effect of S-multiplexing on SNR, as compared to raster-scanning is investigated, in the context of shot-noise limited measurements and quantitative estimation.
Theoretical derivations and simulations show a global S-multiplexing disadvantage over raster-scanning, when the error is averaged over the whole object. S-multiplexing leads to an average MSE twice as worse as with raster-scanning. This corresponds to a loss in SNR of $\sqrt{2}$, and is due to the noise properties, the multiplexing matrix and the estimation method.
The average MSE is an interesting figure-of-merit, but is not sufficient to compare S-multiplexing with raster-scanning. A more detailed analysis of the distribution of the MSE over the object indicates that S-multiplexing reduces the error on object bright regions and increases it on dim parts. More precisely, it reduces the error on object regions at least twice as bright as the object mean signal, and degrades it on regions dimer than this value. We also saw that including positivity constraints into the estimation can, in some cases, help mitigating the S-multiplexing disadvantage and bring a substantial reduction of the error on dim pixels, at the expense of an increased bias. Finally, we show simple experimental results that confirm the theoretical and numerical predictions.

Altogether, these results show that the choice of raster-scanning or S-multiplexing, as well as the choice of the estimation strategy, depends on the nature of the object and on the user's interest (e.g. quantitative estimation, detection, contrast). We sum up the few investigated case in Table. 6.1. For relatively homogeneous objects, raster-scanning should be preferred over S-multiplexing. Otherwise, for inhomogeneous objects exhibiting some peaks, S-multiplexing favours bright pixels, and the brighter the pixels, the more S-multiplexing is advantageous for them. Therefore, S-multiplexing may bring a great advantage over raster-scanning for sparse objects, to perform quantitative estimation on the main object peaks, and probably to localize bright peaks. However, at extremely low flux, raster-scanning may still be preferred to localise peaks since no noise is introduced on the background. Furthermore, if the user is seeking to optimize the contrast, or if quantitative estimation is equally important over all the object pixels, raster-scanning should be preferred over S-multiplexing. Last but not least, S-multiplexing should *not* be used for objects composed of peaks of very different brightness or for dim species embedded into a bright background. Indeed, the error increase on faint parts could lead to bury a dim peak into the the photon-noise of the bright ones.

Experimentally, S-multiplexing could for instance be advantageous to image sparse fluorophores of comparable intensities with low background, or to record very sparse Raman spectra with low background and with spectral lines of similar intensity. However, as soon as there are dim peaks, some fluorescence background, or imperfectly removed Rayleigh line, it would present a disadvantage.

| | Quantitative estimation (everywhere) MSE | Quantitative estimation (on the peaks) MSE | Contrast SBR |
|---|---|---|---|
| Homogeneous | Raster-scanning<br>Slight S-multiplexing disadvantage | - | - |
| Peaks-structure, low-background | Raster-scanning<br>S-multiplexing increases error on background and reduces it on peaks | S-multiplexing<br>S-multiplexing substantial advantage on bright and/or sparse peaks | Raster-scanning |
| Peaks-structure, very different brightnesses | Raster-scanning<br>S-multiplexing may bury dim peaks into noise | Raster-scanning<br>S-multiplexing may bury dim peaks into noise | Raster-scanning |

Table 6.1: Preferred choices between S-multiplexing and raster scanning for a few classes of objects and figures of merits. -: not applicable.

### 6.6.2 Discussion and perspectives

To begin with, we would like to emphasize that the study was carried at fixed integration time and laser power. We tried to counterbalance the intuition that "since multiplexing gives more photons, one needs to integrate shorter times". Indeed, we saw that, at *fixed integration times*, S-multiplexing leads to higher number of photons than raster-scanning, but to higher errors on the estimated object. The error is already worse with more photons: decreasing the integration time associated with S-multiplexing would simply degrade its performances even more. A similar reasoning can be applied to laser-power. Therefore, associating less integration time or laser-power to S-multiplexing as compared to raster-scanning - i.e. carrying the study with a fixed number of detected photons - would just degrade more the performances of S-multiplexing. Nevertheless, such an approach can be interesting in some cases: if S-multiplexing improves the MSE by $p$ times on one peak of interest, one could apply $p$ times shorter exposures or $p$ times less power

than for raster-scanning. But this only works if only the bright peaks on an object are of interest.

This study was conducted in a specific context, within a relatively narrow framework and on simplistic examples. The fact that the results are object-dependant make general conclusions difficult to draw. The study leads to many questions, and many other directions could be investigated. First, the impact of a more realistic physical model should be studied, in particular the impact of the PSF and of the sampling. Other effect such as other sources of noise (e.g. source fluctuation noise) or non-linear optical contrasts (e.g. Coherent Raman imaging) could also be investigated.
Second, the study could be broaden to other types of multiplexing, that would be very interesting to study and compare, both numerically and experimentally [219]. From some calculations, simulations and reading [52], we surmise that the results would be similar (to a multiplicative factor) for other types of multiplexing with positive values such as Cosine-multiplexing. But our conclusions do not hold for multiplexing with negative values or phase multiplexing for instance.
Third, other estimation strategies including sparsity constraints could be considered. Although the $l1$-norm constraint may bias the estimation quite strongly and give poor MSE performance, it may bring great improvement for localization purposes: it would preferably be used to detect some peaks and their shapes rather than their quantitative value. We note that the $l1$-norm could still be used in combination with LS-estimation to correct for the bias but this is beyond the scope of the study.
Last, it would be very interesting to relate this study to the field of compress-sensing (CS), since it would enable to acquire data sampled at sub-Nyquist and thus fasten the acquisition. It seems that most derivations and algorithms related to compressive sensing are actually based on additive white Gaussian noise models, athough single-pixel cameras systems are used in practise (thus with shot-noise limited measurements). Raginsky et. al. derived performance bounds of CS under shot-noise limited data and found less encouraging results than with the usual additive white Gaussian noise [248]. Thus improvement could surely be brought by CS but may be limited for linear optical systems operating in the shot-noise limit.

While the present study may bring some insights on which acquisition strategy implement for a particular purpose (e.g. parallel, raster-scanned or multiplex measurements - see 1.2.1), it should be connected with technological aspects. Indeed, one should keep in mind that the SNR is not the only bottleneck of an optical system. For instance, recording neuronal activity requires speeds faster than 10 ms, so any system slower than this, even with much better SNR, is useless. Some technological aspects to be consider include speed and cost. Even when S-multiplexing is disadvantageous in terms of SNR, it can present advantages in terms of speed - if it makes use of technology allowing shorter integration times than the raster-scanning technology - or in terms of cost. For example, in imaging, fast light modulators combined to compress sensing can bring significant speed improvement over raster-scanning and reduced costs. Some crucial concerns lie in the speed of spatial light modulators or in the sensitivity and dynamic-range of detectors. We also expect the advent of high speed and high fill-factor shot-noise limited

detector-arrays to be a game changer in the field. Indeed, the previous conclusions only hold when the information is completely multiplexed, i.e. is all mixed into one single-pixel detector. Instead, mixing the information into a few-pixel-array of shot-noise limited detectors would immediately mitigate the disadvantage, since the loss of average MSE is only of 2. Nevertheless, it would depend on how the signal distribution on the detector pixels is achieved. In all, we surmise that a 'few-pixel-camera' allowing shot-noise limited detection is probably one of the best options to achieve significant S-multiplexing advantages on most object classes.

We conclude this study with a final word on its intrinsic link with compressive Raman. CRT is a particular case of the multiplexing scheme presented above: it performs multiplexing in the spectral domain, with a binary matrix. The crucial difference is that, in CRT, *a priori* information is held: it permits to design a multiplexing matrix optimised for a particular problem. The other difference is that CRT seeks to estimate chemical species proportions rather than number of photons. In the CRT results presented in this thesis, we did not include any constraints on the estimate. This allowed us to show that the LS estimator is efficient for our problem, and to derive some interesting properties on the problem intrinsic precision. Nevertheless, in practise, the proportions are positive. Therefore, the estimators presented in this chapter (6.2.5) could be useful, especially when the object is sparse in the proportion space, i.e. when some pure species are present in the sample. In these cases, they may help reduce the variance of the estimation, at the potential cost of a bias. Such an analysis is reported to future work. Yet, when estimating the proportions of the same beads as in Fig. 4.6 with NNLS or EM instead of the usual LS (with zero cropping), we noted that it reduces noise from the PS beads that appeared in the estimation of the dimmest beads (PMMA). This should be investigated in detail in the future as it could be beneficial in some cases.

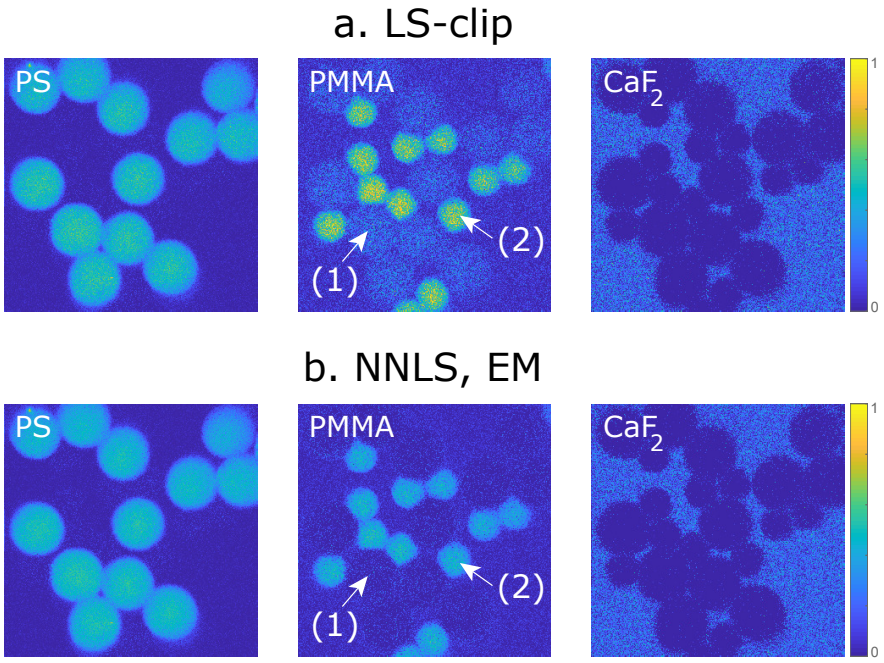


FIGURE 6.20: Estimated proportion maps of PS, PMMA and $CaF_2$, obtained with CRT estimations based on (a) LS-clip and (b) NNLS. The results with LS-clip are the same as in Fig. 4.6. NNLS, that gives similar results that EM on this example, reduces the noise from residual PS estimation (1) on the PMMA map. The estimated proportion of PMMA beads (2) also seems to be slightly lower.

# Conclusion and Perspectives

In this thesis, we investigated some means to perform spontaneous Raman imaging efficiently by considering a priori information, experimental noise, technological constraints, and final application specificity.

To begin with, we featured the main underlying mechanisms of spontaneous Raman scattering. We saw that this label-free and non-destructive optical contrast imprints the signature of molecules, but its extremely weak scattering cross-section hinders its efficiency. We described the conventional method to acquire Raman signal; it results in a hyperspectral image, with two spatial dimensions and one spectral dimension. We saw that this implementation is relatively simple but (i) it requires substantial acquisition times and (ii) it generates overwhelmingly large data sets. We reviewed a few alternative techniques that were proposed to mitigate these flaws, but none have yet demonstrated enough efficiency to replace the conventional systems. Next, we questioned the necessity to collect such large volumes of data: most of the time, the information of interest - extracted from the data cube via postprocessing - is low dimensional. In several cases, one even knows which chemical species are present in the sample. With the latter knowledge, and when the measurement aims to estimate the proportions these, one can use compressive Raman (CRT). Then, the measurement can be designed to directly probe quantities of interest, instead of deducing them from the complete hyperspectral data cube.

In CRT, processing is performed directly into the hardware: programmable optical filters select components of the Raman spectra, which are then combined into a single-pixel-detector. A succeeding estimation step yields chemical species proportion. CRT thus relies on both accurate hardware and signal-processing tools. Based on the physical model and noise properties of the system, we presented a simple strategy to optimize the optical filters and to estimate the species proportions. Experimentally, the measurements are limited by photon-noise: in this case, we derived a lower bound on the proportion estimation precision allowed by CRT. We showed that a simple least-square estimation is unbiased with minimal variance. This is interesting since it is fast and requires low computational cost. We validated the performances of CRT on test samples, and noted that the estimation accuracy is subject to accurate modelling of the physical system. In addition, preliminary results on complex samples indicated the usefulness of CRT on more concrete applications relevant to biomedical imaging, pharmaceutical industry, and environmental science. Employing CRT to these more complex experimental problems also allowed us to identify potentials improvements to both the model and the instrumentation.

Furthermore, we compared the performances of CRT to state-of-the-art conventional hyperspectral systems. We demonstrated fast Raman imaging with CRT acquisition speeds down to about 10 $\mu$s per pixel per spectral filter. These speeds are clearly not achievable with any conventional hyperspectral system (absolute minimum pixel dwell times of about 1 ms). We estimated the limit of detection of our CRT system to be a few tens of photons. This LOD is at the same level as state-of-the-art systems equipped with EMCCD cameras and at least ten times lower than those with CCD cameras. In addition, a CRT system does not require an expensive array detector, making it significantly cheaper than state-of-the-art hyperspectral instruments. It is also versatile: not only can it be employed for CRT measurements but also for standard hyperspectral imaging. Moreover, since the measurement is designed for a specific problem, it can be optimized to favour the estimation of certain predefined species, or to be more resilient in the presence of a given background. Finally, using a single-pixel-detector allows it to resolve fast dynamics: it opens doors to fluorescent gated Raman [128], Raman applications in diffuse optics [249], or correlation spectroscopy [250].

Evidently, the highlighted advantages of CRT hold when the chemical species present in the sample are *a priori* known. CRT will in general be sensitive to the presence of unexpected contaminants. In cases where the pure samples are not readily available or known, alternative approaches can be used [120]. Furthermore, CRT performances depend on the accuracy of the physical model and calibration step. Therefore, a sufficient knowledge of both the sample, experimental conditions and noises is required to employ this technique, which will be most beneficial as the number of chemical species is small.

Although CRT benefits should be further confirmed on more concrete experimental problems, we believe that CRT could largely benefit from several developments. First, it would benefit from a better understanding of the influence of the model on the estimation performances, e.g. on the estimation bias. In general, the impact of many parameters should be further investigated and quantified, such as the effect of the binary modulation, higher number of chemical species, or using alternative estimators to least square, that take into account physical constraints. The model could also be improved by considering various background sources as nuisance parameters [121] or by optimising the exposure time per spectral filter [133]. Secondly, implementing the spectral filters in parallel could lead to a substantial improvement in acquisition speed. A first step is to simply use two detectors (Fig. 4.2, [122]), but one could think of some technological designs to implement an array of photon counting detectors for instance.
Furthermore, CRT could be extended to the classification of chemical species. Throughout this thesis, we used an estimation-based model even when the ultimate purpose of the experiments was to discriminate species classes. Therefore, a model based on classification theory is expected to bring some improvements [181, 182, 251].
Finally, the versatility of the CRT instrument could be further exploited to explore new acquisition strategies, including cases where no spectral information is a priori known. In this thesis, we explored two spatio-spectral acquisition strategies to introduce a line-scanning modality to CRT, via spatial multiplexing. In some situations, this second layer of multiplexing brings advantages

in terms of speed or signal-to-noise ratio, but the shot-noise limited nature of the measurements complicates the analysis. Line-scan CRT could especially be useful when the sample is sufficiently sparse in both the spatial and spectral domains.

To conclude, in this thesis, we have investigated some theoretical and technological aspects of compressive Raman. The results show the potential of CRT for faster, cheaper and more efficient Raman imaging, thereby encouraging to continue exploring and improving this technology.

# Appendix A

# Derivation of the Cramer-Rao lower bound for CRT

In the following we derive the Cramer-Rao lower bound (CRB) in the context of CRT. The complete model can be found in chapter 2. When the measurements are shot-noise limited, the following derivation can be adapted to full Raman spectrum measurements (3.1.1) and to the general model of multiplexing (6.2.2).

Let $n_m$ be the number of photons measured with filter number $m$. $n_m$ is a random variable and the probability law of $n_m$ can be modelled as a Poisson distribution, with mean $b_m = \langle n_m \rangle$. The probability to observe $n_m$ photons with filter $\mathbf{f}_m$ is:

$$P_m(n_m) = e^{-b_m} \frac{b_m^{n_m}}{n_m!} \tag{A.1}$$

Considering statistically independent measurements, the joint probability function, or likelihood, is:

$$P(\mathbf{n}) = \prod_{m=1}^{M} e^{-b_m} \frac{b_m^{n_m}}{n_m!} \tag{A.2}$$

The log-likelihood then reads:

$$L = ln(P(\mathbf{n})) = \sum_{m=1}^{M} [-b_m + n_m ln(b_m) - ln(n_m!)] \tag{A.3}$$

We look for the parameters $c_i$ that maximizes the likelihood to obtain $n_m$ photons. Using the CRT model, in particular $\mathbf{b} = \mathbf{Gc}$ (Eq. (2.3)), leads to:

$$L = \sum_{m=1}^{M} [-\sum_{k=1}^{Q} G_{mk} c_k + n_m ln(\sum_{k=1}^{Q} G_{mk} c_k) - ln(n_m!)] \tag{A.4}$$

$$\frac{\partial L}{\partial c_i} = \sum_{m=1}^{M} [-G_{mi} + n_m \frac{G_{mi}}{\sum_{k=1}^{Q} G_{mk} c_k}] \text{ if } b_m \neq 0, \forall m \tag{A.5}$$

$$\frac{\partial L}{\partial c_i \partial c_j} = \sum_{m=1}^{M} [-n_m \frac{G_{mi} G_{mj}}{(\sum_{k=1}^{Q} G_{mk} c_k)^2}] \tag{A.6}$$

$$\langle \frac{\partial L}{\partial c_i \partial c_j} \rangle = - \sum_{m=1}^{M} b_m \frac{G_{mi} G_{mj}}{(\sum_{k=1}^{Q} G_{mk} c_k)^2} \tag{A.7}$$

$$\langle \frac{\partial L}{\partial c_i \partial c_j} \rangle = - \sum_{m=1}^{M} \frac{G_{mi} G_{mj}}{\sum_{k=1}^{Q} G_{mk} c_k} \tag{A.8}$$

$$\langle \frac{\partial L}{\partial c_i \partial c_j} \rangle = - \sum_{m=1}^{M} \frac{G_{mi} G_{mj}}{b_m} \tag{A.9}$$

$$[\mathbf{I_F}]_{ij} = \sum_{m=1}^{M} \frac{G_{mi} G_{mj}}{b_m} \tag{A.10}$$

Or, in the matrix form, with $\mathbf{B} = diag(\mathbf{b})$:

$$\mathbf{I_F} = \mathbf{G}^T \, \mathbf{B}^{-1} \, \mathbf{G} \tag{A.11}$$

$\mathbf{I_F}$ is the Fisher information matrix, obtained through $[\mathbf{I_F}]_{ij} = -\langle \partial_{c_i} \partial_{c_j} L(\mathbf{n}) \rangle$.

We note that in the above derivation, we need $\forall m, b_m \neq 0$. A regularity condition that must be satisfied for the CRB to be valid is verified in [134], with a similar model. In addition, the **CRB** is defined for the Poisson probability law since its definition domain does not depend of the estimated parameters. The **CRB** matrix is defined as:

$$\mathbf{CRB} = {\mathbf{I_F}}^{-1} \tag{A.12}$$

When $\mathbf{G}$ is square and not singular, the CRB matrix results in:

$$\mathbf{CRB} = \mathbf{G}^{-1} \, \mathbf{B} \, \mathbf{G}^{-T} \tag{A.13}$$

We note than the maximum-likelihood estimator (MLE) estimates the parameter $c_i$ that maximizes the likelihood Eq. (A.2). With $\frac{\partial L}{\partial c_i \partial c_j} \leq 0$, it is solution of:

$$\frac{\partial L}{\partial c_i} = 0 \tag{A.14}$$

In the present case, the MLE consists in solving Eq. (A.5).

# Appendix B

# Cameras and their noise characteristics

## B.1 General description and noise properties

A CCD (charge-coupled device) is a solid-state sensor. It is based on a silicon chip structured as an array of photosensors, that convert photons into a digital signal (Fig. B.1). Incident photons with sufficient energy generate photoelectrons, which are stored in potential wells in each pixel. The electrons are then transmitted line-by-line to a serial readout register, and converted to voltage. Last, an Analog-to-Digital converter (ADC) assigns a digital value to each pixel according to this voltage, with a precision given by the number of bits of the camera.

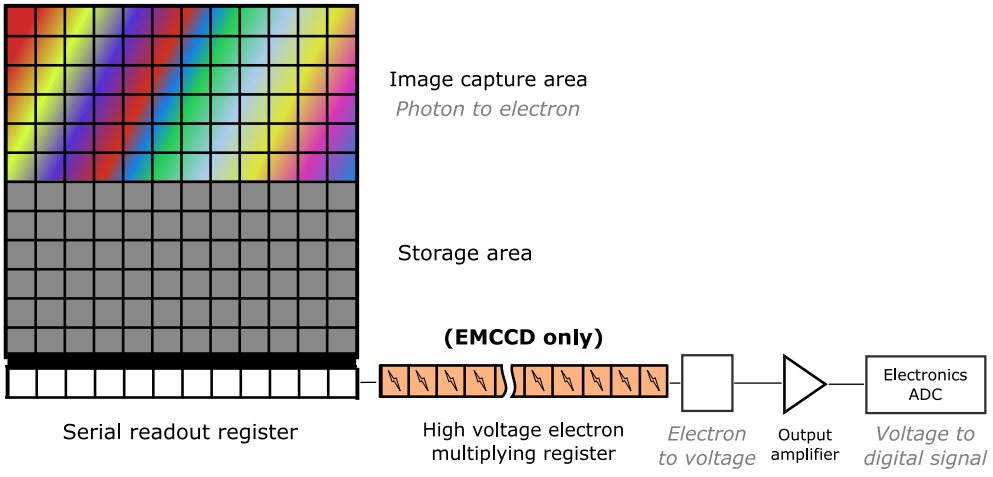


FIGURE B.1: Simplified structure of a CCD (without the multiplying register) and EMCCD (with the multiplying register). Adapted from wikipedia.

Different sources of noise may arise from this conversion process, including:

- Photon-noise, intrinsic to the photon detection

- Dark-noise, arises from thermally-generated electrons, that discharge a pixel as if a photon had hit the pixel. It mainly depends on the integration time and cooling temperature, and follows a Poisson-distribution.

- Read-out noise, includes most other sources of signal-independent noise, arising from the electronics and quantization step (quantization errors are caused by the rounding, since an ADC has a finite precision). It is generally modelled as an AWGN (additive white Gaussian noise) [252]. The readout noise scales with the readout speed, thus reading out the CCD at high speeds causes high readout noise. This noise is generally the limiting source of noise of CCDs is the low flux regime.

Other sources of noise, such as photo response non-uniformity (spatial variation in pixel output under uniform illumination), dark current fixed pattern (dark current variations from one pixel to another), non-linearities in the voltage to electron conversion, etc, could be considered for a more accurate description of the sensor noise. A complete description can be found in [252].

EMCCDs (electron-multiplying charge coupled devices) are similar to CCDs, with an additional multiplication register. This on-chip multiplication step produces a gain (EM gain: $g_{EM}$) through impact ionization in silicon. The subsequent higher number of generated charges results in a negligible readout noise, since the charge-multiplication process happens before any source of readout noise. Although this multiplication step results in a small additional noise $F$ called 'excess noise factor', (approximated to the value 1.4 [253]), the SNR of EMCCDs is dramatically improved as compared to a CCDs at low light levels (Fig.B.2). In addition, most EMCCDs can also be utilized as conventional CCDs (no gain in the multiplying register), which can be useful in high signal regimes (Fig.B.2).

For a fixed number of photons $N$ impinging per camera pixel within a given exposure time, the signal at a given camera pixel is $N \times QE$ ($QE$: quantum efficiency). Accounting for photon-noise ($\sigma_s = \sqrt{NQE}$), dark-noise ($\sigma_{DN}$) and read-out noise ($\sigma_R$), results in the SNR per pixel expressions of Table B.1. It shows the theoretical expressions of the SNRs per pixel for a CCD, EMCCD and PMT detector. Fig. B.2 is the corresponding graphical representation with ideal quantum efficiencies of 100%, a readout noise of 6 electrons per pixel, and a EM gain of 1000. The dark-noise, typically negligible, is discarded here. Then, the CCD SNR is shot-noise limited in the high signal regime, while it is limited by its readout noise in the low signal regime. An EMCCD has a small offset ($F^{-1}$) as compared to the shot-noise limit, but largely outperforms CCD performances in the low signal regime. Last, the PMT is limited by the photon noise at all signal regimes.

| | $\text{SNR}_{CCD}$ | $\text{SNR}_{EMCCD}$ | $\text{SNR}_{PMT}$ |
|---|---|---|---|
| General expression | $\frac{NQE}{\sqrt{\sigma_s^2 + \sigma_{DN}^2 + \sigma_R^2}}$ | $\frac{NQE}{\sqrt{F^2(\sigma_s^2 + \sigma_{DN}^2) + (\sigma_R/g_{EM})^2}}$ | $\frac{NQE}{\sqrt{\sigma_s^2 + \sigma_{DN}^2}}$ |
| High signal limit | $\sqrt{NQE}$ | $F^{-1}\sqrt{NQE}$ | $\sqrt{NQE}$ |
| Low signal limit | $NQE/\sigma_R$ | $F^{-1}\sqrt{NQE}$ | $\sqrt{NQE}$ |

TABLE B.1: Theoretical SNR per pixel of the three detectors

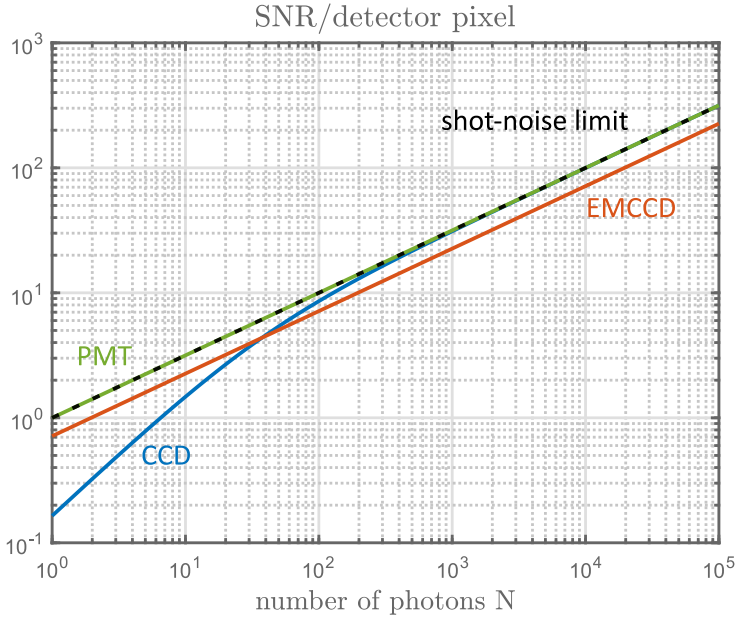


FIGURE B.2: SNR per detector pixel as a function of the number of photons $N$, for a CCD, EMCCD and PMT of ideal QE of 100%. The cameras readout noise is set to 6 electrons per pixel, the EM gain to 1000, and the dark-noise is neglected. Typically, $F = 1.4$ [253], leading to an EMCCD offset of 0.7 as compared to the shot-noise limit.

## B.2 Experimental characterisation of the noise

To gain insight of some noise characteristics of the cameras and verify manufacturers specifications, one can conduct simple experiments. For the two cameras used in the hyperspectral measurements of chapter 3, we acquired dark frames (all sources of light OFF) under the same parameters as for hyperspectral measurements (Table 3.1). This allowed us to estimate the signal-independent sources of noise, i.e. mainly the readout noise (the dark noise being essentially negligible). The mean of the dark frame counts defines the baseline level, and the standard deviation the camera readout noise. Fig. B.3 shows the histograms of the signal recorded from

the dark frames with the CCD and EMCCD. Under the chosen modes, the CCD has a baseline level of about 712 counts and exhibits a Gaussian-like distributed readout noise of about 2.25 counts (i.e. 6.1 electrons/pixel). The EMCCD exhibits a Gamma-like distributed readout noise of about 34 counts (i.e. $\leq$ 1 electron/pixel), with a baseline level of 34 counts. These measurements are consistent with the manufacturer specifications.

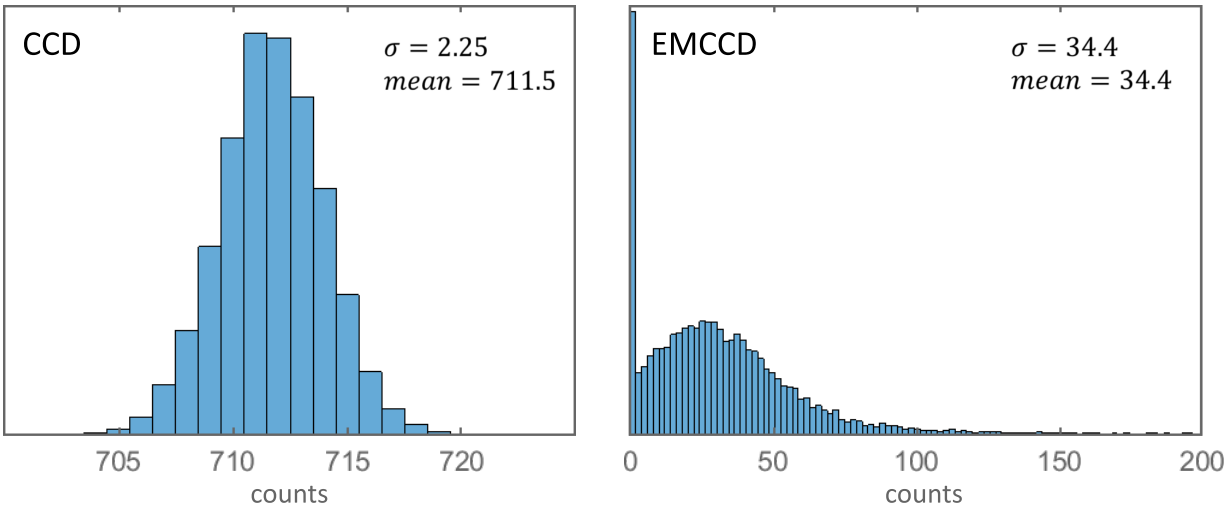


FIGURE B.3: Histograms of CCD and EMMCD dark frames counts. The distribution mean corresponds to the baseline level and the standard deviation to the readout noise.

# Appendix C

# The S-matrix

## C.1 Some properties of the S-matrix

The S-matrix of size (N-1) is built from removing the first row and column of a N-Hadamard matrix, and changing its ones to zeros and minus ones to ones. It is invertible.

The $\mathbf{S}$ matrix of size $N \times N$ has the following properties [52]:

$$\mathbf{S}\mathbf{S}^T = \mathbf{S}^T\mathbf{S} = \frac{N+1}{4}(\mathbf{I} + \mathbf{1}\mathbf{1}^T) \tag{C.1}$$

$$\mathbf{S}^{-1} = \frac{2}{N+1}(2\mathbf{S}^T - \mathbf{1}\mathbf{1}^T) \tag{C.2}$$

Using equation (C.1) and the Sherman-Morrison formula, we derive :

$$\begin{aligned}(\mathbf{S}^T\mathbf{S})^{-1} &= \frac{4}{N+1}(\mathbf{I} + \mathbf{1}\mathbf{1}^T)^{-1} \\ &= \frac{4}{N+1}(\mathbf{I} - \frac{\mathbf{1}\mathbf{1}^T}{1+\mathbf{1}^T\mathbf{1}}) \\ &= \frac{4}{N+1}(\mathbf{I} - \frac{\mathbf{1}\mathbf{1}^T}{1+N})\end{aligned} \tag{C.3}$$

which leads to (for $N \gg 1$):

$$tr((\mathbf{S}^T\mathbf{S})^{-1}) = \frac{4N^2}{(N+1)^2} \tag{C.4}$$

## C.2 S-multiplexing in the shot-noise limited case: Derivation of the MSE

The above properties allows us to derive the mean square error (Eq. (6.3)) associated with the estimate of $\mathbf{x}$, when multiplexing is performed with the S-matrix (*S-multiplexing*), under photon

noise. We consider the model from (Eq. (6.2)):

$$\mathbf{b} = Poisson\mathbf{Ax} \tag{C.5}$$

We derived in chapter 6 the general MSE expression for shot-noise limited measurements (Eq. (6.21)):

$$\overline{MSE}_{mult} = \frac{1}{N} tr(\mathbf{B}(\mathbf{A}\mathbf{A}^T)^{-1}) \tag{C.6}$$

with $\mathbf{B} = diag(\mathbf{Ax})$.

For S-multiplexing, $\mathbf{A} = \mathbf{S}$. Using Eq. (C.4), we can carry the derivation of Eq. (C.6) below:

$$\begin{aligned}
\overline{MSE}_{mult} &= \frac{1}{N} tr(\mathbf{B}(\mathbf{S}\mathbf{S}^T)^{-1}) \\
&= \frac{4}{N(N+1)} tr(\mathbf{B}(\mathbf{I} - \frac{\mathbf{1}\mathbf{1}^T}{1+N})) \\
&= \frac{4}{N(N+1)} tr(\mathbf{B}(\mathbf{I} - \frac{\mathbf{1}\mathbf{1}^T}{1+N})) \\
&= \frac{4}{N(N+1)} (tr(\mathbf{B}) - \frac{tr(\mathbf{B}\mathbf{1}\mathbf{1}^T)}{1+N}) \\
&= \frac{4}{(N+1)^2} tr(\mathbf{B}) && \text{since } \mathbf{B} \text{ is diagonal} \\
&= \frac{4}{(N+1)^2} \sum_i \sum_j a_{ij} x_j \\
&= \frac{4}{(N+1)^2} \sum_j x_j \sum_i s_{ij} \\
&= \frac{2\sum_i x_i}{N+1} && \text{for N odd}
\end{aligned}$$

For N odd, each row of $\mathbf{S}$ contains (N+1)/2 ones, so $\sum_i s_{ij} = (N+1)/2$.

As a comparison, for raster-scanning, $\mathbf{A} = \mathbf{I}$, and Eq. (C.6) becomes:

$$\begin{aligned}
\overline{MSE}_{rs} &= \frac{1}{N} tr(\mathbf{B}) \\
&= \frac{1}{N} tr(\mathbf{I}\mathbf{x}) \\
&= \frac{1}{N} \sum_i x_i
\end{aligned}$$

# List of Figures

# List of Tables

# Abbreviations

| | |
|---|---|
| **AWGN** | Additive white Gaussian noise |
| **CRB** | Cramer Rao lower bound |
| **CRT** | Compressive Raman Technology |
| **CS** | Compressive Sensing |
| **CW** | Continuous wave |
| **DMD** | Digital micromirror device |
| **FRS** | Full Raman spectrum |
| **FOV** | Field-of-view |
| **FWHM** | Full-width half-maximum |
| **IR** | Infrared |
| **MSE** | Mean Square Error |
| **NA** | Numerical aperture |
| **NIR** | Near infrared |
| **OBF** | Orthogonal binary filters |
| **PMMA** | Poly(methyl methacrylate) |
| **PS** | Polystyrene |

| | |
|---|---|
| **PSF** | Point spread function |
| **QE** | Quantum efficiency |
| **SLM** | Spatial light modulator |
| **SNR** | Signal-to-noise ratio |
| **UV** | Ultraviolet |
| **VIS** | Visible |
| $^+$ | pseudo-inverse: $\mathbf{A}^+ = (\mathbf{A}^\mathbf{T}\mathbf{A})^{-1}\mathbf{A}^\mathbf{T}$ |

# Publications based on the Thesis

P. Réfrégier, **Scotté, C.**, De Aguiar H. B., Rigneault H., and Galland F. Precision of proportion estimation with binary compressed Raman spectrum. *J. Opt. Soc. Am. A* 35, 125-134 (2018). doi.org/10.1364/JOSAA.35.000125

**Scotté, C.**, De Aguiar H. B., Marguet D., Green E. M., Bouzy P., Vergnole S., Winlove C. P., Stone N., and Rigneault H. Assessment of compressive Raman versus hyperspectral Raman for microcalcification chemical imaging. *Analytical Chemistry*, 90, 12, 7197–7203 (2018). doi.org/10.1021/acs.analchem.7b05303

**Scotté, C.**, Sivankutty S., Stockton P., Bartels R. A., and Rigneault H. Compressive Raman imaging with spatial frequency modulated illumination. *Optics Letters* 44, 1936-1939 (2019). doi.org/10.1364/OL.44.001936.

# Bibliography


[1] Gerald Jacobs. *Comparative Color Vision*. 1981.

[2] George Sines and Yannis A. Sakellarakis. Lenses in Antiquity. *American Journal of Archaeology*, 91(2):191–196, 1987.

[3] The Nimrud Lens / The Layard Lens.

[4] W. E. Moerner and L. Kador. Optical detection and spectroscopy of single molecules in a solid. *Physical Review Letters*, 62(21):2535–2538, 1989. ISSN 00319007. doi:10.1103/PhysRevLett.62.2535.

[5] Stefan W. Hell, Steffen J. Sahl, Mark Bates, Xiaowei Zhuang, Rainer Heintzmann, Martin J. Booth, Joerg Bewersdorf, Gleb Shtengel, Harald Hess, Philip Tinnefeld, Alf Honigmann, Stefan Jakobs, Ilaria Testa, Laurent Cognet, Brahim Lounis, Helge Ewers, Simon J. Davis, Christian Eggeling, David Klenerman, Katrin I. Willig, Giuseppe Vicidomini, Marco Castello, Alberto Diaspro, and Thorben Cordes. The 2015 super-resolution microscopy roadmap. *Journal of Physics D: Applied Physics*, 48(44), 2015. ISSN 13616463. doi:10.1088/0022-3727/48/44/443001.

[6] James S. Cybulski, James Clements, and Manu Prakash. Foldscope: Origami-based paper microscope. *PLoS ONE*, 9(6), 2014. ISSN 19326203. doi:10.1371/journal.pone.0098781.

[7] Marcus T Cicerone and Charles H. Camp. Histological coherent Raman imaging: a prognostic review. *The Analyst*, 143(1):33–59, 2018.

[8] Jeff W. Lichtman and José Angel Conchello. Fluorescence microscopy. *Nature Methods*, 2(12):910–919, 2005. ISSN 15487091. doi:10.1038/nmeth817.

[9] Harekrushna Sahoo. Fluorescent labeling techniques in biomolecules: A flashback. *RSC Advances*, 2(18):7017–7029, 2012. ISSN 20462069. doi:10.1039/c2ra20389h.

[10] W Demtröder. *Laser Spectroscopy Vol. 1*, volume 1. Springer, laserspect edition, 2008. ISBN 9783540734154. doi:10.1007/978-3-540-73418-5.

[11] Barbara Stuart. Infrared spectroscopy. *Kirk-Othmer Encyclopedia of Chemical Technology*, 2015.

[12] C. V. Raman and K. S. Krishnan. A New Type of Secondary Radiation. *Nature*, 121: 501–502, 1928.

[13] Cees Otto and Vishnu Vardhan Pully. Hyperspectral Raman microscopy of the living cell. In *Applications of Raman Spectroscopy to Biology*, pages 148–173. 2012. doi:10.3233/978-1-61499-020-8-148.

[14] Derek A. Long. *The Raman effect: a unified treatment of the theory of Raman scattering by molecules*. John Wiley & Sons, Ltd, 2002. ISBN 0471490288. doi:10.1002/0470845767.

[15] Ji-Xin Cheng and Xiaoliang Sunney Xie. *Coherent Raman scattering microscopy*. CRC press, 2016.

[16] Nicola Jones. The information factories. *Nature*, (561):163–166, 2018.

[17] Cécile Diguet and Fanny Lopez. L'impact spatial et énergetique des data centers sur les territoires - Rapport Ademe. Technical report, 2019.

[18] Jeremy Hsu. IBM's new brain [News]. *IEEE Spectrum*, 51(10):17–19, 2014. ISSN 0018-9235. doi:10.1109/mspec.2014.6905473.

[19] Bipin Rajendran, Abu Sebastian, Michael Schmuker, Narayan Srinivasa, and Evangelos Eleftheriou. Low-Power Neuromorphic Hardware for Signal Processing Applications. pages 1–24, 2019. URL `http://arxiv.org/abs/1901.03690`.

[20] William Stanley Jevons. *The Coal Question; An Inquiry Concerning the Progress of the Nation, and the Probable Exhaustion of Our Coal Mines*. Macmillan and Co., 1865. ISBN 978-0-678-00107-3.

[21] Jouni Korhonen, Antero Honkasalo, and Jyri Seppälä. Circular Economy: The Concept and its Limitations. *Ecological Economics*, 143(January):37–46, 2018. ISSN 09218009. doi:10.1016/j.ecolecon.2017.06.041.

[22] E.J. Candes and B. Recht. Exact low-rank matrix completion via convex optimization. *2008 46th Annual Allerton Conference on Communication, Control, and Computing*, pages 1–49, 2008. ISSN 1615-3375. doi:10.1109/ALLERTON.2008.4797640.

[23] Nicolas Gillis. The Why and How of Nonnegative Matrix Factorization. pages 1–25, 2014. URL `http://arxiv.org/abs/1401.5226`.

[24] Emmanuel J. Candès. Compressive sampling. *International Congress of Mathematicians, ICM 2006*, 3:1433–1452, 2006. doi:10.4171/022-3/69.

[25] M. F. Duarte. Single-pixel imaging via compressive sampling. *IEEE Signal Process. Mag.*, 25(March 2008):83–91, 2008. doi:10.1109/MSP.2007.914730.

[26] Dana Dudley, Walter M. Duncan, and John Slaughter. Emerging digital micromirror device (DMD) applications. *MOEMS Display and Imaging Systems*, 4985(Dmd):14, 2003. ISSN 0277786X. doi:10.1117/12.480761.

[27] Stephen E. Bialkowski. Species Discrimination and Quantitative Estimation Using Incoherent Linear Optical Signal Processing of Emission Signals. *Analytical Chemistry*, 58 (12):2561–2563, 1986. ISSN 15206882. doi:10.1021/ac00125a043.

[28] Matthew P. Nelson, Jeffrey F. Aust, J. A. Dobrowolski, P. G. Verly, and M. L. Myrick. Multivariate Optical Computation for Predictive Spectroscopy. *Analytical Chemistry*, 70 (1):73–82, 1998. ISSN 00032700. doi:10.1021/ac970791w.

[29] Nguyen The Quyen, Edouard Da Silva, Nguyen Quy Dao, and Michel D. Jouan. New Raman spectrometer using a digital micromirror device and a photomultiplier tube detector for rapid on-line industrial analysis. Part I: Description of the prototype and preliminary results. *Applied Spectroscopy*, 62(3):273–278, 2008. ISSN 00037028. doi:10.1366/000370208783759704.

[30] Zanyar Movasaghi, Shazza Rehman, and Ihtesham U. Rehman. Raman Spectroscopy of Biological Tissues. *Applied Spectroscopy Reviews*, 42(5):493–541, 2007. doi:10.1080/05704920701551530.

[31] Yan Wang, Daniel C. Alsmeyer, and Richard L. McCreery. Raman Spectroscopy of Carbon Materials: Structural Basis of Observed Spectra. *Chemistry of Materials*, 2(5):557–563, 1990. doi:10.1021/cm00011a018.

[32] L. M. Malard, M. A. Pimenta, G. Dresselhaus, and M. S. Dresselhaus. Raman spectroscopy in graphene. *Physics Reports*, 473(5-6):51–87, 2009. ISSN 03701573. doi:10.1016/j.physrep.2009.02.003.

[33] Shiye Zhao, Meghan Danley, J. Evan Ward, Daoji Li, and Tracy J. Mincer. An approach for extraction, characterization and quantitation of microplastic in natural marine snow using Raman microscopy. *Analytical Methods*, 9(9):1470–1478, 2017. ISSN 17599679. doi:10.1039/c6ay02302a. URL `http://dx.doi.org/10.1039/C6AY02302A`.

[34] Morgan Tardivel, Florent Colas, and Emmanuel Rinnert. La spectroscopie Raman pour l'environnement marin. *Photoniques*, pages (96) 30–33, 2019.

[35] P. Vandenabeele. Raman spectroscopy in art and archaeology. *Journal of Raman Spectroscopy*, 35:607–609, 2004. ISSN 03770486. doi:10.1002/jrs.2008.

[36] Adolf Smekal. Zur Quantentheorie der Dispersion. *Naturwissenschaften*, 11(43):873–875, 1923. doi:10.1007/BF01576902.

[37] G.S. Landsberg and L.I. Mandelstam. New phenomenon in scattering of light. *Journal of the Russian Physico-Chemical Society*, 60:335, 1928.

[38] Mark Fox. *Optical properties of solids*. Oxford University Press, second edi edition, 2010. ISBN 9780199573363.

[39] Eric Olaf Putma and Shaul Mukamel. Theory of Coherent Raman Scattering. In Ji-Xin Cheng and X Sunney Xie, editors, *Coherent Raman Scattering Microscopy*, chapter 1, pages 3–42. CRC Press / Taylor & Francis Group, LLC, 2016. ISBN 978-1-4398-6765-5.

[40] Hervé Rigneault and Pascal Berto. Tutorial: Coherent Raman light matter interaction processes. *APL Photonics*, 3(091101):1–35, 2018. ISSN 2378-0967. doi:10.1063/1.5030335.

[41] Xavier Audier. *Spectroscopie Raman stimulée rapide et imagerie hyperspectrale*. PhD thesis, 2018.

[42] Yu Winston Wang, Nicholas P. Reder, Soyoung Kang, Adam K. Glaser, and Jonathan T.C. Liu. Multiplexed optical imaging of tumor-directed nanoparticles: A review of imaging systems and approaches. *Nanotheranostics*, 1(4):369–388, 2017. ISSN 22067418. doi:10.7150/ntno.21136.

[43] Thomas Dieing and Olaf Hollricher. High-resolution, high-speed confocal Raman imaging. *Vibrational Spectroscopy*, 48(1):22–27, 2008. ISSN 09242031. doi:10.1016/j.vibspec.2008.03.004.

[44] Ji Qi, Jingting Li, and Wei-Chuan Shih. High-speed hyperspectral Raman imaging for label-free compositional microanalysis. *Biomedical Optics Express*, 4(11):2376, 2013. ISSN 2156-7085. doi:10.1364/BOE.4.002376.

[45] WiTec. Ultra-Fast Raman Imaging. URL https://www.witec.de/techniques/raman/.

[46] Horiba Scientific. SWIF Ultra Fast Raman Imaging. URL https://www.horiba.com/fr/scientific/products/raman-spectroscopy/raman-imaging/swift/.

[47] N. Keshava and J.F. Mustard. Spectral Unmixing. *IEEE Signal Processing Magazine*, 19 (1):44–57, 2002.

[48] Nirmal Keshava. A Survey of Spectral Unmixing Algorithms. *Lincoln laboratory journal*, 14(1):55–78, 2003.

[49] Rebecca M. Willett, Marco F. Duarte, Mark A. Davenport, and Richard G. Baraniuk. Sparsity and structure in hyperspectral imaging : Sensing, reconstruction, and target detection. *IEEE Signal Processing Magazine*, 31(1):116–126, 2014. ISSN 10535888. doi:10.1109/MSP.2013.2279507.

[50] Marcel J. E Golay. Multi-Slit Spectrometry. *Journal of the Optical Society of America*, 39(6):437–444, 1949. doi:10.1364/JOSA.39.000437.

[51] Peter Hansen and John Strong. High Resolution Hadamard Transform Spectrometer. *Applied Optics*, 11(3):502, 1972. ISSN 0003-6935. doi:10.1364/ao.11.000502.

[52] Martin Harwit, Neil J A Sloane, I Sloane, and Neil James. *Hadamard Transform Optics*. Academic Press, 1979. ISBN 0123300509.

[53] Jeffrey T. Meade, Bradford B. Behr, and Arsen R. Hajian. Simultaneous high-resolution and high-throughput spectrometer design based on virtual slit technology. *Applied Industrial Optics: Spectroscopy, Imaging and Metrology, AIO 2012*, pages 5–7, 2012. doi:10.1364/aio.2012.am2a.2.

[54] Jeffrey T. Meade, Bradford B. Behr, and Arsen R. Hajian. A new high-resolution, high-throughput spectrometer: first experience as applied to Raman spectroscopy. *Next-Generation Spectroscopic Technologies V*, 8374:83740V, 2012. ISSN 0277786X. doi:10.1117/12.919062.

[55] Bradford B. Behr, Jeffrey T. Meade, Yusuf Busmilla, Brandon DesRoches, Andrew T. Cenko, Elizabeth A. Munro, Steve McFadyen, Arie Henkin, Jared Slaa, David Rempel, and Arsen R. Hajian. High-performance spectroscopy using virtual slit optics. *Optics InfoBase Conference Papers*, pages 2–4, 2013. ISSN 21622701. doi:10.1364/aio.2013.am1b.2.

[56] A.T. Meade, J.T., Hajian, A.R., Behr, B.B., and Cenko. Optical slicer for improving the spectral resolution of a dispersive spectrograph, 2015.

[57] Xiangyun Ma, Huijie Wang, Yang Wang, Da Chen, Wenliang Chen, and Qifeng Li. Improving the resolution and the throughput of spectrometers by a digital projection slit. *Optics Express*, 25(19):23045, 2017. ISSN 1094-4087. doi:10.1364/oe.25.023045.

[58] Michael Bowden, Derek J. Gardiner, Graham Rice, and Don L. Gerrard. Line-scanned micro Raman spectroscopy using a cooled CCD imaging detector. *Journal of Raman Spectroscopy*, 21(1):37–41, 1990. ISSN 10974555. doi:10.1002/jrs.1250210108.

[59] Sebastian Schlücker, Michael D. Schaeberle, Scott W. Huffman, and Ira W. Levin. Raman microspectroscopy: A comparison of point, line, and wide-field imaging methodologies. *Analytical Chemistry*, 75(16):4312–4318, 2003. ISSN 00032700. doi:10.1021/ac034169h.

[60] Joanne Hutchings, Catherine Kendall, Brian Smith, Neil Shepherd, Hugh Ban, and Nicholas Stone. The potential for histological screening using a combination of rapid Raman mapping and principal component analysis. *Journal of Biophotonics*, 2(1-2):91–103, 2009. ISSN 1864063X. doi:10.1002/jbio.200810070.

[61] Etienne Gaufrès, Stéphane Marcet, Vincent Aymong, Nathalie Y.Wa Tang, Alexandre Favron, Felix Thouin, Charlotte Allard, David Rioux, Nicolas Cottenye, Marc Verhaegen, and Richard Martel. Hyperspectral Raman imaging using Bragg tunable filters of graphene and other low-dimensional materials. *Journal of Raman Spectroscopy*, 49(1):174–182, 2018. ISSN 10974555. doi:10.1002/jrs.5298.

[62] Nathan Hagen and Michael W. Kudenov. Review of snapshot spectral imaging technologies. *Optical Engineering*, 52(9):090901, 2013. ISSN 0091-3286. doi:10.1117/1.oe.52.9.090901.

[63] Akiako Hirai, Takashi Inoue, Kazuyoshi Itoh, and Yoshiki Ichioka. Application of Measurement multiple-image fourier of fast phenomena transform spectral imaging to measurement of fast phenomena. *Optical Review*, 1(2):205–207, 1994.

[64] Rui Shogenji, Yoshiro Kitamura, Kenji Yamada, Shigehiro Miyatake, and Jun Tanida. Multispectral imaging using compact compound optics. *Optics Express*, 12(8):1643, 2004. ISSN 1094-4087. doi:10.1364/opex.12.001643.

[65] Yuri Murakami, Masahiro Yamaguchi, and Nagaaki Ohyama. Hybrid-resolution multispectral imaging using color filter array. *Optics Express*, 20(7):7173, 2012. ISSN 1094-4087. doi:10.1364/oe.20.007173.

[66] Takayuki Okamoto and Ichirou Yamaguchi. Simultaneous acquisition of spectral image information. *Optics Letters*, 16(16):1277–1279, 1991.

[67] Liang Gao, Robert T. Kester, and Tomasz S. Tkaczyk. Compact Image Slicing Spectrometer (ISS) for hyperspectral fluorescence microscopy. *Optics Express*, 17(15):12293, 2009. ISSN 1094-4087. doi:10.1364/oe.17.012293.

[68] Liang Gao, Robert T. Kester, Nathan Hagen, and Tomasz S. Tkaczyk. Snapshot Image Mapping Spectrometer (IMS) with high sampling density for hyperspectral microscopy. *Optics Express*, 18(14):14330, 2010. doi:10.1364/oe.18.014330.

[69] Liang Gao, Noah Bedard, Robert T. Kester, Nathan Hagen, and Tomasz S. Tkaczyk. Depth-resolved image mapping spectrometer (IMS) with structured illumination. *Optics express*, 19(18):17439–17452, 2011. ISSN 21622701. doi:10.1364/ntm.2011.nwb4.

[70] Jonathan Thompson, Joel N. Bixler, Joel N. Bixler, Marlan O. V.Scully, Gary D. Noojin, Vladislav V. Yakovlev, and Brett H. Hokr. Single-shot chemical detection and identification with compressed hyperspectral Raman imaging. *Optics Letters*, 42(11):2169, 2017. ISSN 0146-9592. doi:10.1364/ol.42.002169.

[71] Jeremy Allington-Smith. Basic principles of integral field spectroscopy. *New Astronomy Reviews*, 50(4-5):244–251, 2006. ISSN 13876473. doi:10.1016/j.newar.2006.02.024.

[72] I. S Bowen. The Image-Slicer, a device for reducing loss of light at slit of stellar spectrograph. *The Astrophysical Journal*, 9(2):9–63, 1938.

[73] T. Walraven and J. H. Walraven. Some features of the Leiden radial velocity instrument. *Auxiliary Instrumentation for Large Telescopes*, pages 175 – 183, 1972.

[74] S. C Barden and Wade A. R. DensePak and spectral imaging with fiber optics. *Fiber Optics in Astronomy Astronomical Society of the Pacific Conference Series*, 3:113– 124, 1988.

[75] Joss Bland-Hawthorn, Julia Bryant, Gordon Robertson, Peter Gillingham, John O'Byrne, Gerald Cecil, Roger Haynes, Scott Croom, Simon Ellis, Martin Maack, Peter Skovgaard, and Danny Noordegraaf. Hexabundles: imaging fiber arrays for low-light astronomical applications. *Optics Express*, 19(3):2649, 2011. ISSN 1094-4087. doi:10.1364/oe.19.002649.

[76] S. Arribas, E. Mediavilla, and J. L. Rasilla. An optical fiber system to perform bidimensional spectroscopy. *Astrophys . J.*, 369(1):260–272, 1991.

[77] D. J. Brady and M. E. Gehm. Compressive imaging spectrometers using coded apertures. *Visual Information Processing XV*, 6246:62460A, 2006. ISSN 0277786X. doi:10.1117/12.667605.

[78] D. J. Brady, M. E. Gehm, R. M. Willett, T. J. Schulz, and R. John. Single-shot compressive spectral imaging with a dual-disperser architecture. *Optics Express*, 15(21):14013, 2007. ISSN 1094-4087. doi:10.1364/oe.15.014013.

[79] Ashwin Wagadarikar, Renu John, Rebecca Willett, and David Brady. Single disperser design for coded aperture snapshot spectral imaging. *Applied Optics*, 47(10):B44, 2008. ISSN 0003-6935. doi:10.1364/ao.47.000b44.

[80] Gonzalo R. Arce, David J. Brady, Lawrence Carin, Henry Arguello, and David S. Kittle. Compressive coded aperture spectral imaging: An introduction. *IEEE Signal Processing Magazine*, 31(1):105–115, 2014. ISSN 10535888. doi:10.1109/MSP.2013.2278763.

[81] D.F.a Galvis-Carreño, Y.H.b Mejía-Melgarejo, and H.c Arguello-Fuentes. Efficient reconstruction of Raman spectroscopy imaging based on compressive sensing. *DYNA (Colombia)*, 81(188):116–124, 2014. ISSN 00127353. doi:10.15446/dyna.v81n188.41162.

[82] Xin Yuan, Patrick Llull, Lawrence Carin, David J. Brady, and Tsung-Han Tsai. Spectral-temporal compressive imaging. *Optics Letters*, 40(17):4054, 2015. ISSN 0146-9592. doi:10.1364/ol.40.004054.

[83] Chen Fu, Michael L. Don, and Gonzalo R. Arce. Compressive Spectral Imaging via Polar Coded Aperture. *IEEE Transactions on Computational Imaging*, 3(3):408–420, 2016. ISSN 2333-9403. doi:10.1109/tci.2016.2617740.

[84] Daniel S. Jeon, Seung Hwan Baek, Shinyoung Yi, Qiang Fu, Xiong Dun, Wolfgang Heidrich, and Min H. Kim. Compact snapshot hyperspectral imaging with diffracted rotation. *ACM Transactions on Graphics*, 38(4):1–13, 2019. ISSN 15577368. doi:10.1145/3306346.3322946.

[85] D.L. Donoho. Compressed sensing. *IEEE Transactions on Information Theory*, 52(4): 1289–1306, 2006. ISSN 0018-9448. doi:10.1109/TIT.2006.871582.

[86] Emmanuel Candes and Terence Tao. Near Optimal Signal Recovery from Random Projections. *IEEE Transactions on Information Theory*, 52(12):5406 – 5425, 2006. ISSN 0018-9448. doi:10.1109/TIT.2006.885507.

[87] E.J. Candes and M.B. Wakin. An Introduction To Compressive Sampling. *IEEE Signal Processing Magazine*, 25(2):21–30, 2008. ISSN 1053-5888. doi:10.1109/MSP.2007.914731.

[88] J. Romberg. Imaging via Compressive Sampling. *IEEE Signal Processing Magazine*, 25 (2):14–20, 2008. ISSN 1053-5888. doi:10.1109/MSP.2007.914729.

[89] Jose Enrique Sánchez, Estanislau Auge, Josep Santaló, Ian Blanes, Joan Serra-Sagristà, and Aaron Kiely. Review and implementation of the emerging CCSDS Recommended Standard for multispectral and hyperspectral lossless image coding. *Proceedings - 1st International Conference on Data Compression, Communication, and Processing, CCP 2011 - IEEE Press*, pages 222–228, 2011. doi:10.1109/CCP.2011.17.

[90] Emmanuel J. Candes and Yaniv Plan. Matrix completion with noise. *Proceedings of the IEEE*, 98(6):925–936, 2010. ISSN 00189219. doi:10.1109/JPROC.2009.2035722.

[91] Marco F. Duarte, Mark A. Davenport, D. Takhar, J N Laska, Ting Sun, Kevin F. Kelly, and Richard G. Baraniuk. Single pixel imaging via compressive sampling. *IEEE Signal Processing Magazine*, pages 83–91, 2008. ISSN 1053-5888. doi:10.1109/MSP.2007.914730.

[92] Vincent Studer, Jérome Bobin, Makhlad Chahid, Hamed Shams, and Emmanuel Candes. Compressive fluorescence microscopy for biological and hyperspectral imaging. *PNAS*, 109(26):1679–1687, 2012. doi:10.1073/pnas.1119511109.

[93] N. Pavillon and N. I. Smith. Compressed sensing laser scanning microscopy. *Optics Express*, 24(26):30038–30052, 2016. ISSN 1094-4087. doi:10.1364/OE.24.030038.

[94] F. Soldevila, E. Irles, V. Durán, P. Clemente, Mercedes Fernández-Alonso, Enrique Tajahuerce, and Jesús Lancis. Single-pixel polarimetric imaging spectrometer by compressive sensing. *Applied Physics B: Lasers and Optics*, 113(4):551–558, 2013. ISSN 09462171. doi:10.1007/s00340-013-5506-2.

[95] Qi Pian, Ruoyang Yao, Lingling Zhao, and Xavier Intes. Hyperspectral time-resolved wide-field fluorescence molecular tomography based on structured light and single-pixel detection. *Optics Letters*, 40(3):431, 2015. ISSN 0146-9592. doi:10.1364/ol.40.000431.

[96] Dushan N. Wadduwage, Vijay Raj Singh, Heejin Choi, Zahid Yaqoob, Hans Heemskerk, Paul Matsudaira, and Peter T. C. So. Near-common-path interferometer for imaging Fourier-transform spectroscopy in wide-field microscopy. *Optica*, 4(5):546, 2017. ISSN 2334-2536. doi:10.1364/optica.4.000546.

[97] K Yuki S Hibuya, T Akeo M Inamikawa, Y Asuhiro M Izutani, H Irotsugu Y Amamoto, K Aoru M Inoshima, T Akeshi Y Asui, and T Etsuo I Wata. Scan-less hyperspectral dual-comb single- pixel-imaging in both amplitude and phase. *Opt. Express*, 25(18):4971–4974, 2017.

[98] Senlin Jin, Wangwei Hui, Yunlong Wang, Kaicheng Huang, Qiushuai Shi, Cuifeng Ying, Dongqi Liu, Qing Ye, Wenyuan Zhou, and Jianguo Tian. Hyperspectral imaging using the single-pixel Fourier transform technique. *Scientific Reports*, 7(February):1–7, 2017. ISSN 20452322. doi:10.1038/srep45209.

[99] Haonan Lin, Chien Sheng Liao, Pu Wang, Nan Kong, and Ji Xin Cheng. Spectroscopic stimulated Raman Scattering imaging of highly dynamic specimens through matrix completion. *Light: Science & Applications*, 7:171–179, 2018. doi:10.1364/MICROSCOPY.2018.MW2A.5.

[100] A Moshtaghpour and L Jacques. Compressive Hyperspectral Imaging : Fourier Transform Interferometry meets Single Pixel Camera. pages 1–5, 2018.

[101] Fernando Soldevila, Jonathan Dong, Enrique Tajahuerce, Sylvain Gigan, and Hilton B. de Aguiar. Fast compressive Raman bio-imaging via matrix completion. *Optica*, 6(3), 2018. ISSN 00445169. doi:10.1016/j.zoolgart.2007.06.004. URL `http://arxiv.org/abs/1811.12389`.

[102] Paul Gattinger, Jakob Kilgus, Ivan Zorin, Gregor Langer, Ramin Nikzad-Langerodi, Christian Rankl, Martin Gröschl, and Markus Brandstetter. Broadband near-infrared hyperspectral single pixel imaging for chemical characterization. *Optics Express*, 27(9):12666, 2019. ISSN 1094-4087. doi:10.1364/oe.27.012666.

[103] Wikipedia. Multivariate optical computing - Wikipedia page, 2019. URL `https://en.wikipedia.org/wiki/Multivariate{_}optical{_}computing`.

[104] AG Ryabenko and GG Kasparov. Numerical study of a pattern recognition multispectral system with optimal spectral splitting. *Pattern Recogn. Image Anal.*, 1:347–354, 1991.

[105] O. Soyemi, D. Eastwood, L. Zhang, H. Li, J. Karunamuni, P. Gemperline, R. A. Synowicki, and M. L. Myrick. Design and testing of a multivariate optical element: The first demonstration of multivariate optical computing for predictive spectroscopy. *Analytical Chemistry*, 73(6):1069–1079, 2001. ISSN 00032700. doi:10.1021/ac0012896.

[106] Frederick G. Haibach, Ashley E. Greer, Maria V. Schiza, Ryan J. Priore, Olusola O. Soyemi, and Michael L. Myrick. On-line reoptimization of filter designs for multivariate optical elements. *Applied Optics*, 42(10):1833, 2003. ISSN 0003-6935. doi:10.1364/ao.42.001833.

[107] Michael N. Simcock and Michael L. Myrick. Precision in imaging multivariate optical computing. *Applied Optics*, 46(7):1066–1080, 2007. ISSN 15394522. doi:10.1364/AO.46.001066.

[108] Joseph A. Swanstrom, Laura S. Bruckman, Megan R. Pearl, Michael N. Simcock, Kathleen A. Donaldson, Tammi L. Richardson, Timothy J. Shaw, and Michael L. Myrick. Taxonomic classification of phytoplankton with multivariate optical computing, Part I: Design and theoretical performance of multivariate optical elements. *Applied Spectroscopy*, 67(6): 620–629, 2013. ISSN 00037028. doi:10.1366/12-06783.

[109] Ryan J. Priore and Joseph A. Swanstrom. Multivariate optical element platform for compressed detection of fluorescence markers. *Next-Generation Spectroscopic Technologies VII*, 9101:91010E, 2014. ISSN 1996756X. doi:10.1117/12.2053570.

[110] Ryan J. Priore and Joseph A. Swanstrom. Multivariate optical computing for fluorochrome discrimination. *Optical Diagnostics and Sensing XV: Toward Point-of-Care Diagnostics*, 9332:933212, 2015. ISSN 16057422. doi:10.1117/12.2080996.

[111] Eric Carre, Ahmed Kenawi, David Topping, and Greg Powers. Laboratory-Quality Optical Analysis in Harsh Environments. *Reservoir Innovations*, (2):1–15, 2013. URL `https://www.halliburton.com/content/dam/ps/public/lp/contents/Books{_}and{_}Catalogs/Reservoir{_}Innovations{_}Four.pdf`.

[112] Christopher Michael Jones, Robert Freese, David Perkins, and Bin Dai. Multivariate optical computing enables accurate harsh-environment sensing for the oil and gas industry. *Laser Focus World*, 50(8):27–31, 2014. ISSN 10438092.

[113] Natallia Uzunbajakava, Peter De Peinder, Gert W. 'T Hooft, and Antonius T.M. Van Gogh. Low-cost spectroscopy with a variable multivariate optical element. *Analytical Chemistry*, 78(20):7302–7308, 2006. ISSN 00032700. doi:10.1021/ac060985o.

[114] Brandon M. Davis, Amanda J. Hemphill, Derya Cebeci Maltaş, Michael A. Zipper, Ping Wang, and Dor Ben-Amotz. Multivariate hyperspectral raman imaging using

compressive detection. *Analytical Chemistry*, 83(13):5086–5092, 2011. ISSN 00032700. doi:10.1021/ac103259v.

[115] Derya Cebeci Maltaş, Kaho Kwok, Ping Wang, Lynne S. Taylor, and Dor Ben-Amotz. Rapid classification of pharmaceutical ingredients with Raman spectroscopy using compressive detection strategy with PLS-DA multivariate filters. *Journal of Pharmaceutical and Biomedical Analysis*, 80:63–68, 2013. ISSN 07317085. doi:10.1016/j.jpba.2013.02.029.

[116] Joseph E. Vornehm, Ava Jingwen Dong, Robert W. Boyd, and Zhimin Shi. Multiple-output multivariate optical computing for spectrum recognition. *Optics Express*, 22(21): 25005, 2014. ISSN 1094-4087. doi:10.1364/oe.22.025005.

[117] E. P Wagner, B. W. Smith, S. Madden, Winefordner J. D, and Mignardi; M. Construction and Evaluation of a Visible Spectrometer Using Digital Micromirror Spatial Light Modulation. *Applied Spectroscopy*, 49(11):1715–1719, 1995. doi:10.1366/0003702953965731.

[118] Zachary J. Smith, Sven Strombom, and Sebastian Wachsmann-Hogiu. Multivariate optical computing for biological samples using a digital micromirror device. *Optics Express*, 19 (18):16950–16962, 2011. ISSN 21622701. doi:10.1364/fio.2011.ftuo4.

[119] David S. Wilcox, Gregery T. Buzzard, Bradley J. Lucier, Ping Wang, and Dor Ben-Amotz. Photon level chemical classification using digital compressive detection. *Analytica Chimica Acta*, 755:17–27, 2012. ISSN 00032670. doi:10.1016/j.aca.2012.10.005.

[120] David S Wilcox, Gregery T Buzzard, Bradley J Lucier, Owen G Rehrauer, Ping Wang, and Dor Ben-Amotz. Digital compressive chemical quantitation and hyperspectral imaging. *The Analyst*, 138(17):4982–90, 2013. ISSN 1364-5528. doi:10.1039/c3an00309d.

[121] Owen G. Rehrauer, Bharat R. Mankani, Gregery T. Buzzard, Bradley J. Lucier, and Dor Ben-Amotz. Fluorescence modeling for optimized-binary compressive detection Raman spectroscopy. *Optics Express*, 23(18):23935, 2015. ISSN 1094-4087. doi:10.1364/OE.23.023935.

[122] Owen G. Rehrauer, Vu C. Dinh, Bharat R. Mankani, Gregery T. Buzzard, Bradley J. Lucier, and Dor Ben-Amotz. Binary Complementary Filters for Compressive Raman Spectroscopy. *Applied Spectroscopy*, 0(0):000370281773232, 2017. ISSN 0003-7028. doi:10.1177/0003702817732324.

[123] Neil Goldstein, Pajo Vujkovic-Cvijin, Marsha Fox, Brian Gregor, Jamine Lee, Jason Cline, and Steven Adler-Golden. DMD-based adaptive spectral imagers for hyperspectral imagery and direct detection of spectral signatures. *Emerging Digital Micromirror Device Based Systems and Applications*, 7210:721008, 2009. ISSN 0277786X. doi:10.1117/12.809129.

[124] Neil Goldstein, Benjamin St. Peter, Jonathan Grot, Michael Kogan, Marsha Fox, Pajo Vujkovic-Cvijin, Ryan Penny, and Jason Cline. Portable, stand-off spectral imaging camera for detection of effluents and residues. In *Next-Generation Spectroscopic Technologies VIII*, volume 9482, pages 1–12, 2015. ISBN 9781628415988. doi:10.1117/12.2179045.

[125] Neil Goldstein, Marsha Fox, Steven Adler-Golden, and Brian Gregor. Infrared adaptive spectral imagers for direct detection of spectral signatures and hyperspectral imagery. *Emerging Digital Micromirror Device Based Systems and Applications V*, 8618:86180D, 2013. ISSN 0277786X. doi:10.1117/12.2007029.

[126] Texas Instruments. DLP NIRscan Nano Evaluation Module. URL `http://www.ti.com/tool/DLPNIRNANOEVM`.

[127] Chen TAO, Chun Sheng LI, Hong Xia WANG, Ya Ru ZHANG, Cheng Wei ZHAO, Zhi Heng ZHOU, Zhen Yu MA, and Di TIAN. Research on Dispersive Detection Technology Based on Digital Micromirror Device by Atomic Fluorescence Spectrometry. *Chinese Journal of Analytical Chemistry*, 46(12):1878–1885, 2018. ISSN 18722040. doi:10.1016/S1872-2040(18)61128-4.

[128] Christopher J. Corden, Dustin W. Shipp, Pavel Matousek, and Ioan Notingher. Fast Raman spectral mapping of highly fluorescing samples by time-gated spectral multiplexed detection. *Optics Letters*, 43(23):5733, 2018. ISSN 0146-9592. doi:10.1364/ol.43.005733.

[129] Kideog Bae, Wei Zheng, and Zhiwei Huang. Spatial light-modulated stimulated Raman scattering ( SLM-SRS ) microscopy for rapid multiplexed vibrational imaging. *Theranostics*, 10(1):312–322, 2019. doi:10.7150/thno.38551.

[130] Derya Cebeci, Bharat Mankani, and Dor Ben-Amotz. Recent Trends in Compressive Raman Spectroscopy Using DMD-Based Binary Detection. *Journal of Imaging*, 5(1):1, 2018. ISSN 2313-433X. doi:10.3390/jimaging5010001.

[131] Philippe Réfrégier, Camille Scotté, Hilton B. de Aguiar, Hervé Rigneault, and Frédéric Galland. Precision of proportion estimation with binary compressed Raman spectrum. *Journal of the Optical Society of America A*, 35(1):125, 2018. ISSN 1084-7529. doi:10.1364/JOSAA.35.000125.

[132] Philippe Réfrégier. *Noise Theory and Application to Physics - From fluctuations to Information*. Springer, 2004. ISBN 978-1-4419-1896-3.

[133] Gregery T. Buzzard and Bradley J. Lucier. Optimal filters for high-speed compressive detection in spectroscopy. (February):865707, 2013. ISSN 0277786X. doi:10.1117/12.2012700.

[134] Ryan D Palkki and Aaron D Lanterman. Algorithms and Performance Bounds for Chemical Identification under a Poisson Model for Raman Spectroscopy. In *Internatinal conference on Information Fusion, 2009*, pages 2231–2238, 2009. ISBN 9780982443804.

[135] Newport. Diffraction Grating Physics: Tutorial. URL https://www.newport.com/t/grating-physics.

[136] Petra Aswendt. Hologram reconstruction using a digital micromirror device. *Optical Engineering*, 40(6):926, 2001. ISSN 0091-3286. doi:10.1117/1.1367346.

[137] Hamamatsu: Photon counting head H7421-40. URL https://www.hamamatsu.com/eu/en/product/type/H7421-40/index.html.

[138] Camille Scotté, Hilton B. De Aguiar, Didier Marguet, Ellen Marie Green, Pascaline Bouzy, Sébastien Vergnole, Charles Peter Winlove, Nicholas Stone, and Herve Rigneault. Assessment of compressive Raman versus hyperspectral Raman for microcalcification chemical imaging. *Analytical Chemistry*, 90(12):7197–7203, 2018. ISSN 15206882. doi:10.1021/acs.analchem.7b05303.

[139] Alfred Vogel and Vasan Venugopalan. Mechanisms of pulsed laser ablation of biological tissues. *Chemical Reviews*, 103(2):577–644, 2003. doi:10.1021/cr010379n.

[140] Lihong V. Wang and Hsin-I Wu. *Biomedical Optics - Principles and Imaging*. John Wiley & Sons, Ltd, 2007. ISBN 978-0-471-74304-0.

[141] Steven L. Jacques. Optical properties of biological tissues: A review. *Physics in Medicine and Biology*, 58(11), 2013. ISSN 00319155. doi:10.1088/0031-9155/58/11/R37.

[142] Chenglin Gu, Dapeng Zhang, Yina Chang, and Shih-Chi Chen. Digital micromirror device-based ultrafast pulse shaping for femtosecond laser. *Optics Letters*, 40(12):2870, 2015. ISSN 0146-9592. doi:10.1364/OL.40.002870.

[143] Texas Instruments. Using Lasers with DLP DMD technology Purpose. Technical Report DLPA037, 2008.

[144] Nadya Chakrova, Bernd Rieger, and Sjoerd Stallinga. Development of a DMD-based fluorescence microscope. *Three-Dimensional and Multidimensional Microscopy: Image Acquisition and Processing XXII*, 9330:933008, 2015. doi:10.1117/12.2077677.

[145] Sébastien Popoff. Setting up a DMD: Diffraction effects, 2016. URL http://wavefrontshaping.net/index.php/component/content/article/57-community/tutorials/spatial-lights-modulators-slms/131-setting-up-a-dmd-diffraction-effects.

[146] R Baker, K D Rogers, N Shepherd, and N Stone. New relationships between breast microcalcifications and cancer. *British Journal of Cancer*, 103(7):1034–1039, 2010. ISSN 0007-0920. doi:10.1038/sj.bjc.6605873.

[147] A S Haka, K E Shafer-Peltier, M Fitzmaurice, J Crowe, R R Dasari, and M S Feld. Identifying microcalcifications in benign and malignant breast lesions by probing differences in their chemical composition using Raman spectroscopy. *Cancer Res*, 62(18):5375–5380, 2002. ISSN 0008-5472.

[148] Sarah Gosling, Robert Scott, Charlene Greenwood, Pascaline Bouzy, Jayakrupakar Nallala, Iain D. Lyburn, Nicholas Stone, and Keith Rogers. Calcification Microstructure Reflects Breast Tissue Microenvironment. *Journal of Mammary Gland Biology and Neoplasia*, 2:333–342, 2019. ISSN 15737039. doi:10.1007/s10911-019-09441-3.

[149] Marleen M. Kerssens, Pavel Matousek, Keith Rogers, and Nicholas Stone. Towards a safe non-invasive method for evaluating the carbonate substitution levels of hydroxyapatite (HAP) in micro-calcifications found in breast tissue. *The Analyst*, 135(12):3156, 2010. ISSN 0003-2654. doi:10.1039/c0an00565g.

[150] Adrian Ghita, Pavel Matousek, and Nick Stone. High sensitivity non-invasive detection of calcifications deep inside biological tissue using Transmission Raman Spectroscopy. *Journal of Biophotonics*, 11(1):1–8, 2018. ISSN 18640648. doi:10.1002/jbio.201600260.

[151] Barbara Sarri, Rafaël Canonge, Xavier Audier, Valérie Lavastre, Géraldine Pénarier, Jean Alie, and Hervé Rigneault. Discriminating polymorph distributions in pharmaceutical tablets using stimulated Raman scattering microscopy. *Journal of Raman Spectroscopy*, 50(August):1896–1904, 2019. ISSN 10974555. doi:10.1002/jrs.5743.

[152] John Haleblian and Walter McCrone. Pharmaceutical applications of polymorphism. *Journal of Pharmaceutical Sciences*, 58(8):911–929, 1969. ISSN 15206017. doi:10.1002/jps.2600580802.

[153] Harry G. Brittain. *Polymorphism in Pharmaceutical Solids: Second edition*, volume 192. 2016. ISBN 9781420073225. doi:10.3109/9781420073225.

[154] Eun Hee Lee. A practical guide to pharmaceutical polymorph screening & selection. *Asian Journal of Pharmaceutical Sciences*, 9(4):163–175, 2014. ISSN 2221285X. doi:10.1016/j.ajps.2014.05.002.

[155] Vishal Koradia, Garima Chawla, and Arvind K. Bansal. Qualitative and quantitative analysis of clopidogrel bisulphate polymorphs. *Acta Pharmaceutica*, 54(3):193–204, 2004. ISSN 13300075.

[156] M. Grant Albrecht and J. Alan Creighton. Anomalously Intense Raman Spectra of Pyridine at a Silver Electrode. *Journal of the American Chemical Society*, 99(15):5215–5217, 1977. ISSN 15205126. doi:10.1021/ja00457a071.

[157] A. Otto, I. Mrozek, H. Grabhorn, and W. Akemann. Surface-enhanced Raman scattering. *Journal of Physics: Condensed Matter*, 4(5):1143–1212, 1992. ISSN 09538984. doi:10.1088/0953-8984/4/5/001.

[158] Katrin Kneipp, Yang Wang, Harald Kneipp, Lev T. Perelman, Irving Itzkan, Ramachandra R. Dasari, and Michael S. Feld. Single Molecule Detection Using Surface-Enhanced Raman Scattering (SERS). *Physical Review Letters*, 78(9):1667–1670, 1997. ISSN 09701591.

[159] Alan Campion, Patanjali Kambhampati, Alan Campion, and Charles Harris. Surface-enhanced Raman scattering. *Chemical Society Reviews*, 27:241–250, 1998.

[160] Ming Li, Scott K. Cushing, and Nianqiang Wu. Plasmon-enhanced optical sensors: A review. *Analyst*, 140(2):386–406, 2015. ISSN 13645528. doi:10.1039/c4an01079e.

[161] Judith Langer, Dorleta Jimenez De Aberasturi, Javier Aizpurua, Ramon A. Alvarez-Puebla, Baptiste Auguié, Jeremy J. Baumberg, Guillermo C. Bazan, Steven E.J. Bell, Anja Boisen, Alexandre G. Brolo, Jaebum Choo, Dana Cialla-May, Volker Deckert, Laura Fabris, Karen Faulds, F. Javier García De Abajo, Royston Goodacre, Duncan Graham, Amanda J. Haes, Christy L. Haynes, Christian Huck, Tamitake Itoh, Mikael Käll, Janina Kneipp, Nicholas A. Kotov, Hua Kuang, Eric C. Le Ru, Hiang Kwee Lee, Jian Feng Li, Xing Yi Ling, Stefan A. Maier, Thomas Mayerhöfer, Martin Moskovits, Kei Murakoshi, Jwa Min Nam, Shuming Nie, Yukihiro Ozaki, Isabel Pastoriza-Santos, Jorge Perez-Juste, Juergen Popp, Annemarie Pucci, Stephanie Reich, Bin Ren, George C. Schatz, Timur Shegai, Sebastian Schlücker, Li Lin Tay, K. George Thomas, Zhong Qun Tian, Richard P. Van Duyne, Tuan Vo-Dinh, Yue Wang, Katherine A. Willets, Chuanlai Xu, Hongxing Xu, Yikai Xu, Yuko S. Yamamoto, Bing Zhao, and Luis M. Liz-Marzán. Present and Future of Surface-Enhanced Raman Scattering. *ACS Nano*, 2019. ISSN 1936086X. doi:10.1021/acsnano.9b04224.

[162] M. Moskovits and J. S. Suh. Surface selection rules for surface-enhanced Raman spectroscopy: Calculations and application to the surface-enhanced Raman spectrum of phthalazine on silver. *Journal of Physical Chemistry*, 88(23):5526–5530, 1984. ISSN 00223654. doi:10.1021/j150667a013.

[163] João Conde, Chenchen Bao, Daxiang Cui, Pedro V. Baptista, and Furong Tian. Antibody-drug gold nanoantennas with Raman spectroscopic fingerprints for in vivo tumour theranostics. *Journal of Controlled Release*, 183(1):87–93, 2014. ISSN 18734995. doi:10.1016/j.jconrel.2014.03.045.

[164] Yufei Ma, Jie Huang, Saijie Song, Huabing Chen, and Zhijun Zhang. Cancer-Targeted Nanotheranostics: Recent Advances and Perspectives. *Small*, 12(36):4936–4954, 2016. ISSN 16136829. doi:10.1002/smll.201600635.

[165] Jie Gao, Maria Sanchez-Purra, Hao Huang, Shunhao Wang, Yunan Chen, Xuefeng Yu, Qian Luo, Kimberly Hamad-Schifferli, and Sijin Liu. Synthesis of different-sized gold nanostars for Raman bioimaging and photothermal therapy in cancer nanotheranostics. *Science China Chemistry*, 60(9):1219–1229, 2017. ISSN 18691870. doi:10.1007/s11426-017-9088-x.

[166] T. Nagy-Simon, M. Potara, A. M. Craciun, E. Licarete, and S. Astilean. IR780-dye loaded gold nanoparticles as new near infrared activatable nanotheranostic agents for simultaneous photodynamic and photothermal therapy and intracellular tracking by surface enhanced resonant Raman scattering imaging. *Journal of Colloid and Interface Science*, 517:239–250, 2018. ISSN 10957103. doi:10.1016/j.jcis.2018.02.007.

[167] Liron Zada, Heather A. Leslie, A. Dick Vethaak, Gerjen H. Tinnevelt, Jeroen J. Jansen, Johannes F. de Boer, and Freek Ariese. Fast microplastics identification with stimulated Raman scattering microscopy. *Journal of Raman Spectroscopy*, 49:1136– 1144, 2018. ISSN 03770486. doi:10.1002/jrs.5367.

[168] Anthony L. Andrady. Microplastics in the marine environment. *Marine Pollution Bulletin*, 62(8):1596–1605, 2011. ISSN 0025326X. doi:10.1016/j.marpolbul.2011.05.030. URL http://dx.doi.org/10.1016/j.marpolbul.2011.05.030.

[169] Mark Anthony Browne, Phillip Crump, Stewart J. Niven, Emma Teuten, Andrew Tonkin, Tamara Galloway, and Richard Thompson. Accumulation of microplastic on shorelines woldwide: Sources and sinks. *Environmental Science and Technology*, 45(21):9175–9179, 2011. ISSN 0013936X. doi:10.1021/es201811s.

[170] Filipa Bessa, Pablo Barr, João M Neto, P G L Frias, Vanessa Otero, Paula Sobral, and João Carlos Marques. Microplastics in juvenile fish from an estuarine environment. *Proceedings of the International Conference on Microplastic Pollution in the Mediterranean Sea*, 128(October 2017):131–135, 2018. ISSN 0025326X. doi:10.1007/978-3-319-71279-6. URL http://link.springer.com/10.1007/978-3-319-71279-6.

[171] GESAMP. Sources, fate and effects of MP in the marine environment: A global assessment. *Journal Series GESAMP Reports and Studies*, 90:98, 2015. ISSN 1020–4873. URL www.imo.org.

[172] Valeria Hidalgo-Ruz, Lars Gutow, Richard C. Thompson, and Martin Thiel. Microplastics in the Marine Environment: A Review of the Methods Used for Identification and Quantification. *Environmental Science & Technology*, 46(6):3060–3075, 2012. ISSN 0013-936X. doi:10.1021/es2031505.

[173] Young Kyoung Song, Sang Hee Hong, Mi Jang, Gi Myung Han, Manviri Rani, Jongmyoung Lee, and Won Joon Shim. A comparison of microscopic and spectroscopic identification methods for analysis of microplastics in environmental samples. *Marine Pollution Bulletin*, 93(1-2):202–209, 2015. ISSN 18793363. doi:10.1016/j.marpolbul.2015.01.015. URL `http://dx.doi.org/10.1016/j.marpolbul.2015.01.015`.

[174] Catarina F. Araujo, Mariela M. Nolasco, Antonio M.P. Ribeiro, and Paulo J.A. Ribeiro-Claro. Identification of microplastics using Raman spectroscopy: latest developments and future prospects. *Water Research*, 142:426–440, 2018. ISSN 00431354. doi:10.1016/j.watres.2018.05.060.

[175] Darena Schymanski, Christophe Goldbeck, Hans-Ulrich Humpf, and Peter Fürst. Analysis of microplastics in water by micro-Raman spectroscopy: Release of plastic particles from different packaging into mineral water. *Water Research*, 129:154–162, 2018. ISSN 9031220280. doi:https://doi.org/10.1016/j.watres.2017.11.011.

[176] L. Frère, I. Paul-Pont, J. Moreau, P. Soudant, C. Lambert, A. Huvet, and E. Rinnert. A semi-automated Raman micro-spectroscopy method for morphological and chemical characterizations of microplastic litter. *Marine Pollution Bulletin*, 113(1-2):461–468, 2016. ISSN 18793363. doi:10.1016/j.marpolbul.2016.10.051.

[177] Morgan Tardivel, Florent Colas, and Emmanuel Rinnert. La spectroscopie Raman pour l'environnement marin. *Photoniques (96)*, pages 30–33, 2019.

[178] R Lenz, K Enders, CA Stedmon, DMA Mackenzie, and TG Nielsen. A critical assessment of visual identification of marine microplastic using Raman spectroscopy for analysis improvement. *Marine Pollution Bulletin*, 100(1):82–91, 2015.

[179] Shiye Zhao, Meghan Danley, J. Evan Ward, Daoji Lia, and Tracy J. Mincer. An approach for extraction, characterization and quantitation of microplastic in natural marine snow using Raman microscopy. *Anal. Methods*, 9:1470–1478, 2017.

[180] Paulo Ribeiro-Claro, Mariela M. Nolasco, and Catarina Araújo. Characterization of Microplastics by Raman Spectroscopy. *Comprehensive Analytical Chemistry*, 75(November): 119–151, 2017. ISSN 0166526X. doi:10.1016/bs.coac.2016.10.001.

[181] Philippe Réfrégier and Frédéric Galland. Bhattacharyya bound for Raman spectrum classification with a couple of binary filters. *Opt. Lett.*, (April), 2019.

[182] Frederic Galland, Philippe Réfrégier, and Emmanuel Chevallier. A compressed Raman classification method with upper bounded error probability. *Optics Letters*, 2019.

[183] Jeffrey Sanders, Ronald G Driggers, and Steven Griffin. Imaging with frequency-modulated reticles. 30(11):1720–1724, 1991.

[184] Greg Futia, Philip Schlup, David G Winters, and Randy a Bartels. Spatially-chirped modulation imaging of absorbtion and fluorescent objects on single-element optical detector. *Optics express*, 19(2):1626–1640, 2011. ISSN 1094-4087. doi:10.1364/OE.19.001626.

[185] Camille Scotté, Siddharth Sivankutty, Patrick Stockton, Randy A. Bartels, and Hervé Rigneault. Compressive Raman imaging with spatial frequency modulated illumination. 44(8):1936–1939, 2019. doi:10.1364/OL.44.001936. URL http://arxiv.org/abs/1901.06828.

[186] J Grainger, J Ring, and J Stell. A multiplex grating spectrometer. *Journal de Physique Colloques*, 28, 1967. doi:10.1051/jphyscol:1967209.

[187] M. J. Selby and L. W. Thorpe. A Telescope Mounted Mock Interferometer for Use on Extended Sources. *Le Journal de Physique Colloques*, 28(C2):144–149, 1967. ISSN 0449-1947. doi:10.1051/jphyscol:1967226.

[188] M. J. Selby. Mock interferometer-I theory. Technical Report 1, 1966.

[189] Daniel J. Higley, David G. Winters, Gregory L. Futia, and Randy A. Bartels. Theory of diffraction effects in spatial frequency-modulated imaging. *Journal of the Optical Society of America A*, 29(12):2579, 2012. ISSN 1084-7529. doi:10.1364/josaa.29.002579.

[190] Daniel J Higley, David G Winters, and Randy A Bartels. Two-dimensional spatial-frequency-modulated imaging through parallel acquisition of line images. *Opt. Lett.*, 38 (11):1763–1765, 2013. doi:10.1364/OL.38.001763.

[191] Jeffrey J. Field, David G. Winters, and Randy A. Bartels. Single-pixel fluorescent imaging with temporally labeled illumination patterns. *Optica*, 3(9):971, 2016. ISSN 2334-2536. doi:10.1364/OPTICA.3.000971.

[192] Jeffrey J. Field, David G. Winters, and Randy A. Bartels. Plane wave analysis of coherent holographic image reconstruction by phase transfer (CHIRPT). *Journal of the Optical Society of America A*, 32(11):2156, 2015. ISSN 1084-7529. doi:10.1364/JOSAA.32.002156.

[193] Ori Katz, Jonathan M. Levitt, and Yaron Silberberg. Compressive fourier transform spectroscopy. *Optics InfoBase Conference Papers*, 2010. ISSN 21622701. doi:10.1364/fio.2010.ftue3.

[194] Maxim Raginsky, Rebecca M Willett, Zachary T Harmany, and Roummel F Marcia. Compressed Sensing Performance Bounds Under Poisson Noise. *IEEE Transactions on Signal Processing*, 58(8):3990–4002, 2010.

[195] Nathan Hagen and Michael W. Kudenov. Review of snapshot spectral imaging technologies. *Optical Engineering*, 52(9):090901, 2013. ISSN 0091-3286. doi:10.1117/1.oe.52.9.090901.

[196] Xiaohan Li, Joel A. Greenberg, and Michael E. Gehm. Single-shot multispectral imaging through a thin scatterer. *Optica*, 6(7):864, 2019. ISSN 2334-2536. doi:10.1364/OPTICA.6.000864.

[197] Marco F. Duarte and Richard G. Baraniuk. Kronecker compressive sensing. *IEEE Transactions on Image Processing*, 21(2):494–504, 2012. ISSN 10577149. doi:10.1109/TIP.2011.2165289.

[198] Daniel D. Lee and H. Sebastian Seung. Learning the parts of objects by non-negative matrix factorization. *Nature*, 401(6755):788–791, 1999. ISSN 00280836. doi:10.1038/44565.

[199] Yang Cao and Yao Xie. Poisson matrix completion. *IEEE International Symposium on Information Theory - Proceedings*, 2015-June(6):1841–1845, 2015. ISSN 21578095. doi:10.1109/ISIT.2015.7282774.

[200] Emmanuel J. Candès and Terence Tao. The power of convex relaxation: Near-optimal matrix completion. *IEEE Transactions on Information Theory*, 56(5):2053–2080, 2010. ISSN 00189448. doi:10.1109/TIT.2010.2044061.

[201] P Jacquinot. Progrès récents en spectroscopie interférentielle. In *Conference of photographic and spectroscopic optics*, volume 4, pages 401–411, 1964.

[202] G Roland. Réflexions sur quelques problèmes rencontrés en spectroscopie par transformation de Fourier. *Journal de Physique*, 28, 1967.

[203] P Connes. Astronomical Fourier Spectroscopy. Technical report, 1970.

[204] P. Fellgett. Conclusions on Multiplex Methods. *Le Journal de Physique Colloques*, 28 (C2):C2–165–C2–171, 1967. ISSN 0449-1947. doi:10.1051/jphyscol:1967230.

[205] N M Larson, R Crosmun, and Y Talmi. Theoretical comparison of singly multiplexed hadamard transform spectrometers and scanning spectrometers. *Applied optics*, 13(11): 2662–8, 1974. ISSN 0003-6935. doi:10.1364/AO.13.002662.

[206] N J Sloane and M Harwit. Masks for Hadamard transform optics, and weighing designs. *Applied optics*, 15(1):107–114, 1976. ISSN 0003-6935. doi:10.1364/AO.15.000107.

[207] E. D. Nelson and M. L. Fredman. Hadamard Spectroscopy. *Journal of the Optical Society of America*, 60(12):1664, 1970. ISSN 0030-3941. doi:10.1364/JOSA.60.001664.

[208] J. A. Decker. Experimental realization of the multiplex advantage with a hadamard-transform spectrometer. *Applied optics*, 10(3):510–514, 1971. ISSN 0003-6935. doi:10.1364/AO.10.000510.

[209] Martin Harwit and J. A. Decker. Modulation Techniques in Spectrometry. *Progress in Optics*, 1974.

[210] J. A. Decker and Hadamard-transform Image-line Coding. Hadamard-Transform Image Scanning. *Applied Optics*, 9(6):1392–1395, 1970. ISSN 00036935.

[211] B E Krivenkov, P E Tverdokhleb, and Yu V. Chugui. Analysis of images by Hadamard optical transform. *Applied Optics*, 14(8):1829–1834, 1975.

[212] Schechner, Nayar, and Belhumeur. A theory of multiplexed illumination. *Proceedings Ninth IEEE International Conference on Computer Vision*, (Iccv):808–815 vol.2, 2003. doi:10.1109/ICCV.2003.1238431.

[213] B. Sun, M. P. Edgar, R. Bowman, L. E. Vittert, S. Welsh, A. Bowman, and M. J. Padgett. 3D computational imaging with single-pixel detectors. *Science*, 340(6134):844–847, 2013. ISSN 10959203. doi:10.1126/science.1234454.

[214] Ming-Jie Sun, Matthew P. Edgar, David B. Phillips, Graham M. Gibson, and Miles J. Padgett. Improving the signal-to-noise ratio of single-pixel imaging using digital microscanning. *Optics Express*, 24(10):10476, 2016. ISSN 1094-4087. doi:10.1364/oe.24.010476.

[215] Ming Jie Sun, Matthew P. Edgar, Graham M. Gibson, Baoqing Sun, Neal Radwell, Robert Lamb, and Miles J. Padgett. Single-pixel three-dimensional imaging with time-based depth resolution. *Nature Communications*, 7(May):1–6, 2016. ISSN 20411723. doi:10.1038/ncomms12010.

[216] Neal Radwell, Kevin J. Mitchell, Graham M. Gibson, Matthew P. Edgar, Richard Bowman, and Miles J. Padgett. Single-pixel infrared and visible microscope. *Optica*, 1(5):285, 2014. ISSN 2334-2536. doi:10.1364/optica.1.000285.

[217] Sadao Ota, Ryoichi Horisaki, Yoko Kawamura, Masashi Ugawa, Issei Sato, Kazuki Hashimoto, Ryosuke Kamesawa, Kotaro Setoyama, Satoko Yamaguchi, Katsuhito Fujiu, Kayo Waki, and Hiroyuki Noji. Ghost cytometry. *Science*, 360(6394):1246–1251, 2018. ISSN 0036-8075. doi:10.1126/science.aan0096.

[218] Qi Pian, Ruoyang Yao, Nattawut Sinsuebphon, and Xavier Intes. Compressive hyperspectral time-resolved wide-field fluorescence lifetime imaging. *Nature Photonics*, 11(7): 411–414, 2017. ISSN 17494893. doi:10.1038/nphoton.2017.82.

[219] Zibang Zhang, Xueying Wang, Guoan Zheng, and Jingang Zhong. Hadamard single-pixel imaging versus Fourier single-pixel imaging. *Optics Express*, 25(16):19619–19639, 2017. ISSN 1094-4087. doi:10.1364/OE.25.019619.

[220] Dong Xiang and Mark A. Arnold. Solid-state digital micro-mirror array spectrometer for hadamard transform measurements of glucose and lactate in aqueous solutions. *Applied Spectroscopy*, 65(10):1170–1180, 2011. ISSN 00037028. doi:10.1366/11-06340.

[221] Erik T. Garbacik, Maria Sanz-Paz, Kyra J.E. Borgman, Felix Campelo, and Maria F. Garcia-Parajo. Frequency-Encoded Multicolor Fluorescence Imaging with Single-Photon-Counting Color-Blind Detection. *Biophysical Journal*, pages 1–12, 2018. ISSN 00063495. doi:10.1016/j.bpj.2018.07.008.

[222] Philip Wijesinghe, Adrià Escobet-Montalbán, Mingzhou Chen, Peter R T Munro, and Kishan Dholakia. Optimal compressive multiphoton imaging at depth using single-pixel detection. pages 1–12, 2019. URL http://arxiv.org/abs/1907.02272.

[223] Matthew P. Edgar, Graham M. Gibson, and Miles J. Padgett. Principles and prospects for single-pixel imaging. *Nature Photonics*, 13(1):13–20, 2019. ISSN 17494893. doi:10.1038/s41566-018-0300-7.

[224] E. Voigtman and J. D. Winefordner. The Multiplex Disadvantage and Excess Low-Frequency Noise. *Applied Spectroscopy*, 41(7):1182–1184, 1987.

[225] Lw Schumann and Ts Lomheim. Infrared hyperspectral imaging Fourier transform and dispersive spectrometers: comparison of signal-to-noise-based performance. *International Symposium on Optical Science and Technology*, 4480(310):1–14, 2002. ISSN 0277786X. doi:10.1117/12.453326.

[226] Günter Nitzsche, Rainer Riesenberg, Physical High, and D Jena. Noise , Fluctuation and Hadamard-Transform-Spectrometry. In *Fluctuations and Noise in Photonics and Quantum Optics*, volume 5111, pages 273–282, 2003.

[227] Andreas Wuttig. Optimal transformations for optical multiplex measurements in the presence of photon noise. *Applied Optics*, 44(14):2710, 2005. ISSN 0003-6935. doi:10.1364/AO.44.002710.

[228] L Streeter, G R Burling-Claridge, M J Cree, and R Künnemeyer. Optical full Hadamard matrix multiplexing and noise effects. *Applied Optics*, 48(11), 2009.

[229] Netanel Ratner and Yoav Y. Schechner. Illumination multiplexing within fundamental limits. *Proceedings of the IEEE Computer Society Conference on Computer Vision and Pattern Recognition*, 2007. ISSN 10636919. doi:10.1109/CVPR.2007.383162.

[230] Stephen E Bialkowski. Overcoming the multiplex disadvantage by using maximum-likelihood inversion. *Applied Spectroscopy*, 52(4):591–598, 1998.

[231] Daniel R Fuhrmann, Chrysanthe Preza, Joseph A O'sullivan, Donald L Snyder, and William H Smith. Spectrum Estimation from Quantum-Limited Interferograms. *IEEE TRANSACTIONS ON SIGNAL PROCESSING*, 52(4):950–961, 2004. doi:10.1109/TSP.2004.824216.

[232] Jeffrey H Shapiro. Computational Ghost Imaging. 2008.

[233] Ori Katz, Yaron Bromberg, and Yaron Silberberg. Compressive ghost imaging. *Applied Physics Letters*, 95(13), 2009. ISSN 00036951. doi:10.1063/1.3238296.

[234] T Hirschfeld. Fellgett's Advanatge in UV-VIS Multiplex Spectroscopy. *Applied Spectroscopy*, 10(1):68–68, 1976.

[235] F. D. Kahn. The Signal: Noise Ratio of a Suggested Spectral Analyzer. *The Astrophysical Journal*, 129(4):518, 1959. ISSN 0004-637X. doi:10.1086/146649.

[236] Janine Connes and Pierre Connes. Near-Infrared Planetary Spectra by Fourier Spectroscopy I Instruments and Results. *Journal of the Optical Society of America*, 56(7):896, 1966. ISSN 0030-3941. doi:10.1364/josa.56.000896.

[237] Dongeek Shin, Ahmed Kirmani, and Vivek K. Goyal. Low-rate Poisson intensity estimation using multiplexed imaging. In *ICASSP, IEEE International Conference on Acoustics, Speech and Signal Processing - Proceedings*, pages 1364–1368, 2013. ISBN 9781479903566. doi:10.1109/ICASSP.2013.6637874.

[238] Ching-Shui Cheng. An application of the Kiefer-Wolfowitz equivalence theorem to a problem in Hadamard transform optics. *The Annals of Statistics*, 15(4):1593–1603, 1987.

[239] Roman Drnovšek. On the S-matrix conjecture. pages 1–6, 2013. URL `http://arxiv.org/abs/1306.6786`.

[240] Netanel Ratner, Yoav Y Schechner, and Felix Goldberg. Optimal multiplexed sensing: bounds, conditions and a graph theory link. *Optics express*, 15(25):17072–17092, 2007. ISSN 1094-4087. doi:10.1364/OE.15.017072.

[241] Moran Mordechay and Yoav Y. Schechner. Matrix optimization for poisson compressed sensing. *2014 IEEE Global Conference on Signal and Information Processing, GlobalSIP 2014*, (8):684–688, 2014. doi:10.1109/GlobalSIP.2014.7032205.

[242] W. H. Richardson. Bayesian-Based Iterative Method of Image Restoration. *Journal of the Optical Society of America*, 62(1):55–59, 1972. ISSN 0391-5603. doi:10.5301/ru.2013.11151.

[243] L. B. Lucy. An iterative technique for the rectification of observed distributions. *The Astronomical Journal*, 79(6):745–754, 1974. ISSN 00358711. doi:10.1046/j.1365-8711.2001.04506.x.

[244] L. A Shepp and Y. Vardi. Maximum Likelihood Reconstruction for Emission Tomography. *Ieee Transactions on Medical Imaging*, MI-1(2):113–122, 1982. ISSN 0278-0062. doi:10.1007/978-3-319-66005-9_18.

[245] Geoffrey J. McLachlan and Thriyambakam Krishnan. *The EM Algorithm and Extensions*. John Wiley & Sons, Ltd, second edi edition, 2007. ISBN 9780471201700. doi:10.1002/9780470191613.

[246] Stephen E. Bialkowski. Expectation Maximization algorithm for regression, deconvolution and smoothing of shot-noise limited data. *Journal of Chemometrics*, 5(3):211–225, 1991.

[247] Zachary T. Harmany, Roummel F. Marcia, and Rebecca M. Willett. This is SPIRAL-TAP: Sparse poisson intensity reconstruction algorithms-theory and practice. *IEEE Transactions on Image Processing*, 21(3):1084–1096, 2012. ISSN 10577149. doi:10.1109/TIP.2011.2168410.

[248] Maxim Raginsky, Rebecca M. Willett, Zachary T. Harmany, and Roummel F. Marcia. Compressed sensing performance bounds under Poisson noise. pages 1–12, 2009. ISSN 1053587X. doi:10.1109/TSP.2010.2049997. URL `http://arxiv.org/abs/0910.5146{%}0Ahttp://dx.doi.org/10.1109/TSP.2010.2049997`.

[249] Michele Lacerenza. Design and Optimization of a Compressive Sensing Time Domain Raman Spectrometer (CS-TDRS) for fast probing of thick diffusive media - Master Thesis. Technical Report 874703, 2018.

[250] Ji Xin Cheng, Eric O. Potma, and Sunney X. Xie. Coherent anti-Stokes Raman scattering correlation spectroscopy: Probing dynamical processes with chemical selectivity. *Journal of Physical Chemistry A*, 106(37):8561–8568, 2002. ISSN 10895639. doi:10.1021/jp025774b.

[251] Ryan D. Palkki. Minimum description length approach to detecting chemicals via their Raman spectra. *Optical Engineering*, 50(8):083601, 2011. ISSN 0091-3286. doi:10.1117/1.3609805.

[252] Mikhail Konnik and James Welsh. High-level numerical simulations of noise in CCD and CMOS photosensors: review and tutorial. pages 1–21, 2014. URL `http://arxiv.org/abs/1412.4031`.

[253] Mark Stanford Robbins, Senior Member, and Benjamin James Hadwen. The Noise Performance of Electron Multiplying Charge-Coupled Devices. *IEEE Transactions on Electron Devices*, 50(5):1227–1232, 2003.